Flexible nanowire light emitting diodes

Julien Bosch

To cite this version:

Julien Bosch. Flexible nanowire light emitting diodes. Physics [physics]. Université Côte d'Azur, 2023. English. NNT : 2023COAZ4111 . tel-04521075

HAL Id: tel-04521075
https://theses.hal.science/tel-04521075

Submitted on 26 Mar 2024

UNIVERSITÉ CÔTE D'AZUR

ÉCOLE DOCTORALE SCIENCES FONDAMENTALES ET APPLIQUÉES

THÈSE DE DOCTORAT

Diodes électroluminescentes flexibles à base de nanofils

Julien BOSCH

Centre de Recherche sur l'Hétéroépitaxie et ses Applications, (CRHEA), CNRS

Présentée en vue de l'obtention du grade de docteur Matériaux d'Université Côte d'Azur
Dirigée par : Jesús Zúñiga-Pérez / Blandine Alloing
Co-encadrée par : Christophe Durand
Soutenue le : 06/12/2023

Devant le jury, composé de :
Agnès Trassoudaine, Professeure, Université Clermont Auvergne
Hannah Joyce, Professeure, University of Cambridge
Amélie Dussaigne, Ingénieure de recherche, Commissariat à l'énergie atomique et aux énergies alternatives (CEA)
Maria Tchernycheva, invitée, Directrice de recherches, Centre de Nanosciences et de Nanotechnologies (C2N)

Diodes électroluminescentes flexibles à base de nanofils

Jury:

Rapporteurs :
Agnès Trassoudaine, Professeure, Université Clermont Auvergne
Hannah Joyce, Professeure, University of Cambridge

Examinateurs :
Amélie Dussaigne, Ingénieure de recherche, Commissariat à l'Energie Atomique et aux Energies Alternatives (CEA)

Invités :
Maria Tchernycheva, Directrice de recherches, Centre de Nanosciences et de Nanotechnologies (C2N)

Diodes électroluminescentes flexibles à base de nanofils

Les dispositifs flexibles ont connu un essor durant la dernière décennie, justifié par la promesse de nouvelles applications. Parmi ses applications, on retrouve des produits de consommation pour particuliers, tels que des textiles intelligents et écrans flexibles, mais également des produits médicaux, tels que les capteurs dits « sur-peau » ou certains autres dispositifs tels que des implants cochléaires optogénétiques.

En ce qui concerne les LEDs, certains procédés ont permis d'aboutir à la construction de dispositifs flexibles fonctionnels, prouvant ainsi la faisabilité du projet. Ces dispositifs sont produits par encapsulation de structures InGaN/GaN à nanofils dans une matrice élastomère, conférant au dispositif les propriétés mécaniques de cette dernière, tout en rendant possible l'émission lumineuse. Les structures sont alors arrachées de leur substrat lors du procédé dit du « peel off ». Dans ces premières études, il a été choisi d'utiliser un procédé de croissance dit autoorganisé pour la fabrication des nanofils. Cette approche permet d'obtenir des structures de grande taille avec une distribution aléatoire, ce qui est avantageux pour l'encapsulation du dispositif. En revanche, cette géométrie avantageuse est obtenue au prix de l'homogénéité des propriétés des nanofils, ce qui signifie que la longueur d'onde d'émission ainsi que l'intensité lumineuse ne sont pas constantes sur la surface du dispositif.

Dans ce doctorat, il a été fixé pour but de réaliser des dispositifs similaires, mais en utilisant des nanofils crus par croissance dite sélective. Cette approche permet de contrôler le positionnement des structures ainsi que d'assurer une grande homogénéité des propriétés. En revanche les dimensions et le positionnement rapproché des structures les unes des autres introduisent des nouvelles problématiques par rapport aux précédents dispositifs, notamment pour l'encapsulation.

Quatre axes de travails ont été choisis dans ce projet :

-Dans un premier temps, une étude du procédé de croissance des nanofils a été réalisée. Cette étude vise à préciser les connaissances concernant la croissance verticale de structures n-GaN par dopage Si.

-Dans un second temps, les connaissances acquises durant cette étude ont été mises à profit pour optimiser la croissance de la coquille, contenant l'hétérostructure active InGaN/GaN ainsi que la couche p-GaN.

-Ces deux études permettant d'optimiser les différentes étapes de la réalisation des structures, il a été choisi ensuite d'utiliser les structures obtenues pour la réalisation de dispositifs flexibles par encapsulation et peel off. L'optimisation du procédé et la mesure de performance des dispositifs obtenus ont été menées à bien et sont détaillées dans ce manuscrit.

-Dans un dernier temps, une étude de la croissance de structures InGaN/GaN a été réalisée sur substrat 2D, particulièrement ici sur graphène. Ce mode de croissance innovant permet de s'affranchir des liaisons covalentes entre le substrat et les matériaux épitaxiés, qui représentent typiquement un obstacle lors de l'étape de peel off.

A la suite de ces différents axes de travail, nous espérons fournir au lecteur une compréhension générale des méthodes et problématiques liées à la croissance de structures InGaN/GaN à nanofils, des défis liés à la fabrication de dispositifs flexibles, et de certaines des approches mises en place dès l'étape de croissance pour contourner ces défis.

Mots Clés:

Nanofils, Puits quantiques, Semiconducteurs, LED

Flexible nanowire light emitting diodes

Flexible devices have boomed in the last decade, motivated by promises of new applications. Among these applications, consumer products can be noted, such as smart textiles and flexible screens, but also medical products, such as so called “on-skin” sensors or devices such as optogenetic cochlear implants.

Regarding LEDs, some processes have allowed to build operating flexible devices, hence demonstrating the feasibility of the project. These devices are made through the encapsulation of InGaN/GaN nanowire structures in an elastomer matrix, giving to the device the mechanical properties of the latter, while enabling light emission. The structures are then ripped from the substrate, through a process called the “peel off”. In these firsthand reports, it was chosen to work with a so called self-assembled growth process for nanowire fabrication. This approach yields structures with important lengths and a random distribution, which is an advantage for encapsulation of the device. However, this advantageous geometry comes at the cost of the homogeneity of the properties of the nanowires, meaning that the wavelength and intensities are not constant on the whole device.

In this PhD, the goal that was set is to fabricate similar devices, but instead using nanowires grown through selective area growth. This method allows to control the position of the structure and ensures high homogeneity of properties. However, the dimension and close spacing of the structures introduce a new issue compared to the previous devices, particularly for encapsulation.

Four areas of work were defined in this project:

- First, a study of the growth process of the nanowires was conducted. This study aims to precise the knowledge regarding vertical growth of Si-doped n-GaN.

-Second, the knowledge acquired in the first study is used to optimize the growth of the shell, which contains the active InGaN/GaN heterostructure as well as the p-GaN layer.

- These two studies allow to optimize each step of the fabrication of the structure, and it was therefore decided to use the obtained samples for the elaboration of flexible devices through encapsulation and peel off. Optimization of the process and characterization of the performances of the obtained device were carried and detailed in this manuscript.

- Last, an investigation of the growth of InGaN/GaN structures was realized on 2D substrates, in the present case on graphene. This innovative growth mode allows to work without covalent bonding between the substrate and the epitaxial material, which hinders the peel off.

Following these work areas, we hope to provide the reader with a general understanding of the methods and problems linked to the growth of InGaN/GaN nanowire structures, of the challenges linked to the fabrication of flexible devices, and of the alternative approaches used as early as the growth stage to avoid these issues.

Keywords:

Nanowires, Quantum Wells, Semiconductors, LED

Contents:

Chapter 3: Effect of Si on GaN nanowires core growth 99

Chapter 4: Toward fully emissive core-shell nanowire structures 123

Chapter 5:From a core shell nanowire heterostructure to a flexible LED 144

Introduction:

In recent years, the fabrication of flexible devices has been a subject of growing interest[1,2]. In electronics, they provide a wide variety of new possibilities ranging from consumer products to medical applications including skin sensors. In the particular case of LEDs, the development of flexible displays is very attractive for the consumer market. In the medical domain in particular, recent improvements in the field of optogenetics[3] represent a new application for flexible light sources. With this technic, neural cells can be genetically modified to be stimulated or inhibited by visible light. Is it thus now possible to transmit a signal from an optoelectronic system to a neuronal system. This approach is particularly interesting, as it does not require any physical contact or chemical exchange between the electronic system and the neurons. This approach is already being studied for applications such as cochlear implants[4], which could allow for a breakthrough in solving partial and complete auditory losses. The use of visible InGaN/GaN heterostructures for this specific process is relevant, as there is already a known process to make neurons sensitive to blue light. Indeed, the genetically modified neurons are able to express Channelrhodopsin-2[5], a protein with a fast response time and a sensitivity between 400 and 500 nm[6], which is the range of maximum efficiency for light emission in InGaN/GaN QWs[7]. However, while InGaN/GaN LEDs are a promising candidate for cochlear implants, the shape and dimensions of the cochlea requires the device to be small and flexible [4].

In the case of flexible devices, several geometries have been used[8–10], but the one that is the most fulfilling for this application is the micro/nanowire geometry[11]. Indeed, this configuration allows to easily encapsulate the semiconducting structure in a flexible polymer and separate it from its substrate. The footprint of the structure is of micrometric scale, which allows for a lower cohesion with the substrate and an easier separation. The footprint is also orders of magnitude lower than the aimed radius of curvature for these devices, and they hence suffer little strain when bending the device. Last, they take advantage of their longitudinal geometry to reach large emission areas despite a small footprint.

In most of the devices presented in the literature, the nanowires used for light emission were grown through a self-organized process[11–14]. Using the MOCVD growth technique, this process allows to grow nanowires with significant length, easily reaching several tens of micrometer. This, along with a low spatial density and a random distribution allow for an easy encapsulation and subsequent peel-off. However, this is done at the cost of the optical properties, which are inhomogeneous and may result in variations of wavelength and light intensity across a single device.

We thus propose an approach based on the selective area growth of GaN by MOCVD: the nanowires positions are determined by the pattern performed in a dielectric mask, on which growth takes place[15]. The main advantage of this process is that it offers a high homogeneity of the nanostructure properties. On the other hand, the structures are usually smaller than what is achieved in self-organized growth, with heights of the order of 10 µm. This is usually compensated by a high density of structures, which allow to get larger emission areas than what would be obtainable on a planar device of the same size[16]. However, the large nanowire density introduces complications in the use of liquids due to capillary effects, which are enhanced by the close spacing between nanowires[17]. Hence, using such structures in the fabrication of flexible devices bring about numerous advantages in terms of properties homogeneity and absolute figures of merit, but requires an optimization to address the new challenges posed by this alternative approach.

In this PhD, we aim at a complete optimization of the different processes that would be used in the fabrication of a SAG based nanowire flexible device, including the growth. The work carried out is presented in 6 chapters:

- In Chapter I, the basis for understanding the material physics discussed in this manuscript are introduced. This is presented through three separated parts. In the first one, the general properties of nitrides will be introduced. The method for growth, including processes and substrates will then be presented. Last, the basic theory for the different processes for nanowire fabrication will be given.
- In Chapter II, the background on the selective area growth of nanowires by MOCVD will be provided. In the second part of the chapter, the basic methods used for the characterization of the heterostructures will be presented.
- Chapter III focuses on the specific case of Si-assisted core nanowire growth. Indeed, nanowire growth is commonly assisted by the growth of a sidewall dielectric layer, which precise nature was unknown at the beginning of this PhD. In this chapter, an investigation on the properties of this layer is provided. The observations made during these studies also allowed to gain some new insight on the kinetics of nanowire growth, and an updated model for GaN nanowire growth by MOCVD is presented.
- In Chapter IV, an optimization of the shell is presented in light of the results obtained while studying core growth. A new step is introduced during the process of growth, leading to an extended area of emission on the sidewalls of the nanowires, overcoming the main problem encountered by such nanowire-based LEDs up to now.
- Based on these optimizations, new structures were processed for the fabrication of flexible devices, with the aim of fabricating a homogeneous flexible light emitting diode. In Chapter V, the work done toward this goal is presented along with the properties of the obtained sample. An emphasis has been put on the encountered challenges and provided solutions, whenever this was possible. Further, clues to further optimize this process will be also described.
- In Chapter VI, an alternative approach for the realization of GaN-based flexible devices is proposed, i.e. the growth on 2D materials. The main advantage of 2D materials is that they lack dangling bonds, meaning that the growth proceeds without the formation of covalent bonds. This greatly reduces the cohesion between the structures and the substrate, which is advantageous for the peel-off step of the process. Hence, we have investigated the possibility of growth on graphene as an alternative way to produce flexible devices. The obtained results will be analyzed along with a discussion on the properties of the fabricated devices.

The work presented in these chapters has been shared between 3 laboratories, each responsible for a different aspect of the work. These laboratories are the Center of Research on HeteroEpitaxy and its Applications in Valbonne (CRHEA), the Center of Nanoscience and Nanotechnologies of Palaiseau (C2N), and the Grenoble Institute for Interdisciplinary Research (IRIG). The combined expertise of these laboratories allowed to address the different challenges of the PhD. CRHEA is an institute where a variety of epitaxial processes are used, which makes it ideal for the study of selective area growth. Besides, CRHEA features some fine characterization equipment that has been used in this PhD, such as cathodoluminescence or transmission electron microscopy. This work is mainly presented in chapters 3 and 4. C2N hosted the fabrication of devices in their cleanroom. Indeed, being the largest academic cleanroom in France, the C2N facility is the perfect environment for developing and optimizing a variety of cleanroom processes. The C2N has also fabricated flexible LEDs[11] in the past, providing expertise in the fabrication. This work is presented in Chapter 5. Last, IRIG is where the growth on 2D materials was explored. Indeed, IRIG has historically been one of the first laboratories to grow self-assembled nanowires[18] and has experience on growing GaN nanostructures on 2D materials[19]. The graphene was fabricated at the CRHEA by propan-CVD, a process developed by A. Michon[20]. The work done in collaboration between the CRHEA and the IRIG is presented in Chapter 6.

BIBLIOGRAPHY

1. Corzo D, Tostado-Blázquez G, Baran D. Flexible Electronics: Status, Challenges and Opportunities. *Frontiers in Electronics*. 2020;1:594003. doi:https://doi.org/10.3389/felec.2020.594003
2. Wang P, Hu M, Wang H, et al. The Evolution of Flexible Electronics: From Nature, Beyond Nature, and To Nature. *Advanced Science*. 2020;7(20):2001116. doi:https://doi.org/10.1002/advs.202001116
3. Häusser M. Optogenetics: The age of light. *Nat Methods*. 2014;11:1012-1014. doi:https://doi.org/10.1038/nmeth.3111
4. Goßler C, Bierbrauer C, Moser R, et al. GaN-based micro-LED arrays on flexible substrates for optical cochlear implants. *J Phys D Appl Phys*. 2014;47(20):205401. doi:10.1088/0022-3727/47/20/205401
5. Boyden ES, Zhang F, Bamberg E, Nagel G, Deisseroth K. Millisecond-timescale, genetically targeted optical control of neural activity. *Nat Neurosci*. 2005;8:1263-1268. doi:https://doi.org/10.1038/nn1525
6. Bregestovski P, Mukhtarov M. Optogenetics: Perspectives in biomedical research. *Modern Technology in Medicine*. 2016;8(4):212-221. doi:10.17691/stm2016.8.4.26
7. Auf Der Maur M, Pecchia A, Penazzi G, Rodrigues W, Di Carlo A. Efficiency Drop in Green InGaN/GaN Light Emitting Diodes: The Role of Random Alloy Fluctuations. *Phys Rev Lett*. 2016;116(2):027401. doi:10.1103/PhysRevLett.116.027401
8. Chen J, Wang J, Ji K, et al. Flexible, stretchable, and transparent InGaN/GaN multiple quantum wells/polyacrylamide hydrogel-based light emitting diodes. *Nano Res*. 2022;15:5492-5499. doi:https://doi.org/10.1007/s12274-022-4170-4

9. Asad M, Li Q, Sachdev M, Wong WS. Thermal and optical properties of high-density GaN micro-LED arrays on flexible substrates. *Nano Energy*. 2020;73:104724. doi:https://doi.org/10.1016/j.nanoen.2020.104724

10. Chung K, Yoo H, Hyun JK, et al. Flexible GaN Light-Emitting Diodes Using GaN Microdisks Epitaxial Laterally Overgrown on Graphene Dots. *Advanced Materials*. 2016;28(35):7688-7694. doi:https://doi.org/10.1002/adma.201601894

11. Dai X, Messanvi A, Zhang H, et al. Flexible Light-Emitting Diodes Based on Vertical Nitride Nanowires. *Nano Lett*. 2015;15(10):6958-6964. doi:https://doi.org/10.1021/acs.nanolett.5b02900

12. Chung K, Beak H, Tchoe Y, et al. Growth and characterizations of GaN micro-rods on graphene films for flexible light emitting diodes. *APL Mater*. 2014;2(9):092512. doi:https://doi.org/10.1063/1.4894780

13. Jeong J, Wang Q, Cha J, et al. Remote heteroepitaxy of GaN microrod heterostructures for deformable light-emitting diodes and wafer recycle. *Sci Adv*. 2020;6(23). doi:https://doi.org/10.1126/sciadv.aaz5180

14. Lee CH, Kim YJ, Hong YJ, et al. Flexible inorganic nanostructure light-emitting diodes fabricated on graphene films. *Advanced Materials*. 2011;23(40):4614-4619. doi:10.1002/adma.201102407

15. Hersee SD, Sun X, Wang X. The controlled growth of GaN nanowires. *Nano Lett*. 2006;6(8):1808-1811. doi:https://doi.org/10.1021/nl060553t

16. Waag A, Wang X, Fündling S, et al. The nanorod approach: GaN NanoLEDs for solid state lighting. *Physica Status Solidi (C) Current Topics in Solid State Physics*. 2011;8(7-8):2296-2301. doi:https://doi.org/10.1002/pssc.201000989

17. Toshihiko Tanaka, Mitsuaki Morigami, Nobufumi Atoda. Mechanism of Resist Pattern Collapse during Development Process. *Jpn J Appl Phys*. 1993;32(12S):6059. doi:10.1143/JJAP.32.6059

18. Koester R, Hwang JS, Durand C, Le Si Dang D, Eymery J. Self-assembled growth of catalyst-free GaN wires by metal-organic vapour phase epitaxy. *Nanotechnology*. 2010;21(1):015602. doi:10.1088/0957-4484/21/1/015602

19. Barbier C. *Epitaxie de GaN Sur Substrat de Graphène*. Sorbonne Université; 2021. https://theses.hal.science/tel-03469445

20. Michon A, Ѵezian S, Ouerghi A, Zielinski M, Chassagne T, Portail M. Direct growth of few-layer graphene on 6H-SiC and 3C-SiC/Si via propane chemical vapor deposition. *Appl Phys Lett*. 2010;97(17):171909. doi:https://doi.org/10.1063/1.3503972

Chapter 1:

III-Nitride materials: the case of GaN

CONTENTS

In this PhD, we aimed to develop 1D nano-objects with a core-shell geometry in order to build a complex device, being a flexible LED. We sought to take advantage of the properties associated with this morphology combined with the intrinsic properties of the chosen material. To understand choices made in this work, it is therefore necessary to have a first-hand understanding of the properties of the material in these devices. In this chapter, we aim to talk about the basic properties of III-Nitride semiconductor materials with an emphasis on GaN, present the main strategies of growth, and explain how the nanowire geometry came to be the main object of this work.

1. BASIC PROPERTIES

III-nitride is a subclass of III-V materials, consisting of an atom from the Boron group (column III) and an atom from the Nitrogen group (column V), and their alloys. They are found in a wide range of applications because of their tunable direct bandgap[1] and their ability to make high electron mobility components[2]. They are thus used for optoelectronic[3] and power[4] applications. Moreover, the bandgap of this family of materials covers a wide part of the light spectrum ranging from infrared for InN[5] to deep UV for AlN[6], including the visible spectrum. In this part, the properties of III-nitrides and especially of GaN will be presented.

1.1 STRUCTURAL PROPERTIES

1.1.1 CRYSTALLINE STRUCTURE

III-nitrides can crystalize in three forms: Wurtzite, Zinc Blende, and rock-salt. The first one is a hexagonal wurtzite (WZ) lattice, while the two others are cubic structures. However, both the Zinc Blende (ZB) and rock salt configurations are metastables[7,8], and hence less commonly encountered than their WZ counterpart. This document will thus mostly focus on WZ GaN, and it will be considered as the default crystallographic configuration unless specified.

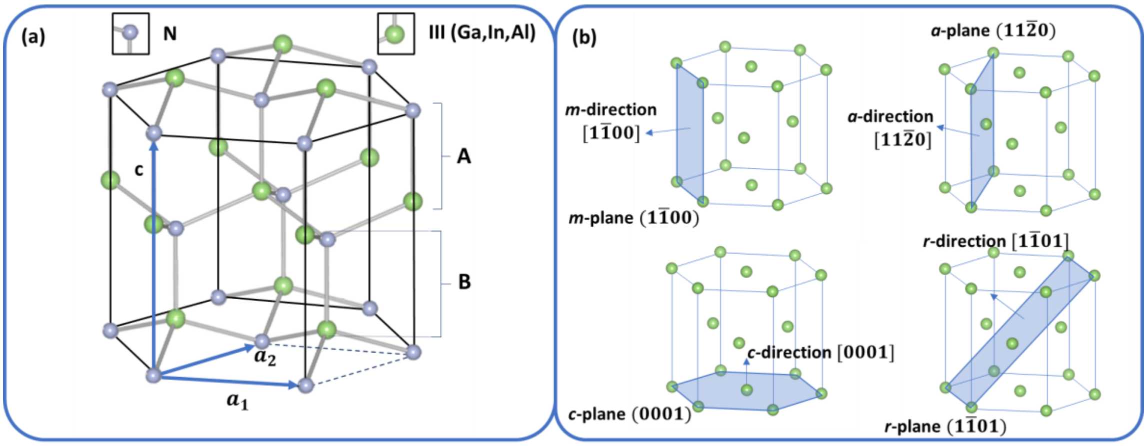

Figure I-1: *Crystallographic structure of WZ III-Nitride(a), main crystallographic planes and their corresponding directions (b). the nitrogen atoms have been removed in (b) for better visual clarity.*

The wurtzite structure is represented in Fig. I-1(a). It can be described using the unit vectors $(\mathbf{a_1}, \mathbf{a_2}, \mathbf{c})$, which define the unit cell of the lattice. As can be seen, each atom is bounded with four atoms of the opposite specie. The two N and III atoms are organized following the same compact hexagonal packing, shifted by $\mathbf{u} = (3/8) \cdot \mathbf{c}$. Because of this hexagonal symmetry, the crystal is usually described using Bravais-Miller indexes, $(\mathbf{h}, \mathbf{k}, \mathbf{i}, \mathbf{l})$ instead of the regular Miller indexes $(\mathbf{h}, \mathbf{k}, \mathbf{l})$. The additional term $\mathbf{i}$ allows to consider the rotational symmetries present in hexagonal structures and is defined such as $\mathbf{i} = -(\mathbf{h} + \mathbf{k})$. Overall, the lattice can be described using only a and c, with $a = \|\mathbf{a_1}\| = \|\mathbf{a_2}\|$ and $\mathsf{c} = \|\mathbf{c}\|$. The values of a and $\mathbf{c}$ are given for each nitride specie in Table I-1.

	AlN [9]	GaN [9]	InN [10]
a (Å)	3.111	3.189	3.539
c (Å)	4.979	5.178	5.708

Table I-1: *Lattice parameters of AlN, GaN, and InN.*

The Zinc Blende[11] structure is presented in Fig. I-2. While less common than wurtzite GaN, this structure may be encountered as part of the work realized in this project. Similarly, to the Wurtzite structure, each atom is bounded to 4 neighboring atoms. The structure III and N atoms both follow a Face Centered Cubic configuration, shifted by $\mathbf{u} = \frac{1}{4}\mathbf{a_1} + \frac{1}{4}\mathbf{a_2} + \frac{1}{4}\mathbf{a_3}$.

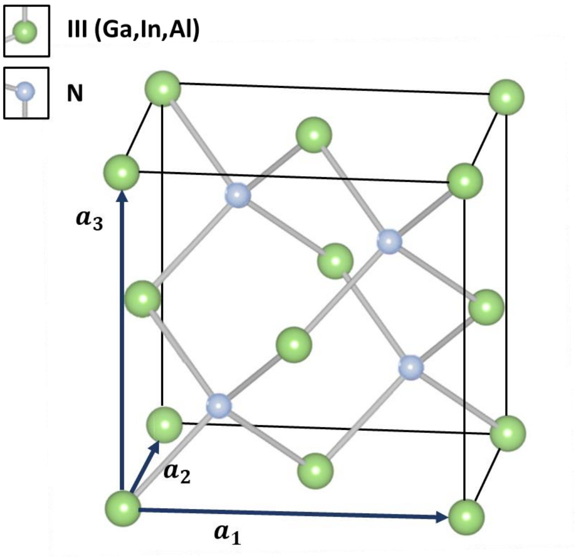

Figure I-2: *Crystallographic structure of Zinc Blende III-nitrides*

Because of their similar coordination number, both Zinc Blende and Wurtzite structure share some similarity. However, there is a key difference to both structures, which is the stacking, as can be seen in Fig. I-3. In the case of the WZ structure, the stacking follows an AB configuration[12], where a pattern of two layers composed of a III-sublayer and a N sublayer alternate along the *c*-direction. In the zinc Blende structure, the stacking is presented along the $[1, -1, 1]$ direction and follows an ABC stacking[12], the pattern is constituted of three repeating layers, instead of two.

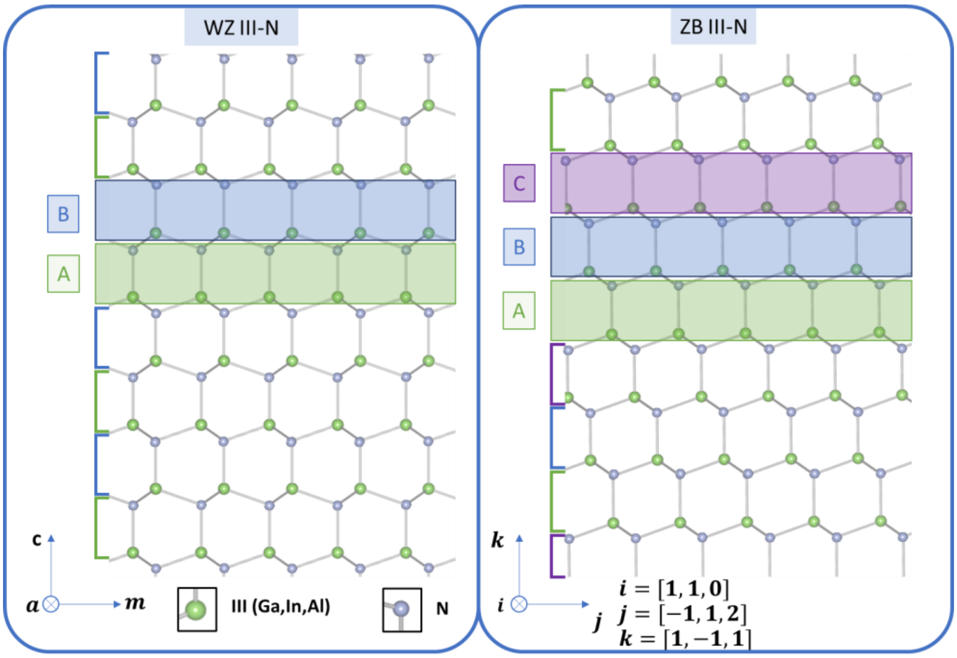

Figure I-3: *Comparison in the stacking in WZ-GaN and ZB-GaN*

1.1.2 SPONTANEOUS AND PIEZOELECTRIC POLARIZATION

The difference of electronegativity between N and the III elements are significant (1.04, 1.13 and 1.27 for GaN, InN and AlN respectively[13]), meaning that the barycenter of charges is separated along the chemical bonds. From this simple fact, one can expect polarization to occur if the dipoles do not compensate each other because of the crystalline structure. Two different types of polarization can be distinguished: polarization caused by the arrangement of the atoms in the crystal, called spontaneous polarization, and polarization caused by a distortion in the lattice caused by strain, called piezoelectric polarization. In this part, we will explain why wurtzite nitride compounds maybe subjected to both.

There are two separate explanations for the spontaneous polarization in III-Ns, which both contribute to the creation of a large dipole over the whole crystal:

- The first explanation that has been provided is the non-ideality of the WZ structure in nitrides. Indeed, the bonds around the atoms form tetrahedra, which is regular only if $\frac{c}{a} = \frac{2\sqrt{6}}{3} \approx 1.632$. However, the measured values give slightly lower values, such as reported in ref.[14] , or as be calculated from Table I-1. The non-ideality discrepancy δ in nitrides goes such as $\delta_{\mathrm{GaN}} < \delta_{\mathrm{InN}} < \delta_{\mathrm{AlN}}$, which is consistent with the fact that the spontaneous polarization P goes such as $\mathrm{P}_{\mathrm{GaN}} < \mathrm{P}_{\mathrm{InN}} < \mathrm{P}_{\mathrm{AlN}}$. The main consequence of this irregularity of tetrahedron is an unbalance in the dipoles around the III atom, that results in a dipole along the c-direction. In 1993, Hanada *et al.*[14] used this explanation as the sole responsible for piezoelectric polarization, but it would later be shown that it is not the case.

- Bernardini *et al.*[15] calculated that even in an ideal tetrahedron structure, the polarization in WZ nitrides would not be zero, proving the presence of another contribution to polarization. As shown in Fig. I-4, the wurtzite structure, is non-centrosymmetric, and the (0001) and $(000\bar{1})$ direction are not equivalent. This, combined with the strong separation of dipoles in the III-nitride materials, leads to the apparition of a spontaneous polarization along the c-axis. It also means that the individual dipoles in the lattices can add up to form a long-range polarization across the crystal.

This nonequivalence of the +c and -c directions in the crystal structure imply that they need to be differentiated, as shown in Fig. I-4. If the bottom atom of the vertical bond is a III atom, the crystal is said to have a III-polarity, whereas if it is a N atom, the crystal has a N-polarity. The III-polar and N-polar configurations also exhibit different properties, such as the number of dangling bonds for III and N atoms. This induces differences in chemical, thermodynamical and structural properties. One example lies in the ability to attack N-polar III-nitrides with KOH, in opposition to III-polar structures which are resistant. One proposed is that the OH^- group in KOH bounds to a III dangling bound as the first step of the attack before attacking the Ga-N bond of the surface but is screened by a N dangling bond[16]. The N-polar structure features one dangling bond per N atom, and three dangling bonds per III atom, meaning that the OH^- groups can easily bound to the structures. On the other hand, III-polar GaN only features one dangling bond per III atom, and three dangling bond per N atom, meaning that the OH^- group is going to be screened. This example shows that in most cases, the different properties between III and N-polar is caused by the different density of both III and N dangling bonds, which have different properties.

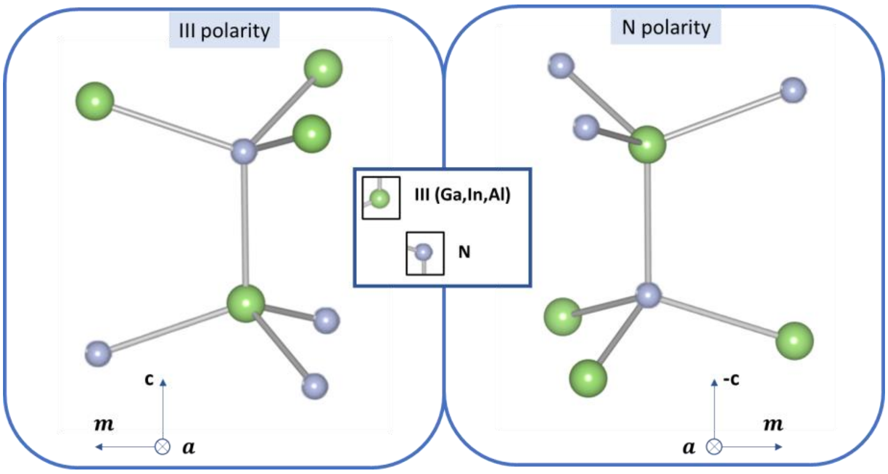

Figure I-4: *Stacking around the (0001) III-N bond in III polar and N polar configurations.*

Piezoelectric polarization is the second source of polarization in III-Nitrides. It is caused by strain of the material, which will also deform the unit cell and hence add further displacement of the charge barycenter. This phenomenon hence arises when forming heterostructure with materials, which lattice is not matched with the one of the III-N. The two main cases in which this effect is encountered is the growth on a non-native substrate, and the growth of III-N heterostructures such as quantum wells.

1.1.3 COMMON CRYSTALLINE DEFECTS

Defects in semiconductors have an important role in the properties of a given material, both the macroscopic and microscopic scale in the semiconductor. For example, Takeya *et al.* suggested a direct link between the diffusion of point defects toward and the failure of AlInGaN lasers[17]. Hence, it is necessary to present the common defects that can be found in III-N semiconductors to better understand how different properties can emerge from them.

1.1.3.1 POINT DEFECTS

Point defects are defect created at a single atomic point in the crystalline lattice and are hence zero dimensional. They can be classified in 3 categories, with different notations that will be used in the rest of this work, and are represented in Fig. I-5:

- vacancies, in which an atom is lacking in the lattice. For example, a Ga vacancy has the following notation: $\mathrm{v_{Ga}}$

- substitutional, in which an atom occupies the position of another in the crystal. For example, a Si atom occupying a Ga site will have the following notation: $\mathrm{Si_{Ga}}$

- interstitial, in which an atom is found outside of a predicted site in the lattice. For example, a Si interstitial will be noted has: $\mathrm{Si_i}$

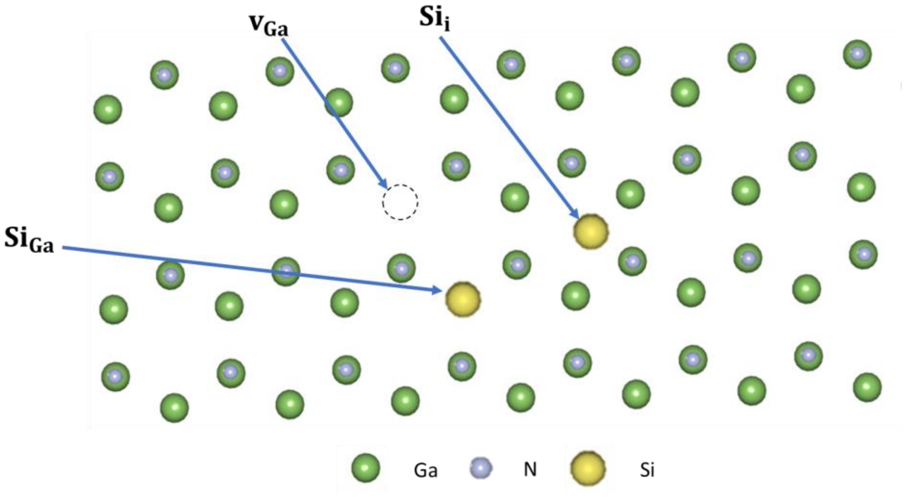

Figure I-5: *Illustration of the different types of crystallographic defects with examples in GaN across the c-plane.*

Substitutional or interstitial defects are called intrinsic if they imply only atoms present already in the crystal (for example in GaN, a Ga atom on a N site, or an interstitial Ga), and extrinsic if it implies an impurity atom (such has an interstitial Si in GaN).

Point defects can also associate to create defect pairs. Two cases can arise. First, the Frenkel defect, in which an atom leaves its site to become an interstitial defect. In the case of GaN, the two possible Frenkel defects are $v_{Ga}Ga_i$ and $v_N N_i$[18] .The second case is the Schottky defect, which is a pair of vacancies of both the anion and the cation. In GaN, a Schottky defect would mainly be made of $v_{Ga}v_N$. It should be noted that an array of other defects pairs or clusters[19] can be created. For example, in GaN, the formation of defect pair such as $v_{Ga}O_N$ and $C_N O_N$ are both suspected as potential centers for common defect related emissions[20], that will be discussed in a later paragraph. These defects have associated formation energies and migration barriers, allowing to assess their stability in the material as well as their ability to diffuse[20].

The presence of these defects induces mechanical distortion in the matrix because of the breaking of the lattice, but also electrostatic ones because of the modification of the local arrangement of charges. Hence a high density of defects can be responsible for a modification of the properties of the material. In semiconductors, the inclusion of point defects often results in the modification of electronic properties such as the conductivity. In the example of GaN, Si_{Ga}[21] and Mg_{Ga}[22] are often used as n and p-dopant respectively. Another noteworthy behavior of defects in semiconductor is that in the case of light emission, defects tend to act as so-called deep centers and non-radiative centers (NRCs), hence responsible for parasitic contributions as well as a drop in the efficiency of the overall light emission. Such cases will be seen in further details in a latter part.

1.1.3.2 DISLOCATIONS

A second case of common defect in crystalline materials is the dislocation. Dislocations are long range linear defects and are usually seen as the manifestation of irreversible deformation, called plastic deformation, in the material. They typically consist in a discontinuity in the arrangement of an atomic column, leading to the intercalation of a new atomic column. In the case of epitaxial material, dislocations are mainly created because of the coalescence of two nuclei[23,24], or because of lattice mismatch[25]. It is important to note that in that latter case, the deposited layer must exceed a critical thickness for plastic deformation to occur[26]. Dislocations are generally separated in two categories, namely the screw and edge dislocations, which usually accommodate twist between two nuclei and lattice mismatch between two structures respectively[27]. A dislocation can be characterized by its Burger vector, which represents the magnitude and direction of the crystalline distortion induced by the dislocation. The main difference between the edge and screw dislocation is that in the case of an edge dislocation, the burger vector is in the same direction as the propagation (Fig. I-6(a)), whereas a screw dislocation has its burger vector perpendicular to propagation (Fig. I-6(b)). In the case of screw dislocation, the direction of propagation tends to rotate during growth, creating a pyramidal dislocation such as described in ref.[28] . This spiraling growth is the reason why it is called screw dislocation. The last kind of dislocation is the mixed dislocation, as shown in Fig. I-6(c). In mixed dislocation, the dislocation line changes direction within the crystal, and can be decomposed at each point into a screw and edge dislocation.

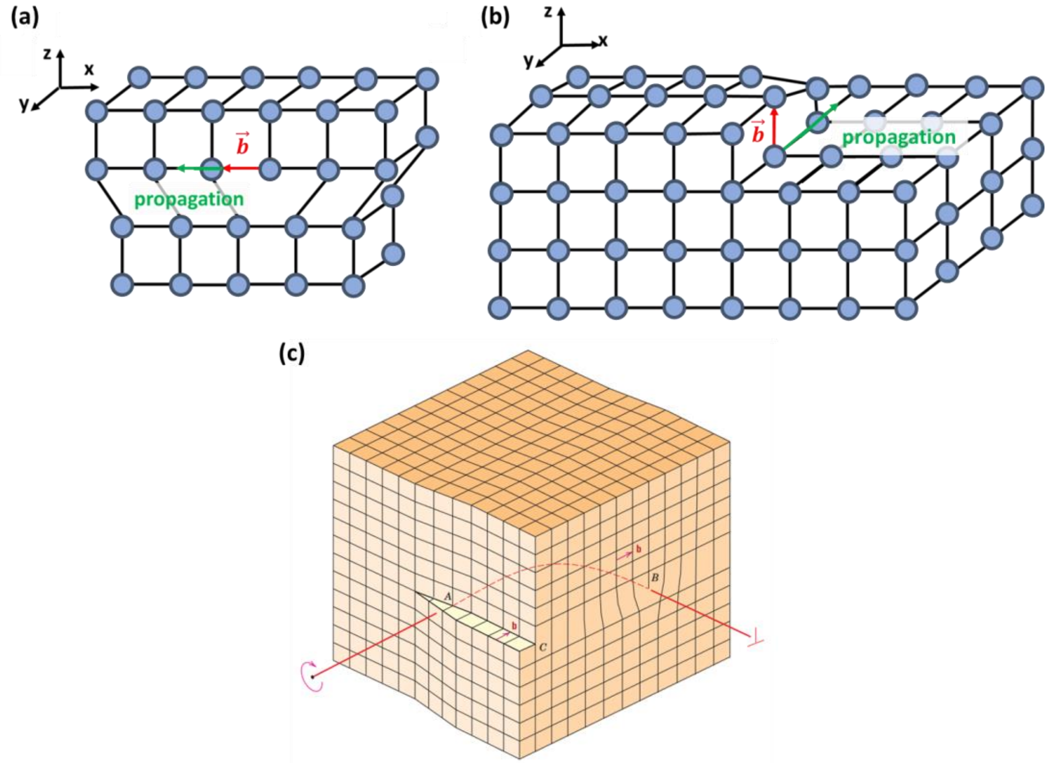

Figure I-6: *Edge (a), screw (b), and mixed type dislocations ((c) taken from ref.* [29] *)*

Different kinds of dislocations are expected to form during epitaxial growth. First, in the case of nucleus coalescence[30], edge dislocation accommodate twist (difference of rotation around the ***c*** axis), while screw dislocation accommodate tilt (difference of rotation around the **a** axis)[31]. Also, heteroepitaxy on a wafer with a high lattice mismatch will create edge dislocation with a burger vector along the **a** direction. Such dislocation can also be part of a mixed dislocation, and eventually transition to a threading ***c*** screw dislocation going to the surface of the material.

1.1.3.3 STACKING FAULTS

Stacking faults (SFs) are the last defects that have been playing a role in this work. They are a 2D defect and will hence extend to a whole atomic plane in the material and occur when the rules of stacking in the material are locally broken. There are several kinds of stacking faults in nitride systems, and a quick overview of the characteristics of these defects will be provided in this paragraph.

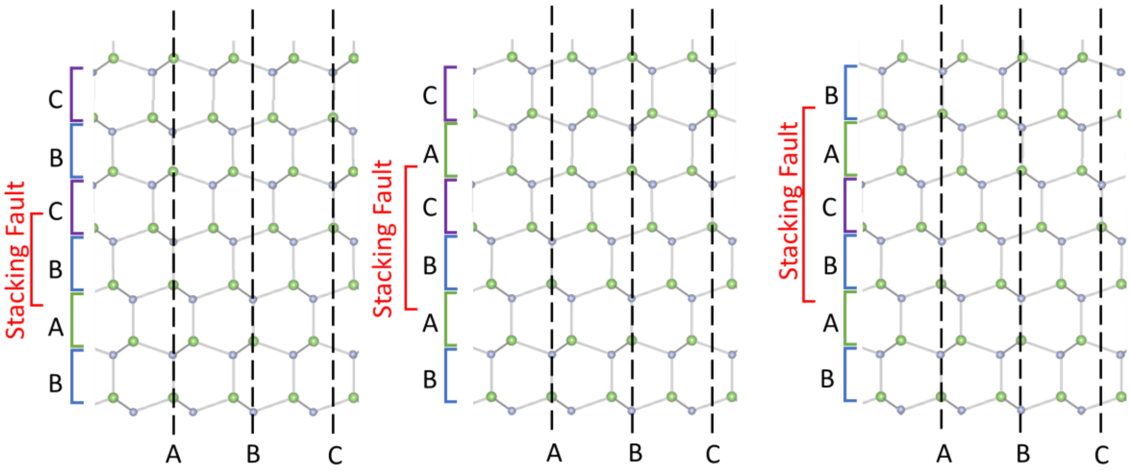

Figure I-7: *I1 (a), I2 (b) and E (c) configuration for basal stacking faults.*

The basal stacking fault is the most common of the SFs in nitride compounds (BSFs). It usually consists in the inclusion of one (I1), two (I2) or more (E) bilayers of Zinc Blende structure within a Wurtzite crystal (Fig. I-7). I1 and I2 are intrinsic stacking faults, meaning that they are essentially a shift between two purely wurtzite structures, while E is an extrinsic, meaning that the stacking fault introduces a sequence that is absent from the wurtzite structure, and cannot be obtained from shifting two wurtzite structures only[32,33].

While the basal stacking fault is the most encountered in nitride materials[34], other kinds of stacking faults are also commonly found. Indeed, in opposition to basal stacking faults, which form along the hexagonal c-plane of the material, some stacking fault also form along the m and a-planes of the material[34]. These planes are the facets of a hexagonal prism along the c-plane base and are hence sometimes called prismatic crystallographic planes. Hence, m and a-plane stacking faults are called prismatic stacking faults (PSFs). In the literature, most reports regarding PSFs talk about the two stable configurations of $(11\bar{2}0)$ a-plane stacking faults[35].

The last kind of stacking faults encountered in nitrides is the inversion domain boundary (IDB) and double positioning boundaries (DPB) sometimes called stacking mismatch boundary (SMB) when observed at the interface between two grains nucleated on different terraces[36]. In the previously presented cases of stacking faults, the stacking fault was a local perturbation of the stacking, but the crystalline directions were the same on each side of the defect. In the case of IDBs and DPBs, some of the crystallographic directions are modified by the defect. In the case of the IDB, the defect is characterized by an inversion of the polarity at the defect. Several models have been proposed to describe the local arrangement at the boundary in nitrides[37], with the most observed one corresponding to the results of Northrup *et al.*[38], who propose that at the IDB, the crystal is also shifted by $\frac{1}{2}\mathbf{c}$ to avoid creating unfavorable III-III and N-N bonds (Fig. I-8). In the case of the DPB, the boundary separates two twin crystallites[39], meaning that the boundary acts as a plane of symmetry for both crystals. In this case, the boundary is considered as non-coherent, meaning that the twin boundary exhibits some distortion to accommodate both structures. The DPB will not be represented, as it is not commonly encountered.

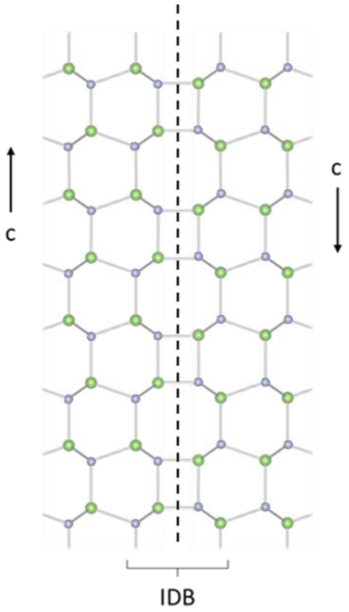

Figure I-8: *Inversion Domain Boundary in GaN*

1.2 OPTOELECTRONIC PROPERTIES

As stated previously, III-N materials are of particular interest for light emitting devices because they allow to cover a large portion of the electromagnetic spectrum, from deep UV to close infrared, as disclosed in Fig I-9. In this part, the band structure of III-N will be presented, and further attention will be given on the luminescence of GaN and InGaN compounds.

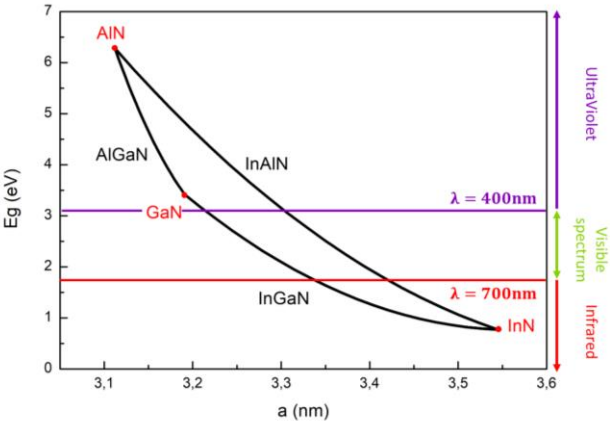

Figure I-9: *Bandgap as a function of lattice parameters for binary wurtzite III-N compounds.*

1.2.1 BAND STRUCTURE AND TRANSITIONS

The band structure of GaN and other III-N materials have been thoroughly studied in the last decade, and several theoretical studies as well as measurements have allowed to draw a clear picture of the electronic structure of these materials (Fig. I-10). In their Wurtzite configuration, III-N materials are direct bandgap, meaning that the minimum in the conduction band and the maximum of the valence band are both located at the Γ point (k=0). They do not require thus the presence of phonons to achieve a direct transition, which makes them efficient candidates for light emissions.

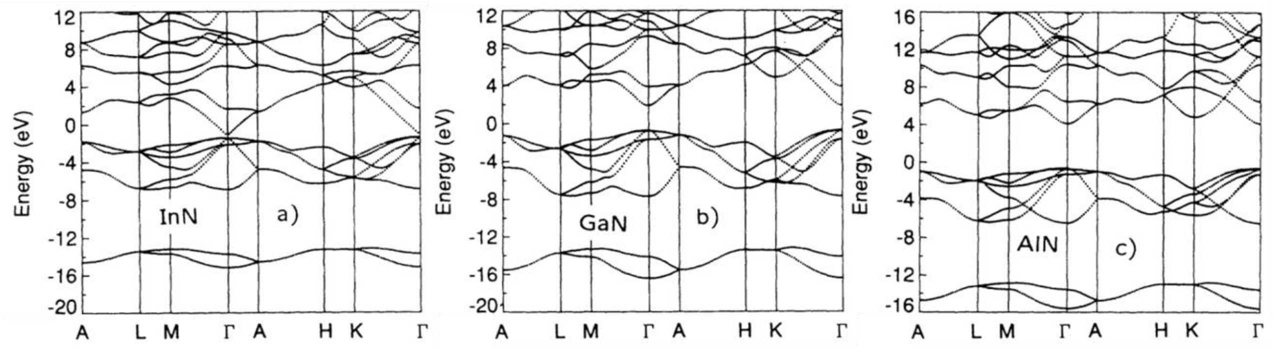

Figure I-10: *Band structure of III-nitrides (taken from ref.* [40] *)*

In the case of the study of direct bandgap semiconductor, the Γ point and its vicinity, will describe most of the transitions. We will hence only focus on this point of the graph in this paragraph.

The band structure around the gap is represented in Fig. I-11. As represented, the structure differs for GaN and AlN, with InN having a structure similar to that of GaN, with different energy values. In this figure, only the lowest point in the conduction band is represented, as the electrons often thermalize toward the lowest possible value of the conduction band before an optical emission, making the study of the other conduction bands useless when it comes to light emission.

The calculation of energy levels is performed by integrating the Schrodinger equation for each orbital in the crystal. However, because this calculation is both long and technical, we will not showcase it here, and rather present the main conclusions of this calculation. In III-nitrides, the three highest valence bands correspond to the three levels of outer p orbitals. In Zinc Blende compounds, these three states are equivalent, and would only account for a single 3-fold degenerate band. However, the geometrical imbalance in the wurtzite lattice breaks the symmetry allowing for this degeneracy, and hence creates a splitting between p_z and both p_x and p_y orbitals. This effect is called the crystal field splitting and can be characterized by the energy difference between p_z and the two-fold degenerate p_x/p_y band, called Δ_{CF}. In the case of GaN and InN[41], Δ_{CF} is positive, meaning that the bands related to p_x/p_y is going to be higher in energy than the one of p_z, while in AlN[42], Δ_{CF} is negative, meaning that the p_z band is the highest of the valence band. This is responsible for a difference in the polarization of the emitted light by GaN, InN and AlN: in GaN and InN, the polarization is mostly longitudinal, while in AlN, it is mostly transversal. However, this model assumes that the p_x/p_y are degenerate, which is inconsistent with what is measured in reality. Another source of splitting between the bands exists and must be considered to precisely describe their properties.

This second source of splitting is the spin orbit coupling, which describes the interaction between the spin of a particle and its movement or its energy level. While the details of calculation of spin orbit coupling won't be provided here, it is important to understand its consequences. Mainly, spin orbit coupling lifts the degeneracy between the levels corresponding to the p_x and p_y orbitals. Since each of these orbitals is constituted of two electrons of opposite spin, it is also responsible for further splitting of each energy level into two sub bands. However, the energy difference between two sub bands associated to same orbitals are generally small when compared to the difference between two orbitals, especially around the Γ point, and are usually considered as degenerated. Also, the energy difference between the levels corresponding to the p_x and p_y orbitals in AlN is small when compared to Δ_{CF}, and it is generally accepted to consider these two orbitals as degenerated.

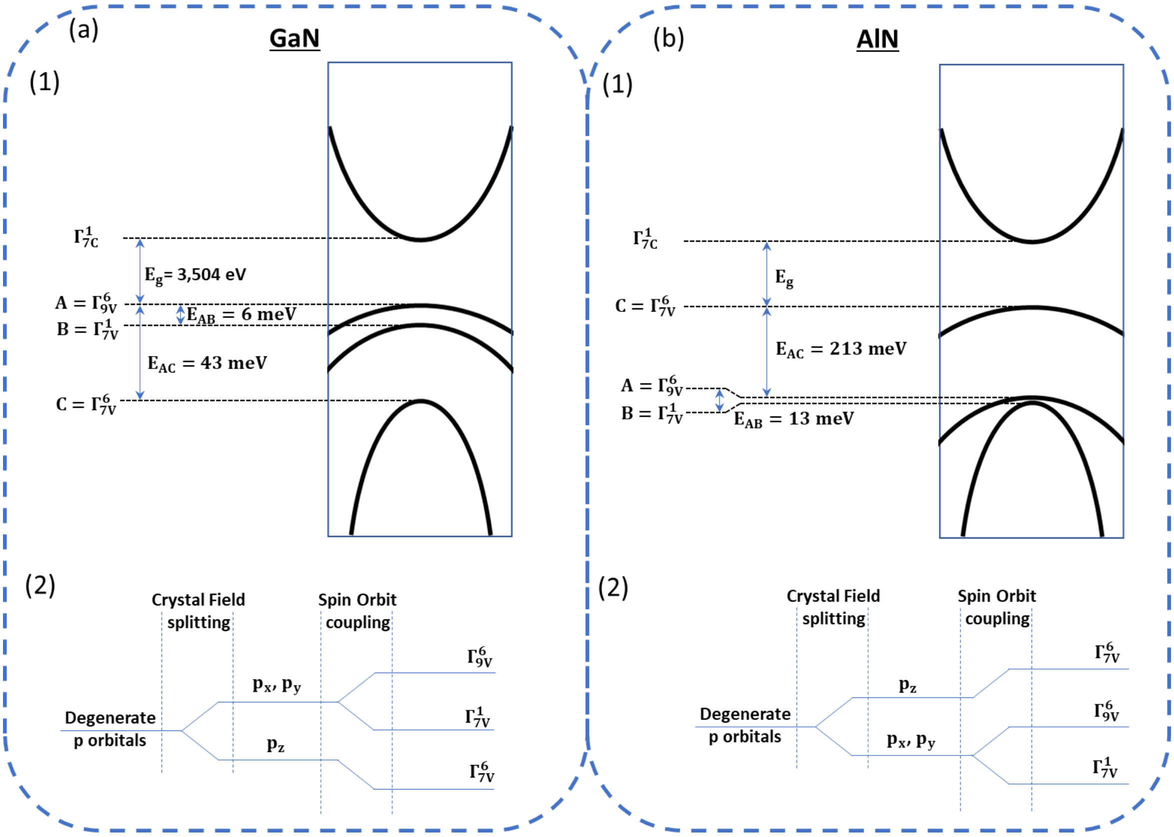

Figure I-11: *Band configuration around the Γ point in GaN/InN (a) and in AlN (b)*

When an electron receives enough energy to get to the conduction band, it creates a free negative charge in the crystal. For this charge to be compensated, a positive hole is created in the valence band. This can create a dipole binding the two particles with coulombic forces, responsible for the creation of a quasi-particle named exciton. The exciton is created through the binding of a positive and negative charge, separated by a given radius. In inorganic semiconductors, excitons are typically bounded by a length greater than the lattice of the crystal, reaching several nanometers in some cases. Because Excitons are created when a transition occurs, they are part of the light emission process in LEDs. The collapse of an exciton leads to the emission of a photon of energy:

$$E_{FX} = E_G - E_B \; \mathbf{(1.1)}$$

E_B being the binding energy of the exciton, E_G the gap energy, and E_{FX} the energy of the free exciton.

In a semiconductor, the presence of impurities and crystalline defects, can also create inter-band energy levels (Fig. I-12). These levels can bind to exciton, or even act as levels to which carriers will recombine. An impurity with a level above Fermi level will be classified as a donor, while an impurity with a level below Fermi energy will be classified as an acceptor. The different energy transition occurring in semiconductors are exhibited in Fig. I-12. It should be noted that in the case of nitrides, there are 3 types of free excitons noted A, B and C, which correspond to the transitions from the conduction bands to the respective valence levels in Fig. I-11.

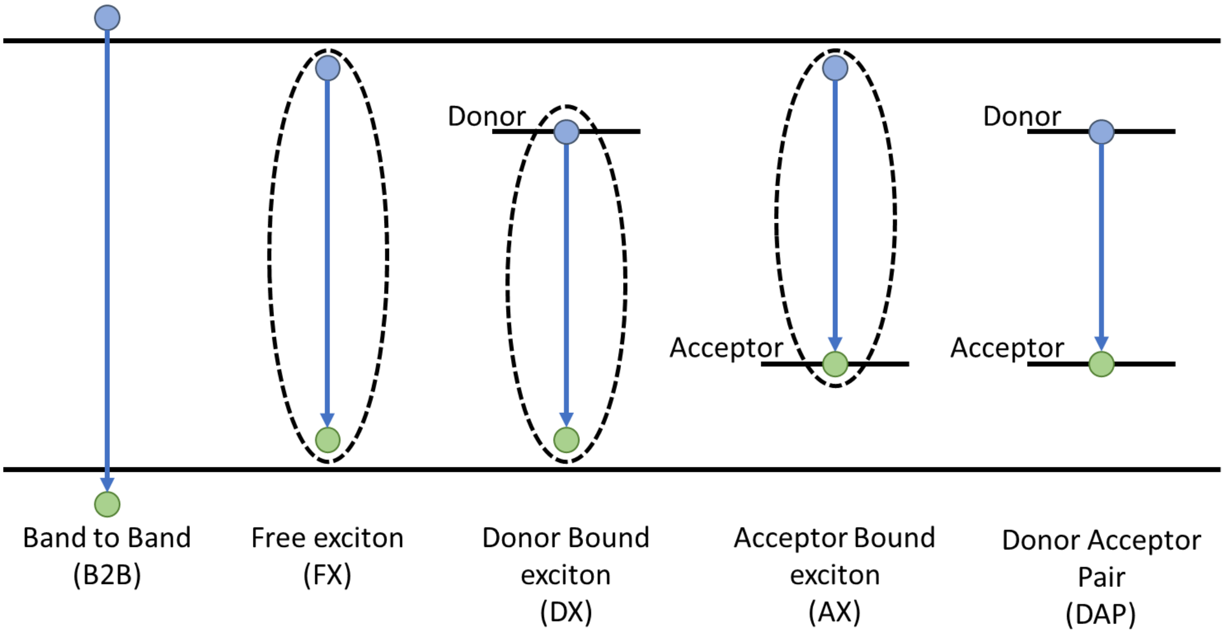

Figure I-12: *Radiative recombination pathways in direct bandgap semiconductors.*

1.2.2 LUMINESCENCE

1.2.2.1 MAIN CONTRIBUTIONS

Regarding the radiative recombinations in the bulk material, they are close to the value of the gap, which are provided in the Table I-2. In this work, the main band edge emission encountered is the one of GaN, which, at room temperature, is dominated by free exciton recombination[43]. The associated band edge of the material is sensitive to its properties, such as its lattice parameter or chemical composition in the case of an alloy these variations of the band edge are sometimes used to probe some of the properties of the material, such as its crystalline quality through its full width at half maximum, or its strain through its position.

	AlN[1]	GaN [1]	InN [1]
E_G (eV)	6.2	3.39	1.9-2.05

Table I-2: *Bandgap energies for AlN, GaN and InN at 300 K.*

Contrarily to the near band edge, the contribution coming from the quantum well can be tuned by modifying either the depth or the thickness of the quantum well (QW). In the case of InGaN QWs, the following equations gives the energy of emission of a fraction of In x and a thickness h[44].

$$E_{QW}(x,h) = E_g(x) + e_1(x,h) + hh_1(x,h) - R_y(x,h) - e \cdot F(x) \cdot h \quad \mathbf{(1.2)}$$

With:

- $E_g(x)$ being the gap energy of the $In_xGa_{1-x}N$ alloy, usually calculated such as[45]:

  $$E_g(x) = x \cdot E_g^{InN} + (1-x) \cdot E_g^{GaN} - b \cdot x \cdot (1-x) \quad \mathbf{(1.3)}$$

  b being the bowing parameter, susceptible to variation because it is linked to the strain in the material.

- $e_1(x,h)$ and $hh_1(x,h)$ are the lowest level of an electron / highest level of a hole in the quantum well, typically calculated with the Schrodinger equation. Note that these parameters are a function of both the In composition, x, and of the width of the well h.
- $R_y(x,h)$ is the binding energy of the exciton formed by the transition of an electron from e_1 to hh_1. Here again, This a parameter are a function of x and h.
- $F(x)$ is the term describing the internal electrical field. This term can arise either from the polarization due to Quantum Confined Stark Effect (discussed in more details in 3.1.2), or from piezoelectric polarization.
- e is the charge of a single electron

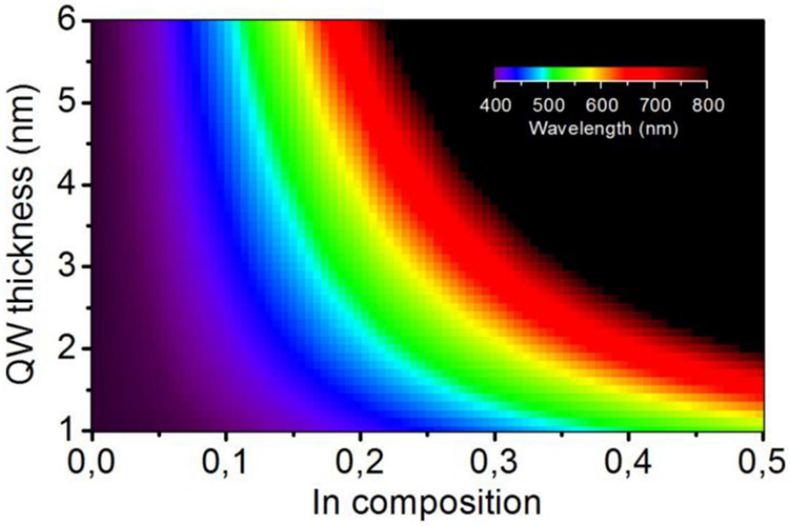

Figure I-16: *Energy of emission of an InGaN QW as a function of it thickness and In mole fraction grown on c-plane surface (taken from ref.*[46] *)*

This formula can be used as a parametric equation, by using $E_g(x)$ as a parameter and used to draw the curve of the set of x and h that will result in the emission of a photon of a given wavelength (i.e.: energy). A representation over the visible spectrum is given in Fig. I-16. As one can notice, a combination of low QW thickness and low In composition will result in a short wavelength emission. An emission of a longer wavelength would require to either increase In composition or make larger QWs on standard c-plane growth.

In the last paragraph, we have presented the main emissions expected in a pristine QW LED. However, it is common to observe other peaks, and the observed values for the band edge can sometimes vary from the expected values. In the next paragraphs, we will present some of the factor that can modify the luminescence of a QW LED, as well as lead to the apparition of unexpected contributions.

1.2.2.2 DEFECT CONTRIBUTIONS

As specified quickly before, crystallographic defects in GaN can be responsible for an array of different contributions. In this paragraph, we will provide an overview of the main defect emissions in GaN. It should be noted that not all defects are radiative. This is for example the case of dislocations[47], which can be monitored in cathodoluminescence as they create dark spots because they locally decrease the light emission. Point defects can also act as non-radiative centers by introducing deep levels between the conduction and the valence band. This level can then be used by the carriers to relax without light emission, in a process called the Shockley-Read Hall recombination (SRH)[48,49], also called a trap assisted recombination. The presence of these non-radiative pathways is responsible for a drop in the internal quantum efficiency, as it means that part of the energy provided to the carriers will be lost in the form of heat upon recombination. The presence of these pathways is also suspected to be partly responsible for a further reduction of efficiencies at high operating currents called the droop, that will be discussed later in this manuscript.

In their report entitled "luminescence of defects in GaN", Reshchikov *et al.*[20] identify at least 60 different defect contributions in the luminescence of GaN alone, showing how a spectrum can be modified by the presence of defects in the material. Without unnecessarily drawing up an exhaustive list, we will give a quick overview of the different defects encountered during this work, as well as defects that could arise from impurities that may have contaminated our material (mainly Mg, Si, C and O). It should be noted that the main contributions expected in a GaN/InGaN quantum well array are represented in Fig. I-17, which is a reconstituted spectrum made by adding photoluminescence (PL) and photoluminescence excitation (PLE) spectra taken at room temperature.

The most prevalent of the defect contributions in GaN is the **Yellow Luminescence band**, often noted YL, which is a broad signal observed between 2.0 and 2.25 eV. It is obtained with all growth methods, under different conditions, and has hence been the subject of numerous publications[20]. However, no precise origin for this contribution has been identified, the literature even shows contradictory reports. For example, G. Li *et al.*[50] claim that the presence of the YL correlates to the presence of structural defects such as dislocations, while X. Li *et al.*[51] claim that YL is enhanced in absence of structural defects. The main candidates for this transition are a Ga vacancy complex[52], such as $v_{Ga}O_N$, or a carbon substitutional complex, such as C_NO_N, with some authors suggesting the possibility of a $v_{Ga}C_N$ complexes[53] combining both. Another theory hypothesized that the yellow band is the sum of several independent common contributions[54,55], which would explain why different authors get various and even sometimes opposite results when studying the YL. This has been further suggested by the fact that the YL intensity has a complex behavior when varying the temperature of measurement[56], which confirms that it involves several different recombination processes. It has been observed that Si n-doping increases the intensity of the YL in the material [57] , which has been attributed to Si-induced v_{Ga} formation [58].

Another prevalent defect contribution is the so-called **Blue Luminescence band**, which is common in Mg p doped GaN by MOCVD and HVPE[59], centered around 2.9eV. A similar blue luminescence has also been observed in Zn p-doped GaN[60]. In the first case, the transition is suspected to be a Donor Acceptor Pair transition, implying a $Mg_{Ga} - v_N$ deep donor[20,59] and an unknown acceptor. This blue luminescence is often associated with an ultraviolet shallow DAP band around 3.2eV, also attributed to Mg[20]. However, this band has not been observed during this work, and will hence not be discussed in further details here. It should be noted that because the deposition of the p-doped layer is usually the last step of the process, the BL can sometime hinder photoluminescence measurement by absorbing the higher energy photon coming from the quantum wells of the active layer, and hence lower the relative intensity of the quantum well. Hence, when working uniquely on the radiative properties of the quantum wells, it is usually preferred not to grow any p-GaN layer.

Impurity is not the only source of parasitic contributions in GaN, and some structural defects can also have an effect on the spectrum of the sample. This is the case of the **basal stacking faults**. Indeed, we have previously showed that the BSFs can be described as zinc blende inclusions of a few layers in a wurtzite layer. The band edge of ZB GaN is around 3.27eV[61], which is lower than the 3.39eV bandgap of WZ GaN[1]. From this, we expect the BSF to act as a quantum well, and hence to have a characteristic emission. This emission has been observed and shown to occur around 3.4eV[62,63]. For I1 and I2 BSFs, this luminescence is only measurable at low temperatures, as it collapses when going close to room temperature[64].

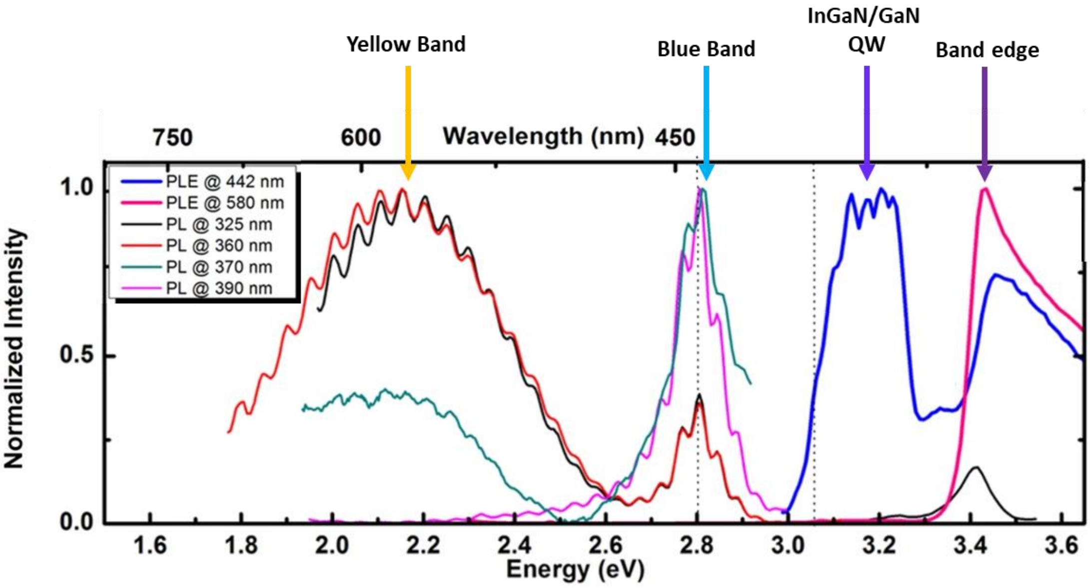

Figure I-17: *Spectra of an InGaN/GaN heterostructure with commonly measured emissions captured with photoluminescence (PL) and photoluminescence excitation (PLE) spectroscopy at room temperature (taken from[65])*

1.2.2.3 EFFECTS OF THE TEMPERATURE

Structural and chemical factors are not the only ones that impact the optical properties of a material. Another key parameter of the luminescence in nitrides is the temperature of the PL measurement.

As can be seen in Fig. I-18, the band edge energy is shifted toward higher energy towards higher energies at low temperature, as first described by Y.P. Varshni[66]. In this work, the author shows that these effects can be observed for a wide variety of semiconductors, and two mechanisms are proposed to explain the phenomenon. First, the lattice parameters are temperature dependent, and we have previously explained that the band structure of the material is calculated using the lattice. Second, the interaction itself between carriers and the lattice are temperature dependent. From these suppositions, the author made the following empirical model to describe energy bandgap variation with temperature:

$$\mathrm{E_G(T)} = \mathrm{E_G(0K)} - \frac{\alpha \cdot \mathrm{T}^2}{\beta + \mathrm{T}} \quad \mathbf{(1.4)}$$

With T being the temperature, α and β two constants with typical values in the range of 0.566-1.28 meV.K^{-1} and 600-1190K respectively[67].

Another effect, which can be observed for band edge[43], quantum well[68] and a some of the defect related emissions[64,69] is the luminescence quenching by increasing T. In this context, quenching can be defined as the reduction of the luminescence efficiency due to the formation of thermally activated non-radiative recombination pathways[43]. While the general case says that the intensity of a contribution will decrease by increasing the temperature, it is not true for every case, and some contributions can also be thermally activated, which is called a negative quenching. While this behavior is not common it has been reported, for example, in the case of YL[70]. Last, some cases exhibit a multi-step quenching with more than one activation temperature[71] or even an alternation of quenching and negative quenching, such as for the GaN B free exciton in ref.[43].

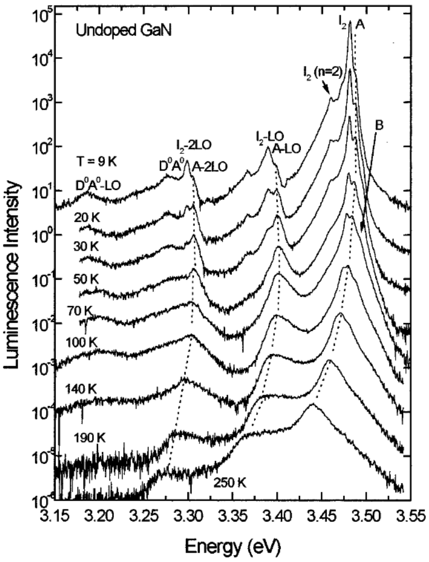

Figure I-18: *Evolution of the photoluminescence of GaN around its band edge at different temperatures*[43].

Strain is the second critical parameter when measuring the luminescence of a nitride material. In the next paragraph, we will explain the effect of strain on the GaN luminescence.

1.2.2.4 EFFECT OF THE STRAIN

When working with epitaxial films grown on a foreign substrate, there are two main sources of strain: Thermal expansion, as explained in the previous paragraph, and lattice mismatch. Both effects will be discussed in detail in 2.2.1.2 in the case of GaN grown on several commonly used substrates. In both cases, this results in the presence of biaxial stress in the material in the c-plane. In the case of semiconductor, the introduction of foreign atoms with different radiuses will create hydrostatic stress in the lattice. As evidenced by Gil *et al.*[72], this strain can modify the energies of the free excitons of the band edge, which has been responsible for a dispersion in the values reported for these excitons for GaN in the literature. In this work, the authors provide a model allowing to directly estimate the variation of energy when knowing the strain in the material. It is also shown that there is a correlation between the variation of energy of the A, B and C excitons (as defined in 1.2.1) under strain.

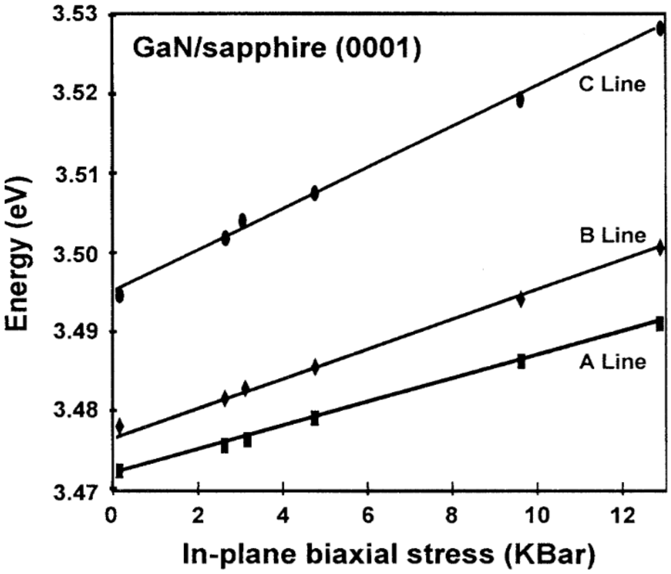

Figure I-19: *Energy of emission of the A, B and C free excitons versus in-plane biaxial stress (taken from* [72]*).*

This model is however complex, and will not be fully presented here because, as it will be explained later, the approach adopted in this PhD allows to get rid of the strain coming from the substrate. However, it allows to measure the deformation in a sample using only its luminescence spectrum[72,73]. in the case of a sample under biaxial strain, and for small deformation, the energy of the free excitons varies linearly with the strain, as shown in Fig. I-19, meaning that $\mathrm{Cste} = \partial E_A / \partial \varepsilon_{xx}$ ($\varepsilon_{xx} = \varepsilon_{yy}$ being the in-plane strain) is constant. Hence, we get the following formula:

$$E_A = E_{A0} + \mathrm{Cste} \cdot \varepsilon_{xx} \quad \mathbf{(1.5)}$$

E_{A0} being the energy of the A exciton in unstrained GaN.

2. GaN GROWTH: AN OVERVIEW

2.1. GROWTH METHODS

In the previous paragraphs, we discussed about the properties of the three main III-V semiconductors, namely AlN, InN and GaN. In this part however, we will focus on the elaboration methods specifically for (In)GaN, as these are the materials that make up the bulk of visible InGaN/GaN LEDs. The three main technics used to grow GaN are the followings:

2.1.1 MOLECULAR BEAM EPITAXY

Molecular Beam Epitaxy (MBE) is a method that uses beams of elements in a gaseous form to deposit material on a heated substrate under ultra-high vacuum. In the case of GaN, the sources of Ga and N are of different nature. Ga is used in its solid form and is evaporated through a Knudsen or Effusion cell by sublimation at high temperature. Once evaporated, the atoms are deposited on the facing substrate. Indeed, the high vacuum allows to reduce the probability of an evaporated atom entering in collision with another gaseous specie inside the chamber, i.e., the free mean path is larger than the distance between the cell and the sample. This ensure that the evaporated Ga atoms will follow straight trajectories, explaining the name “molecular beam epitaxy”. Nitrogen element is obtained from gaseous precursors such as NH_3 (ammonia -assisted MBE) or N2 (Plasma-assisted MBE as the N_2 molecules are cracked by plasma). The heated substrate also allows diffusion on the substrate, which is critical for epitaxy as it allows the adatoms to organize themselves.

When compared to other methods that will be presented here, the growth rates obtained by MBE are low, as the maximum deposition rate will be in the order of 1 µm/h[74]. This means that MBE is not appropriate for the elaboration of thick devices, but rather for the control of the properties of the material up to the atomic monolayer. The high vacuum used inside the chamber allows to monitor the surface using Reflection High-Energy Electron Diffraction (RHEED). This allows to see changes in the crystalline structure of the surface, count the numbers of monolayer deposited or to see the nucleation and ripening of crystalline islands.

2.1.2 Hydride Vapor Phase Epitaxy

Hydride Vapor Phase Epitaxy (HVPE) is a form of Chemical Vapor Phase (CVD) method, in which a solid is grown by using chemical reactions in gaseous form at high temperatures. This leads to the formation of reaction intermediates, which are gaseous species (sometimes in a radical form) with poor stability in the reactor’s condition. These species diffuse on the surface, until they stabilize by forming a covalent bond with the growth surface, which will in turn make the solid grow. HVPE uses the reaction between NH_3 and various Gallium Chloride compounds that are produced by exposing metallic Ga to a flux of HCl at high temperatures (Fig. I-20). Most reactors use a horizontal geometry, and the production of chlorides happen upstream of the growth zone, in the so-called source zone. This reaction can also be assisted by carrier gases such as H_2 and N_2, which fulfill multiple roles, such as equilibrating pressure or reacting with impurities in the case of H_2. The gaseous mix then reaches the growth zone where it mixes and react with NH_3. The substrate is rotated in the growth zone in order to limit inhomogeneities that could be caused by the directional flux of gases.

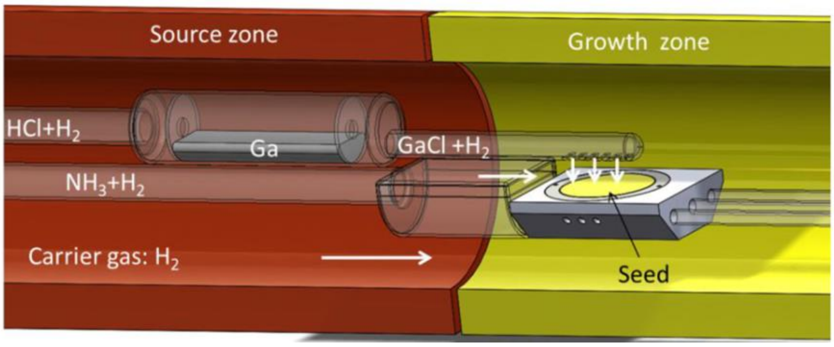

Figure I-20: *Scheme showing the introduction of precursors in an HVPE reactor (from ref.* [75]*)*

Contrarily to MBE, HVPE has a fast rate of growth (can be above 100 µm/h)[74], and is a method of choice to grow thick planar layers, such as the ones used to make GaN substrates. The other advantage is the use of reactive precursor such as HCl, which has been suggested to limit the formation of parasitic nuclei in the vapor phase[76]. These nuclei can cause the deposition of large crystalline structures on the sample during the growth. One could also mention that the precursors used in HVPE are cheap and easy to produce (contrarily to those used in Metal-Organic Vapor Phase Epitaxy), and their reaction in the source zone is mainly driven by heat. However, this method is not suitable to realize heterostructures with abrupt interfaces because the precursors pass through a blending zone before the deposition.

2.1.3 METALORGANIC VAPOR PHASE EPITAXY

Metal-Organic Vapor Phase Epitaxy (MOVPE), also called Metal-Organic Chemical Vapor Deposition (MOCVD), is also a CVD process that uses different precursors in order to grow GaN. In this case, the compounds are Metal-Organic gases, such as TriMethylGallium (TMGa) or TriEthylGallium (TEGa). This main difference with HVPE is that the metal-organic precursors are directly injected in the chamber without the need for a blending zone prior to the reaction chamber. This gives more flexibility on the thermokinetics of the reaction, through the choice of organometallics: For example, switching from TMGa to TEGa during a process will slow the growth. It also open other geometries of reactor, since there is no need for a source zone, and hence, MOCVD reactors can be horizontal or vertical, and can also mix the gases with a shower head, with can help with homogeneity. However, organometallics are unstable compounds that are known to be pyrophoric and will readily react with unwanted species in the gas mix, such as oxygen and water. This could lead to their incorporation in the grown GaN, and the reaction need to be carried out in an inert atmosphere.

The growth rate of MOVPE is an intermediate between MBE and HVPE and is 1 to 5 µm per hour[74]. This makes MOVPE a polyvalent method, which can be used to grow structure on the scale of several hundreds of nm to several tens of µm, while keeping a good control over composition and structure. This makes it a method of choice for the growth of µLEDs;

In this PhD, MOVPE has been the technique employed for growing samples, as it enables structures with the appropriate size for a device to be produced while keeping a good control over the heterostructure properties.

2.2 HETEROSTRUCTURE GROWTH

2.2.1 SUBSTRATES

2.2.1.1 GaN NATIVE SUBSTRATE

In any kind of epitaxial growth, the choice of the substrate is the key to master the properties of the grown device, as the crystallographic structure is transferred to the grown material. Hence, the best-case scenario implies homoepitaxy, in which the growth of a material is performed on a substrate of the same material. Indeed, this consist in replicating the same crystallographic structure on top of the substrate with limited amounts of defects.

In the case of common substrates for the semiconductor industry, such as Si and sapphire substrate, the wafer is made using the Czochralski method. This process makes it easy to produce large quantities of suitable quality wafers, making wafers produced through this method readily accessible and cheap. However, GaN cannot be melted, as doing so will result in its decomposition into its elemental constituents, Ga, and N. Hence, different methods are used to grow Gallium Nitride substrates. The three main that have been identified as suited for the industry are[77]:

- Ammonothermal growth[78], which dissolves the Ga from either polycrystalline GaN or Ga metal samples in supercritical NH_3 and redeposit it on a monocrystalline GaN seed. Ga solubility is enhanced using mineralizers which may cause presence of impurities in the material.
- Na-flux, which relies on the diffusion of dissolved N atoms in a Na-Ga melt, growing GaN on an MOCVD or HVPE seed. The process is driven by the supersaturation of nitrogen in the atmosphere of the reactor. The growth process allows to reduce dislocation density compared to the seed by one or more orders of magnitude[79], at the cost of a high process length[80].
- HVPE grown, which relies solely on the hydride vapor phase growth of GaN. This process has the advantage of being mature, and it allows to grow at a very fast pace (up to 1,8 mm/h)[81]. While the grown material is known to be reasonably pure, and can be doped, it usually contains a density of threading dislocations of the order of 10^6 cm^{-2}, which is two orders of magnitude higher than what is achievable with the two other methods.

Despite these existing processes, GaN is still grown heteroepitaxially in most cases. Indeed, while these methods allow to grow native GaN substrate, their cost is still a lot greater than those of other commonly used substrate: a centimeter square of native GaN will cost around 1000 €, while a SiC substrate of the same size will cost around 100 € and Sapphire around 50 €. Hence, in most applications templated GaN on foreign substrate is used instead.

2.2.1.2 HETEROEPITAXY CHALLENGES AND NON-NATIVE SUBSTRATES

While heteroepitaxy on non-native substrates is common, it comes with several issues, on a chemical or structural level, which need to be considered when making structures. The most common issue is strain. There are two origins for strain, which are lattice mismatch and thermal expansion coefficient. Indeed, because the process is performed at high temperature, if the grown GaN has a great difference of thermal expansion coefficient with the substrate, the cooldown after the process will cause strain to appear. Strain can have three different effects in a material. First, reversible strain, called elastic strain, occurs when the mismatch between the two lattices is limited. This kind of strain can be responsible for piezoelectric polarization, as explained previously. This will also influence light emission, causing blue shift or red shift depending on if the strain is compressive or tensile.

Plastic strain is irreversible and will create defects such as threading dislocations in the material. One solution found to counteract this issue is the use of buffer layers having a lattice parameter between that of the substrate and of the grown material. Doing so allows to gradually decrease the strain over a larger thickness of the material, allowing it to relax elastically. This method is used for example in the case of the growth of GaN on Si, where layers of AlGaN with varying can be introduced before the GaN growth, resulting in a decrease in cracks and dislocations[82]. There are other various methods for the reduction of threading dislocations created through heteroepitaxy on a foreign substrate, some of which will be discussed in this manuscript, and it exhibit that it is one of the main challenges in the integration of GaN devices in industrial process.

Last, if the strain is too strong, one of the layers might start displaying cracks. This appears mainly during the cooling process and is due to the difference of thermal expansion coefficient. Cracking can occur over time at room temperature, or after several heating/cooling cycles in a reactor.

The last issue is the chemical compatibility of the substrate which may react with carrier gases, or GaN itself under growth conditions. This is especially the case for Si, as pure Si is known to react with Ga under conditions found in MOCVD, leading to the growth of a Ga:Si compound[83,84]. This issue is called meltback etching and can lead to the destruction of entire wafers in some cases. While solutions exist to counteract this issue (such as using specific gas mixes[84], or a buffer layer[83]), it should be noted that it is exacerbated by cracking, as it exposes more Si to the reactor conditions. Such issues are fortunately specific to Si, and do not affect the growth on other substrates such as sapphire and SiC. However, some studies suggest that growth on these foreign substrates might lead to the contamination[85] of the grown structures by atomic diffusion. This can lead to the introduction of extrinsic defect in the grown structures, which can be responsible for non-radiative centers or deep levels in the material.

Despite the aforementioned issues with non-native substrates, the cost and production issues linked to the production of freestanding GaN wafers imply that most device, both experimentally and industrially, are grown on non-native substrates. Commonly used substrate materials include sapphire, silicon and in some cases, silicon carbide, to grow GaN. their lattice and thermal expansion mismatches, are displayed in Table I-2.

	Sapphire (0001)	Si (111)	6H-SiC (0001)
Lattice mismatch (%)	16.1	-17.0	3.5
Thermal expansion mismatch (%)	-25.5	116	19

Table I-2: *Relative lattice and thermal expansion mismatches of several substrates with GaN*[73].

Sapphire is the most used substrate for GaN growth[86], which can be explained by several arguments. Sapphire is a compromise between material suitability and cost, mainly because of its thermal expansion mismatch significantly lower than that of Si, at a cost lower than that of SiC. Sapphire is a material composed of Al_2O_3 crystallizing in a rhombohedral system. When rotated by 30° in the basal plane, this configuration yields a hexagonal configuration which can be used for the epitaxial growth of GaN[87]. Another key point of sapphire is that it can be nitrated at high temperature, which will help converting the first surface few monolayers in AlN[88]. From here, the material can be used to grow AlN as a buffer layer, and then deposit a GaN layer.

Not surprisingly, Si has also been used for the growth of GaN[89] despite having a lattice mismatch higher than sapphire, but more importantly a high thermal expansion mismatch. The main reason for that is that Si wafers are very cheap thanks to easy melt processing as well as resource availability. Another important point for Si is that it is currently the most used semiconductor, and a good part of the industry is built around Si processing, which is a key argument driving growth of GaN on Si. Since Si is a cubic ZB material, the surface used correspond to its (111) plane, which is hexagonal.

Last, SiC has been used for GaN growth[90], despite not being very common. Indeed, while more difficult and expensive to manufacture than the other presented substrates, SiC is a very appropriate non-native substrate for GaN growth, with low lattice and thermal expansion mismatches. Indeed, while SiC has different polytypes, 2H-SiC correspond to a wurtzite structure, similar to the one of GaN. Some very commonly used 4H and 6H substrates could be seen as a WZ bilayer with a stacking fault and WZ trilayer with two stacking faults respectively[91]. This similar structure and close properties to GaN make SiC a good candidate for heteroepitaxial growth of high quality GaN, but its cost makes it an uncommon option.

2.2.1.3 EPITAXY ON 2D MATERIALS

We have seen in the last paragraphs that the choice for a substrate for GaN growth is non-trivial. Indeed, homoepitaxy on a native substrate is expensive, and because only few methods can produce free standing GaN substrates, it also limits the panel of properties that can be tuned for specific growth. On the other hand, while heteroepitaxy on a foreign substrate is inexpensive and now well mastered, it comes with a high density of defects due to lattice mismatch, thermal expansion mismatch, and contamination of the grown structure. Another solution exists, which consists in obtaining GaN monocrystals without using covalent epitaxy (Fig. I-21).

Indeed, a class of materials called 2D materials has become of great interest recently. It includes materials such as graphene, Transition-Metal Dichalcogenides, and hBN (which is a 2D III-V compound). Such materials consist in a single crystallographic plane, which is why they are called 2D materials. In contrast to the surfaces of most materials, 2D materials have no dangling bonds, as their structure is contained within a plane. This is a consequence of the sp^2 hybridization of the carbon atoms in graphene that planarize the three sp^2 bonds around the carbon, while the pure p orbital is shared between all atoms in the crystal. This means that a pristine 2D material is not able to form any covalent bonding with adatoms, and hence that growing GaN on a material like that would not occur through covalent epitaxy. It means that growth on 2D materials is performed without any issue related to lattice mismatch or thermal expansion mismatch. Because of their lack of dangling bonds, 2D materials are also chemically resistant, meaning that the chances of contaminations of these materials is low. Last, the absence of covalent bonding between the grown structure and the substrate means that the grown structures can easily be removed of the substrates without inducing damages to the substrate, meaning that it might be reused for additional growths. On the other hand, the absence of dangling bonds at the surface of the 2D materials is responsible for a low surface energy. This means that nucleating on such a layer can be a challenging process, which leads to low density of growing nanostructures. Another consequence of this low surface energy is that feature such as defects in the layer, or even holes, may become preferential nucleation points as they may feature covalent bonds, leading to covalent epitaxy, which defeats the purpose. One last consequence is that the low nucleation rate of GaN may lead to Ga accumulation on the surface, which ultimately forms metallic Ga droplets[92] that may preferentially incorporate more Ga adatoms as the growth proceeds.

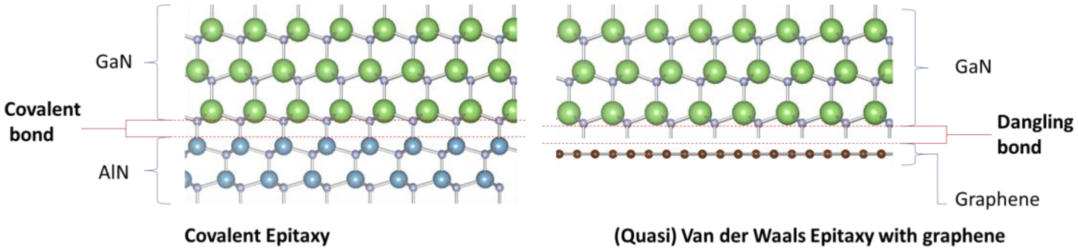

Figure I-21: *Covalent epitaxy of GaN on AlN compared to Van Der Waals epitaxy of GaN on graphene.*

Growth on 2D materials can be performed through several process[93], but mainly through Van der Waals (VdW) epitaxy and remote epitaxy. In VdW epitaxy[94,95], the growth is driven by Van Der Waals interactions between adatoms and the 2D material. Technically speaking, true VDW epitaxy happens when both the substrate and the deposited structures are 2D materials and do not have dangling bonds. Hence in the case of GaN growth on a 2D materials, it would be more correct to talk about quasi Van Der Waals, as the GaN surface facing the 2D material would feature dangling bonds. However, this technicality is often ignored in the literature, and we will hence refer to this process as VdW epitaxy in the rest of this manuscript. An example of VdW epitaxy is provided in Fig. I-22(a), with the growth of AlGaN on graphene/amorphous SiO_2 [96]. Because the underlying substrate is amorphous, there is no transfer of crystalline structure between the grown structure and the underlying substrate. On the contrary, remote epitaxy[97–100] relies on the presence of a crystalline material under the graphene. In principle, this method can be seen as a combination of covalent and VDW epitaxy. Indeed, in remote epitaxy, the grown material follows the crystal structure of this material, while the 2D material acts as a buffer to avoid the formation of covalent bonding. An example of remote epitaxy of GaN on graphene/6H-SiC can be seen in Fig. I-22(b), as it is possible to get a TEM image showing the crystalline structure of both structures, meaning that they share crystalline directions.

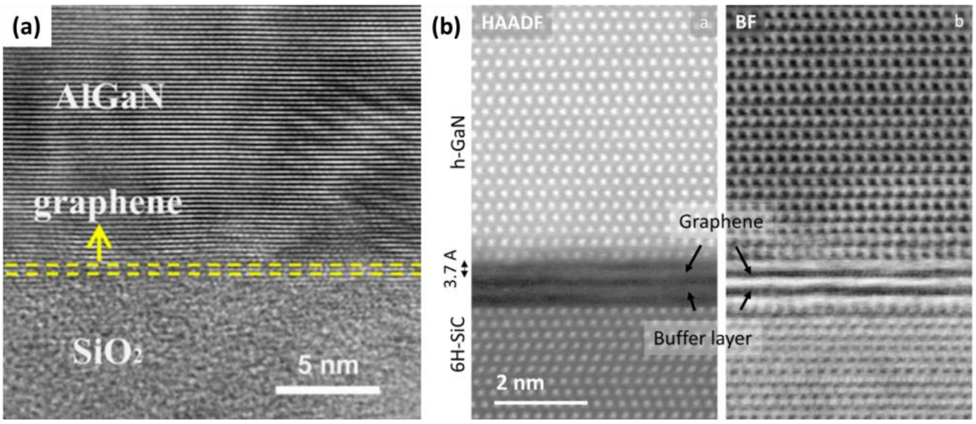

Figure I-22: *Van der waals epitaxy of AlGaN on graphene/amorphous SiO_2*[96] *(a) and remote epitaxy of GaN on graphene/6H-SiC*[97] *(b).*

Ultimately, growth on 2D materials comes with some challenges to overcome, mainly due to low surface energy. Indeed, the fact that the adatom cannot easily form covalent bonds with the surface means that it behaves as a mask, which is not appropriate when it comes to grow crystalline structures. However, it comes with several unique advantages when compared to other options, mainly the possibility of growing relaxed structures without using an expensive freestanding GaN substrate. Hence, it recently attracted the attention as a potential for the growth of high quality GaN. During this PhD, we studied the growth of luminescent InGaN/GaN nanostructures on graphene, as their low cohesion is an advantage to remove GaN nanostructures for flexible LED processing. Hence, we dedicated Chapter 6 to talk about this subject in more details.

2.2.2 LED HETEROSTRUCTURE

2.2.2.1 BASICS OF LED STRUCTURE

In the scope of this PhD, the main goal has been to fabricate LEDs with an emission wavelength in the visible spectrum. This can be achieved with III-Nitride systems through the use of an InN and GaN alloy. A scheme of the basic InGaN/GaN LED structure is provided in Fig. I-23. We can separate the LEDs in 5 parts: the n-doped GaN, the p-doped GaN, the active layer containing the quantum wells), the Electron Blocking Layer, and last the metal contacts. In this part, an overview of the different layers and their properties will be provided (except for the quantum wells, that have been already described in 1.2.2.1)

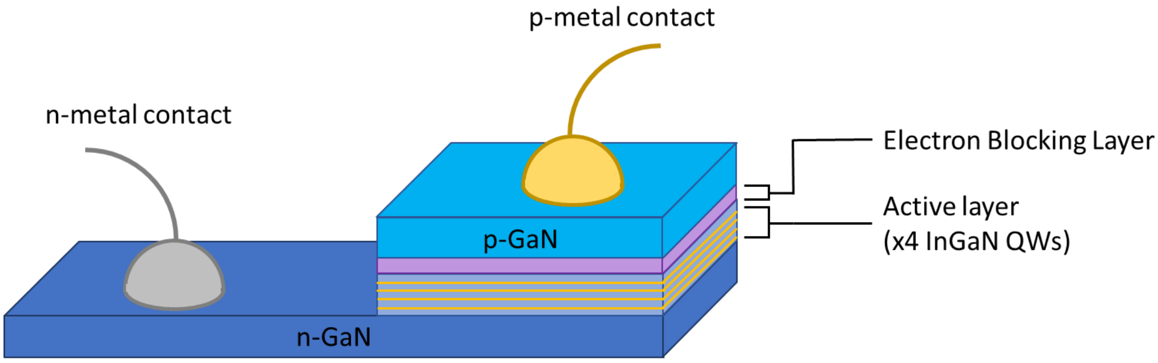

Figure I-23: *Scheme of a classical planar LED structure for visible emission.*

The LED device relies on a so-called **p-n junction**. On either side of the junction, the semiconductors are "doped" by introducing charges in the material, through foreign atoms of different electronic structures. In some cases, the foreign atom provides a negatively charged free electrons, making it a n-dopant, while in others, it provides a positive free hole, making it a p-dopant. It should be noted that dopants are ionized when providing a free carrier, which ensures the overall electrical neutrality of the material. GaN is usually n-doped using atoms such as Si (and rarely Ge), while p-doping is achieved with Mg (and rarely Zn). While the presence of free charges helps with conductivity, the important feature is the p-n junction. When putting a p-doped and n-doped layer next together, Coulombic interaction between free carriers pushes positive holes into the n-side, and negative electrons into p-side, where electron-holes start to recombinate. This locally decreases the amount of free carriers in the material (hence the name "depletion region" given to the junction and its close proximity), and leaves only ionized dopants. The consequence is that a built-in local electric field is created, preventing further diffusion of carriers, and hence current conduction. If an external electric field is applied in the same direction as this built-in electric field, the depletion layer extends on each side of the junction, and no current is transmitted. On the other hand, if an electric field strong enough is applied in the opposite direction, the depletion layer disappears, and it is possible to conduct a current through the junction. It should be noted that because the current is mainly carried by holes in p-GaN, and by electrons in n-GaN, current conduction is driven through recombination at the junction. This makes the p-n junction an appropriate area of the device to put an active layer with quantum wells, as can be seen on Fig. I-24.

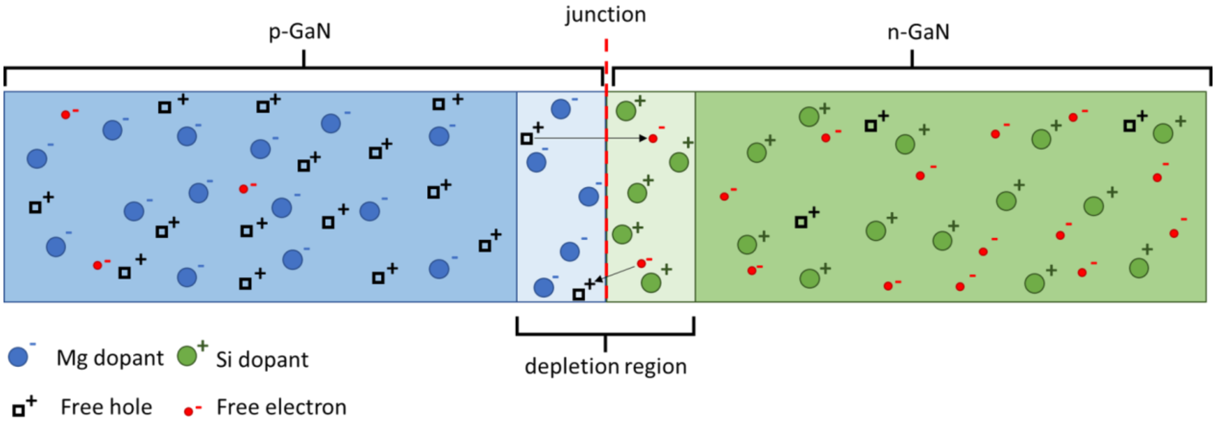

Figure I-24: *Behavior of dopants and free carrier inside of a p-n junction.*

Apart from the active region, the second feature that lies within the p-n junction is **the Electron Blocking Layer**. While this layer is not critical for the overall function of the LED, it is used in order to improve the efficiency of the LED. Indeed, it prevents the electrons to diffuse out of the active area into the p-GaN layer, where they will recombine with holes [101]. Hence, in order to ensure recombination in the quantum well, it is critical to block the electrons from entering the p-GaN, which is the role of the electron blocking layer. These layers are classically made with p-doped AlGaN[102], which has a higher gap than the surrounding GaN. This has the effect of creating a barrier of potential that confines the electron inside the active region (see Fig. I-25).

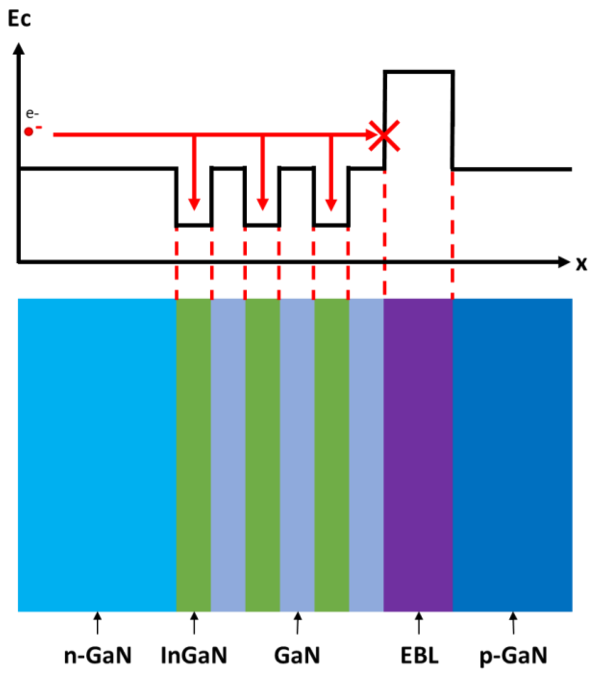

Figure I-25: Scheme of a non-polar LED with an electron blocking layer and corresponding energy of the conduction band.

The last key element of LEDs is **the metal contact,** to inject electrical currents in the LED. In both cases, the contact should be with low resistance and ohmic, meaning that the current is a linear function of the applied potential. Different metal combination may be used for the n-GaN, with the one being used in this work being Ti/Al/Ti/Au[103]. When it comes to p-GaN however, several issues limit the number of options available to do the electrical contact. These issues are a poor ohmicity of the electrical contacts[104] (caused by the large bandgap, leading to the formation of significant Schottky barriers, most important for p-type material[105]) the need for a transparent contact, a low free carrier concentration in Mg and the need for an EBL. Currently, the most used contacts for Mg-doped GaN are NiAu[106] (which can sometimes be oxidized by annealing under air into NiOAu) and Indium Tin Oxide[107] (ITO).

2.2.2.2 ISSUES WITH III-NITRIDE LEDS

Despite being appealing for their tunable wavelengths, high efficiencies and high operating powers, III-nitride LEDs suffer from several issues. In the following paragraphs, we will present the most important ones and suggest ways to solve them.

2.2.2.2.1 N-VACANCIES AND UNDERLAYERS

GaN is thermally unstable and will decompose at temperature lower than usual process temperatures in MOCVD. To solve this issue large partial pressures of NH_3 is used to grow a crystal. However, some issues linked to this behavior still arise. It has been shown that when growing an InGaN QW on 1 µm-thick GaN buffer, the QW intensity will dramatically decrease when increasing the temperature of growth of said buffer, sometimes by more than two orders of magnitude[108]. It was also showed that covering the GaN with a low In-content InGaN layer (called underlayer, UL) before growing the quantum well allowed to suppress this effect.

This issue has been the object of several publications in order to identify its origin and has allowed to set aside a few possible causes, such as dislocations and strain[109]. The current accepted mechanism behind this issue is the formation of thermally activated surface defects in GaN, and especially v_N defects[108]. These defects are unstable in bulk GaN and will hence keep on moving toward the surface of the material during growth. This means that these defects cannot be buried and need to be stabilized by being complexed. Hence, it has been shown that the introduction of a low temperature GaN or AlGaN layer was ineffective. Since these non-radiative centers seemed to preferentially segregate inside In containing compounds, such as InGaN and AlInN, it has been suggested that v_N would form a stable complex with In or one of its defects, with the main candidate being v_Nv_{In}.

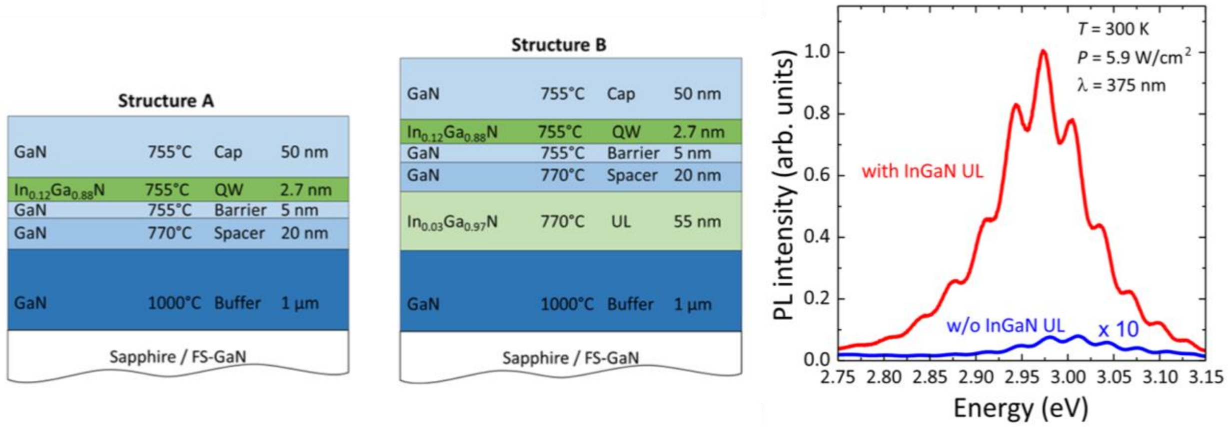

Figure I-26: *Structures of a sample without and without InGaN underlayer, and respective emission spectra (taken from ref. [109]).*

There is currently two ways to reduce NRCs affecting the light emission in the quantum wells, which is to use an UL or to grow additional sacrificial quantum wells. In the first case, the strategy consists in the growth of a thick low In-content layer before quantum well. This strategy has been proven to be effective and may also act as a buffer layer in order to reduce strain due to lattice mismatch with InGaN QW layers. Indeed, Fig. I-26 shows a two orders of magnitude difference in the PL intensity produced by a single InGaN QW on two similar structures, with the only difference being the growth of an InGaN underlayer with low In content after the high temperature GaN buffer growth. However, the presence of the UL will introduce an optical contribution between band edge and the quantum well. The other solution is to use the first two quantum wells in the active layer as sacrificial layers. Indeed, it has been shown that like the UL, the In in the quantum well can act as segregation layers for the non-radiative defects, and that when growing quantum wells, the first two quantum well would trap the majority of NRCs[110]. This allows the growth of several defect-free quantum wells however the first few quantum wells are also the ones that are injected more efficiently. This means that this method may in fact concentrate the defects in the area where most of the light emission process is happening.

2.2.2.2.2 DEFECTS IN INGAN LAYERS

In most semiconductors, especially III-V, the presence of dislocations in a LED structure is a synonym of poor efficiency, because they are sites of non-radiative recombination[111]. However, the presence of dislocations does not directly threaten the efficiency of InGaN/GaN LEDs.

In his 2014 Nobel prize lecture, S. Nakamura[111] shows that GaN, as well as several other arsenide and phosphide compounds have external quantum efficiencies of 20% and below for dislocation densities between 10^6 and 10^7 cm^{-2}. This behavior would be an issue to make LEDs with GaN on sapphire, as its expected density value of 10^9 cm^{-2} for GaN. However, InGaN LEDs are unexpectedly not as sensitive to dislocations, with some compounds reaching efficiencies above 80% for dislocations densities of this magnitude[111]. An explanation to this phenomenon has been proposed and relies on the localization of carriers due to In composition fluctuations, which creates local additional potential wells inside the InGaN layers. This makes InGaN/GaN heterostructures a very versatile tool for light emission, as their light emission efficiency will not be greatly affected by being grown on lattice mismatched substrates.

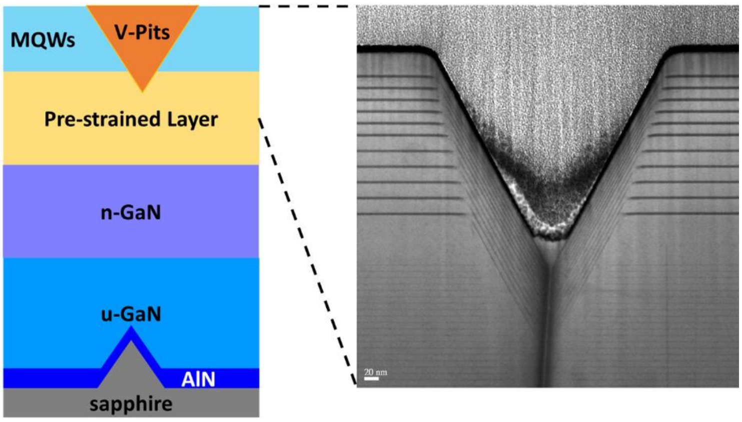

Figure I-27: V-pit caused by a dislocation in a GaN/InGaN heterostructure (taken from ref. [112]).

However, the strain can have other effects on the light emission. First, it has been reported that strain can also increase the density of stacking faults, which is especially true for heterostructures grown on non-polar planes[113]. However, one critical defect in quantum wells is the so-called V-defects or v-pits, as shown in the Fig. I-27). V-defects are inverse pyramidal shaped holes, which are initiated in the InGaN layers, either by dislocations[114] or by stacking mismatch boundaries[115]. They correspond to local inclusions of semi-polar $[10\bar{1}1]$ planes in c-plane polar layer and will hence not appear in non-polar QWs. Their presence may locally interrupt the QWs in the active layer[114,115], creating a local drop in the intensity of the luminescence[116,117]. In other cases, the quantum wells conform to the V-defect, and are hence grown on semi-polar planes of GaN[118]. Because semi-polar planes have different thermodynamical properties than the polar c-plane, the quantum well inside a v-pit is expected to have a smaller thickness, but a larger In incorporation due to strain relaxation. This effect, combined to the fact that semi-polar planes are not fully affected by the quantum confined stark effect (see 3.2.1) means that the emission wavelength of a quantum well located on a V-defect is expected to be blue-shifted[119] or red-shifted[120] . On the other hand, some authors suggest that V-defects may have a beneficial effect on devices by promoting carrier localization, which reduces the amount of non-radiative recombination[120].

2.2.2.2.3 DROOP

Droop is a name given to an empirical phenomenon observed in nitride LEDs, including InGaN QWs. It describes the decrease in emissive power and internal quantum efficiency[121] above a threshold operating current density, as illustrated in the Fig. I-28. The two main contributions to the droop, are Schockley-Read-Hall (SRH) recombinations and Auger recombinations[122]. SRH recombination has been introduced in 1.2.3.2 and is essentially non-radiative trap assisted recombination. In Auger recombination, the energy produced by a recombination is directly used by a third electron in the conduction band to reach a higher level. This electron will then lose this energy through thermalization, which is not a radiative process. This second mechanism hence requires having a large density of carriers in the material, as it relies on their proximity to function. Some sources also count leakage as a source of droop, as it does lower efficiency at high operating currents, but it should be noted that it is not related to recombination pathways and will hence have no effect on the Internal Quantum Efficiency, that accounts only for the efficiency of the recombination processes. In practice, the droop is often represented by the ABC model[123], which is formulated as follow:

$$\mathrm{I_{QW}} = \mathrm{I_{SRH}} + \mathrm{I_{Radiative}} + \mathrm{I_{Auger}} = q \cdot V_{QW} \cdot (A \cdot n + B \cdot n^2 + C \cdot n^3) \quad \mathbf{(1.6)}$$

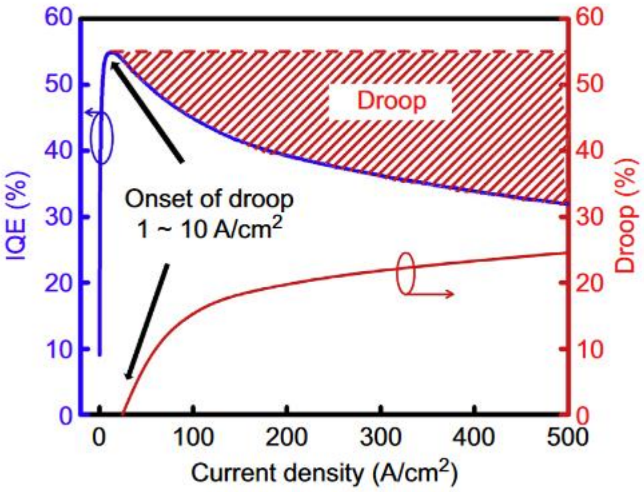

Figure I-28: Representation of droop in a typical InGaN/GaN LED (from ref. [122]).

With $\mathrm{I_{QW}}$ the current flowing through the QW, $\mathrm{I_{SRH}}$, $\mathrm{I_{Radiative}}$ and $\mathrm{I_{Auger}}$ the flow of electron undergoing SRH, radiative and auger recombination respectively, q the charge on an electron, V_{QW} the volume of the QW, n the density of carriers inside the QW, and last A,B and C coefficient for SRH, radiative and Auger recombination, respectively. As can be seen with this equation, Auger recombination becomes dominant at high carrier density, corresponding to high operating currents, suggesting that it is the dominant mechanism behind the droop. This model ignores some other sources of non-radiative recombination in the LED as it aims to link theoretical and experimental results and to allow a quick but truthful analysis of the dominating processes inside a nitride LED.

3 NANOWIRE-BASED LED STRUCTURES

To solve part of the problems that have been evoked, it was chosen to work with a nanowire geometry. Indeed, the nanowire structure presents some advantages over planar geometry, that will be evoked in the next paragraphs. The different geometries and strategies for their fabrication will also be presented.

3.1 ADVANTAGES OF CORE-SHELL STRUCTURES FOR LED ELABORATION

In this PhD, the strategy that has been used to fabricate nanowire LED is the core shell structure by selective area growth. Some elements are provided to understand the main advantages of this choice over other strategies.

3.1.1 A LARGER EMISSION AREA

A first advantage of the core-shell structure is to get a greater area of emission than their planar counterparts when the nanowire reached a given length. In this paragraph, we will provide a short demonstration of this, and we will calculate the minimal length at which this is verified in the case of the geometry used in this work.

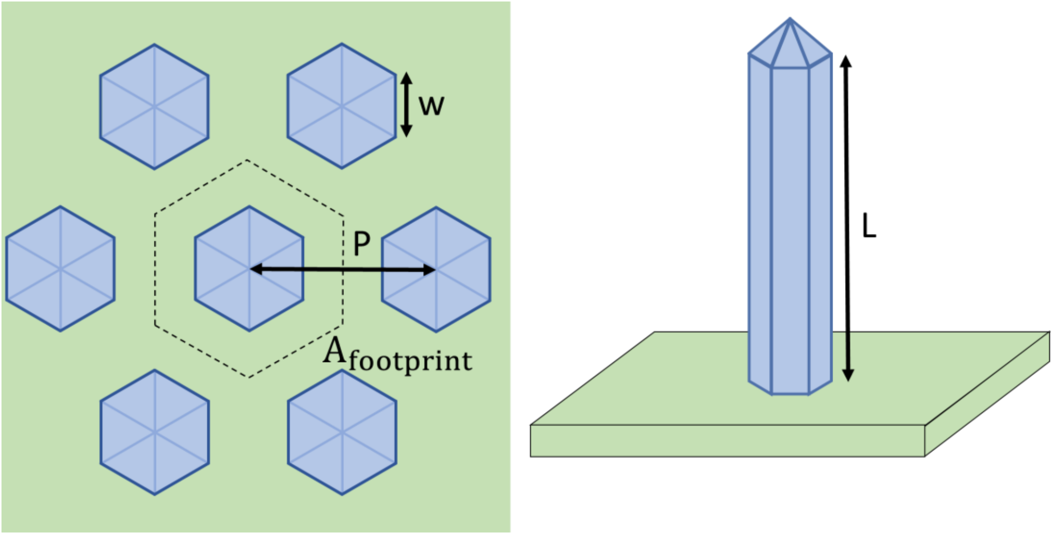

Figure I-33: Geometric configuration of a nanowire array grown by SAG.

Let's consider a regular hexagonal nanowire array as presented in Fig. I-33. Each nanowire is separated from one another by a distance P center to center (also called pitch). We can now define a footprint area, noted $A_{footprint}$, which is the area of emission on a planar LED equivalent to the surface occupied by one nanowire, which is the doted hexagon on Fig. I-33. By looking at the scheme, we can see that the footprint is a hexagon of width P. From this, we can calculate:

$$A_{footprint} = \frac{\sqrt{3}}{2} \cdot P^2 \quad \mathbf{(1.7)}$$

For this calculation, we will consider that the only source of emission in the nanowire is going to be the sidewall, with each sidewall having a length L and a width W. Hence the total area of emission of a nanowire is the sum of the individual area of emission of each sidewall, hence:

$$A_{emission} = 6 \cdot W \cdot L \quad \mathbf{(1.8)}$$

From this, we can conclude that both W and L can be used to increase the area of emission of the nanowire. However, because the section area of a nanowire cannot exceed its footprint, W is limited, such as $W \leq P/\sqrt{3}$. It should be noted that in the case where $W = P/\sqrt{3}$, the nanowires are fully coalesced, and the situation is equivalent to a planar device with no non-polar surfaces. Hence, it is usually preferred to work by enhancing L rather than W. We now want to find the value of L for which $\mathrm{A_{emission}} \geq \mathrm{A_{footprint}}$. Hence:

$$L \geq \frac{1}{4 \cdot \sqrt{3}} \cdot \frac{P^2}{W} \approx 0.144 \cdot \frac{P^2}{W} \quad \mathbf{(1.9)}$$

In the case of this work, the values used for P and W were be 1.5 µm and 0.25 µm respectively. Hence, we get a minimum value of L of 1.3 µm to get an area of emission greater than an equivalent planar LED. Knowing than the average nanowire grown on these samples could reach a length of 5 µm or more, the area of emission of a core-shell nanowire grown by SAG can theoretically have an area of emission several times higher than for a planar LED for a sample of the same size[124]. This increase in active area is not only beneficial for light emission, but also for current injection in the material. Indeed, as the active area gets greater, the current density inside the LED gets reduced, which also limits the efficiency droop.

3.1.2 NO/REDUCED QUANTUM CONFINED STARK EFFECT

One of the most interesting points of the core-shell structure is that it allows to emit light from non-polar planes. Indeed, one element that has not been mentioned until now is the effect of the spontaneous polarization on the band structure. Indeed, spontaneous polarization creates a field inside the lattice, which interacts with the potential in the material. A representation of the distortions induced by Quantum Confined Stark Effect (QCSE) is provided in Fig. I-34. The first and most notable effect is the shift of the energy levels if the electron and hole closer together, which reduces the energy of transition. In practice this effect red shifts the emission[125,126]. These consequences can sometimes be used to reach higher wavelength of emission, but it come at a cost. Indeed, in the presence of a high density of carriers in the QW, a local potential may appear counteracting the effect of QCSE. If the density of carriers gets high enough, the QCSE may be entirely compensated, and the wavelength of emission will be similar than that of an equivalent non-polar QW[126,127]. However, this also means that modifying the power injected in a polar QW will also modify its wavelength of emission.

The second effect of QCSE is the separation of the electron and hole wavefunctions. Indeed, because the QW is shifted, it becomes asymmetrical, and the overlap between electron and hole wavefunctions is reduced, which is detrimental for the recombination efficiency: the radiative lifetime[126] is considerably increased and the carrier radiative recombination are exposed to much stronger competition with non-radiative processes, which have short lifetimes, and can hence become preferential pathways for carrier recombination. We hence chose to work on the non-polar sidewalls of the nanowires.

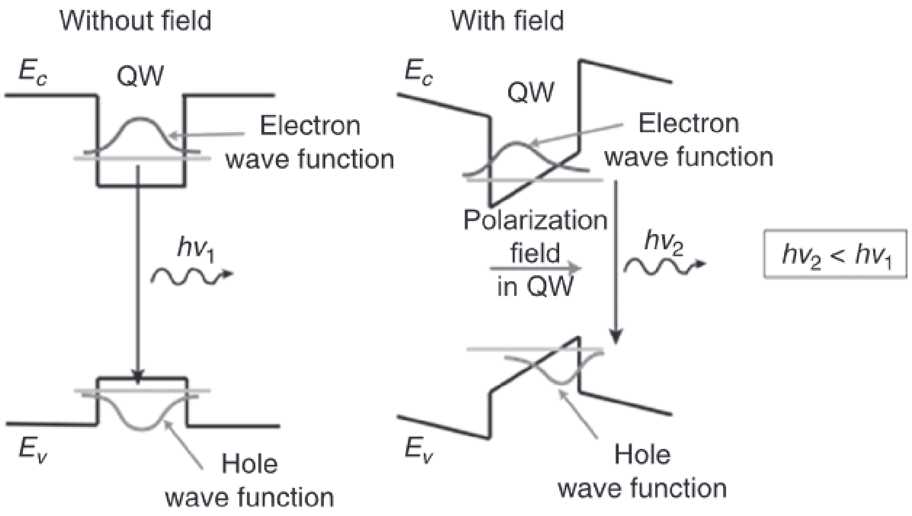

Figure I-34: *Effects of the Quantum Confined Stark Effect in a nitride QW (taken from ref.* [126]*).*

3.1.3 A HIGH CRISTALLINE QUALITY

The last big advantages of core shell nanowires grown through SAG is that it allows to dramatically reduce the amount of dislocation in the active nanowires. This happens through two processes, called dislocation bending and dislocation filtering.

In nanowires, the high amount of free surfaces in nanowires allow to yield relaxed GaN above lengths of the order of several hundred of nm, which is also true for top-down structures[128]. However, in bottom-up growth, the free surfaces already present during growth are also responsible for dislocation bending, which results in the absence of dislocations in the nanowire. One proposed mechanism of formation is the following[129] : during the first stage of the growth, the vertical growth rate is higher than the lateral growth rate (as shown in ref. [130], which was done in an MBE setup but relies on diffusion and plane stability, and could hence be applicable to MOCVD setups) and the nuclei will start displaying some semi-polar planes, which will become more prevalent as the growth continues. Because the dislocations are thermodynamically inclined to thread toward the closest free surface, they will gradually bend to reach the semipolar planes, which is observed experimentally as a 90° bending in the (0001) plane. In practice this mean that apart from the dislocation located at the very center of the nuclei, all dislocations (transferred from the template or created through the coalescence of several crystallites) will be bent toward the lateral facets of the nanowire (Fig. I-35(b)). The main consequence is that a GaN nanowire is dislocation free above a given height, which is generally of the order of 100nm in our case[73].

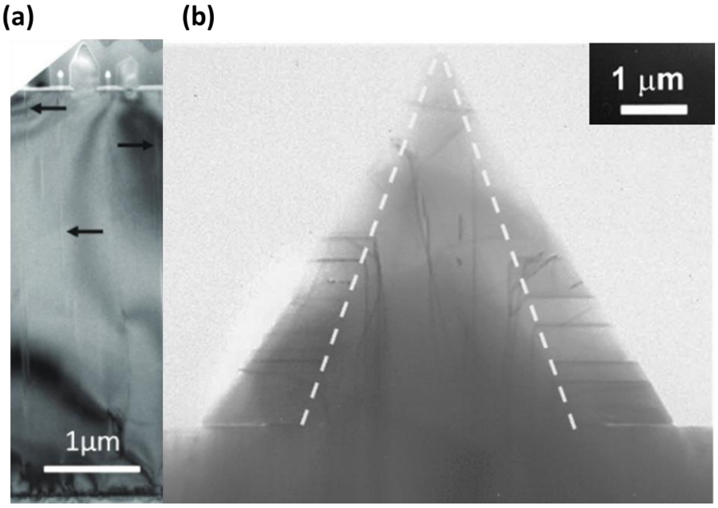

Figure I-35: *Filtered dislocations on a SAG mask for NW growth (indicated with black arrows) and bent dislocations (taken from refs.* [131] *and* [129] *respectively)*

This tool has also been applied to planar growth, through a method called Epitaxial Lateral Overgrowth[132]. In this method, the growth is switched to a 3D growth mode through a mask which will filter part of the dislocations (Fig. I-36(a)). The 3D growth of pyramidal nuclei bends the dislocations in the basal plane. At the coalescence between two nuclei, the dislocations meet, and those with opposite burger Vector annihilate. When the growth is switched again to a lateral growth mode, the remaining dislocations will bend toward the (0001) plane once again. It should be noted that unlike nanowire growth, because ELO switches back to planar growth, the dislocations are not all cancelled, and some will remain concentrated in some areas, leaving large dislocation free areas (Fig. I-36(b)).

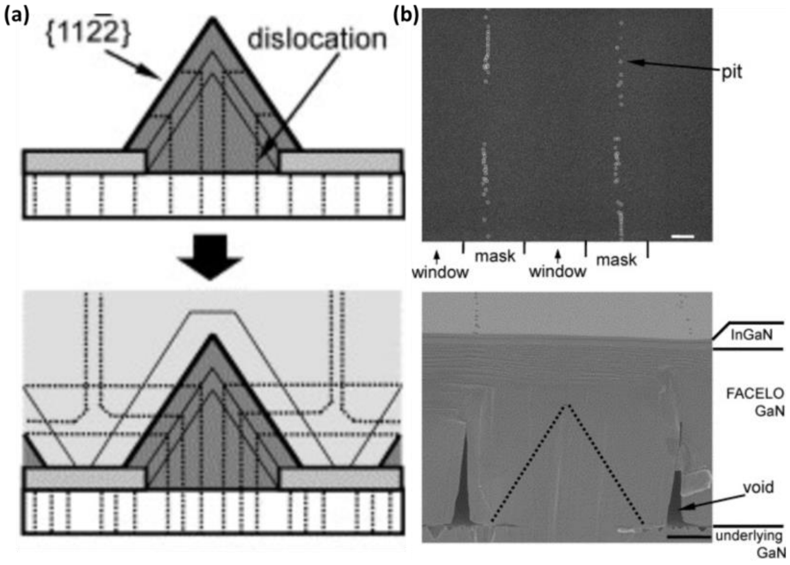

Figure I-36: *Basic mechanism of ELO (a) and (b) top and transverse view of a planar device made using an Epitaxial Lateral Overgrowth method (from ref.* [133]*).*

The last point is specific to SAG: Dislocation filtering[131] occurs because of the homoepitaxial of growth of GaN on GaN through a selective mask. Indeed, when working with SAG nanowires, the growth is done through a mask on planar GaN grown generally on Saphire, which has a typical dislocation density of the order of 5.10^8 cm^{-2}. This means that threading dislocations that are not terminating in one of the openings of the mask are essentially filtered (Fig. I-35(a)). It is possible to estimate the quantity of dislocation filtered using only the geometry of the mask. As an example, let's consider a masked array following a geometry as described in 3.3.1 with circular openings of a diameter of d=500nm, and a pitch of p=1.5µm. The amount of filtered dislocations filtered can be calculated as $n = \frac{A_{oppening}}{A_{footprint}} = \frac{\pi}{2 \cdot \sqrt{3}} \cdot \frac{D^2}{p^2}$, which in our case gives a value of $n = 0.10$. This means that 10% of the dislocations are expected to be transmitted to the nanowires, hence a reduction of dislocations of one order of magnitude.

Thanks to both dislocation filtering and dislocation bending, the main source of dislocations in SAG nanowires are the one created by lattice mismatch during the heteroepitaxy of InGaN on GaN during active layer growth. In the last paragraphs, we have mainly focused on intrinsic properties of GaN core shell grown by SAG.

3.1.4 FLEXIBLE NANOSTRUCTURES

In this manuscript, we have given little attention to the mechanical properties of GaN, as it is not critical to understand LED processing and semiconductors in general. The young and shear moduli of GaN are estimated to be above 300GPa and 150GPa respectively[134], with a fracture toughness lower than 1 $\mathrm{MPa} \cdot \sqrt{\mathrm{m}}$ [135]. This means that bending GaN elastically requires a lot of force, and that fractures may easily appear. Indeed, with such properties, building a flexible device using a large planar LED structure has some inherent limitations. One recent study[136] reports the successful transfer and characterization of a large area planar LED on a PAAM hydrogel, reporting enhanced PL intensity of the device due to the compensation of QCSE by piezoelectric polarization under bending. However, this study does not provide precise and reproducible radii of curvature and does not report on the evolution of the performance of the device under multiple bending cycles, or the appearance of macroscopic defects such as cracks. One solution would be to encapsulate a dense array of small individual LEDs in a flexible material like a polymer, with SAG core shell nanowires perfectly fitting this description. Once the structures are encapsulated, it is possible to remove the structures from the substrates. Indeed, thanks to GaN low fracture toughness and the large aspect ratio of the nanowires, bending the nanowire will result in its breaking at the base. The membrane can then be processed to deposit both p and n contacts at the top and bottom of the nanowires respectively, at which point the device can then be electrically injected to produce light.

3.2 CORE-SHELL GAN NANOWIRES: DIFFERENT GROWTH STRATEGIES

The nanowire morphology has been studied thoroughly on a wide range of materials for a lot of different applications, such as lasers[137], water splitting[138], flexible LEDs[139], high electron mobility transistors[140] or piezo generators[141] to cite only the case of nitrides. To understand the differences associated with each nanowire geometry, a general outline of the different approaches will be provided in the following paragraphs. The structure used in this PhD is the core shell structure, which relies on the first growth of a GaN core, and the subsequent growth of a shell containing the InGaN/GaN heterostructure around the core. This is by opposition to the axial geometries that can be grown through MBE, that include the growth of the InGaN/GaN in the growth of the nanowire itself[142].

In this PhD, we will call *the core* the bulk part of the nanowire, in opposition to *the shell* that refers to the close surface of the nanowire, where the QWs and subsequent p-GaN will be grown. The main aim of core growth is going to be the optimization of the geometrical properties of the nanowire, whereas the shell focuses on optical properties. We will discuss here the different techniques that exist to grow the core, with special interest on the MOCVD technique.

3.2.1 TOP-DOWN APPROACH

The top-down approach to nanowire fabrication consists in growing a thick planar layer of GaN following the classical process used for the elaboration of planar devices. The planar layer is then masked using either a metallic or dielectric layer, and the GaN is then selectively removed using wet etching[143], dry etching[144] or sublimation[145] respectively. This method allows the best control over the size, geometry, and morphology of the nanowires. The main disadvantage however is that the selective removal of the GaN may introduce defects on the top a lateral facet, especially when using dry etching, which can be problematic if the structure contains an active layer. This effect may however be counteracted using wet etching[146], which can successfully remove the surface states introduce by the plasma, or even entirely remove the top defective layer of GaN. Another disadvantage is that this method does not benefit from the effects of dislocation bending and filtering which will be presented later in this document, meaning that nanowires produced through this method may also contain more structural defects such as dislocation than their counterparts produced through bottom-up processes. The last disadvantage of using top-down fabrication of nanowires is that nanowires will not exhibit sharp crystalline facets with their associated precise properties. The evolution of some GaN nanowires during top-down etching process is presented in Fig. I-29.

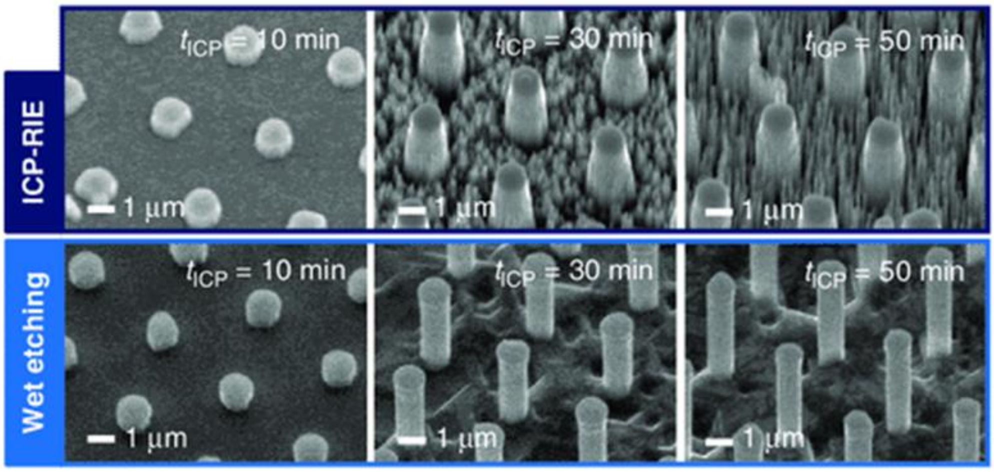

Figure I-29: *Elaboration of GaN nanowires through the top-down approach (dry and wet etching respectively) (taken from ref.* [143]*).*

3.2.2 BOTTOM-UP APPROACH

In the bottom-up approach, the nanowires are grown directly on the substrate instead of being carved out of a planar GaN layer. While this has the advantage of not introducing defects in the structures, it makes the process more difficult requiring specific methods to achieve high aspect ratio. We will present several of those techniques that are used to grow nanowires.

3.2.2.1 CATALYZED GROWTH

One of the most critical aspects in the growth of nanowires is the nucleation. Furthermore, controlling the positioning of the nanowires is an important feature, as it allows to have control over the density of the array, The first method used to grow nanowires circumvented this issue by using catalyzed growth, a process in which the nanowires grow on previously deposited metallic seeds[147].

The idea of using metal catalyst to grow nanowires is not new and not unique to GaN. Indeed, the first reported use of this process dates to 1954, when Johnson and Amick[148] first reported Si nanowires growth, using Zn vapors as a catalyst. However, the first report of nanowire growth using a metallic seed would only be published in 1964 by Wagner *et al.*[149] who used solid gold seeds to grow Si nanowires. This method has been declined in two different strategies, Vapor-Liquid-Solid[150] (VLS) growth, where the metal seed liquifies during growth (Fig. I-30), and Vapor-Solid-Solid[151] (VSS), where the metal seed stays solid. In both cases, the mechanism of growth is the same[151–153]: the metal catalyst acts as a collector for the gas-phase reactants by creating a ternary alloy in the case of GaN. This process goes on until the alloy reaches saturation, at which point it will start segregating a GaN compound. From this, the reaction will go on until no new reactant is being collected by the catalyst. It should be noted that this process has been verified by filming the in-situ growth of Au-catalyzed GaAs nanowires[154].

This method has several advantages and disadvantages. On the advantages, this method allows to control not only the positioning of the nanowires, but also their diameter. Indeed, this growth mode allows to achieve very thin nanowires[155], thanks to a limited lateral growth and an initial diameter depending only on the size of the catalyst seed. It should be noted however that the size of the droplet is limited, and there is minimum droplet radius achievable with this method[156]. Growing thick nanowires would also be challenging, as the raising the droplet radius would result in a lowering of the contact angle with the substrate, which is a critical parameter of growth and may be responsible for inhomogeneities[157]. However, this does not limit the length of the nanowire, since GaN nanowires grown by VLS can reach lengths of several tens of micrometers with a diameter lower than 100 nm[158], which gives an aspect ratio of 100 or more. Last, the use of a metal catalyst allows nanowires to be grown on a large variety of substrates, since the growth is driven by segregation of the GaN out of the catalyst, and not by actual epitaxial deposition of adatoms.

However, this growth mode comes with a few issues. The first one is that the difficulty to control of the nanowire crystallographic orientations. It has also been reported that some catalyst may incorporate as point defects in the nanowires and have been attributed to deep level transition[159,160], as well as structural defects[161,162]. Finally, it should be noted that even if the metal catalyst does not incorporate in the GaN during the growth, it may also create a pollution in the reactor. Metallic particulates are thus to avoid in an MOCVD reactor.

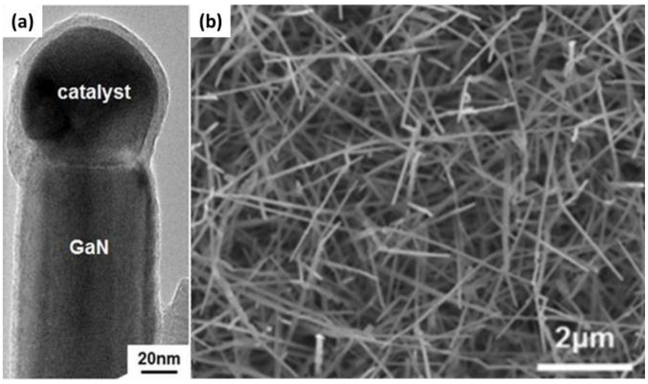

Figure I-30: *Close up view of an Au-Ni catalyzed GaN nanowire (a) and corresponding sample morphology (b) (taken from ref* [163]*)*

3.2.2.2 SELF-ORGANIZED GROWTH WITHOUT CATALYST

Because of these disadvantages, an alternative growth approach without catalyst has been developed. Catalyst free processes must overcome issues such as positioning, nucleation, that had been previously solved using metal catalyst seeds. One alternative method is to use self-organized growth[164], relying on a precise control of the thermodynamical parameters of the growth to achieve an irregular array of nanowires (Fig. I-31(a)).

The growth process relies on a first *in-situ* preparation of the surface of the sample in order to obtain nanowire growth. The first step is to obtain nucleation layer. This can be done either by AlN in-situ deposition[165], or by nitridation of a sapphire substrate under NH_3 at high temperatures[88,164]. This step is followed by the growth of a thin (~2 nm) *in-situ* porous SiN_x mask[164,165], which helps promoting local growth of GaN seeds. This step is critical, as this layer is going to be responsible for the nanowire density, as well as their crystalline quality. Indeed, the authors of the ref.[164] observed that a long growth time of this SiN_x layer would result in poor crystalline quality of the wires, which they correlated with a change in the seed morphology[164]. Subsequent GaN nucleation is performed, followed with growth under optimized conditions to favor the vertical growth as described in chapter 2.

The advantage of this method is that it can be entirely performed *in-situ*, which makes it time and cost effective, but also prevents contaminations and damages to occur to the sample. It also allows to yield nanowires with lengths of several tens of micrometers (Fig. I-31(b)), owing them the name of microwires, which is favorable for polymer encapsulation such as found in the flexible device fabrication[139,166,167] . The main disadvantage of this technique is that it does not control the position, morphology and polarity of each individual nanowire, which is responsible for inhomogeneities in size, density, and optical/electrical properties. One structural defect prevalent in self-organized nanowires is the IDB, which is caused by the coalescence of nuclei of Ga and N-polar polarity[168,169].

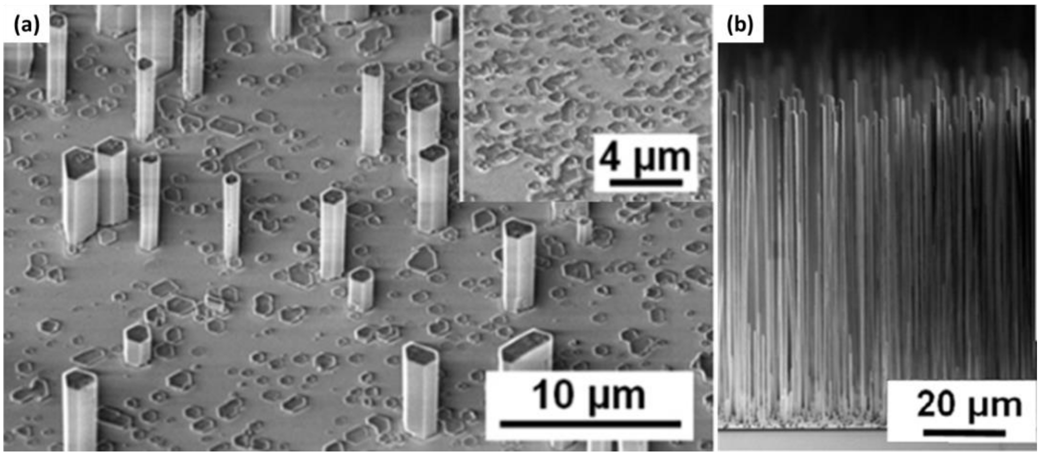

Figure I-31: *SEM images of GaN nanowires grown by self-organized growth with different growth parameters (taken from ref.* [164]*).*

3.2.2.3 SELECTIVE AREA GROWTH WITHOUT CATALYST

Selective Area Growth (SAG) is the inverse philosophy of self-organized growth and has been first reported by Hersee et al. in 2006 [170] . Selective Area Growth relies on *ex-situ* preparation of the sample, which includes the deposition and patterning of a thick (~30 nm) SiN_x or SiO_x mask. This allows to get a very homogeneous array of nanowires, at the cost of a more complicated and expensive preparation. Different methods can be used to do the patterning, but this PhD mainly focused on Displacement Talbot Lithography (DTL)[171], with several tries with Electron Beam Lithography (EBL), which is also commonly used, and microsphere lithography, which is a more unusual method of patterning.

The growth process of the nanowires themselves is very similar to the one used in self-organized growth, with key differences in the nucleation step. Indeed, selective area growth is dependent on the depth profile of the opening, as it is a key factor for nucleation. Gačević *et al.*[130] reported that during the first steps of nucleation of GaN nanowires by MBE, the first crystallites started to grow at the periphery of the hole in the mask, which is consistent with observation made on other cases of selective area growth by MOCVD[172]. This make sense, the driving mechanism behind this mode of growth is diffusion of adatoms on the mask until the specie either desorbs or gets to an opening. The crystallites will then start to coalesce, until they form a unique crystal in the opening. The last step is the morphological of the crystallite through the formation of stable crystallographic facets.

This means however that selective area growth is lithography dependent, as the nucleation is sensitive to the opening profile. It requires thus a great care during the *ex-situ* masking process, as well as a precise control over growth parameters. It allows to get a dense regular array of nanowires with homogeneous properties on surfaces of the order of the cm^2 (Fig. I-32). The fact that the nanowires can be directly grown through homoepitaxy on a GaN template also means that the crystallographic orientation as well as polarity are controlled, which efficiently prevents the apparition of defects such as dislocations and IDBs.

Self-organized and selective area growth can thus be used in complementarity of one another. Self-organized growths being simpler and faster make it a great tool for research and establishing proof of concepts. However, when it comes to process optimization and device fabrication, the control and homogeneity offered by selective area growth make it an appropriate method.

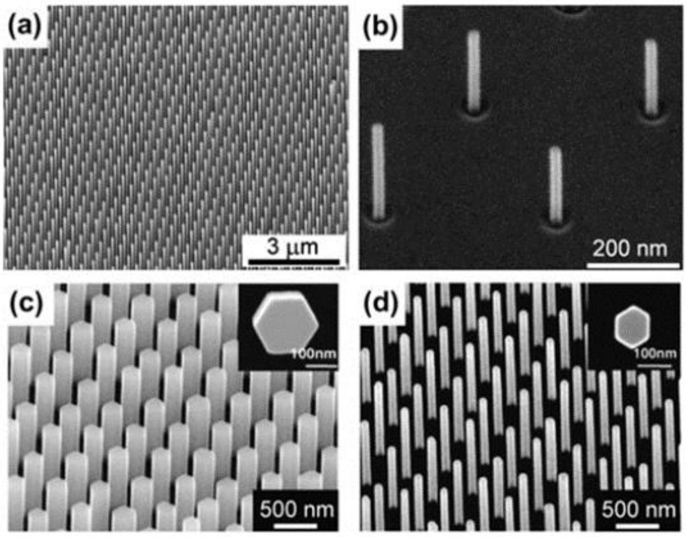

Figure I-32: *Examples of GaAs nanowire arrays grown by selective area growth (taken from ref.* [173] *)*

3.2.2.4 MIXED APPROACH

The mixed approach[174,175] attempts to associate the top down and bottom-up approaches to easily produce nanowires of good quality. The idea behind this approach is that using a top-down approach will allow to get a regular array of nanowire with precise control of the geometrical features of the nanowires. Once the nanowire produced, the defects introduced by the dry or thermal etching can be removed by doing a wet etching, which tends to introduce less defects in the material. From then, the sample is put in a growth reactor in order to grown GaN on top of the nanowire, which may under specific condition help to regrow some crystalline facets on the nanowire. The main advantage of this method is that it allows to easily get a regular array of nanowires, as can be obtained with a top-down process. However, the subsequent etching and regrowth allow to improve the crystalline quality of the structures, as it would be the case in bottom-up growth. However, this method also requires a lot of steps, using several different techniques, which adds complexity to the process.

4 CONCLUSION

In this chapter, we have provided an overview of nitride semiconductor properties, focusing on GaN for visible LEDs applications, with an emphasis on the nanowire geometry. While this overview was necessary to understand the context and the stakes of the use of nitride in optoelectronic devices, we still need to present in detail the growth of core-shell SAG nanowire LEDs by MOCVD, including the mechanism of growth and critical parameters. We also need to present the tools used to characterize such structures on the morphological, structural, and optical point of view. This will be the subject of the next chapter.

BIBLIOGRAPHY

1. Michael E. Levinshtein, Sergey L. Rumyantsev, Michael S. Shur. *Properties of Advanced Semiconductor Materials: GaN, AIN, InN, BN, SiC, SiGe*.; 2016.

2. Weng YC, Wu CC, Chang EY, Chieng WH. Minimum power input control for class-e amplifier using depletion-mode gallium nitride high electron mobility transistor. *Energies (Basel)*. 2021;14(8):2302. doi:10.3390/en14082302

3. Nakamura S, Mukai T, Senoh M. High-power GaN p-n junction blue-light-emitting diodes. *Jpn J Appl Phys*. 1991;30(12A):1998-2001. doi:10.1143/JJAP.30.L1998

4. Fletcher ASA, Nirmal D. A survey of Gallium Nitride HEMT for RF and high power applications. *Superlattices Microstruct*. 2017;109:519-537. doi:10.1016/j.spmi.2017.05.042

5. Mi Z, Zhao S. Extending group-III nitrides to the infrared: Recent advances in InN. *Phys Status Solidi B Basic Res*. 2015;252(5):1050-1062. doi:10.1002/pssb.201451628

6. Taniyasu Y, Kasu M, Makimoto T. An aluminium nitride light-emitting diode with a wavelength of 210 nanometres. *Nature*. 2006;441(7091):325-328. doi:10.1038/nature04760

7. Xie Y, Qian Y, Zhang S, Wang W, Liu X, Zhang Y. Coexistence of wurtzite GaN with zinc blende and rocksalt studied by x-ray power diffraction and high-resolution transmission electron microscopy. *Appl Phys Lett*. 1996;69(3):334-336. doi:10.1063/1.118051

8. Rawat V, Zakharov DN, Stach EA, Sands TD. Pseudomorphic stabilization of rocksalt GaN in TiN/GaN multilayers and superlattices. *Phys Rev B Condens Matter Mater Phys*. 2009;80(2):024114. doi:10.1103/PhysRevB.80.024114

9. Qian W, Skowronski M, Rohrer GS. Structural defects and their relationship to nucleation of GaN thin films. *MRS Online Proceedings Library* . 1996;423:475-486. doi:https://doi.org/10.1557/PROC-423-475

10. Maleyre B, Ruffenach S, Briot O, Van Der Lee A. Lattice parameters of relaxed wurtzite indium nitride powder obtained by MOCVD. *Superlattices Microstruct*. 2004;36(4-6):527-535. doi:https://doi.org/10.1016/j.spmi.2004.09.052

11. Galsin JS. Crystal Structure of Solids. In: *Solid State Physics*. Elsevier; 2019:1-36. doi:10.1016/b978-0-12-817103-5.00001-3

12. Faria Junior PE, Sipahi GM. Band structure calculations of InP wurtzite/zinc-blende quantum wells. *J Appl Phys*. 2012;112(10):103716. doi:10.1063/1.4767511

13. Tantardini C, Oganov AR. Thermochemical electronegativities of the elements. *Nat Commun*. 2021;12(1):2087. doi:10.1038/s41467-021-22429-0

14. Hanada T. Basic Properties of ZnO, GaN, and Related Materials. In: *Oxide and Nitride Semiconductors* . Vol 12. ; 2009:1-19. doi:https://doi.org/10.1007/978-3-540-88847-5_1

15. Bernardini F, Fiorentini V, Vanderbilt D. Spontaneous polarization and piezoelectric constants of III-V nitrides. *Phys Rev B*. 1997;56(16):R10024-R10027. doi:https://doi.org/10.1103/PhysRevB.56.R10024

16. Lai YY, Hsu SC, Chang HS, et al. The study of wet etching on GaN surface by potassium hydroxide solution. *Research on Chemical Intermediates*. 2017;43(6):3563-3572. doi:10.1007/s11164-016-2430-1

17. Takeya M, Mizuno T, Sasaki T, et al. Degradation in AlGaInN lasers. *Physica Status Solidi C: Conferences*. 2003;0(7):2292-2295. doi:10.1002/pssc.200303324

18. Li H, Huang M, Chen S. First-principles exploration of defect-pairs in GaN. *Journal of Semiconductors*. 2020;41(3):032104. doi:10.1088/1674-4926/41/3/032104

19. Dreyer CE, Alkauskas A, Lyons JL, Speck JS, Van De Walle CG. Gallium vacancy complexes as a cause of Shockley-Read-Hall recombination in III-nitride light emitters. *Appl Phys Lett*. 2016;108(14):141101. doi:10.1063/1.4942674

20. Reshchikov MA, Morkǫ H. Luminescence properties of defects in GaN. *J Appl Phys*. 2005;97(6):061301. doi:10.1063/1.1868059

21. Bogusławski P, Bernholc J. Doping properties of C, Si, and Ge impurities in GaN and AlN. *Phys Rev B Condens Matter Mater Phys*. 1997;56(15):9496-9505. doi:10.1103/PhysRevB.56.9496

22. Nakamura S, Mukai T, Senoh M, Iwasa N. Thermal annealing effects on p-type Mg doped GaN films. *Jpn J Appl Phys*. 1992;31:L139-L142. doi:10.1143/JJAP.31.L139

23. X. J. Ning, F. R. Chien, P. Pirouz, J. W. Yang, M. Asif Khan. Growth defects in GaN films on sapphire: The probable origin of threading dislocations. *J Mater Res*. 1996;11:580-592. doi:https://doi.org/10.1557/JMR.1996.0071

24. Vennéguès P, Beaumont B, Haffouz S, Vaille M, Gibart P. Influence of in situ sapphire surface preparation and carrier gas on the growth mode of GaN in MOVPE. *J Cryst Growth*. 1998;187(2):167-177. doi:https://doi.org/10.1016/S0022-0248(97)00875-0

25. Romanitan C, Mihalache I, Tutunaru O, Pachiu C. Effect of the lattice mismatch on threading dislocations in heteroepitaxial GaN layers revealed by X-ray diffraction. *J Alloys Compd*. 2021;858:157723. doi:10.1016/j.jallcom.2020.157723

26. Tomasz Wcislo, Maria Dabrowska-Szata, Lukasz Gelczuk. Critical thickness of epitaxial thin films using Finite Element Method. In: *International Students and Young Scientists Workshop "Photonics and Microsystems."* ; 2010:82-85. doi:10.1109/STYSW.2010.5714177

27. Martin J. *Etude Par Épitaxie En Phase Vapeur Aux Organométalliques de La Croissance Sélective de Nano-Hétéro-Structures de Matériaux à Base de GaN*. Université de Lorraine; 2018. https://hal.univ-lorraine.fr/tel-01752653

28. lvan V Markov. *Crystal Growth for Beginners: Fundamentals of Nucleation, Crystal Growth and Epitaxy*.; 1995. doi:https://doi.org/10.1142/5172

29. Callister WD. *Materials Science and Engineering : An Introduction*.; 2007.

30. Twigg ME, Koleske DD, Wickenden AE, Henry RL, Fatemi M, Culbertson JC. Structural defects in nitride heteroepitaxy. In: *III-Nitride Semiconductors: Electrical, Structural and Defects Properties*. Elsevier; 2000:339-381. doi:https://doi.org/10.1016/B978-0-444-50630-6.X5000-4

31. Liliental-Weber Z, Zakharov D, Jasinski J, O'Keefe MA, Morkoc H. Screw Dislocations in GaN Grown by Different Methods. In: *Microscopy and Microanalysis*. Vol 10. ; 2004:47-54. doi:10.1017/S1431927604040309

32. Lele S, Prasad B, Rama Rao P. Stacking faults in double hexagonal close-packed crystals. *Materials Science and Engineering*. 1969;4(5):262-270. doi:https://doi.org/10.1016/0025-5416(69)90002-0

33. Wright AF. Basal-plane stacking faults and polymorphism in AlN, GaN, and InN. *J Appl Phys*. 1997;82(10):5259-5261. doi:https://doi.org/10.1063/1.366393

34. Ruvimov S. Defect engineering in III-nitrides epitaxial systems. In: *III-Nitride Semiconductors: Electrical, Structural and Defects Properties*. ; 2000:51-75. doi:https://doi.org/10.1016/B978-044450630-6/50004-0

35. Ruterana P, Béré A, Nouet G. Formation and stability of the prismatic stacking faultin wurtzite (Al,Ga,In) nitrides. *MRS Internet Journal of Nitride Semiconductor Research* . 2000;5(Suplemental Issue 1):266-272.

36. Smith DJ, Tsen I SCY, Sverdlow BN, Martin G, Morko H. Stacking mismatch boundaries in GaN: Implications for substrate selection. *Solid State Electron*. 1997;41(2):349-3524.

37. Umar MMF, Sofo JO. Inversion domain boundaries in wurtzite GaN. *Phys Rev B*. 2021;103(16):165305. doi:10.1103/PhysRevB.103.165305

38. Northrup JE, Neugebauer J, Romano LT. Inversion Domain and Stacking Mismatch Boundaries in GaN. *Phys Rev Lett*. 1996;77(1):103-106. doi:10.1103/PhysRevLett.77.103

39. Xin Y, Brown PD, Humphreys CJ, Cheng TS, Foxon CT. Domain boundaries in epitaxial wurtzite GaN. *Appl Phys Lett*. 1997;70(10):1308-1310. doi:https://doi.org/10.1063/1.118520

40. Christensen NE, Gorczyca I. Optical and structural properties of III-V nitrides under pressure. *Phys Rev B*. 1994;50(7):4397-4415. doi:10.1103/PhysRevB.50.4397

41. Chen GD, Smith M, Lin JY, et al. Fundamental optical transitions in GaN. *Appl Phys Lett*. 1996;68(20):2784-2786. doi:https://doi.org/10.1063/1.116606

42. Li J, Nam KB, Nakarmi ML, et al. Band structure and fundamental optical transitions in wurtzite AlN. *Appl Phys Lett*. 2003;83(25):5163-5165. doi:10.1063/1.1633965

43. Leroux M, Grandjean N, Beaumont B, et al. Temperature quenching of photoluminescence intensities in undoped and doped GaN. *J Appl Phys*. 1999;86(7):3721-3728. doi:https://doi.org/10.1063/1.371242

44. Damilano B. *Habilitation à Diriger Les Recherches : Diodes Électroluminescentes Multicolores à Base de (Ga,In)N*. 2020.

45. Orsal G, El Gmili Y, Fressengeas N, et al. Bandgap energy bowing parameter of strained and relaxed InGaN layers. *Opt Mater Express*. 2014;4(5):1030. doi:10.1364/ome.4.001030

46. Hussain S. *Structural and Optical Characterization of Green-Yellow Light Emitting Devices with High Indium Concentrated (In , Ga) N Quantum Wells*. Université Nice Sophia Antipolis; 2014. https://theses.hal.science/tel-01130108/

47. Rosner SJ, Carr EC, Ludowise MJ, Girolami G, Erikson HI. Correlation of cathodoluminescence inhomogeneity with microstructural defects in epitaxial GaN grown by metalorganic chemical-vapor deposition. *Appl Phys Lett*. 1997;70(4):420-422. doi:10.1063/1.118322

48. Shockley W, Read Jr WT. Statistics of the Recombinations of Holes and Electrons. *Physical Review*. 1952;87(5):835-842. doi:10.1103/PhysRev.87.835

49. Hall RN. Electron-Hole Recombination in Germanium. *Physical Review*. 1952;87(2):387-387. doi:10.1103/PhysRev.87.387

50. Li G, Chua SJ, Xu SJ, et al. Nature and elimination of yellow-band luminescence and donor-acceptor emission of undoped GaN. *Appl Phys Lett*. 1999;74(19):2821-2823. doi:https://doi.org/10.1063/1.124025

51. Li X, Bohn PW, Coleman JJ. Impurity states are the origin of yellow-band emission in GaN structures produced by epitaxial lateral overgrowth. *Appl Phys Lett*. 1999;75(26):4049-4051. doi:https://doi.org/10.1063/1.125532

52. Reshchikov MA, Demchenko DO, Usikov A, Helava H, Makarov Y. Carbon defects as sources of the green and yellow luminescence bands in undoped GaN. *Phys Rev B Condens Matter Mater Phys*. 2014;90(23):235203. doi:10.1103/PhysRevB.90.235203

53. Toshio Ogino, Masaharu Aoki. Mechanism of Yellow Luminescence in GaN. *Jpn J Appl Phys*. 1980;19(12):2395. doi:10.1143/JJAP.19.2395

54. Reshchikov MA, McNamara JD, Helava H, Usikov A, Makarov Y. Two yellow luminescence bands in undoped GaN. *Sci Rep*. 2018;8:8091. doi:https://doi.org/10.1038/s41598-018-26354-z

55. Reshchikov MA. On the Origin of the Yellow Luminescence Band in GaN. *Phys Status Solidi B Basic Res*. 2022;260(8):2200488. doi:https://doi.org/10.1002/pssb.202200488

56. Zhang R, Kuech TF. Photoluminescence of carbon in situ doped GaN grown by halide vapor phase epitaxy. *Appl Phys Lett*. 1998;72(13):1611-1613. doi:https://doi.org/10.1063/1.121144

57. Kaufmann U, Kunzer M, Obloh H, et al. Origin of defect-related photoluminescence bands in doped and nominally undoped GaN. *Phys Rev B*. 1999;59(8):5561-5567. doi:10.1103/PhysRevB.59.5561

58. Uedono A, Chichibu SF, Chen ZQ, et al. Study of defects in GaN grown by the two-flow metalorganic chemical vapor deposition technique using monoenergetic positron beams. *J Appl Phys*. 2001;90(1):181-186. doi:https://doi.org/10.1063/1.1372163

59. Wang J, Wang X, Shu W, Zeng X, Chen J, Xu K. Origin of blue luminescence in Mg-doped GaN. *AIP Adv*. 2021;11(3):035131. doi:https://doi.org/10.1063/5.0037047

60. Reshchikov MA, Morkoç H, Molnar RJ, Tsvetkov D, Dmitriev V. Blue Luminescence in Undoped and Zn-doped GaN. *MRS Online Proceedings Library*. 2002;743:111. doi:https://doi.org/10.1557/PROC-743-L11.1

61. Wu J, Yaguchi H, Onabe K, Ito R, Shiraki Y. Photoluminescence properties of cubic GaN grown on GaAs(100) substrates by metalorganic vapor phase epitaxy. *Appl Phys Lett*. 1997;71(15):2067-2069. doi:https://doi.org/10.1063/1.119344

62. Albrecht M, Christiansen S, Salviati G, et al. Luminescence Related to Stacking Faults in Heterepitaxially Grown Wurtzite GaN. *MRS Online Proceedings Library*. 1997;468:293-298. doi:https://doi.org/10.1557/PROC-468-29

63. Stampfl C, Van De Walle CG. Energetics and electronic structure of stacking faults in AlN, GaN, and InN. *Phys Rev B*. 1998;57(24):R15052-R15055. doi:10.1103/PhysRevB.57.R15052

64. Lähnemann J, Jahn U, Brandt O, Flissikowski T, Dogan P, Grahn HT. Luminescence associated with stacking faults in GaN. *J Phys D Appl Phys*. 2014;47(42):42301. doi:10.1088/0022-3727/47/42/423001

65. Ben Sedrine N, Esteves TC, Rodrigues J, et al. Photoluminescence studies of a perceived white light emission from a monolithic InGaN/GaN quantum well structure. *Sci Rep*. 2015;5:13739. doi:https://doi.org/10.1038/srep13739

66. Varshni YP. Temperature dependence of the energy gap in semiconductors. In: *Physica*. Vol 34. ; 1967:149-154. doi:https://doi.org/10.1016/0031-8914(67)90062-6

67. Vurgaftman I, Meyer JR. Band parameters for nitrogen-containing semiconductors. *J Appl Phys*. 2003;94(6):3675-3696. doi:10.1063/1.1600519

68. Cho YH, Gainer GH, Fischer AJ, et al. "S-shaped" temperature-dependent emission shift and carrier dynamics in InGaN/GaN multiple quantum wells. *Appl Phys Lett*. 1998;73(10):1370-1372. doi:https://doi.org/10.1063/1.122164

69. Reshchikov MA, Albarakati NM, Monavarian M, Avrutin V, Morkoç H. Thermal quenching of the yellow luminescence in GaN. *J Appl Phys*. 2018;123(16):161520. doi:https://doi.org/10.1063/1.4995275

70. Wang X, Wang T, Yu D, Xu S. Large negative thermal quenching of yellow luminescence in non-polar InGaN/GaN quantum wells. *J Appl Phys*. 2021;130(20):205704. doi:https://doi.org/10.1063/5.0064466

71. Reshchikov MA. Two-step thermal quenching of photoluminescence in Zn-doped GaN. *Phys Rev B Condens Matter Mater Phys*. 2012;85(24):245203. doi:10.1103/PhysRevB.85.245203

72. Gil B, Briot O, Aulombard RL. Valence-band physics and the optical properties of GaN epilayers grown onto sapphire with wurtzite symmetry. *Phys Rev B*. 1995;52(24):R17028-R17031. doi:10.1103/PhysRevB.52.R17028

73. Coulon PM. *Croissance et Caractérisation de Nanofils/Microfils de GaN*. Université Nice Sophia Antipolis; 2014. https://theses.hal.science/tel-01002342

74. Barbier C. *Epitaxie de GaN Sur Substrat de Graphène*. Sorbonne Université; 2021. https://theses.hal.science/tel-03469445

75. Bockowski M, Iwinska M, Amilusik M, et al. Doping in bulk HVPE-GaN grown on native seeds – highly conductive and semi-insulating crystals. *J Cryst Growth*. 2018;499:1-7. doi:https://doi.org/10.1016/j.jcrysgro.2018.07.019

76. Bohnen T, Ashraf H, Van Dreumel GWG, et al. Enhanced growth rates and reduced parasitic deposition by the substitution of Cl2 for HCl in GaN HVPE. *J Cryst Growth*. 2010;312(18):2542-2550. doi:https://doi.org/10.1016/j.jcrysgro.2010.04.010

77. Pimputkar S. Gallium nitride. In: *Single Crystals of Electronic Materials: Growth and Properties*. Elsevier Ltd; 2019:351-399. doi:https://doi.org/10.1016/B978-0-08-102096-8.00011-2

78. Suihkonen S, Pimputkar S, Sintonen S, Tuomisto F. Defects in Single Crystalline Ammonothermal Gallium Nitride. *Adv Electron Mater*. 2017;3(6):1600496. doi:https://doi.org/10.1002/aelm.201600496

79. Si Z, Liu Z, Hu Y, et al. Growth behavior and stress distribution of bulk GaN grown by Na-flux with HVPE GaN seed under near-thermodynamic equilibrium. *Appl Surf Sci*. 2022;578:152073. doi:https://doi.org/10.1016/j.apsusc.2021.152073

80. Imade M, Imanishi M, Todoroki Y, et al. Fabrication of low-curvature 2 in. GaN wafers by Na-flux coalescence growth technique. *Applied Physics Express*. 2014;7(3):035503. doi:10.7567/APEX.7.035503

81. Yoshida T, Oshima Y, Watanabe K, Tsuchiya T, Mishima T. Ultrahigh-speed growth of GaN by hydride vapor phase epitaxy. *Physica Status Solidi (C) Current Topics in Solid State Physics*. 2011;8(7-8):2110-2112. doi:https://doi.org/10.1002/pssc.201000953

82. Xu PQ, Jiang Y, Ma ZG, et al. The influence of graded AlGaN buffer thickness for crack-free GaN on Si(111) substrates by using MOCVD. *Chinese Physics Letters*. 2013;30(2):028101. doi:10.1088/0256-307X/30/2/028101

83. Zhang Z, Yang J, Zhao D, et al. The melt-back etching effect of the residual Ga in the reactor for GaN grown on (111) Si. *AIP Adv*. 2022;12(9):095106. doi:https://doi.org/10.1063/5.0105524

84. Khoury M, Tottereau O, Feuillet G, Vennéguès P, Zúñiga-Pérez J. Evolution and prevention of meltback etching: Case study of semipolar GaN growth on patterned silicon substrates. *J Appl Phys*. 2017;122(10):105108. doi:https://doi.org/10.1063/1.5001914

85. Popovici G, Kim W, Botchkarev A, Tang H, Morkoç H, Solomon J. Impurity contamination of GaN epitaxial films from the sapphire, SiC and ZnO substrates. *Appl Phys Lett*. 1997;71(23):3385-3387. doi:https://doi.org/10.1063/1.120343

86. Amano H, Akasaki I, Hiramatsu K, Koide N, Sawaki N. Effects of the buffer layer in metalorganic vapour phase epitaxy of GaN on sapphire substrate. *Thin Solid Films*. 1988;163:415-420. doi:https://doi.org/10.1016/0040-6090(88)90458-0

87. Dovidenko K, Oktyabrsky S, Narayan J, Razeghi M. Aluminum nitride films on different orientations of sapphire and silicon. *J Appl Phys*. 1996;79(5):2439-2445. doi:https://doi.org/10.1063/1.361172

88. Grandjean N, Massies J, Leroux M. Nitridation of sapphire. Effect on the optical properties of GaN epitaxial overlayers. *Appl Phys Lett*. 1996;69(14):2071-2073. doi:https://doi.org/10.1063/1.116883

89. Chen KJ, Haberlen O, Lidow A, et al. GaN-on-Si power technology: Devices and applications. *IEEE Trans Electron Devices*. 2017;64(3):779-795. doi:10.1109/TED.2017.2657579

90. Zhang L, Yu J, Hao X, et al. Influence of stress in GaN crystals grown by HVPE on MOCVD-GaN/6H-SiC substrate. *Sci Rep*. 2014;4:4179. doi:https://doi.org/10.1038/srep04179

91. Langpoklakpam C, Liu AC, Chu KH, et al. Review of Silicon Carbide Processing for Power MOSFET. *Crystals (Basel)*. 2022;12(2):245. doi:https://doi.org/10.3390/cryst12020245

92. Gruart M, Feldberg N, Gayral B, et al. Impact of kinetics on the growth of GaN on graphene by plasma-assisted molecular beam epitaxy. *Nanotechnology*. 2020;31(11):115602. doi:10.1088/1361-6528/ab5c15

93. Kumaresan V, Largeau L, Madouri A, et al. Epitaxy of GaN Nanowires on Graphene. *Nano Lett*. 2016;16(8):4895-4902. doi:https://doi.org/10.1021/acs.nanolett.6b01453

94. Bakti Utama MI, Zhang Q, Zhang J, et al. Recent developments and future directions in the growth of nanostructures by van der Waals epitaxy. *Nanoscale*. 2013;5(9):3570-3588. doi:https://doi.org/10.1039/C3NR34011B

95. Koma A, Yoshimura K. Ultrasharp interfaces grown with Van der Waals epitaxy. *Surf Sci*. 1986;174(1-3):556-560. doi:https://doi.org/10.1016/0039-6028(86)90471-1

96. Song W, Ren F, Wang Y, et al. Gan-based leds grown on graphene-covered sio2/si (100) substrate. *Crystals (Basel)*. 2020;10(9):787. doi:https://doi.org/10.3390/cryst10090787

97. Journot T, Okuno H, Mollard N, et al. Remote epitaxy using graphene enables growth of stress-free GaN. *Nanotechnology*. 2019;30(50):505603. doi:10.1088/1361-6528/ab4501

98. Kim Y, Cruz SS, Lee K, et al. Remote epitaxy through graphene enables two-dimensional material-based layer transfer. *Nature*. 2017;544:340-343. doi:https://doi.org/10.1038/nature22053

99. Qu Y, Xu Y, Cao B, et al. Long-Range Orbital Hybridization in Remote Epitaxy: The Nucleation Mechanism of GaN on Different Substrates via Single-Layer Graphene. *ACS Appl Mater Interfaces*. 2022;14(1):2263-2274. doi:https://doi.org/10.1021/acsami.1c18926

100. Jeong J, Jin DK, Choi J, et al. Transferable, flexible white light-emitting diodes of GaN p–n junction microcrystals fabricated by remote epitaxy. *Nano Energy*. 2021;86:106075. doi:https://doi.org/10.1016/j.nanoen.2021.106075

101. Piprek J, Li S. Electron leakage effects on GaN-based light-emitting diodes. *Opt Quantum Electron*. 2010;42(2):89-95. doi:https://doi.org/10.1007/s11082-011-9437-z

102. Han SH, Lee DY, Lee SJ, et al. Effect of electron blocking layer on efficiency droop in InGaN/GaN multiple quantum well light-emitting diodes. *Appl Phys Lett*. 2009;94(23):231123. doi:https://doi.org/10.1063/1.3153508

103. Wang DF, Shiwei F, Lu C, et al. Low-resistance Ti/Al/Ti/Au multilayer ohmic contact to n-GaN. *J Appl Phys*. 2001;89(11):6214-6217. doi:https://doi.org/10.1063/1.1350617

104. Sarkar B, Reddy P, Klump A, et al. On Ni/Au Alloyed Contacts to Mg-Doped GaN. *J Electron Mater*. 2018;47(1):305-311. doi:https://doi.org/10.1007/s11664-017-5775-3

105. Greco G, Iucolano F, Roccaforte F. Ohmic contacts to Gallium Nitride materials. *Appl Surf Sci*. 2016;383(15):324-345. doi:https://doi.org/10.1016/j.apsusc.2016.04.016

106. Chen J, Brewer WD. Ohmic Contacts on p-GaN. *Adv Electron Mater*. 2015;1(8):1500113. doi:https://doi.org/10.1002/aelm.201500113

107. Wang L, Zhang Y, Li X, et al. Interface and transport properties of GaN/graphene junction in GaN-based LEDs. *J Phys D Appl Phys*. 2012;45(50):505102. doi:10.1088/0022-3727/45/50/505102

108. Chen Y, Haller C, Liu W, Karpov SY, Carlin JF, Grandjean N. GaN buffer growth temperature and efficiency of InGaN/GaN quantum wells: The critical role of nitrogen vacancies at the GaN surface. *Appl Phys Lett*. 2021;118(11):111102. doi:https://doi.org/10.1063/5.0040326

109. Haller C, Carlin JF, Jacopin G, Martin D, Butté R, Grandjean N. Burying non-radiative defects in InGaN underlayer to increase InGaN/GaN quantum well efficiency. *Appl Phys Lett*. 2017;111(26):262101. doi:https://doi.org/10.1063/1.5007616

110. Armstrong A, Henry TA, Koleske DD, Crawford MH, Lee SR. Quantitative and depth-resolved deep level defect distributions in InGaN/GaN light emitting diodes. *Opt Express*. 2012;20(56):A812-A821. doi:https://doi.org/10.1364/OE.20.00A812

111. Nakamura S. *Nobel Lecture: Background Story of the Invention of Efficient Blue InGaN Light Emitting Diodes*.; 2014. https://www.nobelprize.org/uploads/2018/06/nakamura-lecture.pdf

112. Chen SW, Li H, Chang CJ, Lu TC. Effects of nanoscale V-shaped pits on GaN-based light emitting diodes. *Materials*. 2017;10(2). doi:https://doi.org/10.3390/ma10020113

113. Cho YS, Sun Q, Lee IH, et al. Reduction of stacking fault density in m -plane GaN grown on SiC. *Appl Phys Lett*. 2008;93(11). doi:10.1063/1.2985816

114. Sharma N, Thomas P, Tricker D, Humphreys C. Chemical mapping and formation of V-defects in InGaN multiple quantum wells. *Appl Phys Lett*. 2000;77(9):1274-1276. doi:10.1063/1.1289904

115. Cho HK, Lee JY, Yang GM, Kim CS. Formation mechanism of V defects in the InGaN/GaN multiple quantum wells grown on GaN layers with low threading dislocation density. *Appl Phys Lett*. 2001;79(2):215-217. doi:10.1063/1.1384906

116. Jeong MS, Kim YW, White JO, et al. Spatial variation of photoluminescence and related defects in InGaN/GaN quantum wells. *Appl Phys Lett*. 2001;79(21):3440-3442. doi:https://doi.org/10.1063/1.1420489

117. Yapparov R, Chow YC, Lynsky C, et al. Variations of light emission and carrier dynamics around V-defects in InGaN quantum wells. *J Appl Phys*. 2020;128(22):225703. doi:https://doi.org/10.1063/5.0031863

118. Tsai HL, Wang TY, Yang JR, et al. Observation of V defects in multiple InGaN/GaN quantum well layers. *Mater Trans*. 2007;48(5):894-898. doi:https://doi.org/10.2320/matertrans.48.894

119. Kurai S, Gao J, Makio R, et al. Study on higher-energy emission observed locally around V-pits on InGaN/GaN quantum wells grown on moderate-temperature GaN. *J Appl Phys*. 2021;130(5):053103. doi:https://doi.org/10.1063/5.0056025

120. Kim MK, Choi S, Lee JH, et al. Investigating carrier localization and transfer in InGaN/GaN quantum wells with V-pits using near-field scanning optical microscopy and correlation analysis. *Sci Rep*. 2017;7:42221. doi:https://doi.org/10.1038/srep42221

121. Mukai T, Yamada M, Nakamura S. Characteristics of InGaN-Based UV / Blue / Green / Amber / Red Light-Emitting Diodes. *Jpn J Appl Phys*. 1999;38:3976-3981. doi:10.1143/JJAP.38.3976

122. Fu H, Zhao Y. Efficiency droop in GaInN/GaN LEDs. In: *Nitride Semiconductor Light-Emitting Diodes (LEDs): Materials, Technologies, and Applications: Second Edition*. Elsevier; 2018:299-325. doi:https://doi.org/10.1016/B978-0-08-101942-9.00009-5

123. Prajoon P, Nirmal D, Anuja Menokey M, Charles Pravin J. A modified ABC model in InGaN MQW LED using compositionally step graded Alternating Barrier for efficiency improvement. *Superlattices Microstruct*. 2016;96:155-163. doi:https://doi.org/10.1016/j.spmi.2016.05.013

124. Waag A, Wang X, Fündling S, et al. The nanorod approach: GaN NanoLEDs for solid state lighting. *Physica Status Solidi (C) Current Topics in Solid State Physics*. 2011;8(7-8):2296-2301. doi:https://doi.org/10.1002/pssc.201000989

125. Takeuchi T, Sota S, Katsuragawa M, et al. Quantum-Confined Stark Effect due to Piezoelectric Fields in GaInN Strained Quantum Wells. *The Japan Society of Applied Physics* . 1997;36:L382-L385. doi:10.1143/JJAP.36.L382

126. Verma J, Verma A, Protasenko V, Islam SM, Jena D. Nitride LEDs based on quantum wells and quantum dots. In: *Nitride Semiconductor Light-Emitting Diodes (LEDs): Materials, Technologies and Applications*. ; 2014:368-408. doi:https://doi.org/10.1533/9780857099303.2.368

127. Deguchi T, Sekiguchi K, Nakamura A, et al. Quantum-confined stark effect in an AlGaN/GaN/AlGaN single quantum well structure. *Japanese Journal of Applied Physics, Part 2: Letters*. 1999;38:L914-L916. doi:10.1143/JJAP.38.L914

128. Hugues M, Shields PA, Sacconi F, et al. Strain evolution in GaN nanowires: From free-surface objects to coalesced templates. *J Appl Phys*. 2013;114(8):084307. doi:https://doi.org/10.1063/1.4818962

129. Vennéguès P, Beaumont B, Bousquet V, Vaille M, Gibart P. Reduction mechanisms for defect densities in GaN using one- or two-step epitaxial lateral overgrowth methods. *J Appl Phys*. 2000;87(9):4175-4181. doi:https://doi.org/10.1063/1.373048

130. Gačević Ž, Gómez Sánchez D, Calleja E. Formation mechanisms of gan nanowires grown by selective area growth homoepitaxy. *Nano Lett*. 2015;15(2):1117-1121. doi:https://doi.org/10.1021/nl504099s

131. Coulon PM, Alloing B, Brändli V, Vennéguès P, Leroux M, Zúñiga-Pérez J. Dislocation filtering and polarity in the selective area growth of GaN nanowires by continuous-flow metal organic vapor phase epitaxy. *Applied Physics Express*. 2016;9(1):015502. doi:10.7567/APEX.9.015502

132. Beaumont B, Vennéguès P, Gibart P. Epitaxial lateral overgrowth of GaN. *Phys Status Solidi B Basic Res*. 2001;227(1):1-43. doi:https://doi.org/10.1002/1521-3951(200109)227:1%3C1::AID-PSSB1%3E3.0.CO;2-Q

133. Hiramatsu K, Nishiyama K, Onishi M, et al. Fabrication and characterization of low defect density GaN using facet-controlled epitaxial lateral overgrowth (FACELO). *J Cryst Growth*. 2000;221(1-4):316-326. doi:https://doi.org/10.1016/S0022-0248(00)00707-7

134. Fujikane M, Leszczyński M, Nagao S, et al. Elastic-plastic transition during nanoindentation in bulk GaN crystal. *J Alloys Compd*. 2008;450(1-2):405-411. doi:https://doi.org/10.1016/j.jallcom.2006.10.121

135. Drory MD, Ager JW, Suski T, Grzegory I, Porowski S. Hardness and fracture toughness of bulk single crystal gallium nitride. *Appl Phys Lett*. 1996;69(26):4044-4046. doi:https://doi.org/10.1063/1.117865

136. Chen J, Wang J, Ji K, et al. Flexible, stretchable, and transparent InGaN/GaN multiple quantum wells/polyacrylamide hydrogel-based light emitting diodes. *Nano Res*. 2022;15:5492-5499. doi:https://doi.org/10.1007/s12274-022-4170-4

137. Li Q, Wright JB, Chow WW, et al. Single-mode GaN nanowire lasers. *Opt Express*. 2002;20(16):17873-17879. doi:10.1364/OE.20.017873

138. Han S, Noh S, Yu YT, Lee CR, Lee SK, Kim JS. Highly Efficient Photoelectrochemical Water Splitting Using GaN-Nanowire Photoanode with Tungsten Sulfides. *ACS Appl Mater Interfaces*. 2020;12(52):58028-58037. doi:https://doi.org/10.1021/acsami.0c17811

139. Guan N, Dai X, Messanvi A, et al. Flexible White Light Emitting Diodes Based on Nitride Nanowires and Nanophosphors. *ACS Photonics*. 2016;3(4):597-603. doi:https://doi.org/10.1021/acsphotonics.5b00696

140. Santoruvo G. *AlGaN/GaN Nanowires: From Electron Transport to RF Applications*. Ecole Polytechnique Fédérale de Lausanne; 2020.

141. Jamond N, Chrétien P, Houzé F, et al. Piezo-generator integrating a vertical array of GaN nanowires. *Nanotechnology*. 2016;27(32):325403. doi:10.1088/0957-4484/27/32/325403

142. Tourbot G, Bougerol C, Grenier A, et al. Structural and optical properties of InGaN/GaN nanowire heterostructures grown by PA-MBE. *Nanotechnology*. 2011;22(7):075601. doi:10.1088/0957-4484/22/7/075601

143. Yulianto N, Refino AD, Syring A, et al. Wafer-scale transfer route for top–down III-nitride nanowire LED arrays based on the femtosecond laser lift-off technique. *Microsyst Nanoeng*. 2021;7:32. doi:https://doi.org/10.1038/s41378-021-00257-y

144. Behzadirad M, Nami M, Wostbrock N, et al. Scalable Top-Down Approach Tailored by Interferometric Lithography to Achieve Large-Area Single-Mode GaN Nanowire Laser Arrays on Sapphire Substrate. *ACS Nano*. 2018;12(3):2373-2380. doi:https://doi.org/10.1021/acsnano.7b07653

145. Damilano B, Vézian S, Brault J, Alloing B, Massies J. Selective Area Sublimation: A Simple Top-down Route for GaN-Based Nanowire Fabrication. *Nano Lett*. 2016;16(3):1863-1868. doi:https://doi.org/10.1021/acs.nanolett.5b04949

146. Hartensveld M, Ouin G, Liu C, Zhang J. Effect of KOH passivation for top-down fabricated InGaN nanowire light emitting diodes. *J Appl Phys*. 2019;126(18):183102. doi:https://doi.org/10.1063/1.5123171

147. Alloing B, Zúñiga-Pérez J. Metalorganic chemical vapor deposition of GaN nanowires: From catalyst-assisted to catalyst-free growth, and from self-assembled to selective-area growth. *Mater Sci Semicond Process*. 2016;55:51-58. doi:https://doi.org/10.1016/j.mssp.2016.03.025

148. Johnson ER, Amick JA. Formation of single crystal silicon fibers. *J Appl Phys*. 1954;25(9):1204-1205. doi:https://doi.org/10.1063/1.1721838

149. Wagner RS, Ellis WC. Vapor-liquid-solid mechanism of single crystal growth. *Appl Phys Lett*. 1964;4(5):89-90. doi:https://doi.org/10.1063/1.1753975

150. Gottschalch V, Wagner G, Bauer J, Paetzelt H, Shirnow M. VLS growth of GaN nanowires on various substrates. *J Cryst Growth*. 2008;310(23):5123-5128. doi:https://doi.org/10.1016/j.jcrysgro.2008.08.013

151. Maliakkal CB, Hatui N, Bapat RD, Chalke BA, Rahman AA, Bhattacharya A. The Mechanism of Ni-Assisted GaN Nanowire Growth. *Nano Lett*. 2016;16(12):7632-7638. doi:https://doi.org/10.1021/acs.nanolett.6b03604

152. Duan X, Lieber CM. Laser-assisted catalytic growth of single crystal GaN nanowires. *J Am Chem Soc*. 2000;122(1):188-189. doi:https://doi.org/10.1021/ja993713u

153. Lee SK, Choi HJ, Pauzauskie P, et al. Gallium nitride nanowires with a metal initiated metal-organic chemical vapor deposition (MOCVD) approach. *Phys Status Solidi B Basic Res*. 2004;241(12):2775-2778. doi:https://doi.org/10.1002/pssb.200404989

154. Harmand JC, Patriarche G, Glas F, et al. Atomic Step Flow on a Nanofacet. *Phys Rev Lett*. 2018;121(16):166101. doi:10.1103/PhysRevLett.121.166101

155. Chen X, Xu J, Wang RM, Yu D. High-quality ultra-fine GaN nanowires synthesized via chemical vapor deposition. *Advanced Materials*. 2003;15(5):419-421. doi:https://doi.org/10.1002/adma.200390097

156. Huang MH, Wu Y, Feick H, Tran N, Weber E, Yang P. Catalytic growth of zinc oxide nanowires by vapor transport. *Advanced Materials*. 2001;13(2):113-116. doi:https://doi.org/10.1002/1521-4095(200101)13:2%3C113::AID-ADMA113%3E3.0.CO;2-H

157. Dubrovskii VG. Development of Growth Theory for Vapor-Liquid-Solid Nanowires: Contact Angle, Truncated Facets, and Crystal Phase. *Cryst Growth Des*. 2017;17(5):2544-2548. doi:https://doi.org/10.1021/acs.cgd.7b00076

158. Zhong Z, Qian F, Wang D, Lieber CM. Synthesis of p-type gallium nitride nanowires for electronic and photonic nanodevices. *Nano Lett*. 2003;3(3):343-346. doi:https://doi.org/10.1021/nl034003w

159. Yoo J, Hong YJ, An SJ, et al. Photoluminescent characteristics of Ni-catalyzed GaN nanowires. *Appl Phys Lett*. 2006;89(4):043124. doi:https://doi.org/10.1063/1.2243710

160. Park JB, Kim NJ, Kim YJ, Lee SH, Yi GC. Metal catalyst-assisted growth of GaN nanowires on graphene films for flexible photocatalyst applications. *Current Applied Physics*. 2014;14(11):1437-1442. doi:https://doi.org/10.1016/j.cap.2014.08.007

161. Tham D, Nam CY, Fischer JE. Defects in GaN nanowires. *Adv Funct Mater*. 2006;16(9):1197-1202. doi:10.1002/adfm.200500807

162. Chèze C, Geelhaar L, Brandt O, et al. Direct comparison of catalyst-free and catalyst-induced GaN nanowires. *Nano Res*. 2010;3:528-536. doi:https://doi.org/10.1007/s12274-010-0013-9

163. Wu KL, Chou Y, Su CC, Yang CC, Lee WI, Chou YC. Controlling bottom-up rapid growth of single crystalline gallium nitride nanowires on silicon. *Sci Rep*. 2017;7:17942. doi:https://doi.org/10.1038/s41598-017-17980-0

164. Koester R, Hwang JS, Durand C, Le Si Dang D, Eymery J. Self-assembled growth of catalyst-free GaN wires by metal-organic vapour phase epitaxy. *Nanotechnology*. 2010;21(1):015602. doi:10.1088/0957-4484/21/1/015602

165. Foltynski B, Giesen C, Heuken M. Self-organized growth of catalyst-free GaN nano- and micro-rods on Si(111) substrates by MOCVD. *Phys Status Solidi B Basic Res*. 2015;252(5):1132-1137. doi:https://doi.org/10.1002/pssb.201451508

166. Guan N, Dai X, Eymery J, Durand C, Tchernycheva M. Nitride-nanowire-based flexible LEDs. *SPIE Newsroom*. 2017.

167. Guan N, Dai X, Babichev A V., Julien FH, Tchernycheva M. Flexible inorganic light emitting diodes based on semiconductor nanowires. *Chem Sci*. 2017;8(12):7904-7911. doi:10.1039/c7sc02573d

168. Coulon PM, Mexis M, Teisseire M, et al. Dual-polarity GaN micropillars grown by metalorganic vapour phase epitaxy: Cross-correlation between structural and optical properties. *J Appl Phys*. 2014;115(15):153504. doi:https://doi.org/10.1063/1.4870950

169. Coulon PM, Alloing B. Structural Characterization of GaN Nano and Microwires by Transmission Electron Microscopy (TEM). *Workshop on Nanostructures de semiconducteurs à grande bande interdite*. Published online 2012. https://www.researchgate.net/publication/311257277

170. Hersee SD, Sun X, Wang X. The controlled growth of GaN nanowires. *Nano Lett*. 2006;6(8):1808-1811. doi:https://doi.org/10.1021/nl060553t

171. Coulon PM, Damilano B, Alloing B, et al. Displacement Talbot lithography for nano-engineering of III-nitride materials. *Microsyst Nanoeng*. 2019;5:52. doi:https://doi.org/10.1038/s41378-019-0101-2

172. Winden A, Mikulics M, Stoica T, et al. Site-controlled growth of indium nitride based nanostructures using metalorganic vapour phase epitaxy. *J Cryst Growth*. 2013;370:336-341. doi:https://doi.org/10.1016/j.jcrysgro.2012.08.034

173. Tomioka K, Ikejiri K, Tanaka T, et al. Selective-area growth of III-V nanowires and their applications. *J Mater Res*. 2011;26(17):2127-2141. doi:https://doi.org/10.1557/jmr.2011.103

174. Cameron D, Coulon PM, Fairclough S, et al. Core-Shell Nanorods as Ultraviolet Light-Emitting Diodes. *Nano Lett*. 2023;23(4):1451-1458. doi:https://doi.org/10.1021/acs.nanolett.2c04826

175. Li C, Wright JB, Liu S, et al. Nonpolar InGaN/GaN Core-Shell Single Nanowire Lasers. *Nano Lett*. 2017;17(2):1049-1055. doi:https://doi.org/10.1021/acs.nanolett.6b04483

Chapter 2:

Experimental setup: growth and characterization of GaN nanowires

CONTENTS

In the last chapter, we have provided a description of the basic properties of III-nitrides and the main motivations of the PhD project focused on the use of nanowires for flexible LED devices. In this chapter, the selective area growth (SAG) by MOVPE and characterization of GaN nanowire-based LEDs will be presented, with the aim to provide necessary knowledges to understand the work performed in this PhD.

1. GROWTH BY MOCVD

The principle of growth by MOCVD has been quickly presented in the last chapter, with the aim of exhibiting the main advantages and drawbacks of this method. In the next paragraphs, we will provide the mechanism behind growth by MOCVD in more details, including reactor geometry, nature of used precursors, as well as growth conditions specific to catalyst-free nanowire growth.

1.1 REACTOR GEOMETRY

The nature of MOCVD growth relies on the reaction of gaseous species that are subsequent adsorbed on the substrate. As such, a well-designed reactor aims to have control over both the precursor transport and the thermodynamic parameters to ease epitaxial deposition. Hence, the geometry of the reactor is driven by two main properties: the flow of incoming gas and the temperature gradients within the reactor. Stemming from that, several reactor geometries may be used.

One of the earliest designs is the horizontal reactor[1]. In this geometry, precursors are injected into a horizontal chamber, and flow toward the sample (Fig. II-1 (a)). The main advantage of this design is its simplicity, as it may be built as homemade setup, which is also why this design is also common in other CVD techniques, such as HVPE[2] or graphene CVD[3]. Thought the use of this reactor has been critical in both development and understanding of MOCVD and related materials, this geometry presents some significant drawbacks. For example, because of the flux direction, the properties of the gas flow may be different between the entrance and the exit of the reactor. This can be caused by depletion of the reactants[1], which is the difference of partial pressure of reactants between the front and the back caused by the reactions on the sample. The boundary layer effects[4], defined as the non-uniformity in the laminar flow caused by the proximity of a solid surface, can also be responsible for perturbation of the gas flow. Both these effects cause inhomogeneities in the growth rate and chemical composition of the sample. These inhomogeneities can be fixed by tilting the sample toward the flux[4,5], or by rotating it. The sample rotation is the more effective method to limit inhomogeneities but introduces some challenges to integrate in home-built systems[1,4].

The second common geometry reactor is the vertical reactor[1,4] (Fig. II-1 b), which has become more common in recent years. This harder to build geometry introduces more technical challenges, especially at large scale. One of such challenges is the rotation of the substrate, which is almost systematic on this kind of reactor. Indeed, the rotation symmetry means that the inhomogeneities on the sample only depends on the distance to the center of the susceptor (Fig. II-2 (d)). This rotation has also been reported to create a pulling on the incoming flow[1], by decreasing the pressure around the susceptor through venturi effects, insuring further homogeneity of the properties on the sample. However, the vertical geometry also helps significant convective effects to arise[1,6,7], which have also been reported for the horizontal geometry to some extent.

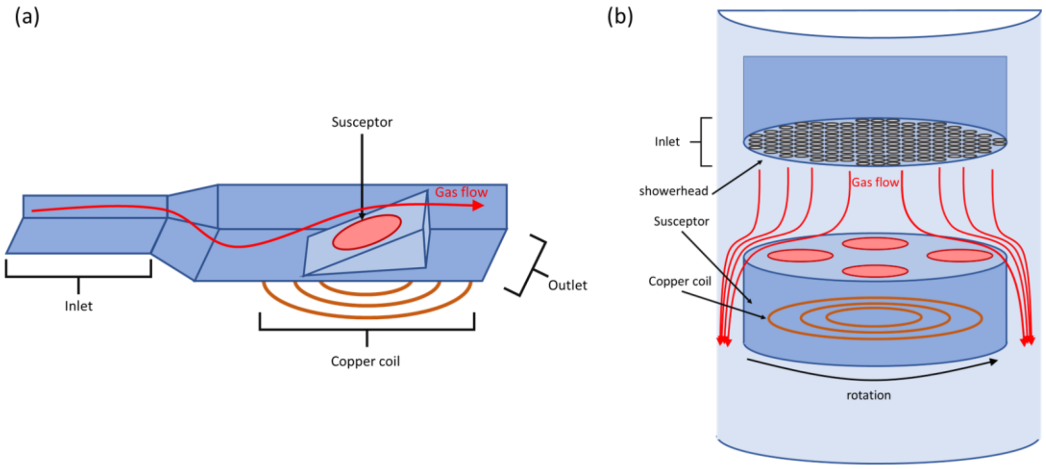

Figure II-1: *Examples of horizontal (a) and vertical (b) reactor geometry.*

Other changes made to the reactor can have significant effects on the flux of precursors and consequently on the quality of the deposited material. For instance, the wall of the reactor might be heated (hot wall reactor), or not (cold wall reactor). This is because by design, the gas flow in a reactor is expected to be laminar, meaning that the path taken by each gaseous species in specific locations do not change over time, and do not mix. In cold wall reactors, a gradient of temperature appears between the susceptor and the chamber, which is responsible for convection movements, or even turbulent flows (in which contrarily to laminar flow, the paths taken by each gaseous species can mix, and are expected to change overtime) in some cases[8]. However, using a cold wall reactor ensures that the gases do not start to react before they get close to the sample. On the other hand, a hot wall reactor ensures a better homogeneity[9], but the reaction between precursors starts as soon as the gases reach the reactor. Other recent improvement made to MOCVD reactors is the use of planetary susceptors[10] and showerheads[11], which both increase the homogeneity. In the first case, not only is the susceptor rotating on itself, each individual pocket for a wafer also rotates on itself, reducing even further the effect of inhomogeneities in the chamber. In showerhead reactors (Fig. II-2 (a) and (c)), the gases are introduced through an array of small holes allowing for efficient mixing of the gases, which limits composition variations in the chamber.

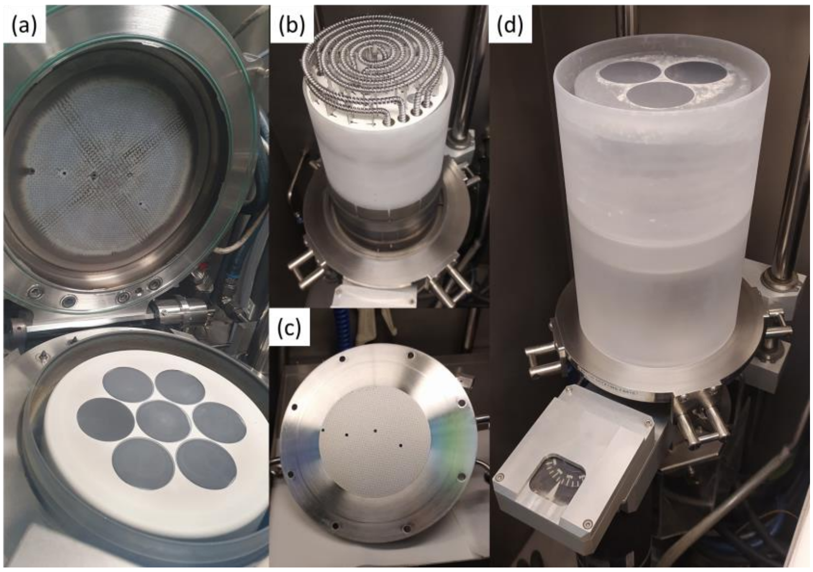

Figure II-2: *Two of the vertical MOVPE reactors used in this work based on showerhead technology: (a) Aixtron 7x2" reactor and (b-d) Thomas Swann 3x2" during a maintenance showing in more details several components, (b) the heating element, (c) the showerhead and (d) the susceptor and the liner.*

In this work, growths have been made on three different vertical showerhead reactors built by the manufacturers Aixtron and Thomas Swann, namely the models Aixtron 7x2" (Fig. II-2(a)) reactor and a Thomas Swann 3x2" (Fig. II-2(b-d)) for nanowires, and a Aixtron close coupled showerhead 3x2" for growth on graphene. These reactors are very similar in their geometry, but it should be noted that MOCVD is a parameter sensitive process, which means that criteria such as origin of reactants and substrates, history of material grown in previous growths[12], susceptor and maintenance of the reactors may also impact the quality of growth in some way. In the next paragraph, the different precursors used in MOCVD will be presented, and a small discussion on their various effects on the growth will be provided.

1.2 GENERAL PROCESS

Metalorganic chemical vapor deposition works similarly to other CVD processes, as described in Fig. II-3. The growth proceeds as follow:

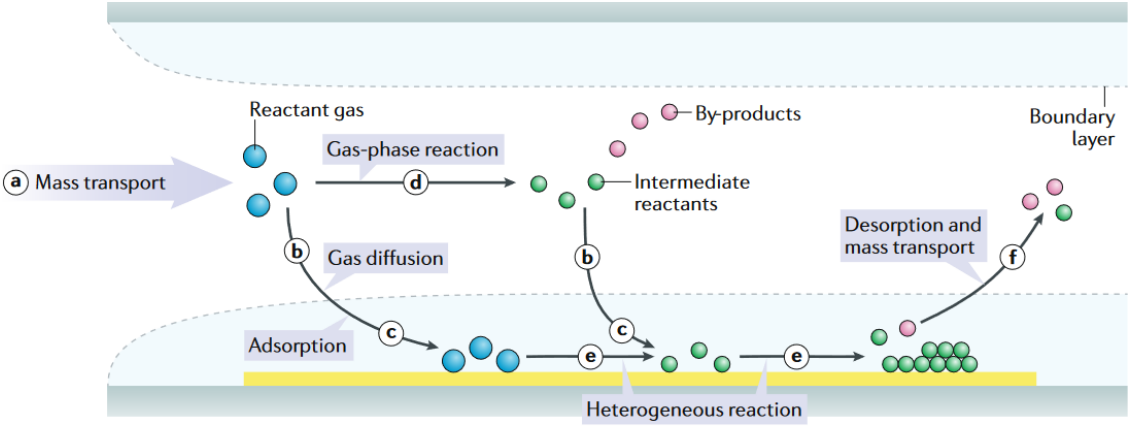

Figure II-3: *step-by-step representation of the process of epitaxy by a CVD process. The surface in yellow represents the substrate, and the surfaces in grey are the walls of the reactor. (from ref [13])*

A flow of reactive gases is first introduced in the reactor, where the substrate of growth lies (a). These gases will either diffuse through the boundary layer (b) and adsorb to the surface of substrate (c), or they will first react in the gas phase to produce reaction intermediates and byproducts (d). For any given CVD process, there is a large variety of possible reaction path and intermediates and is usually of secondary importance when it comes to actual growth. Some of these intermediates will also diffuse through the boundary layer (b) and adsorb onto the substrate (c). Here, the species will diffuse onto the surface until they either further react with atoms in the solid phase (e) or desorb of the substrate and out of the boundary layer. The remaining gas phase, which consists of unreacted precursors, desorbed intermediated or reaction by products is transported out of the chamber. There are hence three limiting factors for CVD growth: kinetics, transports, and desorption. These mechanisms are controlled by temperature and will each limit the growth at different temperature ranges (Fig. II-4). First, at low temperatures, the precursors do not have enough energy to overcome energy activation. Hence, the reaction rates (both in the gas and adsorbed phase) are low, and a small proportion of the precursor will react and participate in the growth, with is therefore kinetics limited. When increasing further the temperature, species will react efficiently, but the growth needs to proceed on available dangling bonds on the growth substrate. An adatom has to diffuse on the surface to get to an appropriate point for deposition. At this stage, further increasing the temperature results in an increase in growth rate, as it promotes transport of the species, and increases the probability of the species to find dangling bonds to form a covalent bond. Further increase in the temperature will start limiting the growth rate at some points. Indeed, when the adatom get enough energy, they will have a significant probability of desorbing before bonding covalently with the surface, meaning that they don't participate in the growth. It can be concluded that the optimal regime for growth is the between transport limited and desorption limited growth, as this is the point that combines a high reaction rate, high diffusion length and low desorption rate.

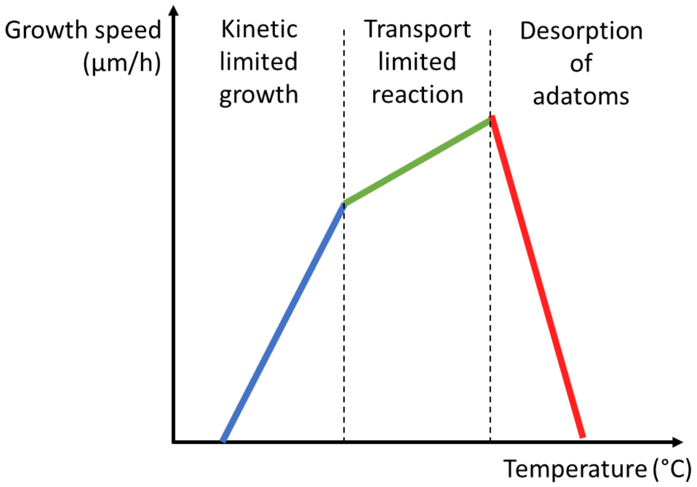

Figure II-4: *Summarize of the evolution of the growth speed with temperature exhibiting the different growth regimes (adapted from ref* [14]*)*

1.3 PRECURSORS

1.3.1 METALORGANIC COMPOUNDS

Metalorganic compounds are the main particularity of MOCVD. It stems from the fact that most metals evaporate at very high temperatures, and using an organometallic compound helps working in vapor phase at lower temperature between 500 to 1200°C, which are achievable with a MOCVD reactor. The main compounds used are either trimethyls or triethyls, bounded with Ga, In or Al. For example, in the case of Gallium, the compounds are trimethylgallium (TMGa) and triethylgallium (TEGa) (Fig. II-5 (a) and (b)). These compounds are very reactive, and are a known source of hazard, due to pyrophoric effect (they will spontaneously combust when exposed to air), and water reaction by acidifying it, meaning that they can cause severe burns and irritation if they encounter any living tissue. Hence, MOCVD reactors are placed in a glovebox with inert nitrogen atmosphere, both for safety reasons for the user and to avoid side reactions with oxygen to occur during growth, which could lead to the residual incorporation of extrinsic defects or dopants in the material. However, because organometallics naturally contain carbon atoms, the use of MOCVD implies that some small quantity of unwanted carbon will always be found in the grown structures.

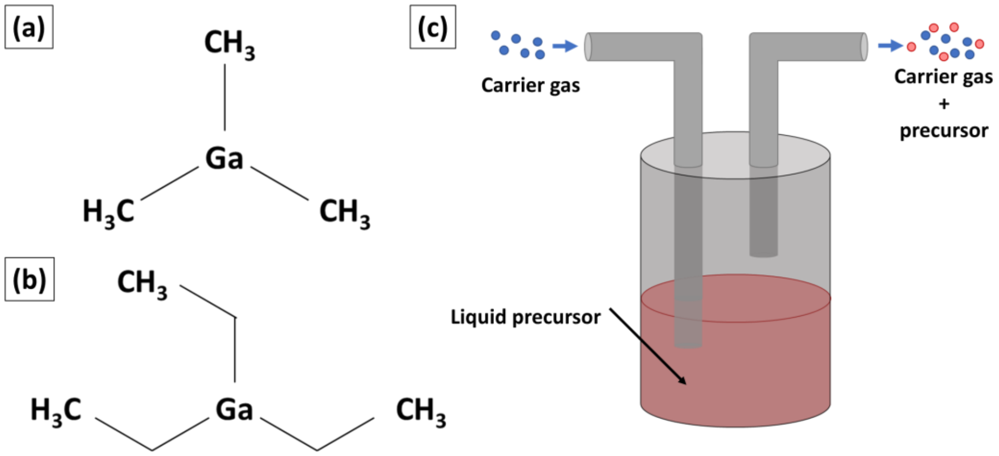

Figure II-5: *Molecule of TMGa (a), TEGa (b) and bubbler setup for metalorganic vaporization (c)*

At room conditions, metalorganic compounds are a liquid with a boiling point above 60°C for TMGa, and even higher for TMIn and TMAl. In MOCVD, there are used as vapors, and are hence kept as liquid in closed metallic containers called bubblers (Fig. II-5 (c)). During growth, a carrier gas, usually H_2, N_2 or a mix of both, is injected into the bubbler, which will have the effect of carrying metalorganic vapors to the reactor. The organometallic vapors are regenerated constantly in the bubbler to maintain their vapor pressure. The pressure inside the bubbler can be controlled through the injection of carrier gases, and the temperature is controlled through a bath maintained at a given temperature. With these parameters, it is then possible to control the vapor pressure of the metalorganic compound, and hence to directly know the actual flux of these compounds in the carrier gases, given in equation 2.1 and 2.2[14].

$$\varphi_{\mathrm{MO}} = \varphi_{\mathrm{carriers}} \cdot \frac{\mathrm{P}_{\mathrm{MO}}}{\mathrm{P}_{\mathrm{tot}}} \quad \mathbf{(2.1)}$$

$$\mathrm{P}_{\mathrm{MO}} = 10^{\mathrm{a}-\frac{\mathrm{b}}{\mathrm{T}}} \cdot \frac{1013.15}{760} \quad \mathbf{(2.2)}$$

with φ_{MO} and $\varphi_{carriers}$ the metalorganic and carrier gas fluxes respectively (mol.min^{-1}), P_{tot} the pressure inside the reactor (mbar), P_{OM} the vapor pressure of the metalorganic compound (mbar), T the temperature of the bubbler (K), and last a and b constants with typical values for TMGa of a=8.07 and b=1703K[14].

1.3.2 AMMONIA

The second important precursor for the fabrication of III-Nitride semiconductor structures is ammonia as Nitrogen source. Indeed, N_2 cracking is only possible at very high temperature non-achievable with an MOCVD setup. Moreover, ammonia is already in gas phase at room conditions and can be hence readily injected into the reactor. On a safety point of view, it should be noted that Ammonia is a toxic gas even at low concentrations and is hence one of the reasons why MOCVD rooms are under negative pressure and equipped with gas detectors. The flow of NH_3 in the reactor is usually given in standard cubic centimeter per minute (sccm) but can be converted to a mol.min^{-1} flow by assuming it behaves as an ideal gas and has hence a molar volume of 22.4 l.mol^{-1}. It should be noted that law can be applied to other gases that may behave as ideal gases, such as carrier gases for example. CH_3

$$\varphi_{mol/min} = \varphi_{sccm} \cdot \frac{1}{22400} \quad \mathbf{(2.3)}$$

1.3.3 DOPANTS

Because this PhD features the growth of an electrically injected device, being able to dope the material is of great importance. For n-doping, it has been previously mentioned that the most common dopant is silicon, but some studies also successfully report the use of germanium[15]. In both cases, the precursor used is the hydride compound, namely either silane (SiH_4) or germane (GeH_4), which are injected in the reactor as diluted gases. While the germanium doping has been reported as interesting in the case of planar growth, the use of silane is critical for the growth of high aspect ratio nanowires thanks for its ability to react with ammonia to form silicon nitride (SiN_x), as it will be explained in more details later. Hence, silane (Fig. II-6 (a)) has been the only n-dopant used in the growth realized during this PhD.

The p-doping of GaN is a challenging process. Indeed, most candidates for p-doping usually end up being compensated in GaN. Usually, magnesium doping is considered as the only option introducing enough carriers, but some reports show that zinc[16] and iron[17] can also induce a p-doped behavior in GaN. In all these cases, the molecules used are metalorganic compounds. In the case of both Mg and Fe, the precursor are ferrocene and magnesocene (Fig. II-6 (b)), presented as Cp_2Mg and Cp_2Fe (Bis-Cyclopentadienyl magnesium or iron respectively). The Zn precursor is either dimethylzinc or diethylzinc. Except for ferrocene, which is stable, these compounds share the pyrophoric and corrosive properties of TMGa and TEGa. Another common point is that they are also introduced in the reactor as vapors through bubbling, rather than as gases directly. In this PhD, we used only Mg doping, which is the most common p-dopant in GaN fabrication.

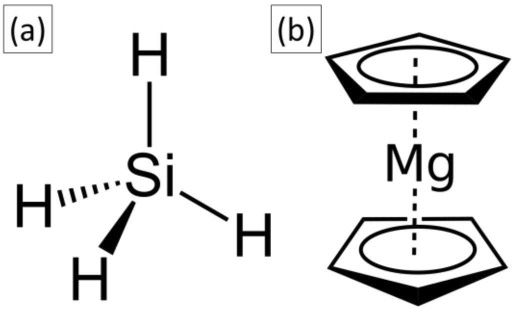

Figure II-6: *Formula of* SiH_4 *(a) and* Cp_2Mg *(b)*

1.4 UNCATALYZED SELECTIVE AREA GROWTH OF NANOWIRES

In this part, a discussion about the general approach to nanowire growth and the impact of growth parameters will be provided. this discussion mainly focuses on obtaining a nanowire structure, while the growth conditions for the shell will be provided in a latter paragraph.

1.4.1 DIFFUSION DRIVEN GROWTH

When doing nanowire growth, the main goal is to reach structures with high aspect ratio, meaning that the growth needs to be anisotropic to favor vertical growth and limit horizontal growth. Hence, the adatoms that participate in nanowire growth are mainly incorporated through the top polar or semi-polar facets. The origin of these adatoms is important, as it allows to understand the main driving factors behind the process. Wang *et al.*[18] studied these contributions, and built the model presented in Fig. II-7.

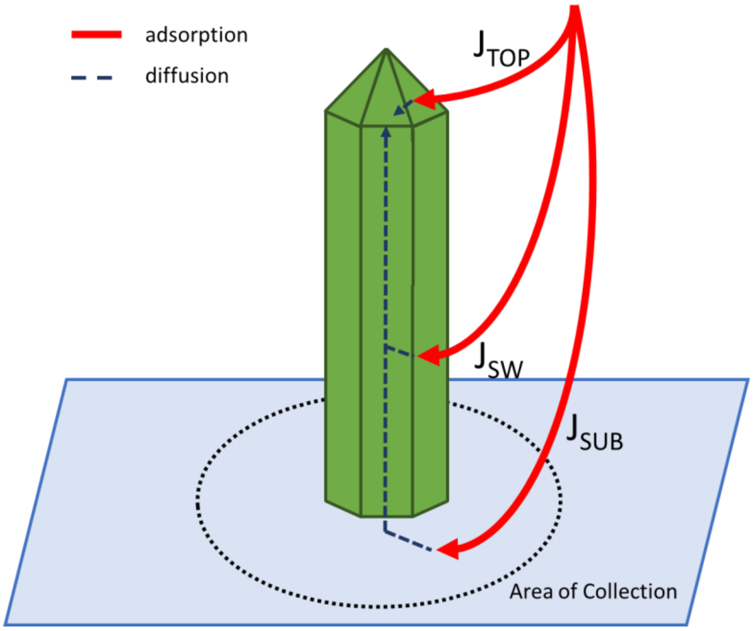

Figure II-7: *Contributions to nanowire growth as described by Wang et al.*[18]

In this work, three contributions are identified as sources of adatoms for incorporation into the crystalline lattice:

-J_{TOP} is the flow of adatoms adsorbed on the top surface. These adatoms do not need to diffuse to participate to the growth. In the case of this work, this contribution will usually be ignored, as the area of the top facets is usually small compared to the sidewalls of the nanowire, or the area of collection on the mask. Also, this contribution is usually almost invariant, as the area of the top facets evolves slowly compared to sidewalls.

-J_{SW} is the flow of adatoms collected on the sidewalls of the nanowire. This contribution requires the adatoms to diffuse toward the top of the structure and is hence diffusion limited. In early stages of the growth, this contribution is expected to be negligible, as the structure features almost no sidewalls. The flow rate of atoms incorporated through J_{SW} then increases with the size, until the length l of the nanowire reaches the diffusion length on the sidewalls, λ_{SW}. At this stage, J_{SW} saturates to a given value, and stays constant up to the end of the growth.

-J_{SUB} is the flow of adatoms coming from the mask around the nanowire. This contribution is important in initial stages, as the small surface of the nuclei means that most of the adatoms used for growth adsorbed on the mask. Hence, at the very beginning of the growth, the area of collection for J_{SUH} is a circle around the nuclei with a radius equal to the diffusion length on the mask λ_{mask}. However, as the nanowire grows, the species also must diffuse on the sidewalls of the nanowire. This limits the effective area of collection, as more diffusion on the sidewalls means less available diffusion on the mask, and the adatoms that the adatom that are incorporated to the top are collected closer from the nanowire as the growth proceeds. Hence, J_{SUB} decreases as the nanowire grows, until the length of the nanowire is equal to the diffusion length of the species on the sidewall. At this point, the area of collection becomes null, and J_{SUB} cease to contribute to the growth, as the adatoms collected on the mask cannot reach the top of the nanowire.

The study of J_{SUB} matters in the case of selective area growth, as it will impact the kinetics of the growth in early stage. Indeed, if the openings in the mask are not spaced enough, the areas of collection of neighboring nanowires might overlap, meaning that in early stages, the structures will compete for adatom collection. This might result in slower growth, as ref[18] shows a decrease in growth rate for nanowire with less pitch after growth is initiated. In extreme cases, this competition between nuclei could lead to empty openings, as the competition in the nucleus stage could lead some of the available openings to never develop nuclei of critical size to initiate growth. Because of all these reasons, it is easy to identify diffusion as a driving force responsible for nanowire growth, and hence most growth parameters needs to be adjusted to optimize diffusion. The next paragraphs aim to present how this is done using simple parameters, such as the gas mixes, the pressure or the temperature.

1.4.2 GROWTH CONDITIONS

1.4.2.1 IMPACT OF GAS RATIOS

The Ammonia flux is a first important parameter for the stability of the GaN material Indeed, c-plane GaN is notorious for having a thermal stability depending on the NH_3 partial pressure, with some reports showing that GaN starts thermally decomposing at temperature as low as 800°C in the vacuum environment of molecular beam reactor[19] because of Nitrogen evaporation. NH_3 only starts to efficiently dissociate around 700°C in MOCVD conditions[20,21], so during the heating step large amounts of NH_3 are injected (typically with a V/III ratio in the range of 1500-3000) to stabilize GaN by preventing nitrogen outgassing, enhancing its thermal stability up to more than 1000°C[22]. On the other hand, a high partial pressure of NH_3 without metalorganics to react with, results in a roughening of GaN[23], partly because of the generation of hydrogen through cracking.

During the nitride growth, the flow ratio between III-metalorganic precursors and ammonia, called the V/III ratio will have a direct impact on the growth of preferential crystallographic planes: For nanowire growth, the V/III is kept at very low values, usually of the order of 10 to 100. Indeed, it has been reported that high partial pressures of NH_3 promotes lateral growth through favorable incorporation of species on m-planes, which is favorable to a planar mode of growth[24,25]. Nanowire growth is achieved through high c-plane growth speed, and stable m-plane ensuring a limited lateral growth, which justifies the use of low NH_3 introduction. Another reason for limiting the NH_3 is that it releases H_2 upon incorporation of the N atom in the structure[26], which stabilizes the Ga-polar semi-polar planes.

Because of that, the ratio H_2/N_2 has been shown also to have an impact on the aspect ratio[27]. As mentioned previously, the hydrogen flux also has a significant effect on the structures, and it is usually compared to the N_2 flux. Indeed, both gases are used as carrier gases, but one is reactive, while this other one is inert. P.M. Coulon[14,28] reported that a high H_2/N_2 ratio reduces the lateral growth rate and improve the inhomogeneity of NW dimensions. Indeed, at a H_2/N_2 equal to 1 or more[27], horizontal is dramatically reduced. Hence, the best strategy to grow nanowires is to keep a H_2/N_2 ratio above 1 to avoid lateral growth.

1.4.2.2 IMPACT OF REACTOR PRESSURE

Pressure is one of the main non-chemical parameters in any MOCVD and may have dramatic impacts on the behavior of the reactants, as it influences most thermochemical processes. However, to stay true to the gas mix, any pressure-dependent study should be done while keeping stable gas mixes (V/III, V/dopants, H_2/N_2, precursors/carriers, etc…). In an MOCVD reactor, the pressure is modified through the flow rate of the gases inside the reactor (and not by adding more of one specific specie), meaning that modifying the pressure is not expected to modify the composition of the gas mix. In Ref[14] , the authors varied the reactor pressure from 100 mbars to 500 mbars while keeping the precursors flow constant and observed an etching of the GaN template at high pressures. The authors concluded that this etching could be due to limited diffusion induced by the high pressure. Other authors published studies about morphology changes in GaN grown by MOCVD when modifying the pressure[29,30]. It was found that planar GaN structure (either c or m-plane) were both prone to faceting when grown at high pressures, which could indeed be caused by a limited diffusion length. Indeed, at high pressures, the adatoms can diffuse toward the most thermodynamically favorable crystalline plane (here, either r-plane or a-plane), leading to their disappearance through outgrowing. On the other hand, ref [29] notes that the structures grown at low temperature had a poor morphology and exhibited roughening. This could be caused by outgassing related to low NH_3 partial pressures, as the partial pressure of a gas is not only related to the relative concentration, but also to the total pressures. Because of this, a balance needs to be found with pressure to promote adatom diffusion while avoiding outgassing caused by low partial pressures.

1.4.2.3 IMPACT OF TEMPERATURE

Temperature is the last of the critical parameters in MOCVD growth of nanowires and is often used to finely optimize the morphology of the nanostructures. This is because temperatures help having direct control over the length of diffusion of adatoms. Other effect of temperature includes modifying the efficiency of thermal cracking of the precursors as well as other reactions in gas phase, and modification of the thermodynamical equilibrium of the different facets (leading to the apparition and disappearance of different morphologies). But the main influence of the temperature is going to be seen in the competition between diffusion and desorption. Indeed, while increasing the temperature increases diffusion length (that is necessary in the growth of high aspect ratio structures [14,28]), it also promotes decomposition of the structure.

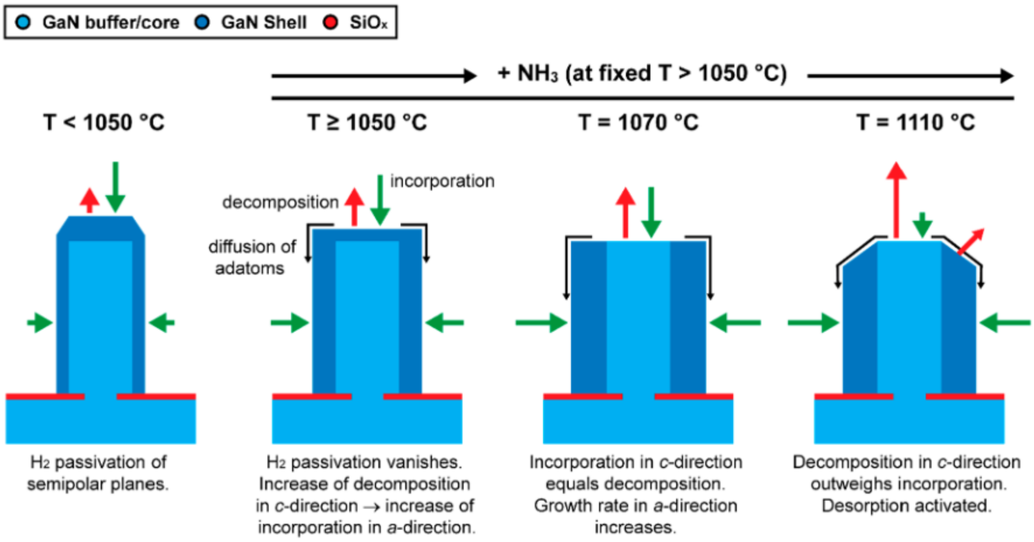

Figure II-8: *Behavior of the growth under different temperatures (from [24])*

For instance, the observed dependance of nanowire morphology from the ref. [24] is as follows shown in Fig. II-8: at low temperature, the diffusion length of the nanowire is reduced, and hence, the maximum height reachable by the nanowire is limited. Because of this reduced diffusion length, the adatoms will also preferentially deposit on lateral sides rather than at the top, meaning that the obtained structures are expected to have low aspect ratios. Further increasing the temperature will induce outgassing from the different facets, starting with the top facet[24], which will compete with the growth, and hence reduce the growth rate[14,28]. At high enough temperatures, sidewall outgassing will also start becoming significant. However, because the growth is optimized to have the lowest possible horizontal growth rate, the decomposition will not be covered by new deposited material, and it will leave ridges and roughness that will still be visible after growth[14,28]. Last, if the temperature gets too hot (>1200°C), a degradation of the pattern is observed[14,28]. In our setup, we found that the best range for growing nanowires is around a setpoint of 1150°C. These temperatures might vary depending on the substrate, the reactor, and the overall growth conditions, but usually occur in a narrower ~20°C window of temperatures in a particular setup.

Growth parameter	Value
Setpoint Temperature	1175°C
V/III	15
H_2/N_2	3
Pressure	100 Torr
SiH_4	>100 nmol.min^{-1}

Table II-1: *Values of critical growth parameters used in this work for GaN core nanowire growth.*

Table II-1 shows a summary of the values used in this PhD for the growth parameters discussed in the previous paragraph. Additionally, nanowire samples presented in this document have been grown on a masked GaN template on Sapphire. The mask geometry and parameters have already been described in part 3.1.1 of Chapter 1. One parameter that has not been introduced is the SiH_4 introduction, which is necessary in order to achieve lengths. However, because this parameter as been the object of advanced studies as a part of this work, it will be discussed in more details in the Chapter 3.

2. CHARACTERIZATION TOOLS FOR GAN

In the scope of this work, several methods of characterization have been used to assess the properties of the samples. In this part of the manuscript, these different methods will be presented.

2.1 LUMINESCENCE

The most accurate way to assess LED performances s would be to grow a full LED structure along with metallic contacts to directly inject current to measure its overall light emission, which is a characterization method called electroluminescence. However, as well as being time-consuming, this method does not probe only the optically active layer of the device, but also the metal contacts that may have their own issues. Fortunately, there are other methods used for the characterization of optically active samples that allow to measure the emission in a material. These two methods, commonly known as cathodoluminescence and photoluminescence, are complementary on some points, and will be presented in the next paragraph.

2.1.1 PHOTOLUMINESCENCE

In photoluminescence (PL), the source of excitation for carrier generation is photons (Fig. II-9) whose energy is greater than the energy of transition in the material. The photon source is usually a laser beam, as it allows to work with coherent and collimated light. In the case of this PhD, the two lasers used were a continuous doubled Ar beam ($\lambda = 244$ nm) and a pulsed YAG ($\lambda = 266$ nm), meaning that in both cases, the energy used was above 4 eV, which is well above the one necessary to induce transition in a GaN or InGaN material. It should be noted that the wavelength used is not a critical parameter as long as its corresponding energy is higher than the recombination that needs to be characterized.

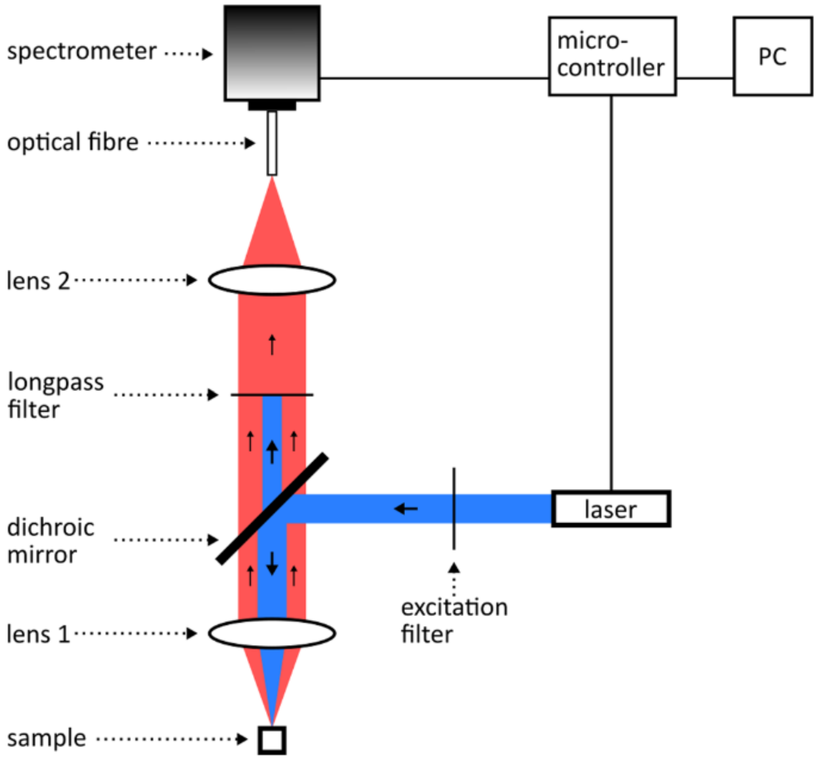

Figure II-9: *Simplified scheme of a confocal PL setup (from [31])*

After excitation, the pathway taken by the carrier toward relaxation will be mainly influenced by the lifetime of each process, which is defined as the average time it takes for a carrier to undergo a specific transition. Indeed, if two pathways are considered, the one with a short lifetime will tend to outcompete the other one. For example, even a small concentration of non-radiative recombination centers in a material can become an issue if the associated lifetime is significantly shorter than the radiative ones.

The first process to occur to the carriers is thermalization. Indeed, because the carriers are excited above the gap energy, they end up carrying excess energy in the form of kinetic energy, which can be seen as excess temperature, which is why these carriers are sometimes referred to as “hot carriers”. These hot carriers are expected to thermalize (Fig. II-10), which means that they will lose their energy and reach the lowest energy in the conduction band through phonon generation, scattering between hot carrier, and interactions with electrons in the lattice. Thermalization has an expected associated lifetime of $5 \cdot 10^{-1}\text{ps}$[32] in InGaN, which is orders of magnitude faster than most pathways for recombination and can hence be considered instantaneous in this context.

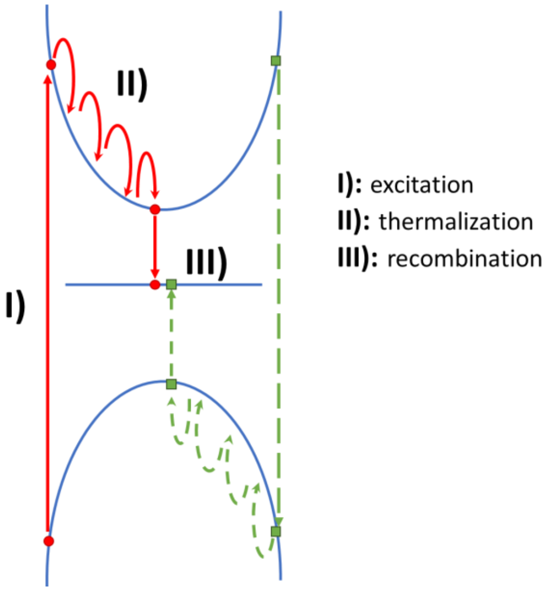

Figure II-10: *Pathway taken by carriers for a defect assisted non-radiative recombination in GaN*

For both radiative and non-radiative recombinations, the lifetime is expected to vary with temperature, which can be used to calculate the Internal quantum efficiency (IQE), that can be defined as the ratio between the number of photons emitted from the active region to the number of injected carriers per second (2.4). Assuming that the intensity of a PL signal is proportional to the number of injected carriers and the radiative recombination constant (2.5), and that the number of injected e-hole pairs is constant with temperature and will recombine either radiatively or not (2.6), we can write that the IQE is determined by the ratio of the radiative recombination rate to the recombination rate due to all processes:

$$\eta_{\mathrm{IQE}} = \frac{\frac{1}{\tau_R(T)}}{\frac{1}{\tau_R(T)} + \frac{1}{\tau_{NR}(T)}} = \frac{\mathrm{k_R(T)}}{\mathrm{k_R(T) + k_{NR}(T)}} = \frac{\mathrm{k_R(T)}}{\mathrm{k}} \quad \mathbf{(2.4)}$$

$$\mathrm{I_{PL}(T) \propto k_R(T) \cdot n} \quad \mathbf{(2.5)}$$

$$\mathrm{k_R(T) + k_{NR}(T) = k} \quad \mathbf{(2.6)}$$

with $\mathrm{I_{PL}}$ the PL intensity, n the number of electron/hole pairs injected, T the temperature, k_R the radiative recombination rate, k_{NR} the non-radiative recombination rate that are defined as $k = \frac{1}{\tau}$ for each contribution, k a constant representing the total number of carrier recombining in a given time, and n the factor between the number of radiative recombinations and the overall PL intensity.

At temperatures close to 0 K, the radiative lifetime of a non-polar InGaN quantum well is expected[33] to be of the order of $1 \cdot 10^{-9}\mathrm{s}$, while the non-radiative lifetime is expected to be several orders of magnitude higher. Hence, it is usually assumed that recombinations at low temperatures happen only through radiative recombinations, which allows to make the following approximation:

$$\mathrm{k_R(0K) \gg k_{NR}(0K) \Longrightarrow k = k_R(0K) + k_{NR}(0K) \approx k_R(0K)} \quad \mathbf{(2.7)}$$

At higher temperatures, non-radiative lifetime decreases strongly, and reaches lifetimes of the order of the ns at room temperature, while the radiative lifetime increases. This means that at higher temperature, non-radiative pathways become preferential for the carriers.

$$\eta_{IQE}(300K) = \frac{k_R(300K)}{k} \approx \frac{k_R(300K)}{k_R(4K)} = \frac{I_{PL}(300K)}{I_{PL}(4K)} \quad \mathbf{(2.8)}$$

Hence, it can be concluded that the ratio of intensity at 4K and 300K allow to give a reasonable approximation of the IQE assuming no non-radiative recombination at low temperature, which is possible with InGaN materials due to the high localization.

The setup of PL itself consists in a laser beam. The beam is then focused on the sample. The difference between PL and µPL, is the spot size: the first one focuses the beam to a spot size of several hundreds of µm, while the second allows the beam to reach a spot size of the order of 1µm. The signal re-emitted by the sample can then be collected and focused on an optical fiber through a filter to remove the laser's signal, where it is sent on a Charge Coupled Device (CCD) sensor through a monochromator (Fig. II-11). The CCD counts the number of photons, while the monochromator separates the different wavelengths. To do this, the setup uses a first mirror to collimate the beam on a grating, which separates the different light wavelengths. These wavelengths are collected by a parabolic mirror, that will focus each wavelength into a point. By varying the angle of this second parabolic mirror, one can scan the wavelengths of the spectrum on through a slit feeding only one wavelength at a time on the CCD, and hence obtain a full spectrum. The width of the spectrum is hence controlled by the range of angles scanned by the parabolic mirrors, while spectral resolution depends on the density of the grating.

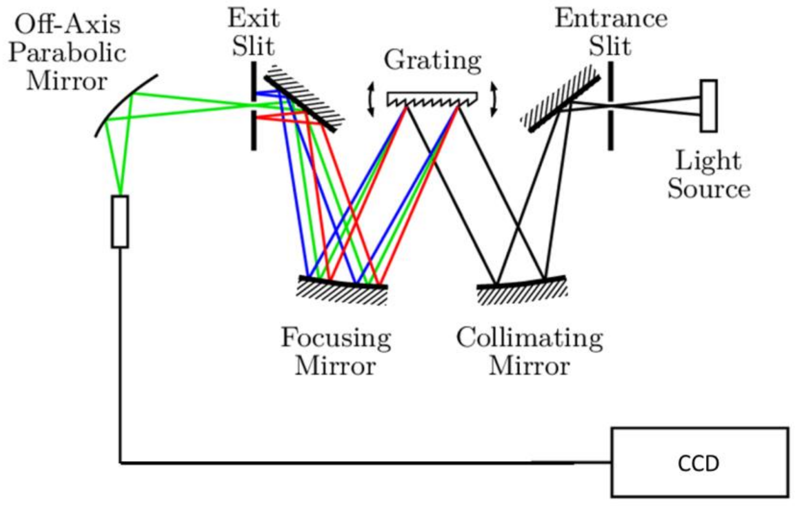

Figure II-11: *Scheme of a monochromator/CCD setup used to measure spectra in PL (adapted from ref[34])*

2.1.2 CATHODOLUMINESCENCE

Cathodoluminescence is in principle quite similar to photoluminescence, in the sense that the source of energy is also a narrow beam of high energy particles. However, in cathodoluminescence, the particle used for the excitation is an electron beam, instead of a photon one. This leads to important differences in how cathodoluminescence characterizes a sample. Indeed, the electron beam can be focused to a spot size of the order of the nanometer using a Scanning Electron Microscope. It is thus possible to make SEM imaging and luminescence spectra when using a CL setup. This allows the identification of features such as alloy composition variation, high densities of non-radiative centers, or even structural defects such as dislocations or stacking faults. The electron beam also has a higher penetration depth than a laser, which can be tuned directly using the energy of the beam, allowing to get the specific contribution of one layer. These properties of the CL make it a suited tool to precisely characterize nanostructures. One limitation appears when working with samples grown on an optically active template, such as the GaN templates used in this PhD. Indeed, the high penetration depth of the electron beam is going to lead to a substrate signal overshadowing the one of the heterostructure. Therefore, it requires some sample preparation, which, in this work, consisted in the transfer of the structure on an optically inert Si substrate using a razor blade. The overall preparation, sample loading and measurement are significantly longer than the ones in PL, and this method of characterization is hence more fitted for fine characterization of a sample rather than quick measurement for optimization purposes. Last, it should be noted that it is significantly more challenging to cool a sample in CL because it is in the chamber of a SEM, and hence, CL setups do not systematically include a system allowing to work at temperatures close to 0K.

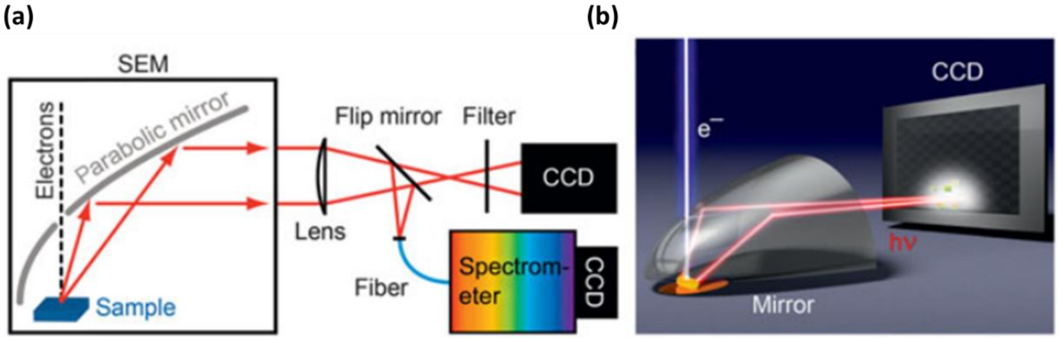

Figure II-12: *Scheme of a cathodoluminescence setup (a) and representation of the parabolic mirror used to focus the light output.*

To measure the cathodoluminescence of a sample, it is necessary to use a SEM equipped with a parabolic mirror, a spectrometer, and a CCD sensor (Fig. II-12). There are three main modes that can be used. The first, named the panchromatic mode, allows to measure the overall light intensity produced at each point of the surface, by measuring the light intensity through the CDD produced at each point during the scan of the beam. This is especially useful when trying to measure the presence of non-radiative structural defects, such as dislocations, that are hence expected to appear as dark spots on the mapping[35]. The second mode implies to use the beam as a PL laser, and measure single spectra on a specific area, by passing the light through a spectrometer before sending it to the CCD. This mode is useful in order to get the emitted spectrum in specific areas, with a precision order of magnitude greater than in PL. Last, it is possible to realize hyperspectral mapping of the sample, which consists in measuring the CL spectrum at each point of a scan. This functionality is by far the most useful, as it also allows to get the information provided by the panchromatic and single spectrum mode (by integrating the light intensity over the wavelength range, or by looking at a single spectrum on a specific point respectively). Because it essentially maps the spectrum of emission, it is a versatile and powerful tool to analyze the presence and properties of quantum wells, defects[36], or alloy fluctuation[37].

2.2 MICROSCOPY

Another critical part of the characterization tool for nanowires is microscopy. Under this term stems a variety of techniques used to assess the structural properties of the material, from the morphology of the nanowire itself to the structural defects contained in the material. In this paragraph, the methods used in this PhD to realize such assessments will be described.

2.2.1 SCANNING ELECTRON MICROSCOPY (SEM)

Scanning electron microscopy (SEM) is a key characterization tool when working with micro or nano structures, as it allows to generate images of the sample at magnification that cannot be resolved using optical microscopy (< 1µm). The microscope works by generating a beam of electrons in an anode, that are then accelerated by applying a high electric potential to a cathode. The beam is then aimed in a column under high vacuum, where an array of electromagnetic lenses will focus the beam to a spot, as well as straightening it and correcting for its astigmatism, as shown in in Fig. II-13. The sample is placed at the focal point of the beam, in a chamber under vacuum. Upon encountering the sample, the incident electron having an energy in the range of 1-20 keV will interact with the surface of the material, producing a variety of emission of particles, as described in Fig. II-14. The area where these interactions occur form a pear-like shape, which depts depends on the energy of the electrons. Different sensors in the chamber will then collect the intensity of emissions of each of these particles on a given point. By scanning a given area on the sample with the beam, it is then possible to map the intensities of these particles and build a corresponding image of the sample.

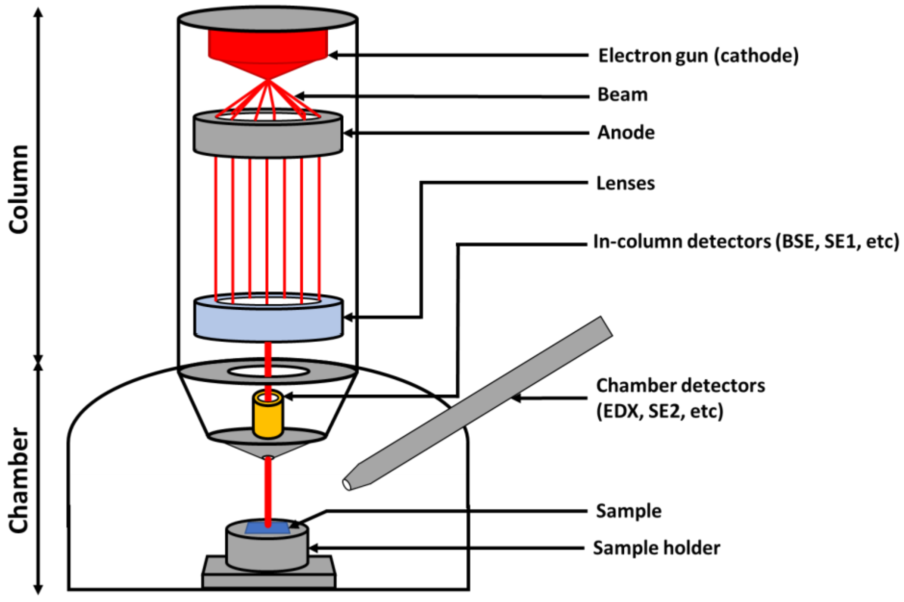

Figure II-13: *Scheme of a basic Scanning Electron Microscope*

It should be noted that the different particles emitted during exposition of the material to the beam may carry different information about the material itself. These particles stem from the different kinds of interaction of the primary beam with the sample, inside the interaction volume (Fig. II-14). The emitted particles include:

- Auger electrons (Fig. II-14(b)), which are produced when the beam ionizes one of the inner shell electrons. A higher shell electron will then relax to its level, releasing energy, which may ionize one of the outer shell electrons, called an Auger electron. By measuring the energies at which auger electrons are produced, one can deduce the atom responsible for their emission. Hence, Auger electron spectroscopy[38] allows to get information about the elements of the first few nanometers of the surface of the material.
- Secondary electrons (SE) (Fig. II-14(c)), which are electrons resulting from the ionization of the material under the beam. This process happens at high energy and is hence concentrated in the first 100nm of the material. They provide topographic information about the surface of the material. It should be noted that second order secondary electrons can be formed by the interaction of the material with other secondary electrons. Hence, secondaries are sometimes separates in first (SE1) and second (SE2) order, with SE1 being significantly more energetic and shallower than SE2[39].
- Backscattered electrons (Fig. II-14(d)), which are electrons of the primary beam that undergo scattering at depths of several hundreds of nm. Because of this, they are not affected by the topology as much as SE and are more sensitive to the atomic number of the atoms of the crystal and their crystalline information. Hence, they are used both to indirectly map the composition[40], and phases of the material, and their diffraction allows to measure the relative orientation of different crystallites[41].
- Continuous X-rays (Fig. II-14(e)), which are caused by the deceleration of electrons through the bremsstrahlung effect, produced in the first few μm of the sample. This effect is thoroughly used in synchrotron facilities to produce X-rays but does not have any significant use in scanning electron microscopy of semiconductors.
- Characteristic X-rays (Fig. II-14(f)), which are produced by excitations and de-excitation of inner shell electrons of the atoms in the material interacting with the beam (also called fluorescence). Their name stands from the fact that their energy directly depends on the atom responsible for the emission, and they hence allow to directly identify the atoms present in a sample, through Energy Dispersive X-ray spectroscopy[42]. Much like continuous X-rays, they are produced in the first few μm of the sample.
- CL radiation (Fig. II-14(g)), which has been described in more details in the last paragraph.

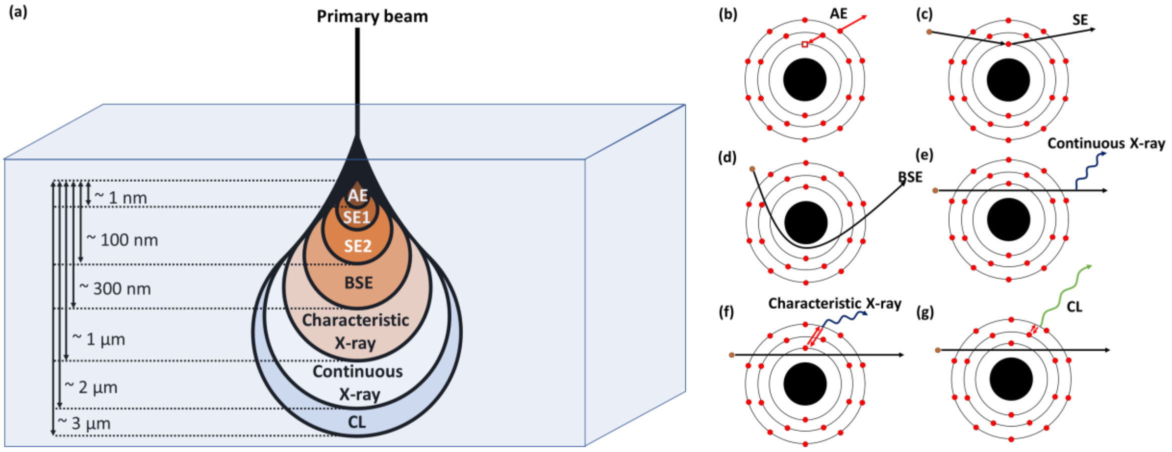

Figure II-14: *(a) Scheme of the interaction volume for each interaction process and (b-g) corresponding interactions*

Because of this variety of characterization technics available to the user, scanning electron microscopy is a versatile tool, allowing for a large variety of analysis of a sample with little to no preparation. However, this technique also has its limitations. Indeed, while its resolution is order of magnitude higher than what is reachable through optical microscopy, the typical size of the beam of the SEMs used in this work are between 2 and 5 nm. While this suggest a nanometric resolution of imaging, it should be noted that the final imaging resolution is also limited by the interaction volume, which depends on the material and parameters used for imaging. This effect is even more pronounced when working with signals with large associated volumes of interactions, such as CL and EDX. On the other hand, SE that typically have a smaller volume of interaction are mainly sensitive to topography, and not to chemical composition. Hence, while the SEM is an adapted tool for the assessment of surface morphology or rough estimation of composition, it does not allow to precisely characterize features such as quantum wells or heterostructures. Hence, for fine analysis, other method of characterization is necessary, and this is where transmission electron microscopy (TEM) starts being useful.

2.2.2 TRANSMISSION ELECTRON MICROSCOPY (TEM)

In Scanning electron microscopy, the collected signal stemmed from the interaction of the electron beam and the surface of the sample. In transmission microscopy, the beam is collected on the other side of the sample, and hence must go across it. Hence, the sample used must be thin enough (maximum a few hundred nm), and the energy provided to the electron beam is typically higher (>60 keV in the case of the TEM used here). In this paragraph, the technique used to prepare the samples for TEM characterization is going to be presented, and an overview of the techniques used in this work will be provided. This list is not exhaustive, since transmission electron microscopy is still evolving nowadays, with new methods of characterization being developed[43].

2.2.2.1 SAMPLE PREPARATION BY FOCCUSED ION BEAM

The typical thickness of a sample used for transmission microscopy is usually less than 100 nm. While this size can be reached using mechanical polishing for bulk sample, working with micro or nanostructures requires the use of specific techniques in order to get samples ready for transmission microscopy. The most used of these techniques is focused ion beam (FIB) milling. This method consists in using a beam of high energy heavy ions, usually Ar or Ga, to locally etch the sample with a precision of the order of 10 nm. This is usually done in a SEM microscope, which allows to observe the sample as it is getting milled. The usual process used for milling is described in Fig. II-15. The sample is first covered with an amorphous conductive layer, usually made of Pt or C, *in situ* deposited by a low energy beam. This step is critical, as the high energy ion beam used for the milling can be responsible for the introduction of extrinsic defects in the lattice. The sample is then exposed to a high energy ion beam, usually using Ga ions. At this step, the goal is to carve the slice that will be used in the TEM chamber. The slice can then be attached to a micro tip using amorphous Pt and transferred to a holder. At this point of the process, the slice has a length and width of the order of several µm. Once attached to the holder, the ion beam can then be used to mill the structure to the desired thickness.

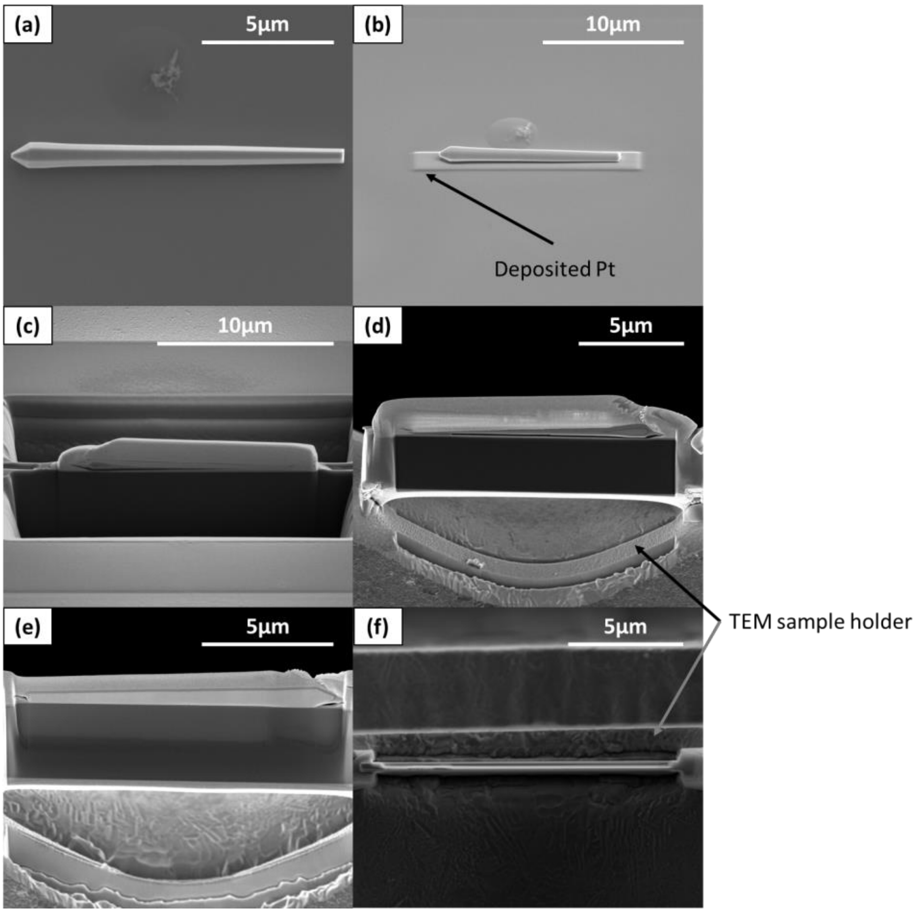

Figure II-15: *TEM sample preparation method using the FIB-SEM technique. (a)Nanowire transferred to a Si-substrate, (b) deposition of Pt protection mask on the sample surface, (c) ion-milling trenches around the sample, (d) sample after transfer to the TEM sample-holder, sample after thinning viewed (e) from the front and (f) from above.*

Thanks to this technique it is possible to manipulate and thin micro-objects. However, the use of this technique comes with a few disadvantages. First, as stated before, the use of a high energy ion beam can be responsible for the introduction of defects. In severe cases, the milling may optically kill the sample. A second issue is that this method is long and costly. Indeed, it takes half a day for an experimented user to produce a single lamella (which was further exacerbated by the fact that this machine was not readily available at the CRHEA), and the operating costs mean that the quantity of samples that can be produced using this method is limited. One last disadvantage is that in the case of the present structures, the dense array and the aspect ratios of the nanowires make it difficult to isolate single structures. Also, the height of the nanowire may require depositing important quantities of Pt to fully encapsulate one nanowire. Because of that, trying to encapsulate nanowires directly on the sample leads to large Pt/nanowires conglomerations, the Pt itself is porous, and both factors make it more challenging to thin the lamella in the proper direction, leading to artefacts during TEM measurement (Annex A). Hence, much like it is the case in CL, nanowires longer than 2μm were systematically transferred on a flat surface before undergoing the FIB process, to make the process easier for the user, and to yield high-quality lamellas. In the studies done in this PhD, two planes were used in order to do the cut and the thinning, which are represented in Fig. II-16. Cuts along the (0001) plane were used to characterize the structure on all the facets of the nanowire at a given height, which allow to compare properties such as the thickness of a layer on all the m-planes (Fig. II-16(b)). Second, $(11\bar{2}0)$ were made along the whole length of the nanowire, such as presented in Fig. II-15 and Fig. II-15 (c). These lamellas allow to image the m-planes quantum well along the whole length of the nanowire. These two kinds of lamellas were studied uniquely in the (0001) and $(11\bar{2}0)$ zone axis respectively and will be referred to as Longitudinal and Transversal lamellas in the next paragraphs for the sake of simplicity.

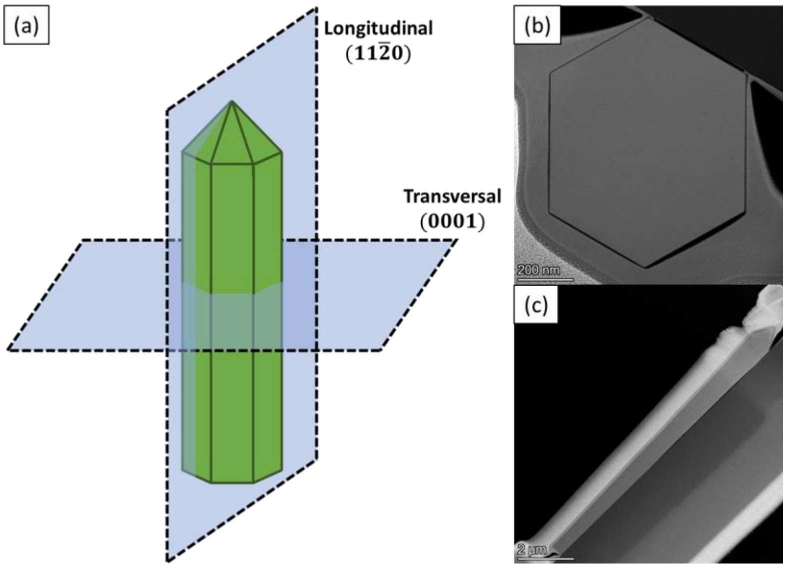

Figure II-16: *(a) schematic representation of a nanowire with the two planes of thinning used in this PhD, along with images of a (b) transversal and (c) longitudinal nanowire lamella.*

2.2.2.2 IMAGING

Once the sample has been prepared, it can be used for its characterization. The characterization of samples in transmission microscopy relies on the electron beam transmission, usually (but not systematically) through a specific crystalline direction, called the zone axis. The provided image is hence a projection of the lattice through this axis. The choice of the zone axis is something that will directly affect the way the sample is prepared, as working without a tilt on a specific zone axis allows for more precise measurements, especially in examples such as EDX measurements. Because the preparation of the sample can define the main 0 tilt zone axis used during observation, the main zone axis is usually chosen before starting the sample preparation.

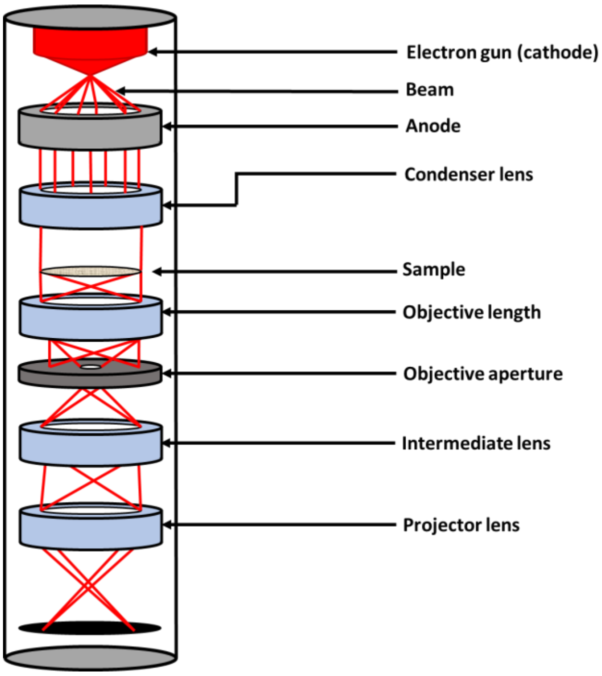

Figure II-17: *Scheme of a basic Transmission Electron Microscope.*

In TEM microscopy, the main interest is to collect the electrons passing through the sample to obtain various information about its microstructure. The main components of a TEM are presented in Fig. II-17. Before encountering the sample, the electron beam can be assimilated to a plane wave, described by a function of the form $\varphi = A \cdot e^{2i\pi\cdot(\boldsymbol{k}\cdot\boldsymbol{r})+\varphi_0}$, with A the amplitude, k the wavevector, r the vector of propagation and φ_0 the phase shift of the wave. Upon encountering a crystalline lattice, the beam will undergo scattering. There are three categories of scattering processes that can occur: coherent elastic scattering, incoherent quasi-elastic scattering and inelastic scattering. The energy lost during inelastic scattering is responsible for the emission of second order particles or quasi-particles, part of which can be measured (such as photon in the form of CL and EDX, or phonon generation in the material). Because of these different emissions, a large variety of TEM uses exist to better fit the need of different fields. Hence, a brief description of the methods used to characterize the sample in this PhD will be provided in this paragraph.

TEM, diffraction, bright field and dark field

The classical use of a TEM[44] is represented in Fig. II-18. As can be seen, the primary beam is parallel, which is done using the condenser lens (Fig. II-17). After encountering the sample, the beams are collected and concentrated by the objective lens. The beam then encounters the intermediate lens, which has a variable focal lens, allowing to switch between diffraction and imaging mode.

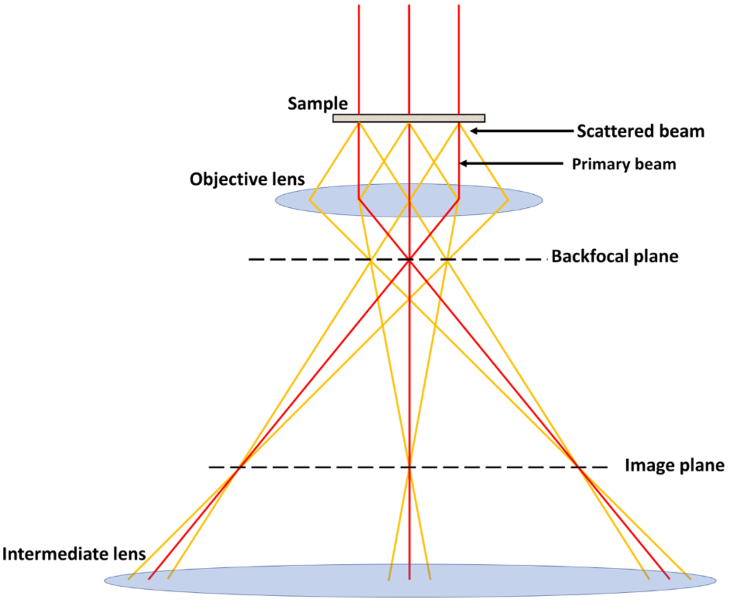

Figure II-18: *Pathway followed by the primary and scattered beam between the objective and intermediate lens in a TEM.*

In diffraction mode, the intermediate lens is adjusted to project the pattern built on the back-focal plane, which is a projection of the reciprocal lattice through Bragg scattering. Hence, each spot on the diffraction pattern corresponds to a specific crystallographic plane, with an associated vector $\boldsymbol{g}_{ihkl}$. Because of this property, it is commonly used to adjust the alignment of the sample with the beam. It can also be used to check the number of crystalline phases in the material. Fig. II-19 (a) shows the patterns obtained by electron diffraction in the case of a sample with a monocrystalline phase. However, this diffraction pattern is also critical to make images.

Indeed, if one were to put a small aperture on the back-focal plane, it would be possible to reconstruct a full image using only one specific contribution of the reciprocal lattice, as can be seen in Fig. II-19. This allows to switch between a bright field image built using the image projected by the transmitted direct beam, or with a scattered beam, leading to the projection of the dark field image. The dark field image is an image built with electrons that underwent scattering. The mainly used method to collect the dark field image is to use deflector lenses to tilt the incident beam to move on the optical axis of the TEM.

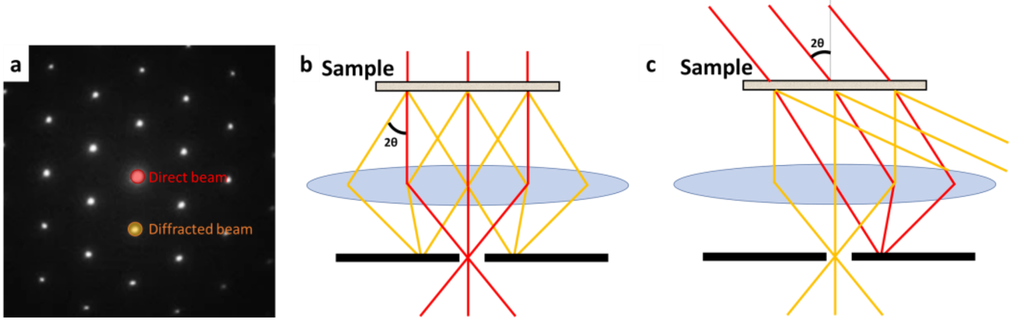

Figure II-19: *(a) Diffraction pattern of a WZ-GaN sample in the (0001) zone axis with diffraction points corresponding to the primary and diffracted beam. (b) bright field setup, (c) dark field setup obtained by tilting the primary beam.*

One of the other reasons to use a diffracted beam instead of the direct one is their sensitivity to some structural defects, such as dislocations and stacking faults. Indeed, in some specific conditions, the contrast associated to some defects can be cancelled, meaning they are invisible. The conditions that describe this phenomenon, called extinctions conditions, vary from one defect to another. For dislocations[14], a dislocation is invisible if its burger vector is perpendicular to $\mathrm{g_{ihkl}}$ such as $\mathbf{b} \cdot \mathbf{g_{ihkl}} = 0$ and if $\mathbf{g_{ihkl}} \cdot \mathbf{b} \times \mathbf{u} = 0$, with $\mathbf{u}$ being the unit vector in the propagation direction of the dislocation. It should also be noted that, in practice, it is observed that dislocation become invisible when $|\mathbf{b} \cdot \mathbf{u}| < \frac{1}{3}$. For stacking faults[14] the extinction rule relies on the displacement vector around the stacking fault, called $\mathbf{R}$. Hence, it can be shown that the stacking fault contrast is extinguished if $\mathbf{g} \cdot \mathbf{R} = \mathrm{n}$, with n being a whole number.

With this basic information about the operation of a transmission electron microscope, it is easy to see that it is a fitted tool for structural characterization. Indeed, it allows to make images up to atomic resolution, chose imaging mode allowing to highlight or erase the presence of some crystalline defect, measure crystalline structure, as well as phases and their relative orientations. However, because the sample is illuminated by a parallel beam, it is difficult to get information that are not already contained in the image, such as chemical composition.

STEM, HAADF and EDX

In Scanning Transmission Electron Microscopy (STEM), the main goal is to image the sample by scanning it with a convergent electron beam and measure the transmitted signal point by point. Hence, it is possible to reconstruct the image from the intensity map, as would be done in a SEM. This method has several advantages. First, because the measurements are done individually at each point, it is possible to couple STEM with another sensor, such as EDX or CL. These measurements can also be done with a TEM setup but would give an average signal on the studied region. To get mappings, the use of a small beam is necessary. Obtaining a small beam requires to use a high convergence angle. Another difference between SEM and STEM is the aberration: in TEM, the aberration occurs at the level of the objective lens, whereas in STEM, it occurs before the beam encounters the sample, in the condenser lenses that are responsible for the size the beam. Hence, to make HR-STEM pictures of samples, STEM setups may require having some form of aberration correction to decrease the beam size and hence, imaging resolution.

Because the STEM method uses a convergent electron beam instead of a set of parallel beams, the interaction with the lattice yields a slightly different diffraction pattern. In Fig. II-20, the three main contributions in the pattern are presented. First, the transmitted beam sits in the center of the pattern, as is the case in TEM. An array of diffracted beams can then be witnessed and contain crystallographic information on the samples. Last, at higher angles sits a halo of inelastically scattered electrons, that are sensitive to atomic number and allows to get a chemical contrast during imaging. Because of this, making images with inelastically scattered electrons is called Z-imaging. Fig II-20 (a) shows how the pattern looks like in the case of a low convergence angle. However, in HRSTEM, with a high convergence angle, the diffraction spots get larger, and tend to overlap, meaning that it becomes difficult to distinguish the transmitted and diffracted beam.

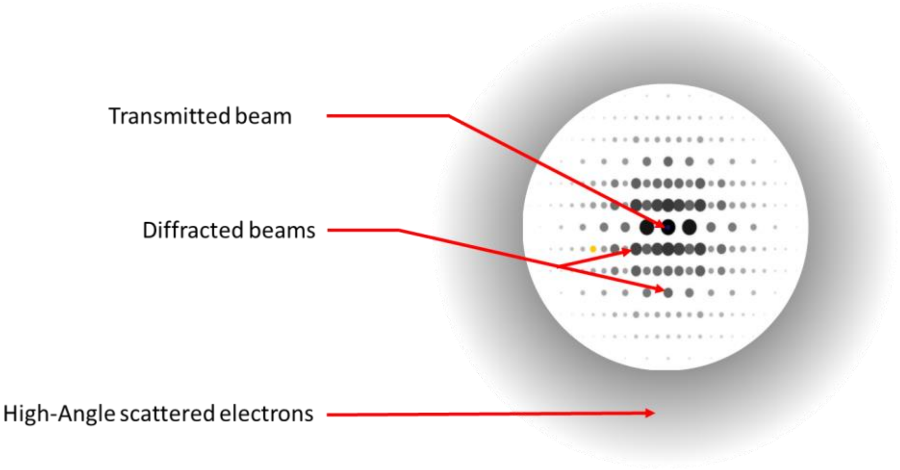

Figure II-20: *Diffraction pattern from a convergent beam in STEM at low (a) and high (b) resolution imaging*

To measure these different contributions, there are several detectors that can be used in STEM microscopy (Fig. II-21). Much like in TEM, the bright field sensor measures the direct transmitted beam, but has not been used in the scope of this work and will not be further detailed here. Then, two annular detectors may be used to measure the diffracted beams and high angle scattered beam, as presented in Fig. II-21 (b). This is done respectively by an Annular Dark Field (ADF) detector and a High-Angle Annular Dark Field detector (HAADF). This configuration is useful to make high quality Z-contrast imaging using the HAADF detector, while simultaneously making a crystallographic contrast image with the ADF detector. By playing with the projector lens, it is possible to adjust the diffraction magnification (camera length) to make sure that the signal received by the ADF detector correspond to diffracted beams, while the HAADF detector receives the electrons scattered at high angles (Fig. II-24 (c))

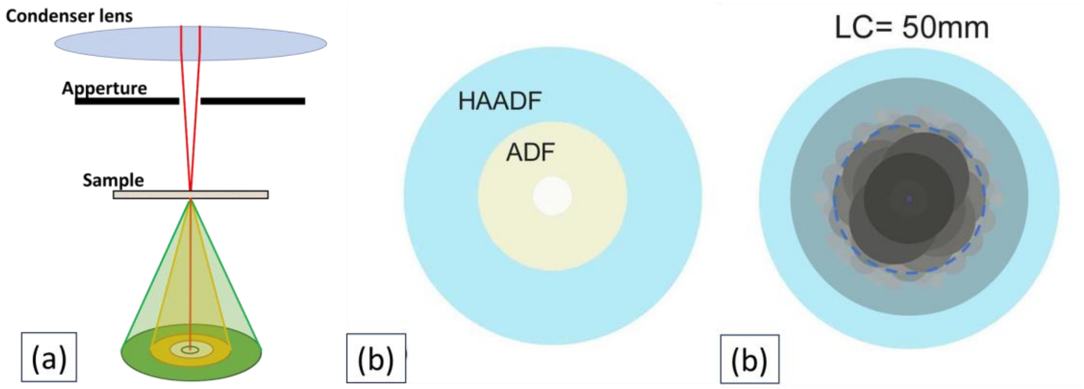

Figure II-21: *(a) schematic representation of STEM characterization, (b) detectors and (c) diffraction pattern under operation for a camera length of 50mm.*

In this work, the imaging methods were also coupled with EDX measurements. The EDX measurements in STEM work following a similar principle than in SEM microscopy, with one difference being that the TEM sample is thin limiting the emitting volume. STEM was carried on an aberration corrected Thermo Fisher Spectra 200 equipped with two rows of ADF/HAADF detectors at different lengths. The STEM is aberration corrected, with a resolution between 0.7 and 1.1Å for acceleration voltages of 60 and 200keV respectively. For this thesis the microscope was always operated at 200kV. Z-contrast images were taken with collection angles between 110 and 200mrad, while crystallographic contrast was obtained between 35 and 200mrad. Two EDX sensors were used for characterization allowing a large detection solid angle of 1.8 sr. The line used for the EDX of Si, Ga and In respectively are the K_α, L_α and L_α Lines.

2.3 X-RAY DIFFRACTION

While TEM is an accurate way to characterize the crystalline structure in a sample, it requires preparation with tools that are not always accessible, working at small scale, which does not allow to get statistical information on the samples. Hence, another method is used to characterize the crystallinity of a sample on a large scale, which is X-ray diffraction (XRD). This method uses an X-ray source to produce a beam that is shone onto a tilted sample. The crystallographic arrangement of the sample will act as a diffraction grating for the X-ray, by following the Bragg's law. Because this phenomenon depends directly on the crystallographic structure of the sample, it allows to get critical information about its crystallography. By scanning the sample with a detector moving at different angles around the sample, it is possible to measure peak intensity corresponding to the diffracted pattern. The diffraction occurs when the Bragg's law is respected (Fig. II-22), meaning that the incidence angle needs to be such as: $n \cdot \lambda = 2 \cdot d \cdot \sin(\theta)$, with n an integer, λ the wavelength of the X-ray beam, d the lattice parameter and θ the incidence angle.

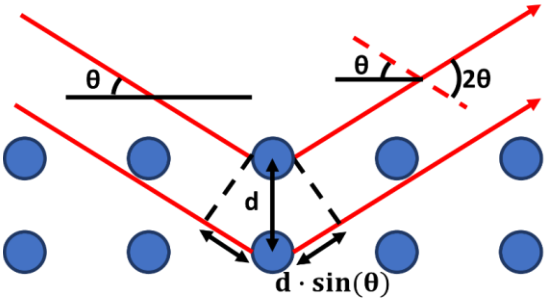

Figure II-22: *Scheme of Bragg diffraction in a crystal*

Other properties can however be measured. In the case of a thin heterostructure, it is for example possible to check relative orientations and tilt of the different layers, or grains in the case of a polycrystalline layer. Also, since Bragg diffraction depend on the lattice parameters, XRD allows to measure the interatomic distance in compounds such as InGaN, which allows to calculate its strain and composition. It should be noted that because XRD is essentially diffraction through a crystalline lattice, it can only provide useful information on crystalline or semi crystalline materials.

Along the uses that can be made of such a technology (such as, for example, powder analysis), the ones that have been used during this PhD will be presented here. In this scope, XRD has mainly be used to characterize nanostructures dispersed on a substrate. In this scope, the method and interpretations are both different from the planar case, in which the material is a monophase and monocrystalline structure, and from the powder case, in which the crystal structure and directions are expected to be different from one crystallite to another.

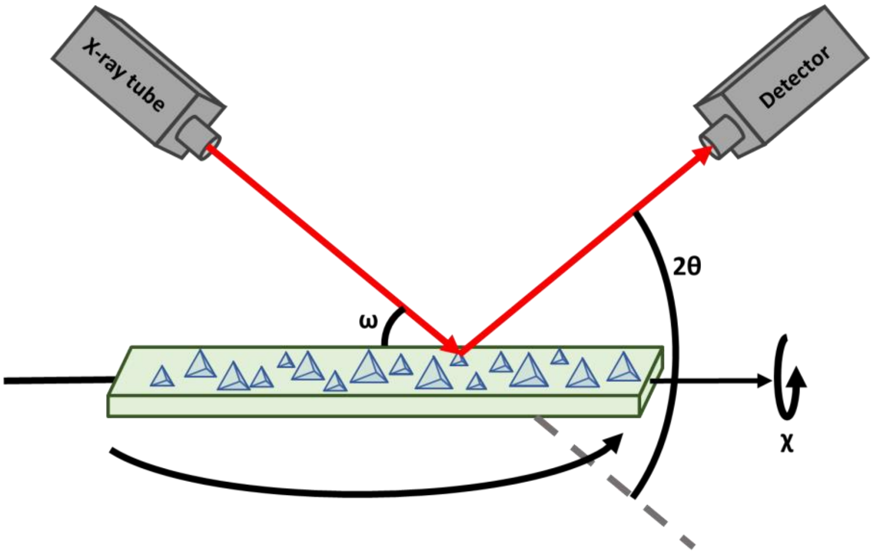

Figure II-23: *Simplified scheme of a X-ray diffraction measurement setup*

In nanowire grown through SAG, the use of XRD is limited due the presence of the underlying substrate and the characterization would require to separate the nanowire from the substrate, and to use an equipment with enough precision to characterize single nanowires[45]. These technical difficulties mean that in this work, XRD has mainly been used to characterize the growth of nanostructures on 2D materials and has not been used in the case of nanowires.

XRD allows first to characterize the main crystallographic planes produced by the growth, which is not always obvious in this context. This can be done simply by scanning the sample through a 2theta-omega scan (Fig. II-23), which measures the intensity of the signal measured by the receptor relative to the value of 2θ. The sample needs to be positioned such as the scan allows to put the investigated planes in Bragg condition. In the case of GaN, this is usually done by placing the sample with the basal c-plane parallel to the holder. During a $2\theta-\omega$ scan, the angle of both the source and the receptor are varied at the same time, and at a similar rate (hence the name $2\theta-\omega$ scan) to measure when the angle of the beam respects the Bragg law, and hence measuring the presence of different crystallographic facets. Moreover an elastically strained material will have a different inter-atomic distance and will therefore have a shifted diffraction angle. It is possible to measure elastic staining by using XRD, which is critical in the case of growth on 2D material, since successful VdW or Remote epitaxy is expected to yield relaxed structures[46].

Another information that is critical in growth on 2D such as graphene is the relative orientation of the grown structure to the material under the graphene. This allows to tell apart VdW and remote epitaxy, as the nanostructure is expected to follow the crystallographic structure of the underlying substrate in the second case. In the case of an asymmetric peak, this can be done by performing a φ scan. Indeed, by setting the system in Bragg conditions and rotating the sample on itself following the φ axis, it is possible to measure the in-plane directions of the crystallographic structures and see if they match.

The last method used to characterize structures grown on 2D materials is the plotting of a rocking curve, which consists in a ω scan. The rocking curve allows to measure the relative rotation between nuclei, and hence characterize the twist and tilt of the structures[47]. To do so, the set-up is positioned to satisfy the Bragg's law, either of the signal of the (0002) for tilt, or one of the $(10\bar{1}X)$ planes (X being an integer) for the twist. The sample is then tilted, leading to the extinction of the diffracted signal. By modifying the angle around the Bragg's peak, one can build a gaussian curve, which is the rocking curve. The FWHM of the rocking curve is directly correlated to the tilt and twist and allows to make qualitative comparison between samples. In case of remote epitaxy, the twist can also be an indicator of the strength of coupling between the underlying substrate and the nuclei.

3. CONCLUSION

In this chapter, we have been able to present the basics of GaN nanowire growth by MOCVD, as well as the methods to characterize them. Understanding this allows to exhibit the basic issues toward their use in flexible devices and give us clues as to how to use the process to solve these issues, and how to verify these results using the characterization tools at our disposal. In the following chapters, we aim to present several studies done toward the elaboration of flexible devices. The first of these studies will focus on the characterization and optimization of the growth process to heighten their properties. The second study will focus on the elaboration of flexible LEDs, and optimization done to fit the use of SAG nanowires. The last paragraph will show the work done toward the growth of optically active nanostructures on graphene.

BIBLIOGRAPHY

1. Thompson AG. MOCVD technology for semiconductors. *Mater Lett*. 1997;30:255-263. doi:https://doi.org/10.1016/S0167-577X(96)00215-7

2. Mohammed Zeghouane. *Contrôle de l'homogénéité et de La Composition En Indium Dans Les Nanofils InGaN Synthétisés Par HVPE*.; 2019. https://theses.hal.science/tel-02409369

3. Zhou S, Gan L, Wang D, Li H, Zhai T. Space-confined vapor deposition synthesis of two dimensional materials. *Nano Res*. 2018;11:2909-2931. doi:https://doi.org/10.1007/s12274-017-1942-3

4. Wang CA. Early history of MOVPE reactor development. *J Cryst Growth*. 2019;506:190-200. doi:https://doi.org/10.1016/j.jcrysgro.2018.10.004

5. Bass SJ. Device quality epitaxial gallium arsenide grown by the metal alkyl-hydride technique. *J Cryst Growth*. 1975;31:1782-178. doi:https://doi.org/10.1016/0022-0248(75)90127-X

6. Mei SZ, Wang Q, Hao ML, et al. Flow Field and Temperature Field in GaN-MOCVD Reactor Based on Computational Fluid Dynamics Modeling. *Chinese Physics Letters*. 2018;35(9):098101. doi:10.1088/0256-307X/35/9/098101

7. Fang H, Zhang Z, Pan Y, Ma R, Liu S, Wang M. Systematic study of epitaxy growth uniformity in a specific MOCVD reactor. *Crystal Research and Technology*. 2014;49(11):907-918. doi:https://doi.org/10.1002/crat.201400254

8. Van Santen H, Kleijn CR, Van Den Akker HEA. On turbulent flows in cold-wall CVD reactors. *J Cryst Growth*. 2000;212(1-2):299-310. doi:https://doi.org/10.1016/S0022-0248(00)00033-6

9. Kakanakova-Georgieva A, Forsberg U, Ivanov IG, Janzén E. Uniform hot-wall MOCVD epitaxial growth of 2 inch AlGaN/GaN HEMT structures. *J Cryst Growth*. 2007;300(1):100-103. doi:https://doi.org/10.1016/j.jcrysgro.2006.10.242

10. Adomaitis R. Uniformity control in planetary chemical vapor deposition reactor systems. In: *IFAC Proceedings* . Vol 17. ; 2008:931-935. doi:10.3182/20080706-5-KR-1001.2390

11. Li H. Mass transport analysis of a showerhead MOCVD reactor. *Journal of Semiconductors*. 2011;32(3):033006. doi:10.1088/1674-4926/32/3/033006

12. Chauhan P, Hasenöhrl S, Vančo, et al. A systematic study of MOCVD reactor conditions and Ga memory effect on properties of thick InAl(Ga)N layers: A complete depth-resolved investigation. *CrystEngComm*. 2020;22(1):130-141. doi:https://doi.org/10.1039/C9CE01549C

13. Sun L, Yuan G, Gao L, et al. Chemical vapour deposition. *Nature Reviews Methods Primers*. 2021;1:5. doi:10.1038/s43586-020-00005-y

14. Coulon PM. *Croissance et Caractérisation de Nanofils/Microfils de GaN*. Université Nice Sophia Antipolis; 2014. https://theses.hal.science/tel-01002342

15. Schiavon D, Litwin-Staszewska E, Jakieła R, Grzanka S, Perlin P. Effects of movpe growth conditions on gan layers doped with germanium. *Materials*. 2021;14(2):354. doi:https://doi.org/10.3390/ma14020354

16. Ito N, Tanaka T, Nakahara K. Zn-Doped GaN Comprising the Gate Structure of Normally Off AlGaN/GaN-HFETs. *IEEE Electron Device Letters*. 2022;43(2):192-195. doi:10.1109/LED.2021.3139615

17. Akinaga H, Németh S, De Boeck J, et al. Growth and characterization of low-temperature grown GaN with high Fe doping. *Appl Phys Lett*. 2000;77(26):4377-4379. doi:https://doi.org/10.1063/1.1335547

18. Wang X, Hartmann J, Mandl M, et al. Growth kinetics and mass transport mechanisms of GaN columns by selective area metal organic vapor phase epitaxy. *J Appl Phys*. 2014;115(16):163104. doi:https://doi.org/10.1063/1.4871782

19. Grandjean N, Massies J, Semond F, Karpov SY, Talalaev RA. GaN evaporation in molecular-beam epitaxy environment. *Appl Phys Lett*. 1999;74(13):1854-1856. doi:https://doi.org/10.1063/1.123691

20. Yamamoto A, Kasashima K, Sugita K, Yasuda M, Kuroda C, Hashimoto A. MOVPE growth of InN under high NH3 decomposition rate conditions. *Physica Status Solidi C: Conferences*. 2005;2(7):2285-2288. doi:https://doi.org/10.1002/pssc.200461409

21. Yamamoto A, Sugita K ichi, Hashimoto A. Elucidation of factors obstructing quality improvement of MOVPE-grown InN. *J Cryst Growth*. 2009;311(22):4636-4640. doi:https://doi.org/10.1016/j.jcrysgro.2009.08.027

22. Koleske DD, Wickenden AE, Henry RL, DeSisto WJ, Gorman RJ. Growth model for GaN with comparison to structural, optical, and electrical properties. *J Appl Phys*. 1998;84(4):1998-2010. doi:https://doi.org/10.1063/1.368353

23. Shin H, Arkun E, Thomson DB, et al. Growth and decomposition of bulk GaN: Role of the ammonia/nitrogen ratio. *J Cryst Growth*. 2002;236(4):529-537. doi:https://doi.org/10.1016/S0022-0248(02)00825-4

24. Manglano Clavero I, Margenfeld C, Hartmann J, Waag A. Facet Control and Material Redistribution in GaN Growth on Three-Dimensional Structures. *Cryst Growth Des*. 2023;23(1):263-272. doi:https://doi.org/10.1021/acs.cgd.2c00989

25. Kapolnek D, Keller S, Vetury R, et al. Anisotropic epitaxial lateral growth in GaN selective area epitaxy. *Appl Phys Lett*. 1997;71(9):1204-1206. doi:https://doi.org/10.1063/1.119626

26. Adhikari S, Lysevych M, Jagadish C, Tan HH. Selective Area Growth of GaN Nanowire: Partial Pressures and Temperature as the Key Growth Parameters. *Cryst Growth Des*. 2022;22(9):5345-5353. doi:https://doi.org/10.1021/acs.cgd.2c00453

27. Bergbauer W, Strassburg M, Kölper CH, et al. Continuous-flux MOVPE growth of position-controlled N-face GaN nanorods and embedded InGaN quantum wells. *Nanotechnology*. 2010;21(30):305201. doi:10.1088/0957-4484/21/30/305201

28. Coulon PM, Alloing B, Brändli V, Lefebvre D, Chenot S, Zúñiga-Pérez J. Selective area growth of Ga-polar GaN nanowire arrays by continuous-flow MOVPE: A systematic study on the effect of growth conditions on the array properties. *Phys Status Solidi B Basic Res*. 2015;252(5):1096-1103. doi:https://doi.org/10.1002/pssb.201451589

29. Miyake H, Motogaito A, Hiramatsu K. Effects of Reactor Pressure on Epitaxial Lateral Overgrowth of GaN via Low-Pressure Metalorganic Vapor Phase Epitaxy. *Jpn J Appl Phys*. 1999;38(9A):L1000. doi:10.1143/JJAP.38.L1000

30. Imer B, Wu F, Craven MD, Speck JS, DenBaars SP. Stability of $(1\bar{1}00)$ m-plane GaN films grown by metalorganic chemical vapor deposition. *Jpn J Appl Phys*. 2006;45(11R):8644-8647. doi:10.1143/JJAP.45.8644

31. Lotter B, Konde S, Nguyen J, Grau M, Koch M, Lenz P. Identifying plastics with photoluminescence spectroscopy and machine learning. *Sci Rep*. 2022;12:18840. doi:https://doi.org/10.1038/s41598-022-23414-3

32. Sun CK, Vallée F, Keller S, Bowers JE, DenBaars SP. Femtosecond studies of carrier dynamics in InGaN. *Appl Phys Lett*. 1997;70(15):2004-2006. doi:https://doi.org/10.1063/1.118803

33. Li T, Fischer AM, Wei QY, Ponce FA, Detchprohm T, Wetzel C. Carrier localization and nonradiative recombination in yellow emitting InGaN quantum wells. *Appl Phys Lett*. 2010;96(3):031906. doi:https://doi.org/10.1063/1.3293298

34. Baumgartner A. Grating monochromator wavelength calibration using an echelle grating wavelength meter. *Opt Express*. 2019;27(10):13596-13610. doi:10.1364/oe.27.013596

35. Miyajima T, Hino T, Tomiya S, et al. Threading dislocations and optical properties of GaN and GaInN. *Phys Status Solidi B Basic Res*. 2001;228(2):395-402. doi:https://doi.org/10.1002/1521-3951(200111)228:2%3C395::AID-PSSB395%3E3.0.CO;2-2

36. Nogues G, Auzelle T, Den Hertog M, Gayral B, Daudin B. Cathodoluminescence of stacking fault bound excitons for local probing of the exciton diffusion length in single GaN nanowires. *Appl Phys Lett*. 2014;104(10):102102. doi:https://doi.org/10.1063/1.4868131

37. Griffiths JT, Ren CX, Coulon PM, et al. Structural impact on the nanoscale optical properties of InGaN core-shell nanorods. *Appl Phys Lett*. 2017;110(17):172105. doi:https://doi.org/10.1063/1.4982594

38. Hartmann J, Wang X, Schuhmann H, et al. Growth mechanisms of GaN microrods for 3D core-shell LEDs: The influence of silane flow. *Physica Status Solidi (A) Applications and Materials Science*. 2015;212(12):2830-2836. doi:https://doi.org/10.1002/pssa.201532316

39. Cazaux J. About the role of the various types of secondary electrons (SE1; SE2; SE3) on the performance of LVSEM. *J Microsc*. 2004;214(3):341-347. doi:https://doi.org/10.1111/j.0022-2720.2004.01326.x

40. Garitagoitia Cid A, Rosenkranz R, Löffler M, Clausner A, Standke Y, Zschech E. Quantitative analysis of backscattered electron (BSE) contrast using low voltage scanning electron microscopy (LVSEM) and its application to Al0.22Ga0.78N/GaN layers. *Ultramicroscopy*. 2018;195:47-52. doi:https://doi.org/10.1016/j.ultramic.2018.08.026

41. Luo JF, Ji Y, Zhong TX, et al. EBSD measurements of elastic strain fields in a GaN/sapphire structure. *Microelectronics Reliability*. 2006;46(1):178-182. doi:https://doi.org/10.1016/j.microrel.2005.05.012

42. Tourbot G, Bougerol C, Glas F, et al. Growth mechanism and properties of InGaN insertions in GaN nanowires. *Nanotechnology*. 2012;23(13):135703. doi:10.1088/0957-4484/23/13/135703

43. Guzzinati G, Altantzis T, Batuk M, et al. Recent advances in transmission electron microscopy for materials science at the EMAT lab of the university of antwerp. *Materials*. 2018;11(8):1304. doi:https://doi.org/10.3390/ma11081304

44. Cancellara L. *Transmission Electron Microscopy Investigations on the Recovery Mechanisms of Epitaxial AlN upon High-Temperature Annealing*. Technischen Universität Berlin; 2023.

45. Favre-Nicolin V, Eymery J, Koester R, Gentile P. Coherent-diffraction imaging of single nanowires of diameter 95 nanometers. *Phys Rev B Condens Matter Mater Phys*. 2009;79(19):195401. doi:10.1103/PhysRevB.79.195401

46. Journot T, Okuno H, Mollard N, et al. Remote epitaxy using graphene enables growth of stress-free GaN. *Nanotechnology*. 2019;30(50):505603. doi:10.1088/1361-6528/ab4501

47. Kobayashi K, Yamaguchi AA, Kimura S, Sunakawa H, Kimura A, Usui A. X-Ray Rocking Curve Determination of Twist and Tilt Angles in GaN Films Grown by an Epitaxial-Lateral-Overgrowth Technique. *Jpn J Appl Phys*. 1999;38(6A):L611. doi:10.1143/JJAP.38.L611

Chapter 3:

Effect of Si on GaN nanowires core growth

CONTENTS

In the first two chapters we described the materials as well as the elaboration and characterization methods that have been used in this PhD. In this chapter we will study in more details the impact of silicon, provided by silane, during the GaN core-nanowire growth.

1. SiGaN ANTISURFACTANT LAYER

1.1 Si-PROMOTED GROWTH MECHANISM

In the previous chapter we went over the main parameters used to control the morphology of GaN grown by MOCVD. However, by varying these parameters alone (i.e. temperature, gas ratios and pressure mainly) it is only possible to obtain microstructures with a maximum height of few µm[1–3]. This can be understood by considering the different contributions to the vertical growth rate and in particular the flux of species coming from the dielectric mask surface[1]. Indeed, the SiN_x mask used to grow the structures is amorphous and it provides no dangling bond that could be used for nucleation. Thus, it acts as a reservoir of adatoms that can be transported toward the top of the nanowire through diffusion. The height of the nanowire is thus limited by the diffusion length of the species on the sidewall, as evidence by the studies on the kinetics of nanowire growth[1,2]. However, several publications reported the growth of much longer nanowires (>10µm in length[4,5]). We conclude that there is thus another way to greatly increase the adatom diffusion on the sidewalls. In the next paragraphs we will present how this result has been reached.

Indeed, it has been discovered that the addition of silane during the growth dramatically increases the vertical growth rate as well as the maximum reachable height for a nanowire[6,7], going from a few µm without silane to several tens of µm, with a high flux of silane typically higher than for n-GaN doping (>100 nmol/min). This phenomenon has been quickly identified as being caused by an increase in diffusion on the sidewalls of the nanowires[1,4,5,8] which is not surprising since the anti-surfactant effects of Si on GaN growth have been known for some time[7,9]. Further investigation on samples grown using this method revealed that the nanowires feature a thin shell that can be revealed through dry etching of the structures. This feature can be seen in transmission microscopy, and EDX measurements indicate that it contains higher quantities of Si than the surrounding material[4].

Following these observations, Tessarek *et al.*[4] concluded that the introduction of silane during growth was responsible for the deposition of a thin SiN layer. This layer is suspected to be the main reason behind the increase of diffusion of adatoms on the sidewalls of the nanowires. In this model (Fig. III-1), Si reacts directly with the ammonia in the chamber to form a SiN layer on the sidewalls of the nanowires. This layer helps the Ga species to diffuse to the top of the nanowire, where they accumulate in the form of a metallic droplet, much like those observed in catalyzed VLS nanowire growth. The droplet is then expected to readily react with any upcoming nitrogen adatom to form GaN. Moreover, both Si and N are expected to have a low solubility in liquid Ga[10,11], and are hence expected to be segregated, which could favor the reaction leading to the formation of SiN. According to this model, the SiN layer has two uses in the growth of nanowires: first, to help diffusion and promote thereby vertical growth, and second, to act as a blocking layer for sidewall growth. This layer is thus sometimes referred to as an antisurfactant layer, and this term will be used to describe a material sharing these properties in this chapter.

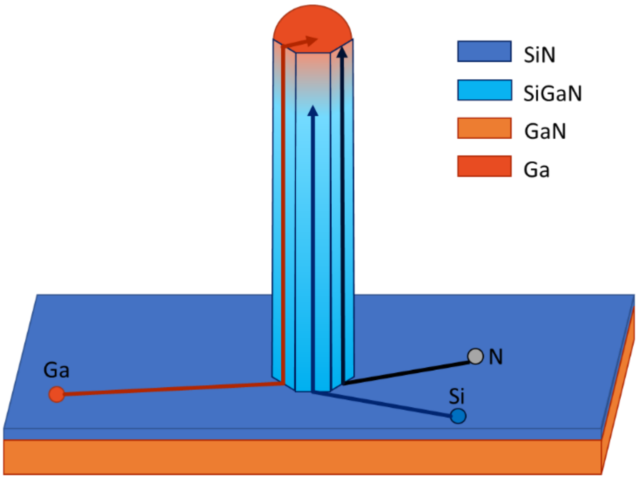

Figure III-1: Schematic representation of the *growth mechanism proposed by Tessarek et al.*[4]

However, some limitations on this model can be noted. First, while the model insists on the presence of a Ga droplet at the top of nanowire during the growth, no direct evidence of its presence has been provided. The main explanation is that the cooling down of the GaN structures is usually performed under N-rich conditions to prevent thermal decomposition of the nanowires, and hence, the metallic droplet is consumed by reacting with ammonia. Also, while the data suggested that the thickness of the layer is probably sub nanometric and contains Si (as confirmed by EDX measurements[4]), this layer was not further investigated in this study. The properties of this antisurfactant layer have yet to be investigated.

1.2 PROPERTIES OF THE SIDEWALL SiGaN

As explained in the last paragraph, the growth of the Si-rich layer is a critical factor in the growth of GaN nanowires by MOCVD, as it extends the diffusion of species on the sidewalls allowing to grow structures with high aspect ratios and lengths above the µm scale. Since the first reported use of Si for the growth of nanowire[4], there has been several direct reports of the presence of the antisurfactant layer. The layer has been first observed by Tessarek et al.[4] in TEM imaging and EDX spectra, confirming the presence of a Si rich layer between the core and the shell of the nanowire. Finer characterization was later done by Hartmann *et al.*[1], which used Auger spectroscopy to measure the thickness of the Si-rich layer and its composition, reporting the presence of Si and O in the layer as well as a varying thickness. Finally, two studies[12,13] report on the presence of Gallium in the layer, suggesting that the compound was a SiGaN compound. However, despite these studies, the data regarding the antisurfactant layer on MOCVD grown nanowires is scarce, and there is no definite conclusion regarding its crystallographic structure or its composition. Hence, as part of this PhD, particular attention has been paid to characterizing this ultra-thin layer to understand its properties.

In the next paragraphs the properties of the Si-rich antisurfactant layer will be investigated by TEM. Two samples have been studied: A core-shell sample of fully n-GaN doped nanowires, referred to as **sample A** in the rest of this paragraph, has been produced by MOCVD in a Thomas Swann showerhead reactor. The core growth was performed at a setpoint of 1175°C, under 100 Torr, for 1800 seconds. The gas mix consisted of 1790 µmol.min^{-1} of NH_3, 110 µmol.min^{-1} of TMGa (giving a V/III ratio of 15), and 400 nmol.min^{-1} of SiH_4, with a carrier gas mix of $H_2/N_2 = 3$. A subsequent shell consisting of 3 InGaN quantum wells has been deposited. For this, a GaN spacer was first grown at a setpoint temperature of 1175°C and 100 Torr pressure for 100 seconds. The gas mix consisted in 130 mmol.min^{-1} and 55 µmol.min^{-1} of NH_3 and TMGa respectively. Then the quantum wells have been grown at 850°C for 360 seconds, using TMGa and TMIn fluxes of 58 and 32 µmol.min^{-1} respectively, using only N_2 in the carrier gas mix, and keeping the other parameters similar to the spacer growth. The quantum wells were systematically capped by raising the temperature to a setpoint of 1060°C and stopping TMIn flow. The second sample, referred to as **sample B**, has been produced with similar core conditions, except for the TMGa and NH_3 that were lowered to 82 and 1340 µmol.min^{-1}, respectively, to emulate a stronger relative SiH_4 flux. Another difference is that the sample does not feature a shell growth and consists uniquely of a core GaN structure. TEM samples were then prepared by FIB milling and observed in a Thermo Fisher SPECTRA 200 aberration corrected TEM microscope.

1.2.1 THICKNESS AND CRYSTALLOGRAPHIC STRUCTURE

First, the thickness of the layer as well as its crystalline structure, which has not been discussed in previous reports to our knowledge, have been investigated. High resolution STEM images measured at CRHEA on a transverse lamella of the nanowire taken at 2/3 of its height (~9µm) are presented in Fig.

III-2. As it can be seen, the thickness of the layer is limited to two monolayers. For clarity, in this chapter, the term monolayer, abbreviated ML, will refer to single GaN monolayer as presented on the schematic in Fig. III-3, in which 1 ML along the *m*-plane is represented when observed along $< 11\bar{2}0 >$ and $< 0001 >$. However, the main result in this image is the crystallinity of the layer, which is surprising since most dielectric masks are amorphous. Here, the crystal structure can be clearly seen extending from the GaN to the InGaN through the SiGaN. A similar result has been obtained in longitudinal lamellas, strongly suggesting that it displays a wurtzite crystalline structure (as it will be shown hereafter in Fig. III-4). Interestingly, Fig. III-2 shows that the GaN spacer grown at the first stage of shell growth has not been deposited, and that the first deposited layer after core growth is InGaN.

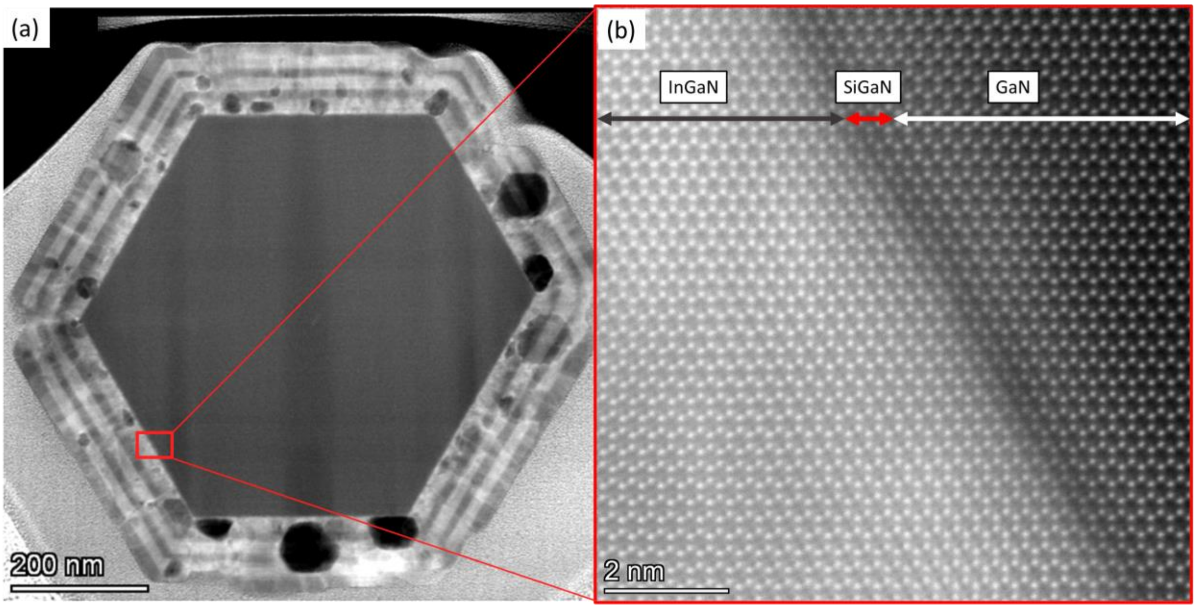

Figure III-2: *STEM images at the junction between core and shell (a) ADF at low and (b) HAADF at high magnification. The high magnification picture features an InGaN quantum well, the GaN core and an ultrathin Si-rich SiGaN layer (Transversal lamella, sample A).*

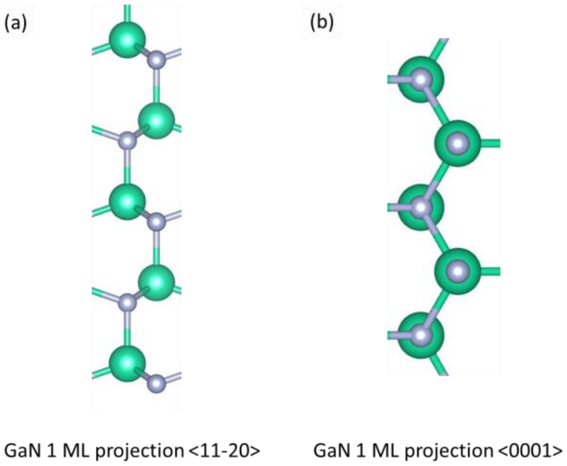

Figure III-3: *Representation of a single GaN monolayer projected along the (a)* $< 11\bar{2}0 >$ *and the (b)* $[0001]$ *directions*

To see how this layer varies along the sidewall of the nanowire, an analysis was performed on sample A, which features a visible Si-rich layer from the top to the bottom of the sidewall *m*-planes. The HAADF images used in this study are presented in Fig. III-4.

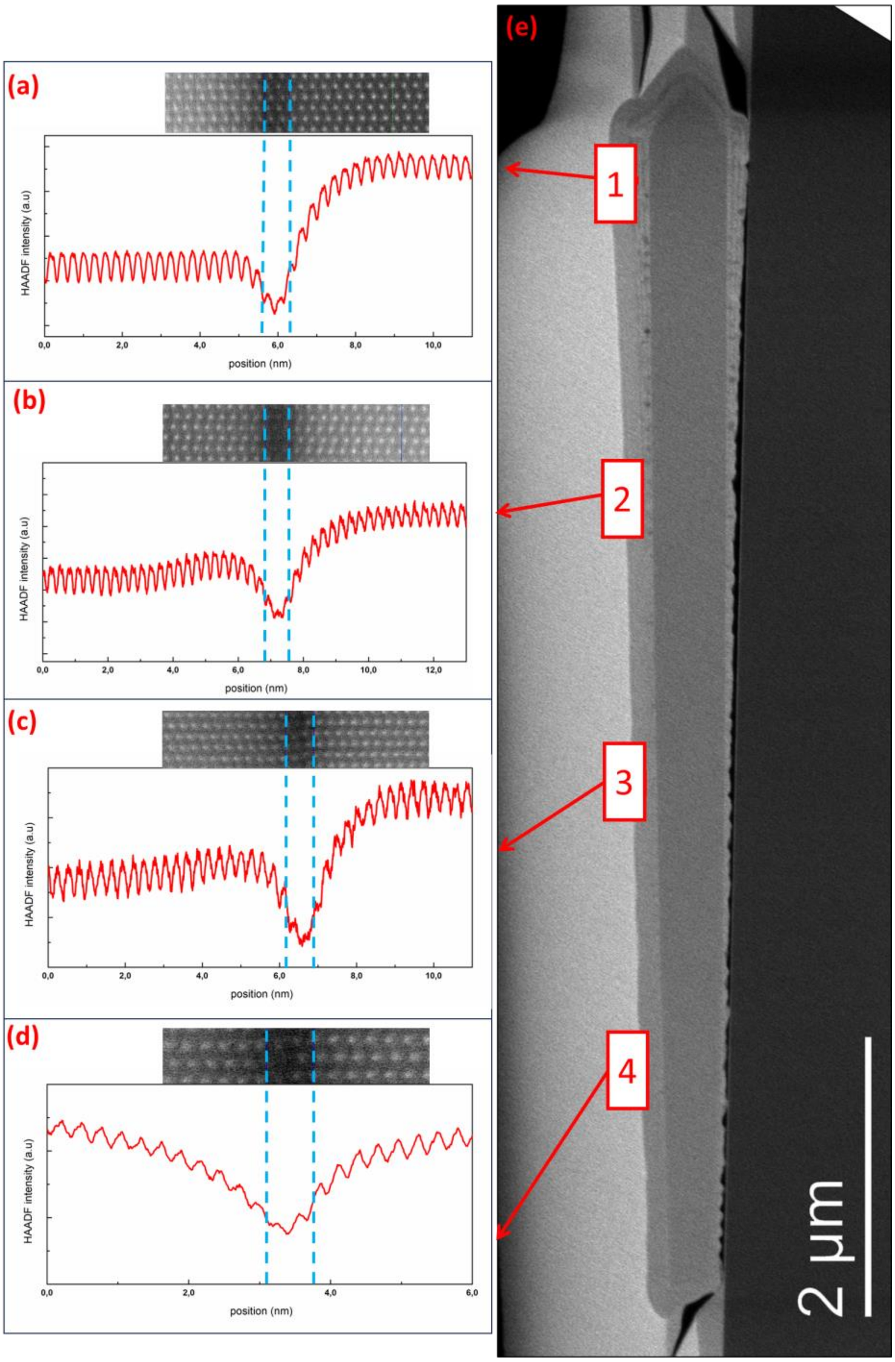

Figure III-4: (a-d) *STEM-HAADF images and corresponding HAADF intensity profiles integrated on the height of the image, taken at the junction between the core and the shell of the nanowire at different longitudinal positions. (e) STEM-HAADF image of one full nanowire with the four locations of the intensity (Longitudinal lamella, sample A).*

Thanks to the Z-contrast imaging conditions used for HAADF, it is possible to precisely deduce the thickness of the Si-rich layer. In Fig. III-4 the HAADF intensity is plotted as a function of the position perpendicular to the shell plane. The periodicity of the crystalline layer leads in HAADF images to oscillations, corresponding to inter-atomic distances. A drop in intensity can be clearly seen at the location of the antisurfactant layer, as evidenced by the superposition of the picture and the corresponding intensity profile. As can be seen on Fig. III-4, the thickness of the Si-rich layer seen in HAADF (with a chemical Z-contrast) corresponds to two oscillations on the intensity profile, i.e. 2 ML across the whole length of the nanowire.

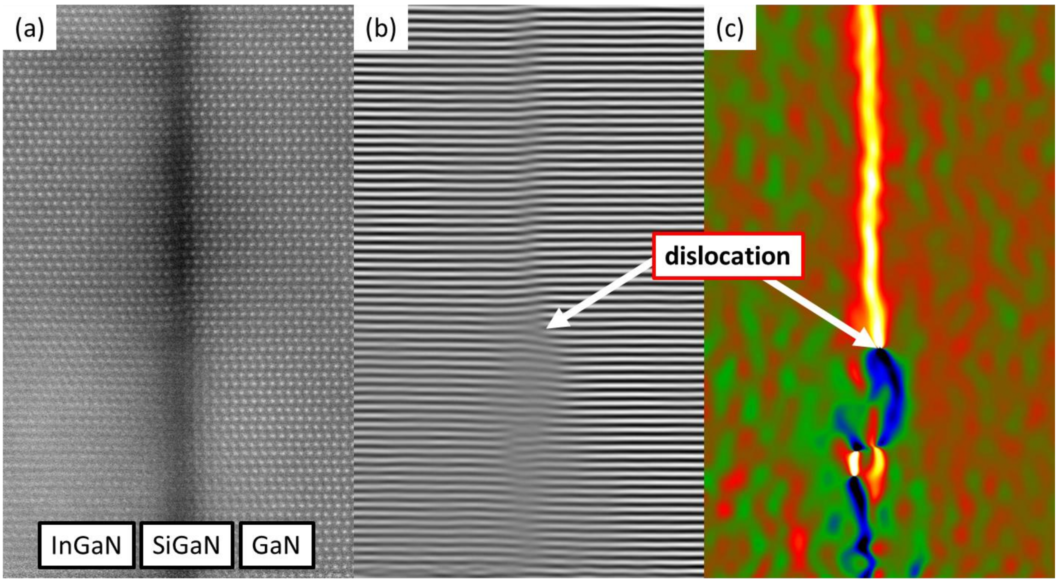

Figure III-5: *(a) STEM-HAADF image, (b) Inverse Fast Fourier Transform showing (0002) atomic planes and (c) Geometrical Phase Analysis (0002) rotation map around the GaN/SiGaN/InGaN junction evidencing the presence of misfit partial dislocations with a (0002) Burgers vector. (Longitudinal lamella, sample A)*

The last feature encountered when analyzing the Si-rich layer is the presence of partial dislocations, originating in or near the Si-rich layer as can be seen on the Fig. III-5 (a,b) and evidenced by GPA analysis on the Fig. III-5 (c). This feature indicates that plastic relaxation is taking place in the material, likely between the GaN and the InGaN.

1.2.2 EDX AND Si COMPOSITION

In recent studies, the composition of the Si-rich layer has been ascribed to different compounds, including pure Si adlayers[1], SiN_x[4] and $SiGa_xN_y$[13]. In addition to the crystallographic structure, it is hence critical to characterize the chemical properties of the layer to confirm its nature. Because the characterization tool used in this work allows us to realize EDX mappings with a resolution on the order of the atomic scale, a study of the layer composition was conducted.

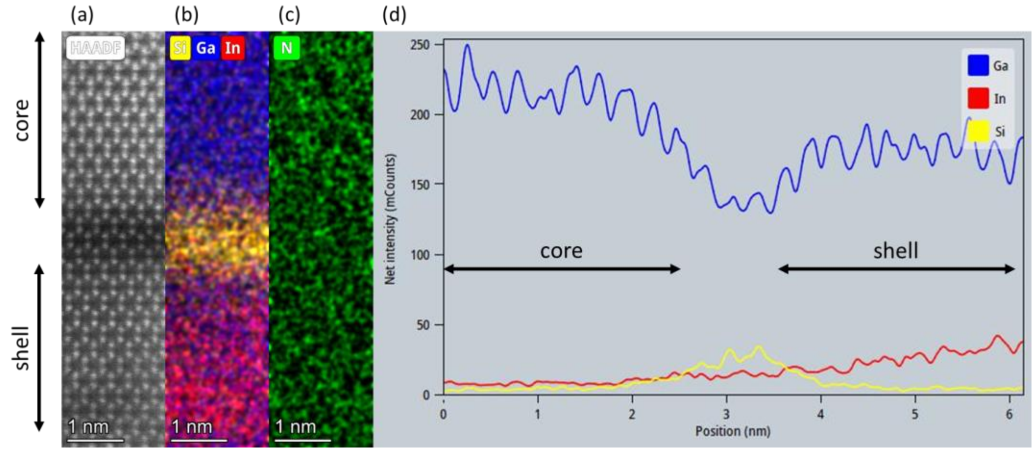

Figure III-6: *(a) STEM-HAADF image, (b) EDX intensity mapping for In/Ga/Si elements and (c) EDX intensity mapping for N around the Si-rich layer, (d) Intensity profile of the mapping presented in (b). (Transversal lamella, sample A)*

The EDX mappings and EDX intensity profiles in Fig. III-6 clearly show the presence of Si in the layer and reveal In diffusion into the Si-rich layer and the GaN core. The quantity of N in the nanowire is not modified in the Si-rich layer (Fig. III-6(c)).

Fig. III-6(d) shows the intensity profile of the EDX signal taken from the chemical map (Fig. III-6(b)). Expected features can be noticed, such as an increase of In composition in the quantum well and the presence of a Si rich layer, with a decrease of the Ga signal in the same layer. However, the signal associated to the Si is detected over a length of 2 nm, which is significantly larger than the Si-rich layer thickness measured from HAADF image intensity (Fig. III-4). This can be explained by the method used to realize the mapping, which uses a convergent beam, which enhances the area of detection and creates a significant overlap between the EDX signals of different regions. However, it is possible to correct this uncertainty by integrating the Si signal and calculating the equivalent intensity for a signal circumscribed on 2ML only. Doing this with data obtained at different points on the nanowire, allowed to get the following mean composition values (considering only the atoms on the cationic sites). The calculation is presented in Annex B .

Longitudinal		
Measurement	C_{Si}	C_{Ga}
1	0,42	0,58
2	0,35	0,65
3	0,34	0,66
4	0,36	0,64
Average	0,37	0,63

Transversal		
Measurement	C_{Si}	C_{Ga}
1	0,32	0,68
2	0,24	0,76
Average	0,28	0,72

Table III-1: *Cationic composition measured in the longitudinal and transveral lamellas (sample A).*

Table III-1 show the values obtained when accounting for beam convergence in the sample, for 4 locations in the longitudinal and 2 locations in the transversal samples. A higher deviation of the values can be observed in the transversal samples. This can be caused by the tapering of the nanowire, which does not allow to have a perfect alignment of the layers on the sidewalls with the zone axis and introduces some uncertainties.

The results presented in Table III-1 suggest that the Si-rich layer grown on the sidewalls of GaN nanowires is a SiGaN layer, with a cationic composition of Si around $1/3$, while the additional $2/3$ of cationic sites are occupied by Ga.

Fig. III-6 shows that some amount of In has been able to diffuse through the SiGaN layer inside the GaN core, which suggests that the In might interact with it and modify its chemical nature. Hence, it was chosen to also investigate a core-only structure in order to avoid any interaction with In and to have a better description of the antisurfactant layer before any epilayer growth (Sample B). TEM observations and EDX mappings were hence done on a transversal lamella of sample B and are presented in Fig. III-7.

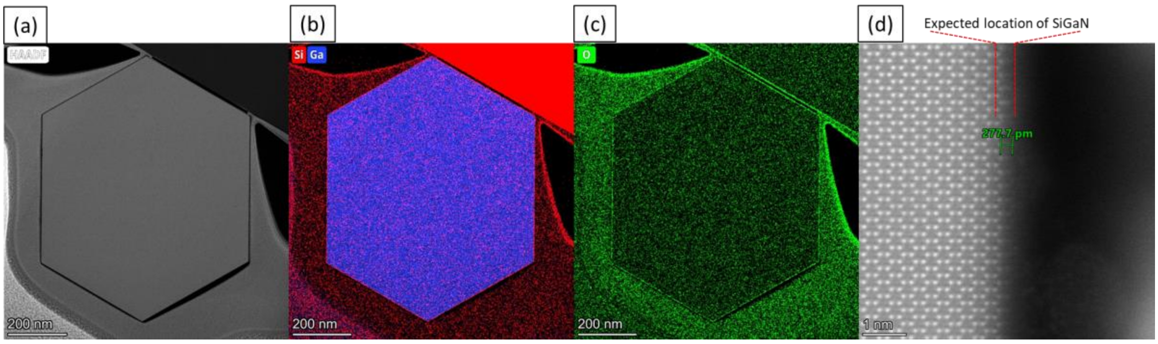

Figure III-7: *STEM-HAADF image (a) and corresponding EDX mapping (b) for Si/Ga elements and (c) O of a transversal lamella of a core n-GaN nanowire. High magnification STEM-HAADF picture of the surface of the nanowire. (Transversal lamella, sample B)*

The measurements presented in Fig. III-7 evidence the presence of a Si-rich layer on the sides of the nanowires, as expected (Fig. III-7(b)). However, this layer also contains significant amounts of oxygen (Fig. III-7(c)), which was unforeseen here: indeed, the reaction is carried out in an MOCVD reactor, within a hydrogen-rich atmosphere and using oxygen free reactants only. Moreover, high resolution pictures of the junction do not show a crystalline highly ordered Si-rich layer (Fig. III-7(d)) as observed in the last paragraph (Fig. III-2), which can be partly explained by the location of the layer. Indeed, being on the surface of the nanowire, the layer is both more difficult to image accurately, but also more prone to be damaged by the FIB preparation, which means that no conclusion can be drawn on this result. We suspect that this oxygen contamination occurred after the growth, either by the surrounding air or during the FIB preparation.

1.3 SiGaN SELF-LIMITING SUPERSTRUCTURES

1.3.1 EVIDENCE OF VACANCIES IN THE SiGaN

From the data presented in the previous paragraphs, the Si-rich antisurfactant layer has been identified as crystalline, and with a $Si_{0.3}Ga_{0.7}N_x$ composition. A material with similar composition has already been described in the literature by Markurt *et al.*[14], who concluded on the presence of vacancies in the structure of the material. This motivated a further investigation on the presence of vacancies in this work.

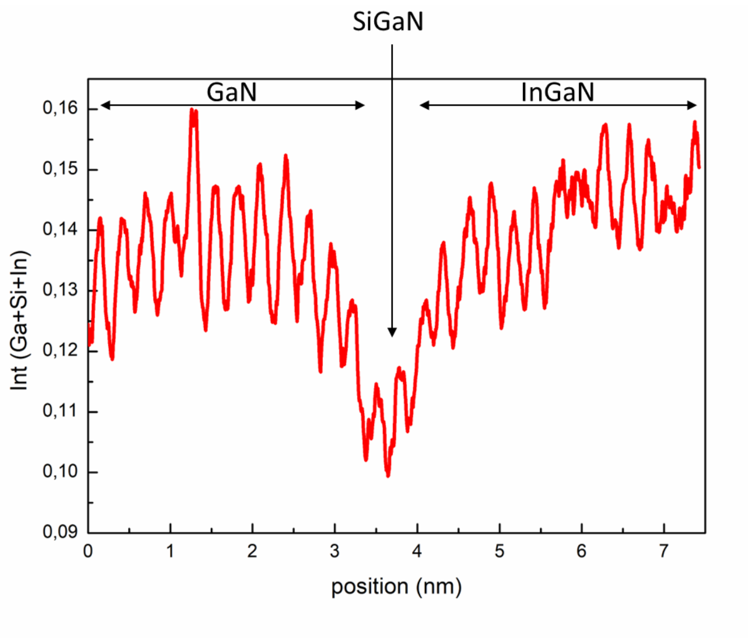

Figure III-8: *Profile of the sum of the EDX signal intensities of Ga, In and Si across the SiGaN*$_x$ *layer. (Transverse lamella, sample A)*

The integrated EDX signal for the cationic species is presented in Fig. III-8. A 30% decrease of the signal can be noted in the SiGaN layer with respect to the same signal obtained in the GaN core and InGaN shell layers. As explained previously, precise EDX measurements are realized using a convergent beam, which means that the signal at each location is overlapped with the neighboring material. In this case, it means that the intensity of the signal in the SiGaN layer is overestimated due to the presence of neighboring materials with higher overall EDX signal for cationic species. While some variation is expected to occur from one atomic species to another due to varying sensitivity of EDX, the experiment was here carried out using peaks located in a low energy range, excluding drastic sensitivities differences for In, Ga and Si. Hence, the observed decrease is a strong indication of a lower concentration of the studied atoms. The nitrogen signal has not been observed to significantly vary at this location, and no other atomic species has been identified. The only possible explanation to this lowered count could be the presence of high densities of cationic vacancies in the material. To confirm this hypothesis, it is possible to model the EDX signal intensity as a function of surface atom density, as is presented in Annex C. Doing so, and comparing the surface atom density in the GaN and the SiGaN reveals a significant drop at the location of the junction, which proves that a significant amount of cationic vacancies is present in the SiGaN.

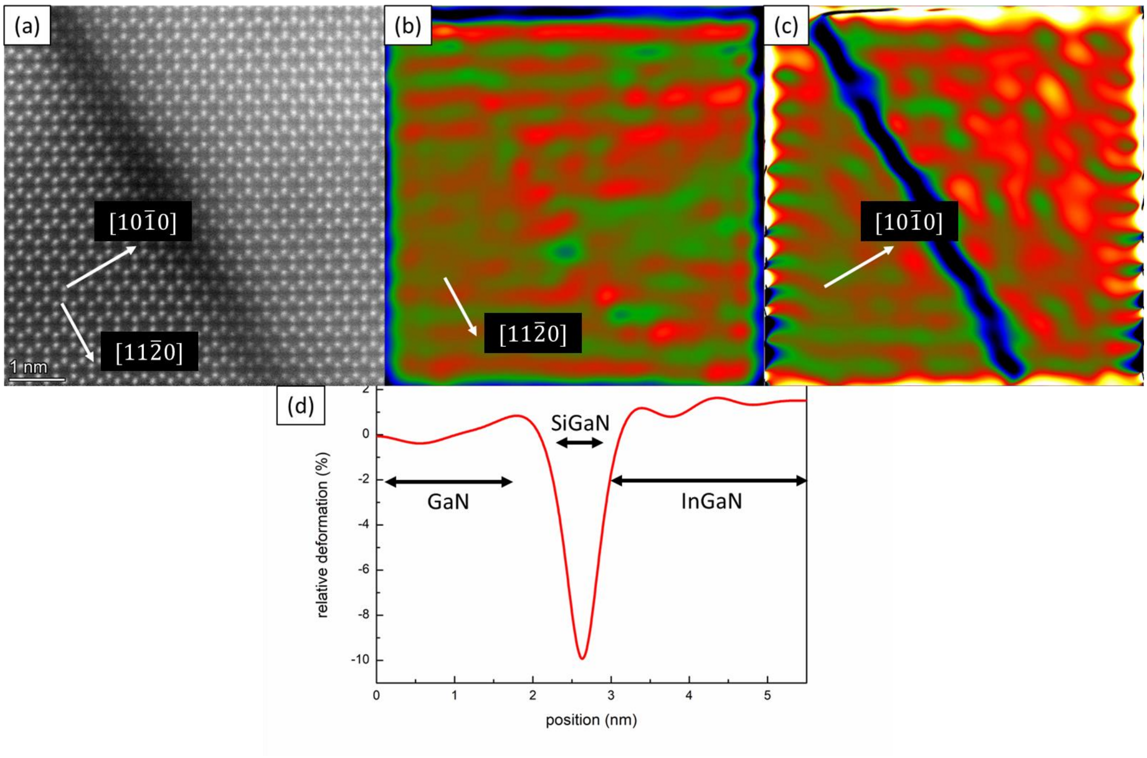

Figure III-9: *(a) STEM-HAADF picture of a transversal TEM slice of sample A, and corresponding Geometrical Phase Analysis strain maps along the* $[11\bar{2}0]$ *(b) and* $[10\bar{1}0]$ *(c) directions. (d) relative deformation profile taken from (c)*

The inter-reticular distance around the GaN/SiGaN/InGaN has also been studied, as presented in Fig. III-9. As expected, the inter-reticular distance differs in the GaN and the InGaN but, more importantly, a 10% contraction is visible at the location of the SiGaN layer along $< 10\bar{1}0 >$ direction. This contraction has been measured in several points of the layer and varies between 7 and 12%. As stated previously and observed in Fig. III-9(a), the SiGaN layer is coherent with GaN along that direction. This deformation could be thus caused by an elastic relaxation of the SiGaN in order to be pseudomorphic with the GaN or, more simply, by the fact that the $\{10\bar{1}0\}$ inter-reticular distances of SiGaN are smaller than those of GaN. However, the inter-reticular distance along the $[11\bar{2}0]$ direction does not feature this contraction (Fig. III-9(b)), which would be expected if the deformation wascaused by lattice mismatch. The large difference in inter-reticular distances in SiGaN compared to GaN can also be related to the presence of vacancies at the cation positions. Therefore, this observation further strengthens the hypothesis of a high presence of vacancies in the SiGaN.

1.3.2 SUPERSTRUCTURED Si-Ga-V_{Ga}-N AND ANTISURFACTANT PROPERTIES

In the previous paragraphs, the structural and chemical properties of the SiGaN layer have been measured, allowing to draw several conclusions. The main results are the following:

- The layer has a SiGaN composition with a 1:2 Si to Ga ratio.
- The WZ crystallinity of the system is maintained through the layer.
- The thickness of the layer is constant and limited to 2 ML.
- Measurements done on the layer are consistent with the presence of vacancies.

- When exposed to air, the SiGaN layer gets oxidized to a $SiGaO_x$ compound.

Some of these properties are in contradiction with results that can be found in the literature. First, it cannot be a crystalline or amorphous SiN_x compound. Indeed, the two known crystal structures of Si_3N_4 are triclinic pedial (C1 group) and hexagonal dipyramidal (C6h group)[15,16]. We have shown however that the SiGaN layer is crystalline and follows a WZ structure. Second, in the present study, the concentration of Si to Ga has been measured throughout the nanowire, and no significant concentration change has been noted on the whole length of the nanowire. This result is significant because the gradient in Ga concentration and in the layer thickness are often the hypotheses introduced to explain the uncomplete coverage of the nanowire [1,4,13,17–21]. Similarly to the composition, the SiGaN layer thickness is also constant. Third, the study reported by Hartmann *et al.*[1] was carried on an uncovered core with significant amounts of oxygen, which is consistent with our observations on sample B and the oxidation hypothesis.

Moreover, we could evidence the anti-surfactant properties of this SiGaN layer. Indeed, in the process used to grow this sample, the core growth is followed by the deposition of a GaN spacer, with the aim of covering the sidewalls of the nanowire. However, it can be clearly seen in Fig. III-6 that this GaN spacer is absent, the first layer grown on the SiGaN is InGaN. This could be explained by the fact that the GaN spacer is grown at a setpoint of 1175°C, while the InGaN is grown at a lower setpoint of 850°C. This behavior shows that growth on the layer can only occur in thermodynamic conditions highly unfavorable for adatom desorption (i.e at low temperature), which is consistent with the properties of a mask.

At this point, it is important to mention that compounds with similar characteristics and properties have already been reported on planar structures. In the case of *c*-plane GaN, Markurt *et al.*[14] noticed that exposing a GaN surface to a silane flux for a few minutes led to the covering of the surface with a SiGaN layer, owing to the formation of a dielectric layer with the properties of a mask. This layer presents some unusual properties: instead of forming an amorphous structure, the covering of GaN by this layer leads to the formation of a 2D superstructure, with a high 1D order and the formula Si-Ga-v_{Ga}-N_3.

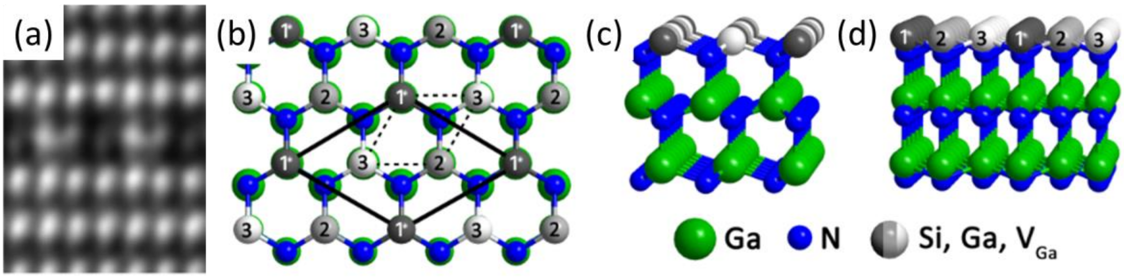

Figure III-10: *High order commensurate superstructure formed by the passivation of GaN by Si in an MOCVD reactor observed in HR-TEM (projection along the m-direction) (a), and model seen by a projection onto the c-plane (b),the a-plane (c), and the m-plane (d) (from ref* [14]*)*

This layer also has the particularity of being one GaN ML thick and with a wurtzite structure. As seen in fig. III-10(d), the compound organize itself in repeating pattern rows of Si, Ga, and gallium vacancies v_{Ga} respectively in a $[10\bar{1}0]$ projection. Using Density Functional Theory calculations on the structure, the authors found that the growth of a GaN monolayer on the superstructure leads to a charge transfer between the cation dangling bonds on the surface and the acceptors state (Ga vacancies, V_{Ga}) in the SiGaN layer, causing the formation of a charged dipole. The dipole moment is then increased for each additional overlayer of GaN on the material, which is thermodynamically unfavorable. Hence, the authors concluded that in this case, the SiGaN acts as a perfect mask. GaN deposition may only proceed through lateral overgrowth from a nucleus grown in an opening in that mask. Similar superstructures have been obtained in the case of AlN[22], leading to an AlSiN compound exhibiting a high order commensurate superstructure too. However, in this later case, this structure may be several ML thick. Interestingly, ref [22] also observes a contraction of the lattice in the AlSiN, which, although relatively smaller, leads the authors to hypothesize that it is linked to the presence of vacancies.

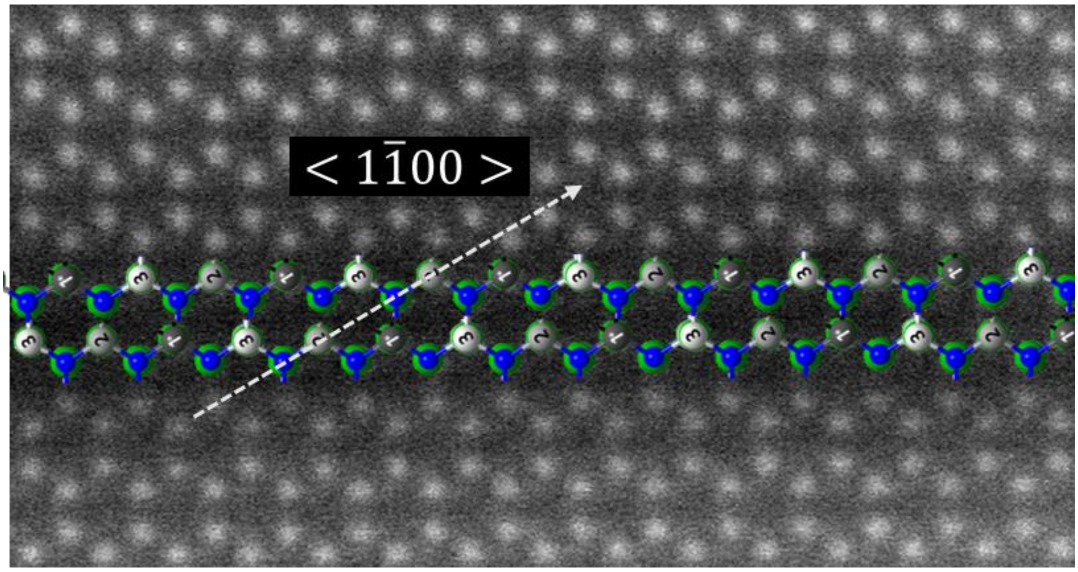

Figure III-11: *Configuration of the* $SiGaN_3$ *described by Markurt et al.* [14] *superimposed on the studied* $SiGaN_x$ *in this PhD, showing the* $< 1\bar{1}00 >$ *axis needed to image the superorder of the layer. The 1, 2 and 3 numbers represent a Si atom, a Ga atom and a* V_{Ga} *respectively.*

Despite these numerous similarities, a direct imaging of the structure would be required to prove that the SiGaN layer in GaN nanowires corresponds to the superstructure material described on *c*-plane GaN. Indeed, while the crystalline structure and the Ga to Si composition are similar, one of the distinctive features of the *c*-plane $SiGaN_x$ is the presence of gallium vacancies as well as their ordered positioning in the superstructure. However, in our case, imaging such an ordered structure is not possible because of crystallographic considerations. Fig. III-11 shows the GaN/SiGaN/InGaN junction, with the SiGaN replaced by the compound described in ref[14]. In order to observe the vacancies in this configuration, the zone axis needs to pass only through vacant sites. As seen in Fig. III-11, this can only be done by choosing a $< 1\bar{1}00 >$ zone axis. However, in the case of the *m*-plane SiGaN, the layer is only 2ML thick in this direction, which means that the signal would be dominated by the material in the front and back of the layer. While some differences have been noted between the reported *c*-plane SiGaN and the currently studied *m*-plane SiGaN, none of the observations made currently have allowed to image the vacancies. If they are present, it is probably caused by a combination of restricted suitable zone axis, and the screening by additional materials such as GaN and InGaN in the sample. However, the Si to Ga ratio, crystalline structure, self-limiting and mask properties of the layer, along with data consistent with the presence of a significant amount of vacancies, strongly point toward a material with similar properties as described in ref[14] and ref[22].

2. Si-RICH GROWTH MARKERS

2.1 ORIGIN

During the TEM observation of the samples presented in this chapter, one interesting feature was noticed. This feature is the presence of periodic growth "markers" in the core structure, that were first observed in ADF pictures (Fig. III-12(a)). Further studies by EDX revealed that these markers contain a higher proportion of Si than the surrounding GaN (Fig. III-12(b)). While Si is expected to incorporate into the core structure and provide a strong n-doping of the GaN, owing to the strong Silane flux a periodic variation of its content in the structure is surprisingly observed. The growth of sample observed here is described in 2.2.

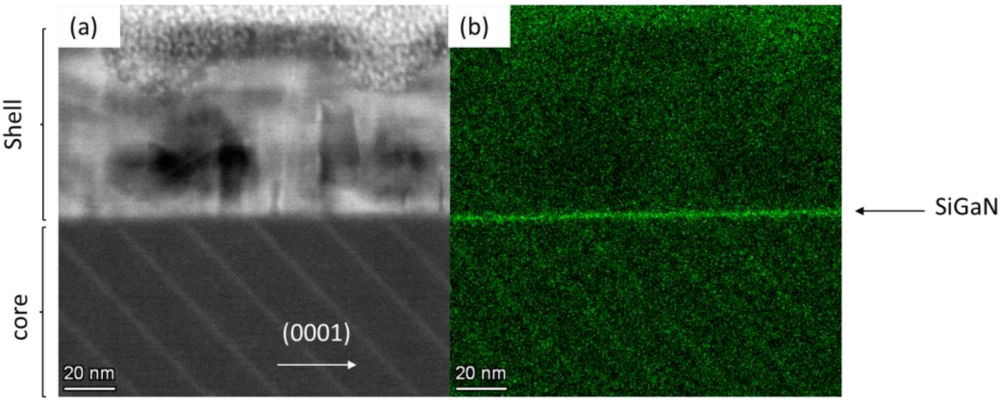

Figure III-12: *(a) ADF and (b) Si-EDX mapping of a nanowire at the junction between the core and the shell (Longitudinal lamella, sample A)*

These markers can be seen along the whole length of the nanowire, as observed in a longitudinal lamella performed along the nanowire, which is shown in the Fig. III-13. A decreasing spatial period is observed when going toward the top of the nanowire. The markers follow the semi-polar planes typically present at the top part of the nanowire.

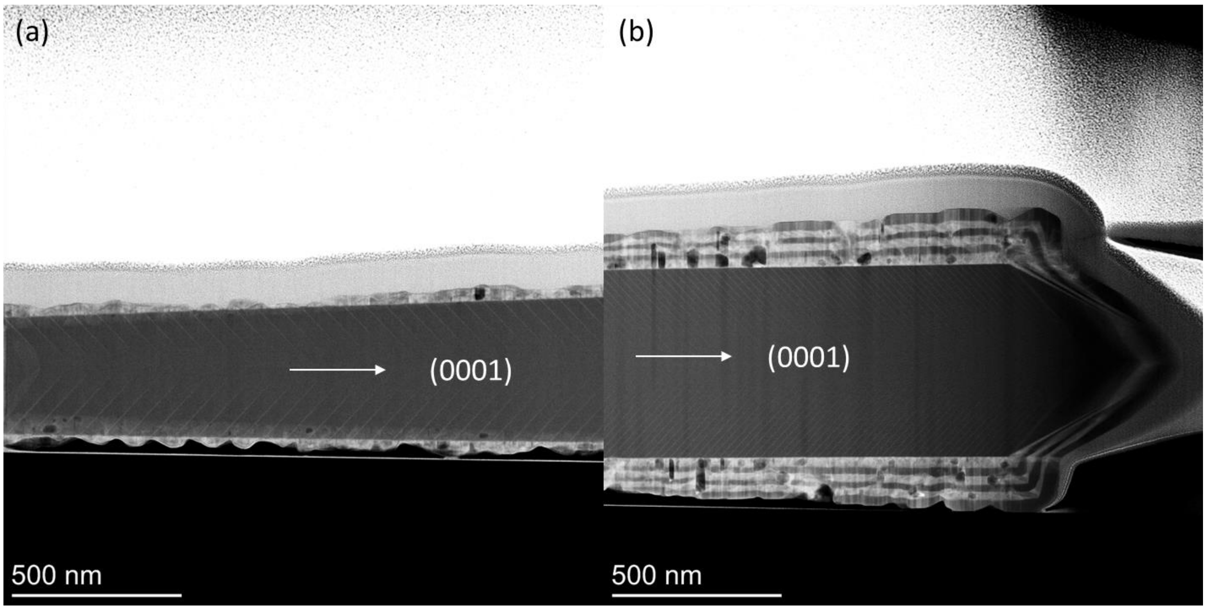

Figure III-13: *ADF picture at the bottom (a) and top (b) of the nanowire featuring growth markers (contrast enhanced) (Longitudinal lamella, sample A).*

However, these markers were always seen on samples grown in a same reactor, namely the Thomas Swann 6x2". To see if this mechanism was representative of the process, it was chosen to search for similar growth markers in samples grown in another reactor (namely, an Aixtron 7x2") with comparable growth conditions (in particular the doping concentration). The HAADF and EDX study of such samples did not feature any growth markers, as shown in the Fig. III-15, showing that this phenomenon is reactor related.

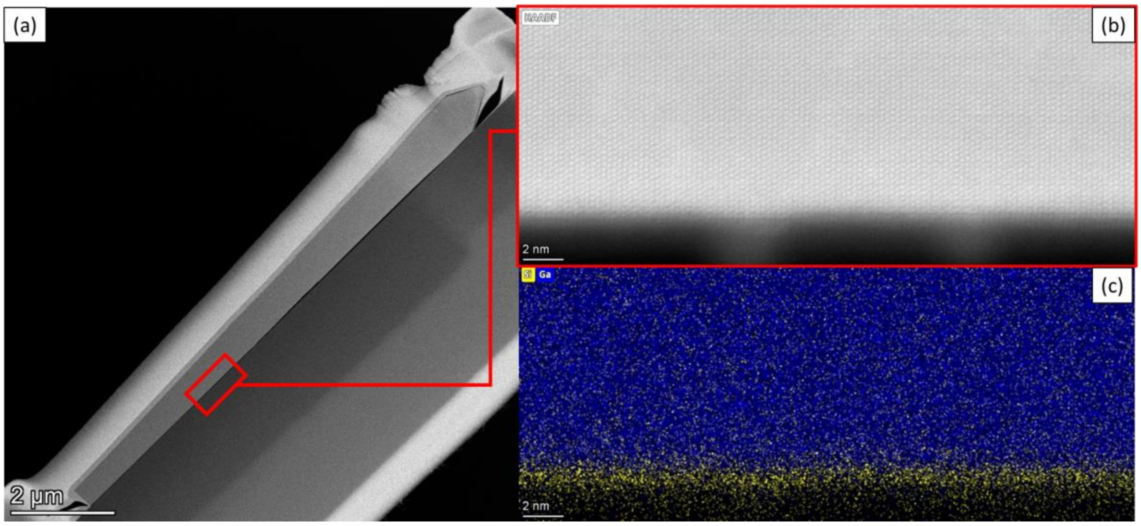

Figure III-15: *(a) STEM ADF longitudinal image of a core nanowire grown in the Aixtron 7x2" reactor under Si-rich conditions, (b) high magnification HAADF image of the surface of the sample and (c) corresponding EDX intensity mapping for Ga and Si.*

Observing the evolution of TMGa partial pressure in Thomas Swann reactor for another nanowire growth allowed to give an explanation to this observation: the partial pressure is oscillating in a periodic way. While the exact explanation of this variation is unkown yet, the oscillation period was measured from Fig. III-16 and was found to be about 13 seconds. In the case of the sample A presented previously, the growth time was 3000 seconds, and 224 accounted markers were estimated on the whole length of the nanowire, so the marker period is around 13 sec, which matches perfectly the TMGa partial pressure variation.

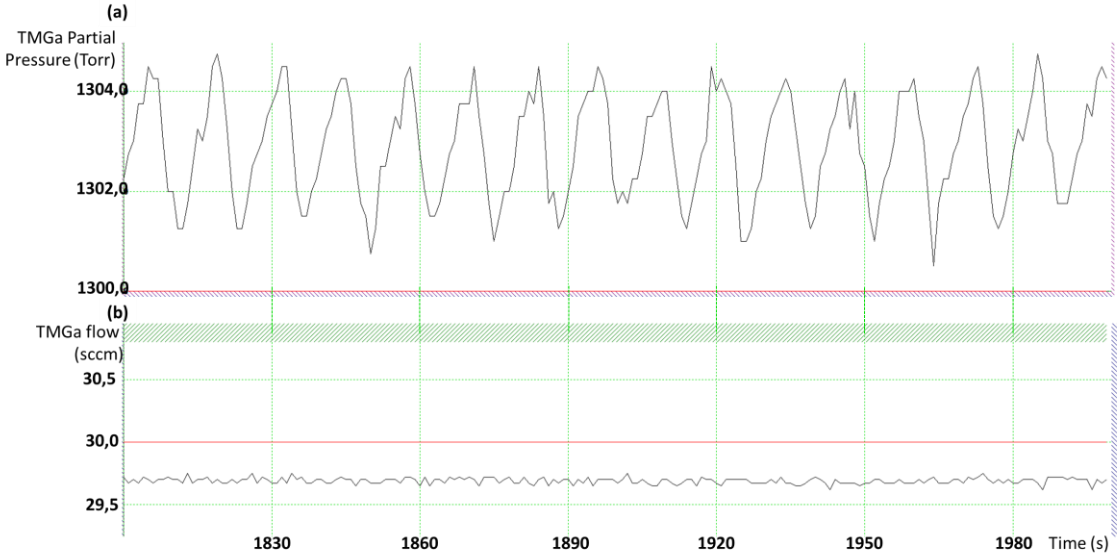

Figure III-16: *(a) TMGa partial pressure and (b) TMGa flow in the Thomas Swann reactor used for nanowire elaboration during n-GaN core growth*

2.2 GROWTH MECHANISM OF GaN NANOWIRES

Once the origin of the markers is identified, we use the marker periodicity to study the evolution of the core growth. Hence, several important features occurring during growth have been observed, allowing to get a precise description of the growth mechanism.

2.2.1 GaN PLANES AND SiGaN FORMATION

First, the markers follow semi-polar $(10\bar{1}1)$ GaN planes from the beginning of the growth. This can be seen in Fig. III-17, at the base of a nanowire of sample B, consisting only in the n-GaN core. It can hence be concluded that the nanowires feature top semi-polar planes during the whole growth, even in early stages, as evidenced by the first marker. Despite the high amount of H_2 during the growth (H_2/N_2 ratio was kept at 3) we thus do not observe any passivation phenomena due to a hydrogen adlayer as it has been previously suggested by Li *et al.*[23] on semi-polar planes of Ga-polar GaN. A difference between this study and the work of *Li et al.*[23] is the use of Silane[23–25], which suggests that the presence of SiH_4 influences the chemistry of the surfaces and could promote *r*-plane growth despite hydrogen-rich conditions.

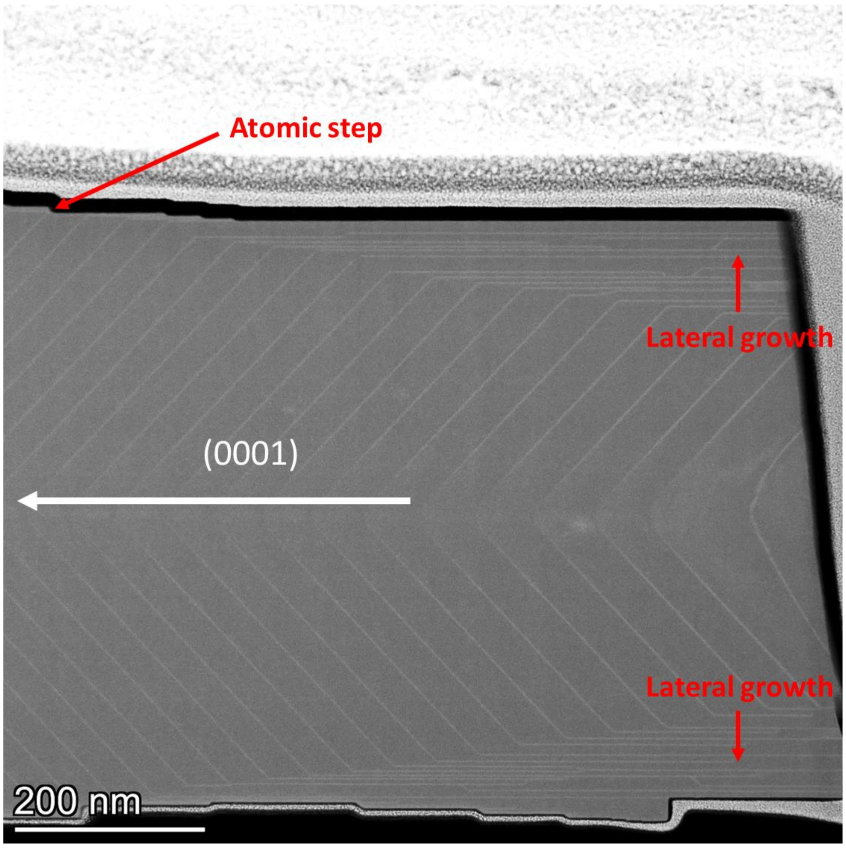

Figure III-17: *ADF picture of the growth markers at the bottom of an n-GaN core nanowire (Longitudinal lamella, sample B)*

The second feature revealed by the growth markers is the presence of growth on the sidewalls. This is especially true in early stages, where *m*-plane makers can also be seen (Fig. III-18(a)), contrary to what is usually seen on the upper parts of the nanowire (Fig. III-18(b)). In later stages (Fig. III-18(b)), *m*-plane growth still slowly occurs, but through atomic steps on the GaN *m*-planes. Here, the nucleation of step seems to be simultaneous with the nucleation of markers, which points to a common origin. However, tapering of the nanowire is a common observation for nanowires grown under similar conditions. Hence, the steps are assumed to not originate from partial pressure variations and have not been the object of further investigation. Last, Fig. III-18(c) presents an HAADF pictures of markers on *m*-plane and *r*-plane, and the similar contrast suggests that their Si-composition is similar.

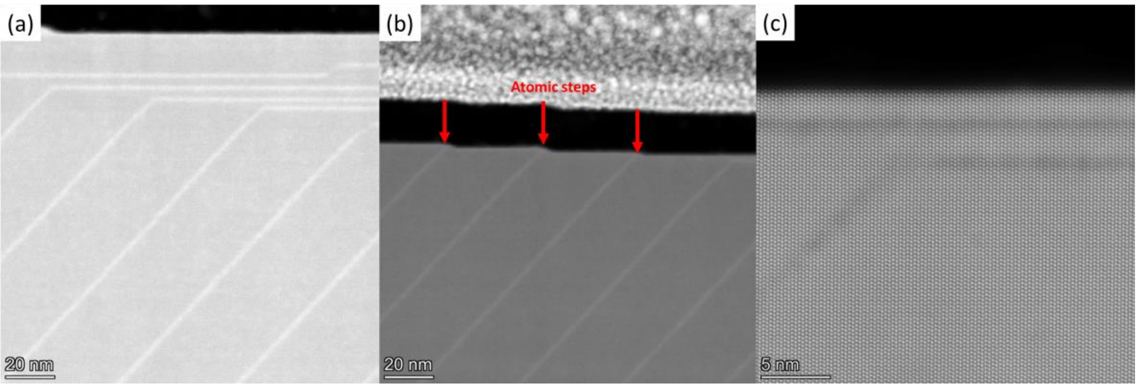

Figure III-18: *ADF pictures zoomed in the sidewall of the nanowire at the bottom (a) and in the middle (b) of the nanowire, and (c) HAADF pictures of the sidewalls at the bottom of the nanowire. (longitudinal lamella, sample B)*

In order to study the Si composition in the markers, an EDX investigation has been conducted on the surface of the nanowires and is presented in Fig. III-19. The profile presented in Fig. III-19(a) clearly shows at the core surface a peak for Si and O corresponding to the oxidized SiGaN layer. At 35 nm from the sidewall surface, 3 peaks of Si concentration are seen, and correspond to the position of markers in the HAADF mapping (Fig III-19(a)). The relative intensities for the markers reveal that the concentration of Si is significant, but lower than in the SiGaN. Because the EDX spectrum in Fig. 19(c) results from an integration of the signal on the whole width of the rectangle in Fig.19(n), the semi-polar marker is not visible on the spectrum. However, the Z-contrast image in Fig. III-18(a) suggests that the Si concentration is the same for both the semi-polar and non-polar markers. This further emphasizes the difference between the markers and the SiGaN, as the SiGaN has a Si composition significantly higher than the markers (Fig III-12, Fig. III-19). Moreover, the makers do not show antisurfactant properties, proving again that the Si-rich markers and the SiGaN are two materials with different structural and chemical properties.

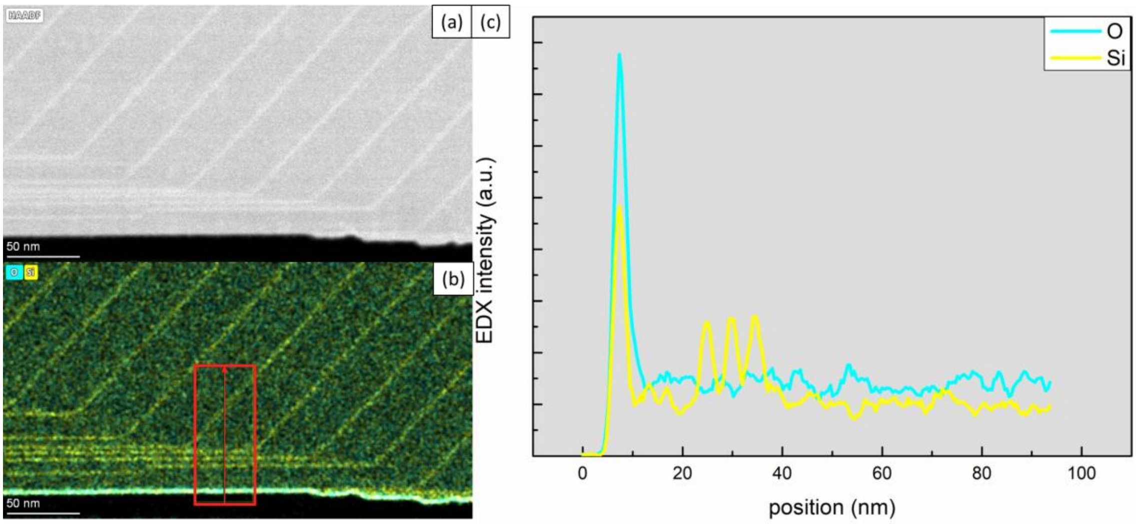

Figure III-19: *(a) HAADF and (b) EDX intensity mapping of a wire of sample B. (c) EDX intensity profile for Si and O taken on the full width of the red rectangle the area seen in (c) (Longitudinal lamella, sample B).*

While the growth of the markers is not related to the one of SiGaN, it holds key information to its formation. Indeed, in the first stages, the markers evidence the occurrence of lateral growth, as showed in Fig. III-17. The EDX profile in Fig. III-19 also reveals that the Si concentration also stays constant in the nanowire, apart from the growth markers.

From these measurements, we conclude that the Si-rich markers and SiGaN layer have different origins. We can thus propose the following successive growth steps: in initial stages, the vertical growth is a result of the growth conditions, such as it is the case in Si-free growth. The *m*-planes of the nuclei are not yet covered by a SiGaN layer, and lateral growth takes place. In this initial stage, the Si accumulates on the sidewalls of the nanowires. This is supported by the absence of a Si concentration gradient in Fig.III-19 (c), which means that during the lateral growth-phase, the accumulated Si stays as an adlayer, and does not get incorporated in the crystal. When a critical surface concentration (corresponding to the concentration of Si in SiGaN) is reached, the adlayers organize into 2ML of SiGaN. At this stage, the lateral growth is stopped by the SiGaN, and the growth proceeds fully vertically. For the rest of growth, the SiGaN is produced in steady state by gradual accumulation of Si adatoms on the GaN sidewalls, and crystallization into SiGaN when enough adatoms are accumulated. From this point on, sidewall growth will stop, and the widening of the nanowire occurs solely through the formation of steps on the sidewalls. This process is described in Fig. III-20.

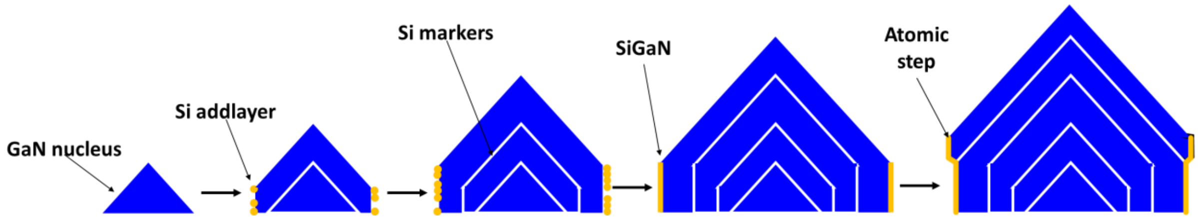

Figure III-20: *Model of crystallization of the SiGaN layer.*

A last interesting point revealed by these markers is that they question the hypothesis of the GaN droplet proposed by Tessarek *et al.*[4]. In this model, Ga does not readily react as an adatom, but rather accumulates as a droplet on the top of the nanowire, that reacts with upcoming nitrogen and silicon. However, if this was the case, the Ga accumulation would be expected to act as a pool and deliver the Gallium in steady state, especially since the Ga variation is small in regard to the value of the partial pressure. In that case, the variation of the partial pressure of TMGa would have little effect on the Ga supply in the solid material, and one would not expect to see such features.

2.2.2 GROWTH RATE

The growth rate, as well as its variations, can reveal the driving force of the growth. In this manuscript it has been pointed out several times that the growth is driven mainly by diffusion. Along the studies supporting this model, some have already carried experiments showing the size of the nanowires as a function of growth time[1,2,26]. In order to do so, the authors of these reports studied the size of the nanowires after different growth times and measured their size with electron microscopy. This method carries the advantage of being simple in terms of characterization, but it also comes at the price of having to grow a sample for each point. In the present case, thanks to the presence of the Si markers, we have access to 216 points over a growth time of 3000 seconds, allowing to get a more precise curve of the growth profile of the nanowire (sample B). In Fig. III-21(a), the height of each marker measured in the center of the nanowire has been plotted relative to the iteration of the marker from bottom to top of the nanowires. Note that the graph is expressed in number of markers (or steps), and not in a unit of time. This graph is compared to a similar study made by Hartmann *et al.*[1], as a similar behavior can be observed.

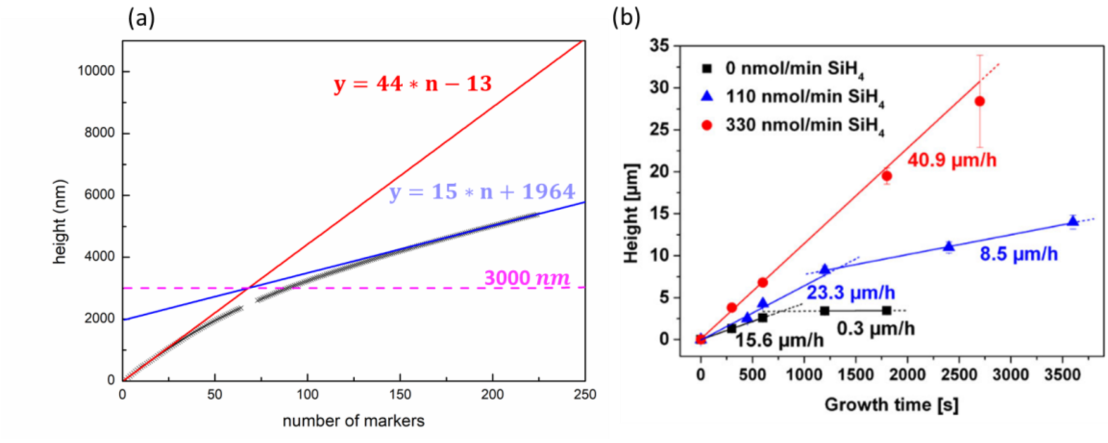

Figure III-21: *(a) Height along the nanowire (sample B) as a function of the number of markers grown, N, measured in this work. The red and blue curves are linear fits of beginning and end of growth. The purple dashed line marks the transition between mask adsorption dominating regime and sidewall adsorption dominating regime. (b) evolution of height and diameter of nanowires reported in ref*[1] *showing a similar trend*

While the curve is not expressed as a function of time, it can be compared to ref [1], in which the authors provide an explanation to this curve and separate it in three stages. These three stages are described in the following paragraphs and schematized in Fig. III-22.

- Stage I: In the first stage of the growth, the main source of atom is the diffusion from adatoms adsorbed on the SiN_x mask (J_{SUB}). This mechanism leads first to a high vertical growth rate due to the large area of the mask in contact with the adatoms.
- Stage II: After some time, the growth process starts being limited by the diffusion length of the adatoms from the mask on the sidewall, λ_{SW}, hence another source of adatoms needs to take over in order for the nanowire to keep growing after having grown higher than diffusion length. This second source of adatom is the adsorption of the adatoms on the sidewalls themselves (J_{SW}). Indeed, while the area of the sidewalls is limited in early stages, it becomes progressively larger as the growth proceed, which means that they adsorb increasingly more atoms.
- Stage III: Once the nanowire has exceeded adatom diffusion length λ_{SW}, the sidewall diffusion J_{SW} becomes the only contribution, and the overall growth rate becomes constant. Indeed, the adatoms collected at the bottom of the sidewalls will progressively be unable to diffuse to the top of the nanowires, and only the adatoms collected within a distance of λ_{SW} from the top.

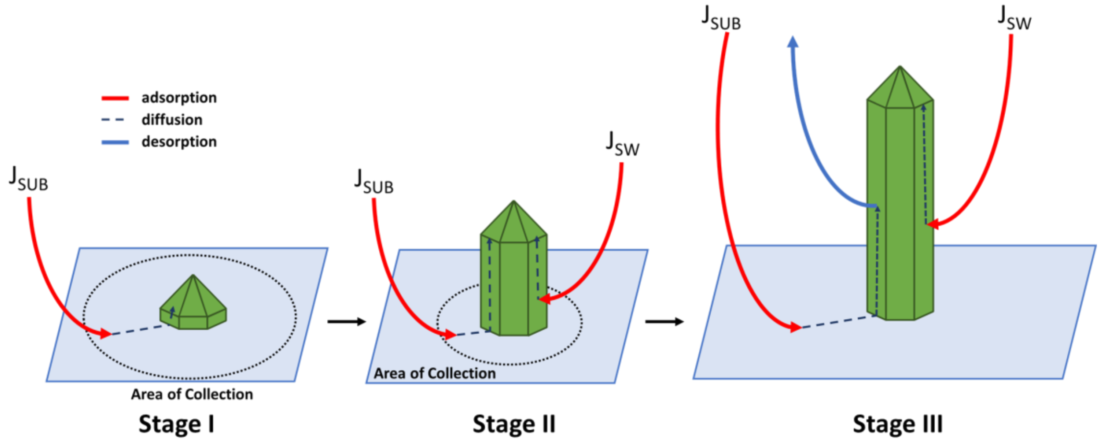

Figure III-22: *Scheme representing the three stages of nanowire growth according to ref*[2].

The data obtained from the markers (Fig. III-21(a)) show a similar trend. However, because of the higher number of data points, some precision can be brought to the overall model. In our experiment, the initial stage of growth follows a linear rate, which is consistent with the presence of a single contribution from the mask J_{SUB}. This linear contribution is fitted by the red curve in Fig. III-21(a), which is estimated to correspond to a growth rate of 12.2 µm/h using the period between each marker. However, contrarily to what is suggested in Fig. III-21(b), the transition between this regime and J_{SW} dominated regime is gradual, and in the case of the studied nanowire, occurs between 1 and 5 µm. This can be explained by the fact that J_{SW} starts contributing as soon as *m*-plane sidewalls are formed and increases continuously as they grow. On the other hand, J_{SUB} decreases continuously as the nanowire grows, until its length exceeds adatom diffusion on the sidewalls, at which point J_{SW} becomes the only significant contribution. In Fig. III-21(a), the growth becomes linear again at this stage, as seen by the fit with the blue curve, corresponding to a 4.1 µm/h growth rate. Following a similar method as used in ref[2], we can estimate λ_{SW} as being equal to the wire's length when J_{SW} becomes dominant, which occurs here at 3 µm. Indeed, while some species are still coming from the mask, J_{SUB} becoming the minor contribution means that the nanowire's length exceeded the mean free path of the adatoms.

This model ignores the presence of a third contribution, which is the contribution from the top semi-polar planes. This approximation however makes sense because it is typically negligible when compared to either J_{SW} or J_{SUB} depending on the growth stage (because of the limited size of the top facets compared to the sidewalls and the mask) and does not dramatically change during the growth, as the area of the top facets only slowly increases. This model does not consider the widening of the nanowire during growth either, which is again negligible considering the nanowire length itself. In both Fig. III-21(a) and Fig. III-21(b), the collection from the mask is higher than the one from the sidewalls, as the growth rate is higher in the J_{SUB} regime than in the J_{SW} regime.

Because the markers allow to have a complete view on the evolution of the geometry of the nanowires, it is possible to know the deposited volume between two markers. This measurement is useful as it allows to understand the variation of incorporated species during the growth. This is especially useful to link the data obtained when studying the length to early stages and build a complete model for nanowire growth. To do so, the following calculations and assumptions are made:

Considering the surface of a marker as the lateral surface of a regular hexagonal pyramid, we can calculate its area A as (Annex D) :

$$A = \cos(\theta) \cdot \frac{\sqrt{3}}{8} \cdot D^2 \ \mathbf{(3.1)}$$

With A the area, θ the angle between the markers and the *c*-plane (which is assumed to be constant), and D the diameter of the core. From here, considering a difference in height dx between one marker and the following along the <0001> direction, we can conclude that:

$$\mathrm{dV} = \mathrm{A} \cdot \mathrm{dx} \propto D^2 \cdot dx \ \ \mathbf{(3.2)}$$

Since dV is proportional to $D^2 \cdot dx$, the constants implied in $\mathbf{(3.1)}$ are going to be ignored in the following paragraphs. To represent dV, Fig. III-23 plots the variation of $D^2 \cdot dx$ as a function of deposited markers:

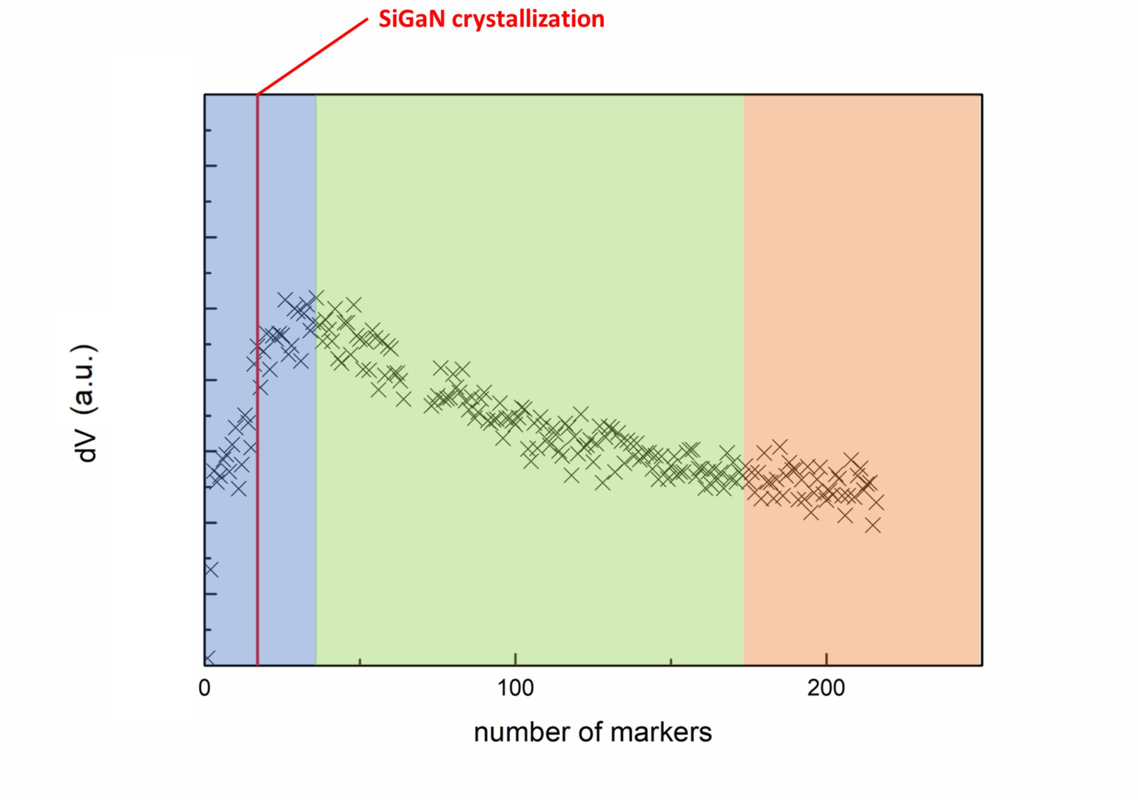

Figure III-23: *Evolution of the volume between two markers as a function of the number of markers (two separate nanowires of sample A). The colors outline the three different regimes described in the last paragraph.*

The growth proceeds as follow: In very initial stages, the growth of the nucleus occurs without SiGaN, which is characterized by both vertical and lateral growth, which is why dV increases strongly in early stages. At the 17th marker, the SiGaN layer crystallizes (Fig. III-17, Fig. III-20), and the dV increase less rapidly, meaning that the SiGaN crystallization is an inflexion point. This can be explained by the almost complete suppression of lateral growth due to antisurfactant effects. Shortly after, dV reaches its maximum, which signifies the beginning of the transition phase toward J_{SW} dominated growth: In Fig. III-18, the maximum in dV corresponds to the point where the height curve (Fig. III-21) starts to move away from the initial linear J_{SUB} regime. Indeed, as the nanowire grows, the area on the mask responsible for the collection of the adatom that will diffuse to the top of the nanowires decreases. Hence, the growth mechanism transitions toward sidewall adsorption driven growth. At one point, dV gets constant, as the nanowire exceeds the diffusion length, and growth occurs only with species adsorbed on the sidewalls within one diffusion length from the top, which corresponds to stage III (region in orange). As explained previously, the growth relies on only one contribution, which is characterized by a constant incorporated volume.

3. CONCLUSION

In this chapter, a complete investigation of the SiGaN layer has been provided. This investigation aimed to discover the chemical composition and crystallographic configuration of the layer. The obtained results suggest that more than a simple antisurfactant layer, this compound is a structured material with unusual properties, such as its self-limiting thickness. Furthermore, the presence of growth markers in the core, presumably caused by a TMGa partial pressure variation, has been used to gain insight on the growth mechanism and evolution, preferential planes of growth, nanowire growth in early stages and driving force behind the growth. While this information proved critical for the precise understanding of the core growth, it also conveys a critical question: while the mask properties of the SiGaN are critical for core growth, what are their impact on shell growt. In the next chapter, this question will be addressed, and additional processes aimed at growing a good quality shell on the nanowire core will be presented.

BIBLIOGRAPHY

1. Hartmann J, Wang X, Schuhmann H, et al. Growth mechanisms of GaN microrods for 3D core-shell LEDs: The influence of silane flow. *Physica Status Solidi (A) Applications and Materials Science*. 2015;212(12):2830-2836. doi:https://doi.org/10.1002/pssa.201532316

2. Wang X, Hartmann J, Mandl M, et al. Growth kinetics and mass transport mechanisms of GaN columns by selective area metal organic vapor phase epitaxy. *J Appl Phys*. 2014;115(16):163104. doi:https://doi.org/10.1063/1.4871782

3. Hersee SD, Sun X, Wang X. The controlled growth of GaN nanowires. *Nano Lett*. 2006;6(8):1808-1811. doi:https://doi.org/10.1021/nl060553t

4. Tessarek C, Heilmann M, Butzen E, et al. The role of si during the growth of gan micro- and nanorods. *Cryst Growth Des*. 2014;14(3):1486-1492. doi:https://doi.org/10.1021/cg500054w

5. Koester R, Hwang JS, Durand C, Le Si Dang D, Eymery J. Self-assembled growth of catalyst-free GaN wires by metal-organic vapour phase epitaxy. *Nanotechnology*. 2010;21(1):015602. doi:10.1088/0957-4484/21/1/015602

6. Tessarek C, Bashouti M, Heilmann M, et al. Controlling morphology and optical properties of self-catalyzed, mask-free GaN rods and nanorods by metal-organic vapor phase epitaxy. *J Appl Phys*. 2013;114(14):144304. doi:https://doi.org/10.1063/1.4824290

7. Haffouz S, Beaumont B, Gibart P. Effect of magnesium and silicon on the lateral overgrowth of GaN patterned substrates by metal organic vapor phase epitaxy. *MRS Internet Journal of Nitride Semiconductor Research*. 1998;3:8. doi:https://doi.org/10.1557/S1092578300000806

8. Eymery J, Salomon D, Chen X, Durand C. Process for catalyst-free selective growth on a semiconductor structure. Published online April 3, 2012.

9. Vennéguès P, Beaumont B, Haffouz S, Vaille M, Gibart P. Influence of in situ sapphire surface preparation and carrier gas on the growth mode of GaN in MOVPE. *J Cryst Growth*. 1998;187(2):167-177. doi:https://doi.org/10.1016/S0022-0248(97)00875-0

10. Schmidt V, Wittemann J V., Gösele U. Growth, thermodynamics, and electrical properties of silicon nanowires. *Chem Rev*. 2010;110(1):361-388. doi:https://doi.org/10.1021/cr900141g

11. Unland J, Onderka B, Davydov A, Schmid-Fetzer R. Thermodynamics and phase stability in the Ga-N system. *J Cryst Growth*. 2003;256(1-2):33-51. doi:https://doi.org/10.1016/S0022-0248(03)01352-6

12. Tessarek C, Rechberger S, Dieker C, Heilmann M, Spiecker E, Christiansen S. Understanding GaN/InGaN core-shell growth towards high quality factor whispering gallery modes from non-polar InGaN quantum wells on GaN rods. *Nanotechnology*. 2017;28(48):485601. doi:10.1088/1361-6528/aa9050

13. Kapoor A, Finot S, Grenier V, et al. Role of Underlayer for Efficient Core-Shell InGaN QWs Grown on m-plane GaN Wire Sidewalls. *ACS Appl Mater Interfaces*. 2020;12(16):19092-19101. doi:https://doi.org/10.1021/acsami.9b19314

14. Markurt T, Lymperakis L, Neugebauer J, et al. Blocking growth by an electrically active subsurface layer: The effect of si as an antisurfactant in the growth of GaN. *Phys Rev Lett*. 2013;110(3):036103. doi:10.1103/PhysRevLett.110.036103

15. Du Boulay D, Ishizawa N, Atake T, Streltsov V, Furuya K, Munakata F. Synchrotron X-ray and ab initio studies of β-Si3N 4. *Acta Crystallogr B*. 2004;60(4):388-405. doi:https://doi.org/10.1107/S010876810401393X

16. Mauri A, Celino M, Castellani N, Erbetta D. Crystalline and liquid Si3N4 characterization by first-principles molecular dynamics simulations. *EPJ Web Conf*. 2011;15:02008. doi:https://doi.org/10.1051/epjconf/20111502008

17. Ren CX, Tang F, Oliver RA, Zhu T. Nanoscopic insights into the effect of silicon on core-shell InGaN/GaN nanorods: Luminescence, composition, and structure. *J Appl Phys*. 2018;123(4):045103. doi:https://doi.org/10.1063/1.5008363

18. Puchtler TJ, Wang T, Ren CX, et al. Ultrafast, Polarized, Single-Photon Emission from m-Plane InGaN Quantum Dots on GaN Nanowires. *Nano Lett*. 2016;16(12):7779-7785. doi:https://doi.org/10.1021/acs.nanolett.6b03980

19. Kapoor A, Guan N, Vallo M, et al. Green Electroluminescence from Radial m-Plane InGaN Quantum Wells Grown on GaN Wire Sidewalls by Metal-Organic Vapor Phase Epitaxy. *ACS Photonics*. 2018;5(11):4330-4337. doi:https://doi.org/10.1021/acsphotonics.8b00520

20. Grenier V, Finot S, Gayral B, et al. Toward Crack-Free Core–Shell GaN/AlGaN Quantum Wells. *Cryst Growth Des*. 2021;21(11):6504-6511. doi:https://doi.org/10.1021/acs.cgd.1c00943

21. Bosch J, Coulon PM, Chenot S, et al. Etching of the SiGaxN yPassivation Layer for Full Emissive Lateral Facet Coverage in InGaN/GaN Core-Shell Nanowires by MOVPE. *Cryst Growth Des*. 2022;22(9):5206-5214. doi:https://doi.org/10.1021/acs.cgd.2c00286

22. Dagher R, Lymperakis L, Delaye V, et al. Al5+αSi5+δN12, a new Nitride compound. *Sci Rep*. 2019;9:15907. doi:https://doi.org/10.1038/s41598-019-52363-7

23. Li SF, Fuendling S, Wang X, et al. Polarity and Its Influence on Growth Mechanism during MOVPE Growth of GaN Sub-micrometer Rods. *Cryst Growth Des*. 2011;11(5):1573-1577. doi:https://doi.org/10.1021/cg101537m

24. Adhikari S, Lysevych M, Jagadish C, Tan HH. Selective Area Growth of GaN Nanowire: Partial Pressures and Temperature as the Key Growth Parameters. *Cryst Growth Des*. 2022;22(9):5345-5353. doi:https://doi.org/10.1021/acs.cgd.2c00453

25. Coulon PM, Alloing B, Brändli V, Lefebvre D, Chenot S, Zúñiga-Pérez J. Selective area growth of Ga-polar GaN nanowire arrays by continuous-flow MOVPE: A systematic study on the effect of growth conditions on the array properties. *Phys Status Solidi B Basic Res*. 2015;252(5):1096-1103. doi:https://doi.org/10.1002/pssb.201451589

26. Eymery J, Chen X, Durand C, Kolb M, Richter G. Self-organized and self-catalyst growth of semiconductor and metal wires by vapour phase epitaxy: GaN rods versus Cu whiskers. *C R Phys*. 2013;14(2-3):221-227. doi:https://doi.org/10.1016/j.crhy.2012.10.009

Chapter 4:

Toward fully emissive core-shell nanowire structures

CONTENTS

In the last chapter we studied the properties of the SiGaN layer, and how it leads to a highly anisotropic vertical growth. Among these properties, the layer was described as a perfect mask, which prevents any lateral growths on the core. While this is a key factor for vertical growth, it also means that the subsequent growth of a shell on the SiGaN is expected to be a challenging process. In this chapter we provide a description of the negative effects of the presence of the SiGaN layer on the growth of core-shell heterostructures, as well as the methods that may be used to solve this issue.

1. SiGaN AND SHELL GROWTH

1.1 EFFECTS OF THE SiGaN LAYER ON THE SHELL GROWTH

In this section we will explain in detail how this layer affects the coverage and properties of the shell active layer. Fig. IV-1 shows STEM-HAADF pictures of sample A studied in Chapter 3, with a low magnification image (Fig. IV-1(a)), which gives an overview of the sample, and a higher magnification image (Fig. IV-1(b)), which shows the core and the shell in the lower part of the sample. In this region, the shell growth on the SiGaN layer is clearly discontinuous. Fig. IV-1(c) shows a transversal slice of the sample taken near the top of the nanowire and features white lines and dark spots that are consistent with structural defects and voids respectively.

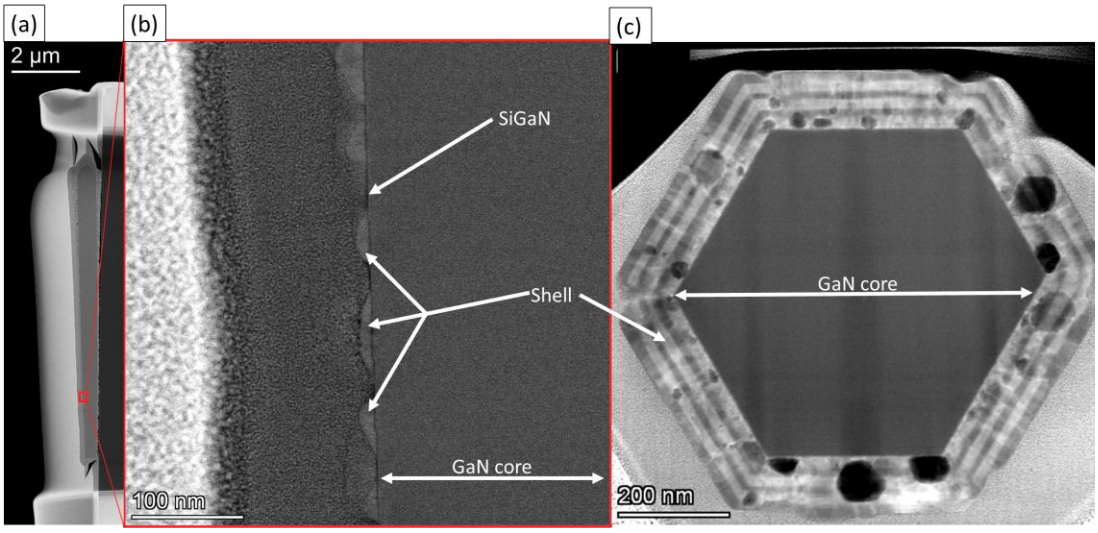

Figure IV-1: *STEM-HAADF pictures of the GaN nanowire (longitudinal lamella) with shell growth at low (a) and (b) high magnification at the bottom of the nanowire, showing the discontinuity of the shell grown on a SiGaN covered core. (c) STEM-HAADF picture of the same sample (transversal lamella) near the top of the nanowire.*

In the previous chapter we have studied the anti-surfactant properties of the SiGaN and concluded that this layer plays the role of a mask. However, this conclusion is incompatible with the growth of a subsequent shell, which has been observed both in this work (previous chapter) and in the literature[1–3]. Several hypotheses can explain the growth of the shell heterostructure on the masked core. The first hypothesis is that the SiGaN layer may vary in thickness and composition from the top to the bottom of the nanowire because of a longer exposition time of the bottom to the growth conditions[1]. This hypothesis supported by Hartman *et al.*[1] is however inconsistent with the results presented in chapter 3, as we observed a constant thickness and no significant composition fluctuation. The second hypothesis could be that the growth of the shell on such layer proceeds from top of the nanowire to bottom. The third possible hypothesis is that the growth of the shell might be possible under thermodynamical conditions unfavorable for adatom desorption. Indeed, in chapter 3, the observation was made that the first layer able to grow on the SiGaN was the InGaN QW, which was explained by the low temperature used for InGaN growth.

Kapoor *et al.*[3] reported the successful growth of a GaN spacer on the SiGaN done at a temperature of 900°C, which is a low temperature for MOCVD GaN. However, the impact of the Si-rich layer on the coverage of the InGaN quantum wells has been reported several times as detrimental [4,5] and even used by some authors to their advantage. For example, Puchtler *et al.*[6] used the local higher In composition variation in the active layer indirectly caused by the SiGaN dielectric layer to create quantum dots. Fig. IV-1 shows the morphology of the shell of sample A presented in chapter 3 at the bottom of the nanowire. Contrarily to the top of the nanowire (Fig. IV-1(c)), the bottom of the shell is very thin and discontinuous, and it is not possible to easily distinguish the InGaN QWs and the GaN spacers.

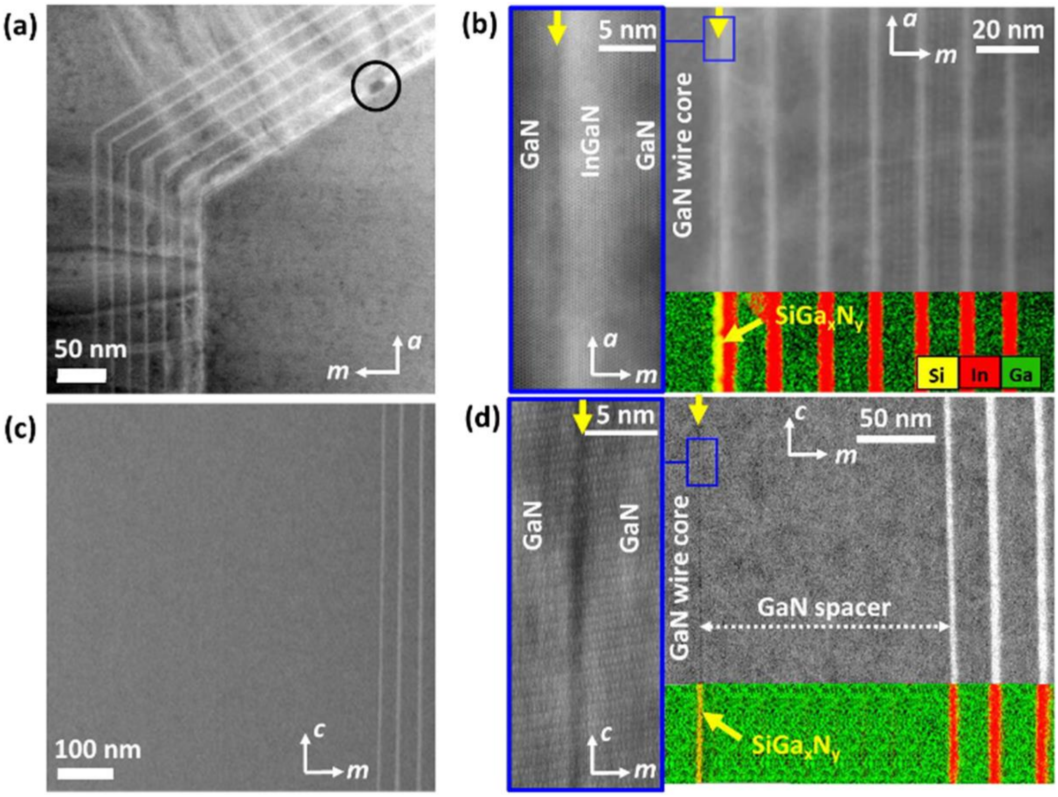

Figure IV-2: *TEM images of an InGaN MQW grown directly on the SiGaN layer (a, b) along the c zone axis, and grown subsequently to a GaN spacer (c, d) along the [10-10] zone axe.*[3]

Another issue caused directly by the presence of the SiGaN between layers is the presence of structural defects in the active layer (Fig. IV-1(c)). Koester *et al.*[7] first described the presence of white threading defects attributed to stacking faults in core-shell structures originating from the junction between the core and the shell which could be due to the presence of the SiGaN layer. The explanation provided by the authors in this study can be related to the strain relaxation of the InGaN layers, like is observed on planar LEDs[8] . This observation was later reported in other studies from the same group[3] (as shown in the Fig. IV-2). However, the growth of a first GaN spacer on the SiGaN before subsequent quantum well growth dramatically reduces the amount of stacking faults in the active layer (Fig. IV-2 (c) and (d)), suggesting that the stacking faults are rather created by the interaction between the InGaN and the SiGaN layer[3]. In some more extreme cases, the impact of the SiGaN layer on the shell is more pronounced: indeed, some reports on the growth of core-shell devices shows a rough and uneven morphology at the bottom of the shell[4,5], which could be caused by the coalescence of large nuclei formed by a small density of nucleation at the bottom of the nanowire. This part of the shell is usually expected to be optically inactive because of a high density of structural defects, or because the inhomogeneities may even keep quantum wells from forming continuous layers. In some other cases, holes in the quantum wells are observed, and they may be observed directly in contact with the SiGaN (Fig. IV-2 (a)), or internally in the shell (dark spots in Fig. III-2 of Chapter III).

Last, the presence of this SiGaN layer is expected to have detrimental effects on the electrical injection. Indeed, although its electronic properties have not been measured, we can suspect that the SiGaN layer has an insulating behavior like SiN_x material. This is particularly an issue in the present case because the SiGaN is located between the n-GaN and the quantum wells. This effect, combined with a limited coverage of active quantum wells, can lead to a higher carrier density in the quantum wells through a reduction of current cross-section, which could be responsible for additional droop in the device, or red shifting of the signal through the heating of the system. It should however be noted that this electrical insulation can also be used in some specific cases. For example, ref [9] describes how a dielectric layer can intentionally be used, for example to isolate the n-GaN core and p-GaN shell layers in the heterostructures.

1.2 EXISTING STRATEGIES

In the last paragraphs we went over some of the issues caused by the SiGaN on the shell intended to become the emitting active region of the nanowire LEDs, which can annihilate some of the theoretical advantages of core-shell nanowires. Indeed, in Chapter I we raised the argument that one of the advantages of the nanowires is an increase of the emissive area as compared to planar devices. This is however not necessarily true if part of the nanowire does not emit light because of the SiGaN formed during core growth. We also pointed out in Chapter II that the growth of high aspect ratio and long nanowires was currently only achievable by MOCVD thanks to this SiGaN. Hence, this layer is beneficial for the growth of the GaN core but detrimental for the subsequent shell growth and, thus, some strategies have already been developed to limit its impact on devices. In the following paragraphs we will talk in more detail about the solutions used to counteract this issue from literature.

1.2.1 NON-INTENTIONNALY DOPED CORE GROWTH

One first strategy is to reduce or stop the Si-flux during the core-growth. According to Kapoor *et al.*[3], the secondary growth phase without silane relies on the residual Si in the reactor, which leads to the deposition of a Ga rich SiGaN layer and allows a vertical growth with limited Si incorporation. In the rest of this manuscript, this method will be referred to as the "doped/non-intentionally-doped" or "n-nid" methods, although the Si concentration in both the n and nid part are estimated to be well above usual doping concentrations in planar GaN heterostructures. However, some drawbacks can still be pointed out.

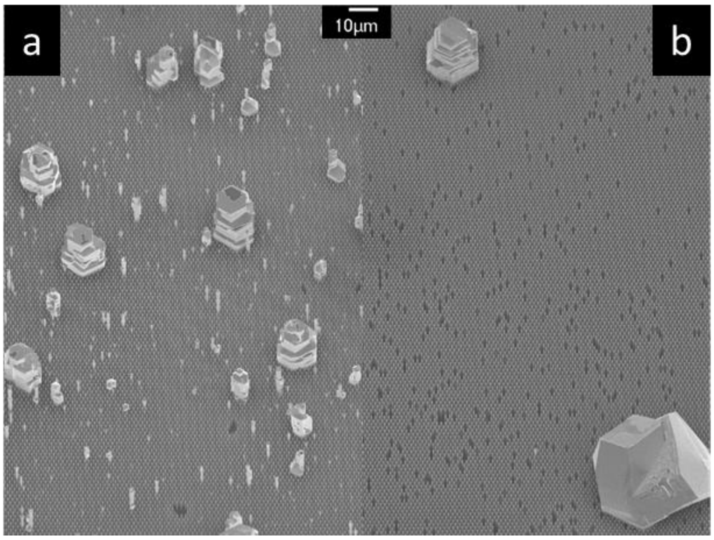

Figure IV-3: *SEM images of 2 samples: core nanowires grown using a 2-steps "doped-undoped" (or n-nid) method(a) and fully doped core nanowire growth (b)*

There are two main drawbacks with this method. First, the doped-undoped (or n-nid) method usually induces a higher density of parasitic particles, that grow uncontrollably to sizes largely exceeding the scale of the nanowires. This parasitic growth is particularly detrimental for SAG nanowires as it disturbs the growth but also the device processing afterward. This is for example visible in Fig. IV-3, where the density of parasitic particles is visibly increased by the use of an n-nid growth method instead of a fully doped method. Another drawback of this method is that there is no published demonstration that this method improves the coverage of the nanowire as compared to a fully-doped nanowire. Tessarek *et al.*[5] noted that the structures obtained with the fully doped nanowires of their work and the partially doped one in the publication of Koester *et al.*[7] are comparable, concluding that this part of the process is unnecessary.

1.2.2 (Al)GaN UNDERLAYER

The second approach used is to bury the SiGaN with another material before initiating the QWs growth. In ref [3], this is done using a GaN layer grown at low temperature (900 °C), which does not introduce any strain in the structure and has a low mismatch with the blue InGaN quantum wells that are presented in the study. However, the growth of GaN on SiGaN is also challenging, and requires specific conditions, such as low temperatures or pressures in this case. It should also be noted that ref [3] does not feature any fully covered nanowire, and any sidewall quantum well, which makes it difficult to really assess the impact of the spacer on the overall coverage.

Another solution could be to use AlGaN instead of GaN[10,11], as Al-containing nitrides are known to be more "sticky" than regular GaN, and hence grow easily even on anti-surfactant surfaces, such as bulk SiN_x. This is due to the low mobility of Al adatoms[12]. However, one should also consider the lattice mismatch between the AlGaN and the GaN, which may introduce strain, or plastic relaxation in the quantum wells. In some cases, cracking has been observed on system including only AlGaN compounds[13,14], and this issue would be worsened using InGaN compounds. Hence, while this solution is an adequate strategy to optimize the coverage of the quantum wells on the nanowire, it may come with a decrease of the overall output due to the presence of non-radiative structural defects in the quantum wells.

1.2.3 ETCHING

One last solution, first suggested by Deeb *et al.*[15] in 2015 consists in etching the SiGaN compound using a wet etching process allowing the shell growth along the whole length of the nanowires. However, this method also has drawbacks. First the sample needs to be taken out of the reactor between core and shell growth, and potentially introduces cracks in the substrate (in the case of nanowires grown on a GaN/Si template) and contaminants on the sample. Second, the etching itself may introduce extrinsic defects in the sample or modify the surface of the nanowire by also etching the GaN. The choice of the method used to etch the SiGaN is thus expected to impact the final properties of nanowires.

2. ETCHING OF THE SiGaN BETWEEN CORE AND SHELL GROWTH FOR FULL LATERAL FACET EMISSIVE COVERAGE

Prior to this work, to our knowledge, no conclusive study had been performed on the impact of the etching of the SiGaN on the subsequent shell growth. Therefore, several methods have been tested in this thesis work, and they will be presented in the next paragraphs.

2.1 METHODS

In this part we aim to study in detail the shell properties through the removal of the SiGaN layer. To draw clear comparison, we choose to work on a single core structure produced in a single MOCVD run on a single wafer, so that the initial core and SiGaN layer are always the same.

The core growth has already been described in the last chapter. Three different processes have been investigated, namely wet, dry, and thermal etching. In wet etching the sample is chemically attacked by a solution, usually a strong acid or a strong base. The second process, dry etching, consist in using a plasma to both physically and chemically etch the surface of the sample. Last, thermal etching relies on the evaporation of the species at high temperature, which can be promoted by adapting the environment inside the MOCVD chamber. We will go into more detail on the chosen processes and on the ways they are expected to interact with the sample. Special attention will be paid to the treatments that are expected to etch the GaN and SiGaN, since it can impact the core material quality.

2.1.1 WET ETCHING

Wet etching consists in placing the sample in a reactive solution and relying on the chemical properties of the sample and the solution. Its main advantages are that it is usually cheap, as it relies on common cleanroom chemicals and do not require complex equipment. Contamination is also an issue with this method, and the cleanliness of the chemicals, the glassware, and the environment of work in general may impact the result. Wet etching can be isotropic or anisotropic depending on the chemicals and considered materials.

In the scope of this work, three different chemicals have been used, namely, a dilute Buffer Oxide Etch (BOE) solution containing diluted HF acid, an H_3PO_4 solution, and a KOH solution. The choice for these solutions has been motivated by different reasons. In the case of BOE, this fluorinated solution is widely used in cleanroom processes for the etching of SiO_x and SiN_x compounds, and therefore seems an appropriate choice in the present case. H_3PO_4[16] and KOH[17] on the other hand have comparable properties, in the sense that they are both able to slowly etch SiN_x compounds but will also etch GaN [18,19]. This may be advantageous as it may further remove surface contaminants, at the risk of degrading the surface or introducing other defects. It should be noted that in the case of N-polar GaN, this etching is expected to be fast and difficult to control, but nonpolar and Ga-polar surfaces are expected to be etched slowly[20]. The conditions at which each etching has been carried are the following:

- **BOE:H_2O – 1:80 %vol, 10 seconds at room temperature**
- **45% KOH, 5 minutes at 75°C**
- **85% H_3PO_4, 10 minutes at 125°C**

One important feature to mention is that the nanowires tend to act as capillaries. This mean that while drying, the top of the nanowires curve under the effect of capillarity and the tip of neighboring nanowires may stick together, as described with resist structures by Tanaka *et al.*[21]. One method that has been found to solve this issue, but that was not yet implemented in this chapter, is to transfer the sample directly from the rinse water beaker to an isopropyl alcohol beaker. By doing so, the water is removed from the substrate, and the low surface tension of isopropyl alcohol weakens the capillary effect.

2.1.2 DRY ETCHING

In dry etching, the sample is attacked by species in a plasma form. This process called reactive ion etching (RIE) can be separated in two mechanisms. The first one is the reactive chemical attack of the material of the sample by the ions from the plasma, which is driven by chemical potentials, and depends hence on the ion nature in the plasma, as well as the sample processed. The second is the physical removing of the atoms by collision with the accelerated ions from the plasma. In this case, the etching is driven by the power transmitted to the plasma and is expected to be more efficient by using heavy atoms in the gas phase. The user may modify both processes, using specific parameters, or gases, but in all cases this process can be made anisotropic.

In this work, the reactor used for dry etching was an Oxford system 100 ECR-RIE apparatus using SF_6 as a gas to form the plasma. The choice of this gas was motivated by the high density of F ions in the SF_6 molecule, which is expected to chemically react with silicon oxides or nitride, in the same way that a BOE or HF solution would. The power of the plasma was kept as low as possible to maintain the plasma, as the ion bombardment can introduce deep levels in the material, which can in some cases compensate the doping and hence significantly impact the device performances. The etching time was also kept low, as the etched layer is thin, and we want to avoid any unnecessary exposition of the sample to the plasma to limit defect implantation. Hence, the parameters used for this process are the following:

- **SF_6, 200 W power, 20 s**

2.1.3 THERMAL ETCHING

The last method of etching, thermal etching, relies on the cohesive properties of the different layers that enable the evaporation of some of the species under specific environmental conditions. The advantage of this method is that, contrarily to the other presented processes, it can be performed *in-situ* in the MOCVD reactor during the growth. This can typically be done by annealing the sample at high temperatures, without NH_3 and may be assisted with the presence of a reactive gas, such as H_2. However, this limits the options of etching gases to the ones available for MOCVD growth. The selectivity of the process is limited, as we expect the GaN to be etched under these conditions, as we have already mentioned that at high enough temperature GaN evaporates in the absence of NH_3.

In the scope of this work, thermal etching was carried out in the same reactor than the one used for growth. However, in order to be able to compare with the samples etched using other methods, it was chosen to proceed in the following way: to the sample was taken out of the reactor at the end of the core growth, as the other samples, and subsequently reintroduced in the reactor for separately do the thermal etching before shell growth. The thermal etching was carried out in the following conditions:

- **H_2 flow of 8 slm, pressure 75 Torr, setpoint 1175 °C for 15 s**

2.1.4 SHELL GROWTH

Once the GaN cores were etched by the different methods presented above, all the samples were reintroduced into the growth reactor and different shells were grown thereon. Three different structures have been tested: One containing an InGaN single quantum well (SQW), one containing an InGaN underlayer (UL) and a SQW (named SQW+UL) and, finally, a sample with three quantum wells, referred to as MQW (multiple QWs). In all cases, the shell growth started by the growth of a GaN spacer at a setpoint temperature of 1175°C and 100 Torr pressure for 100 seconds. This step helps to bury the surface defects on the samples. The gas mix consisted in 0.13 mol.min^{-1}, 55 µmol.min^{-1} of NH_3 and TMGa respectively. The quantum wells have been grown at 850°C for 360 seconds, using TMGa and TMIn fluxes of 58 and 32 µmol.min^{-1} respectively, using N_2 alone as the carrier gas, and keeping the other parameters similar to the spacer growth. The quantum wells were systematically capped by raising the temperature to a setpoint of 1060°C and stopping TMIn introduction. Last, on the sample with the InGaN underlayer, this was grown at 880°C under a TMIn flux of 18 µmol.min^{-1}, while keeping other parameters similar to QW conditions. Note that the shell does not contain a p-GaN layer, as the object of this work is to investigate by cathodoluminescence the optical properties of the shells and their modifications induced by the prior core+SiGaN etching. The 3 shell structures are depicted in the Fig. IV-7.

2.2 SEM AND CATHODOLUMINESCENCE MEASUREMENTS

In the last paragraphs the conditions used for the etching of the SiGaN layers as well as for the shell growth were explained. In the next paragraphs we will observe the effects of the etching on the subsequent quantum well (QW) growth thanks to structural and optical characterization.

2.2.1 SINGLE QUANTUM WELL AND FIRSTHAND RESULTS

To assess the impact of each treatment, we have chosen samples with a thin shell and only one QW, where the impact should be stronger than in the case of a multi QWs structure, where potentially only the first QW could be affected.

First, the samples were observed by SEM after each treatment prior to shell growth, and after shell growth to see the impact on the nanowire morphology. The SEM images are presented in Fig. IV-4.

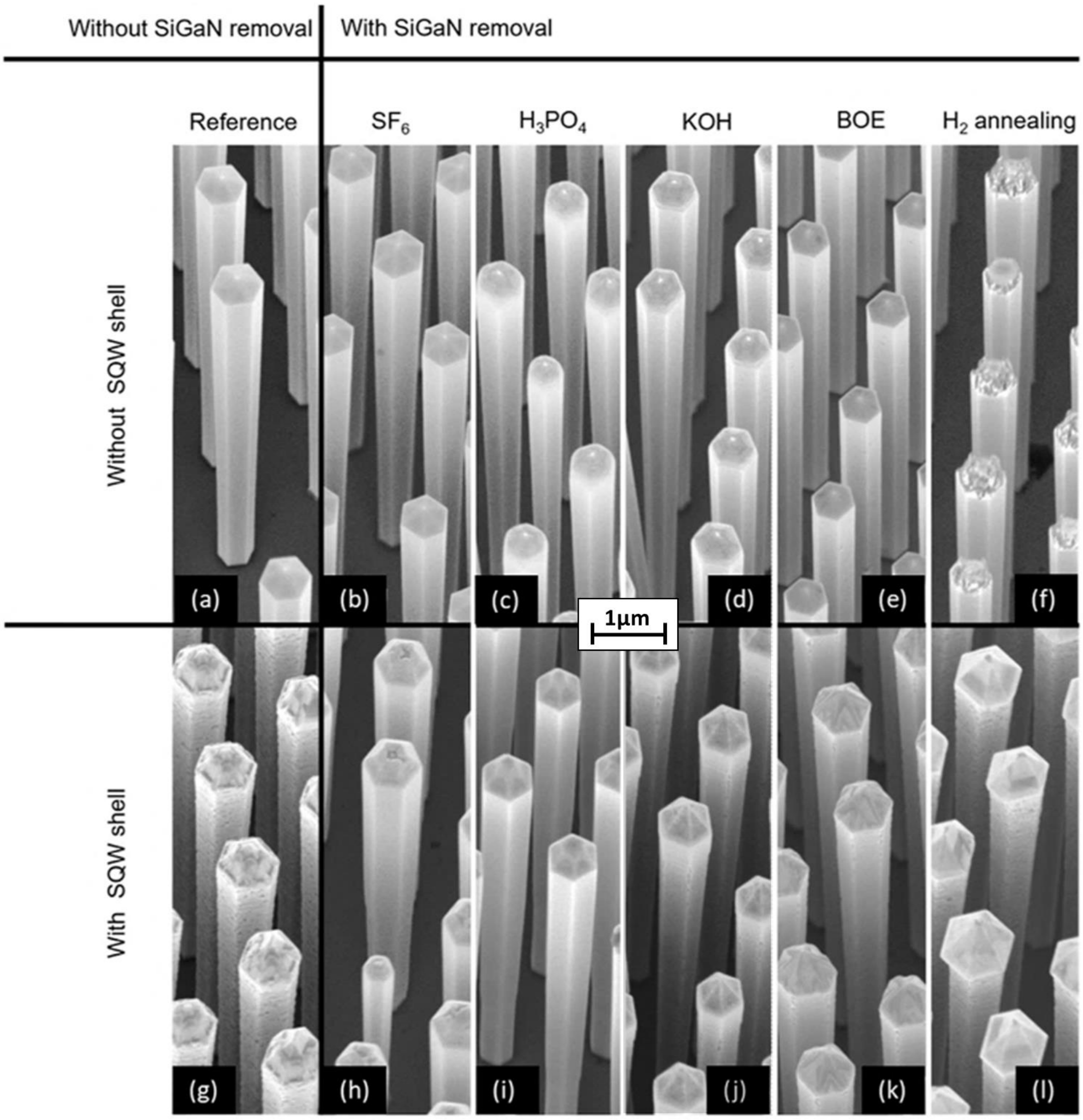

Figure IV-4: *Tilted (25°) SEM images of the samples after treatment (a-f) and after shell growth (g-h). (from ref* [22]*).*

By looking first at the images taken after treatment, two trends can be noticed. First, Fig. IV-4 (a) (reference sample), (b) and (e) show very similar morphologies. This is not surprising, as the treatments used in Fig. IV-4 (b) and (e), namely SF_6 dry etching and BOE wet etching, are not expected to have any impact on the GaN itself. The nanowires treated by BOE appear thinner than the reference, which has been attributed to inhomogeneities of the initial core diameter prior to etching. On the other hand, the samples in Fig. IV-4 (c), (d) and (f) all show evidence of etching of the GaN core itself. In the case of the H_3PO_4, it can be witnessed by a smoothing of the junctions between the lateral non-polar facets and the top semi-polar facet, particularly at the top of the samples. This behavior is consistent with the literature, as it has been reported that the etching of GaN occurred preferentially on the semipolar planes of GaN rather than non-polar[20]. In the case of the thermal etching, the behavior suggests an etching of the structure from the top. Zooming on the sample revealed that the core of the sample seemed to be etched preferentially, leaving a layer on the sidewalls (Fig. IV-5). This could be an indicator that under these conditions, thermal etching preferentially attacks the GaN over the SiGaN (even if the visible layer on the picture cannot be only SiGaN, as it was previously shown that it is 2ML thick and hence cannot be resolved with a SEM). This method is therefore not appropriate.

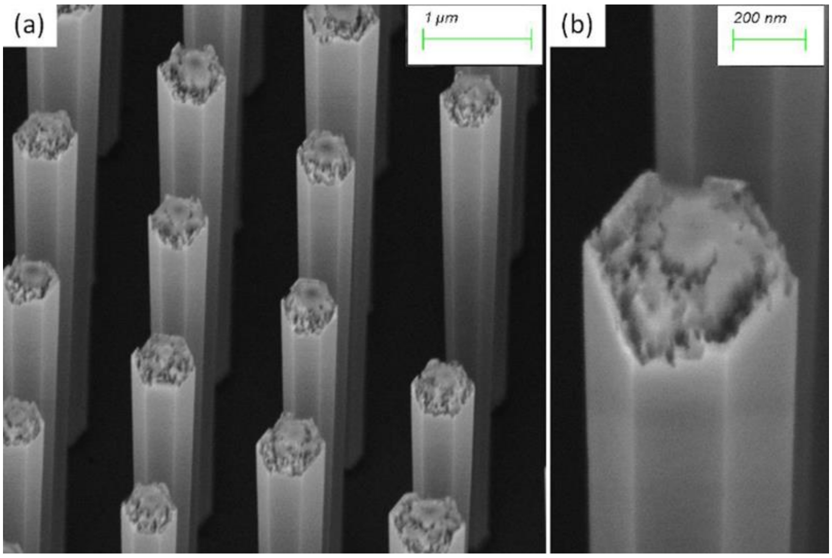

Figure IV-5: *SEM images of GaN doped core structure after H_2 thermal annealing at* low *magnification (a) and* high *magnification (b) (from ref* [22]*).*

The observation of the samples after shell growth (Fig. IV-4 (g-l)) by SEM gives already some indications about the effective etching of the SiGaN layer. As expected, the growth on the reference sample leads to rough sidewalls after the shell growth related to the presence of SiGaN layer. Fig. IV-4 (f and l) shows that the H_2 treatment does not impact the sidewalls (as evidenced by the rough sidewalls after shell growth in Fig. IV-4 (l), which are associated to the nucleation on the SiGaN layer), however the top surface is etched away. The subsequent shell growth leads to the nucleation of pyramidal structures at the top of the nanowire. Likewise, Fig. IV-4 (j) and (k) show that both KOH and BOE feature some roughness on the sidewalls after shell growth, even if it is less evident than on the reference, suggesting that these treatments failed at fully etching the SiGaN. Interestingly, the KOH also features a match head shape structure at the top of the nanowire, which itself seems to be smooth. Last, both the H_3PO_4 and the SF_6 (Fig. IV-4 (h) and (i)) feature smooth sidewalls from top to bottom, suggesting that the treatment has been successful in allowing the growth of a high-quality shell.

In order to confirm these results, cathodoluminescence has been performed on these samples. Using hyperspectral mapping, one can track the intensity as well as the exact emission wavelength for each contribution. Measurements have been performed at 5kV, with a probe current of 5.4nA, and are presented in Fig. IV-6.

Looking at the spectrum for each sample it is possible to see 4 major contributions, marked by a black line on the graph. The first one is the GaN band edge, located around 360 nm. Second, one can notice two peaks, located around 400 and 450 nm, which we attribute to QW emission from different planes (see later). Last, the peak near 550 nm is expected to correspond to the yellow band in GaN. The main observations are first that the signal at 400nm is only present for the H3PO4, SF6 and KOH samples. Second, all samples including the reference one exhibit a signal at 450nm. Third, the signal is very weak and broad from the BOE and H2 treated samples, respectively.

Fig. IV-6 (b-d) allows to get a better idea of the emission location for both the 400 and 450 nm QWs in all samples. It appears that the signal at 400nm corresponds to non-polar QWs, while the 450nm peak corresponds to the QW on the semi polar plane. The only samples that achieved sidewall emission are the SF_6 treated, the H_3PO_4 treated, and the KOH treated samples. Both the BOE treated, and the reference sample do not show the peak at 400nm, which is a clear indication that they have no significant sidewall emission. While this result is surprising in regard to the usual ability of BOE to etch silicon nitride, it can be explained by the fact that the layer is a SiGaN compound and can therefore have different properties from simple SiN_x. The H_2 treated sample shows a significant signal intensity at 400 nm, which is caused by an overlap between its GaN band edge peak at 360 nm and semipolar plane QW peaks at 450 nm

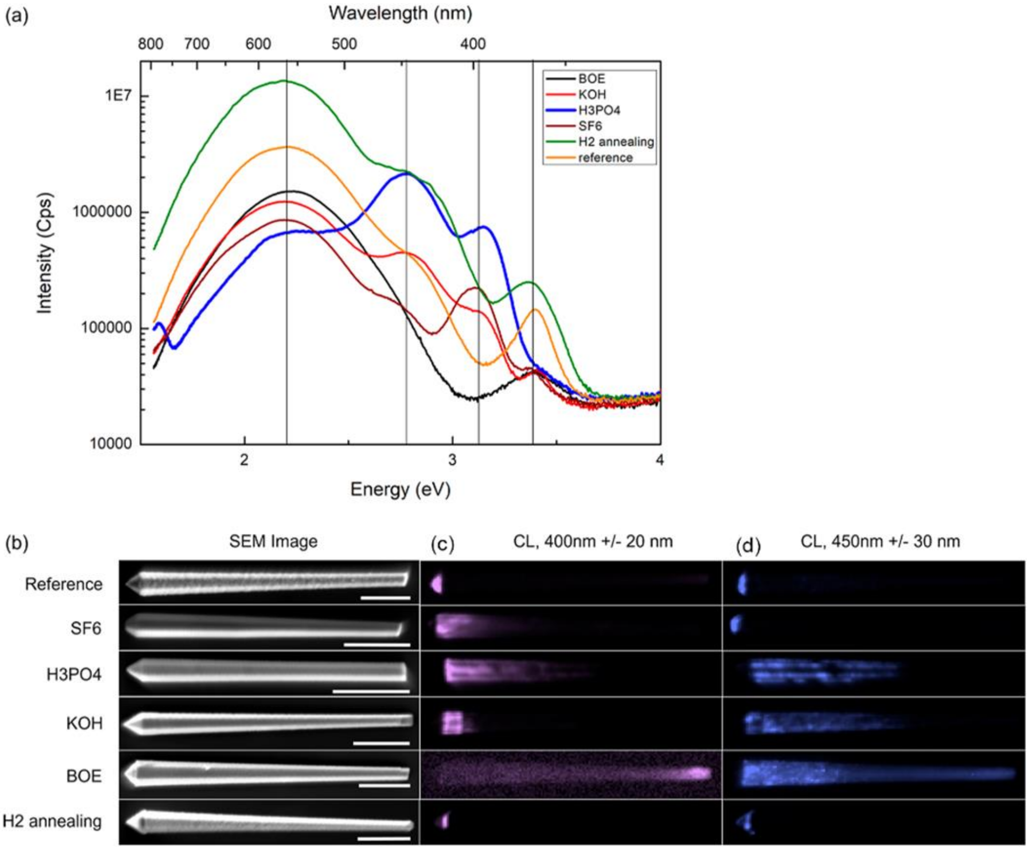

Figure IV-6: *CL spectrum integrated on a whole nanowire for each sample (a). SEM image of a single nanowire for each sample (b), and corresponding CL emission at 400 nm (c) and 450 nm (d). (from ref*[22]*).*

If we look in more detail at the emission signal from the SF_6, H_3PO_4 and KOH samples we see that it is found at different locations within the nanowire. First, in the case of the KOH etching, the emission at 400 nm is only located at the top of the nanowire, corresponding to the smooth area identified in Fig. IV-4. This indicates partial etching of the SiGaN, allowing growth only on the top part of the nanowire. The rest of the sample seems to emit inhomogeneously at 450 nm from its sidewall, but it is unclear if this inhomogeneity is due to alloy variation, deep defects introduced by the KOH, or other factors. In the case of SF_6, the 400 nm signal intensity is stronger at the top of the nanowire, and gradually decreases when descending along the nanowire, while the 450 nm signal is only emitted from semi-polar planes on top of the nanowires. Last, the H_3PO_4 sample features a strong 400 nm signal, which, compared to the other samples, is the one that extends the furthest down the nanowire. The signal seems weaker close to the junction between m-planes facets, which is also where a 450 nm signal can be noticed. This effect has already been reported[23,24] and can be caused by the presence of nanometric *a*-planes at the junction between neighboring *m*-plane surfaces with a higher In incorporation.

In the light of these results, it appears that the only methods that can reliably etch SiGaN on the sidewalls to achieve an extended shell coverage are the wet etching in H_3PO_4 and dry etching with SF_6. These two treatments were therefore chosen to study their impact on core-shell heterostructures including an InGaN underlayer and multiple InGaN QWs.

2.2.2 NON-RADIATIVE CENTERS: UNDERLAYER AND MULTI QUANTUM WELL SAMPLE IN THE LITTERATURE

The underlayer (UL) effect has already been mentioned in Chapter I, part 2. It consists in the growth of a low In content InGaN layer prior to QW growth to trap non-radiative defects, suspected to be nitrogen vacancy V_N defects formed at high temperature, and hence keeping them from diffusing into the active layer. However, while its strong impact has been proven in the case of planar *c*-plane devices[25], there is to our knowledge no demonstration of this effect in the case of nanowires. More than that, Kapoor *et al.*[3] compared the emission of nanowires without UL, with a GaN UL and with an InGaN UL. They concluded that while the presence of an underlayer had a positive impact on the luminescence, no significant difference was noticed between the GaN and the InGaN underlayer. These results suggest that the underlayer is not critical in the case of *m*-plane nanowires, unlike *c*-plane devices.

There are two possible reasons that could explain this phenomenon: First, it is possible that the V_N defects do not diffuse toward *m*-plane GaN surafaces, as they do in *c*-plane GaN. In this case, there is no need to grow an underlayer, as the defects are not concentrated on the surface.

The other explanation could be that defects are generated in the core but are not able to diffuse through the SiGaN layer into the active shell. Indeed, Haller *et al.*[25] proved that these defects were mainly generated during high temperature growth, higher than 900°C. In nanowires, the highest temperature of growth is reached during core growth, while the rest of the growth is carried (except the capping) at temperatures around 900°C or less. Note that the temperature provided at the beginning of 2.1 and 2.2 are setpoint temperatures, and that the real temperature in the reactor is expected to be lower by about 150 °C. Therefore, if the growth does indeed produce point defects, we expect them to be mainly produced during core growth. In this case, does the SiGaN layer stop the diffusion of the defects into the shell? It would mean that removing the SiGaN would allow non-radiative defects to diffuse toward the QWs during shell growth, and that the use of an underlayer is also required for nanowires.

2.2.2.1 EXPERIMENTS

To test this hypothesis, we proceeded to two additional growth runs on SF_6 and H_3PO_4 treated samples. In the first run, a shell consisting of an underlayer and a SQW was grown, while in the second, the shell consisted of an array of three QWs. For simplicity, the samples will be referred to SQW, SQW+UL and MQW for the single QW, single QW with InGaN underlayer, and multiple QWs array samples, respectively. Indeed, according to Armstrong *et al.*[26] the first QWs of the array are expected to bury the non-radiative defects and have a similar effect to the underlayer. Hence, comparing a MQW sample with an SQW+UL sample could provide key information about the mechanisms at play. After growth, the nanowires were subsequently detached and deposited on a Si-substrate and observed by cathodoluminescence.

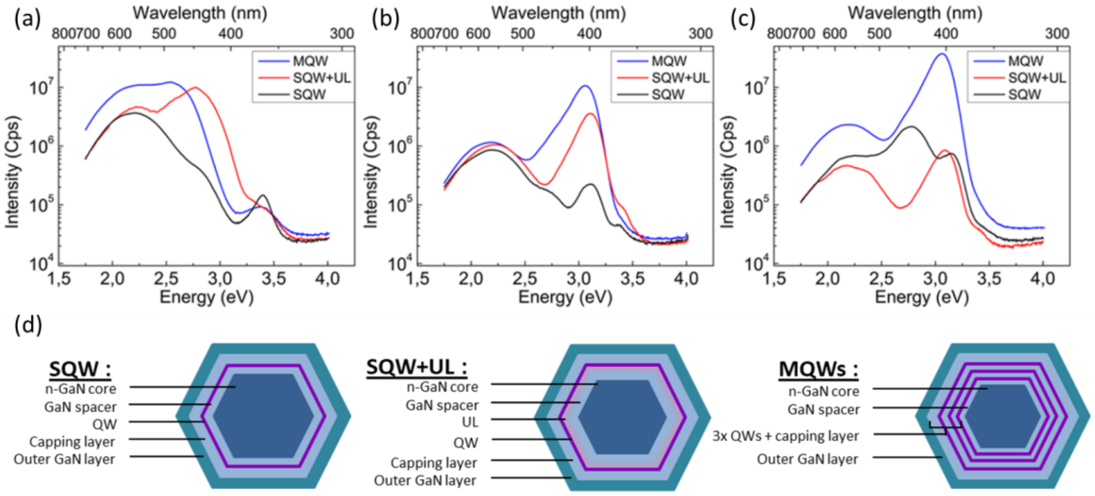

Figure IV-7: *Comparison of the CL spectrum integrated on a full nanowire with an SQW, SQW+UL and MQW shell, without etching (a), after* SF_6 *treatment (b) and after* H_3PO_4 *treatment (c). Sketches of the corresponding SQW, SQW+UL and MQW structures (d) (from ref*[22]*).*

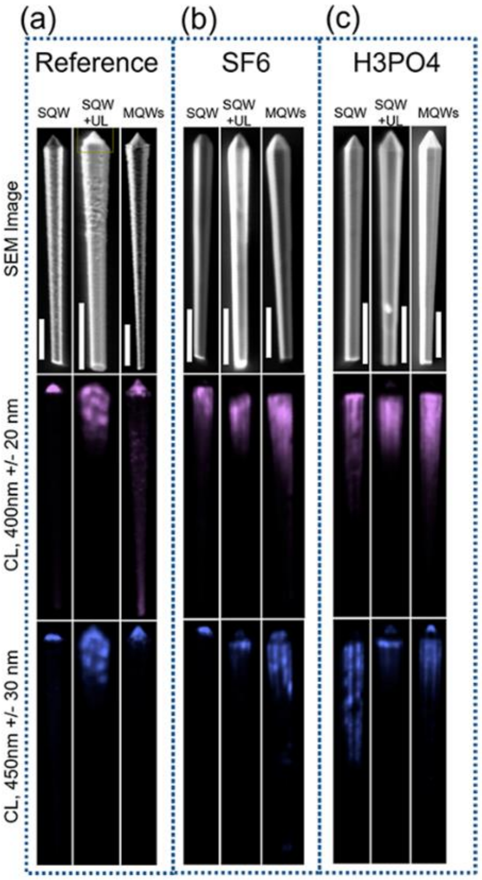

Figure IV-8: *SEM images and CL maps at 400 and 450 nm for the reference sample (a), the* SF_6*-treated one, (b) and the* H_3PO_4*-treated one (c) for SQW, SQW+UL and MQWs structures. The scale bars correspond to 2 µm. (from ref*[22]*).*

The spectra measured on whole nanowires are presented in Fig. IV-7 (a-c), and corresponding mappings are presented in Fig. IV-8 (a-c). In this study, the spectrum and the mapping must be considered jointly, as both the relative intensities and their localization will be used to assess the effectiveness of the treatments. The structures corresponding to SQW, SQW+UL and MQWs are presented in Fig. IV-7 (d). Last, the conditions used to measure the spectra presented in Fig. IV-8 were kept similar for all measurements in order to ensure the possibility of doing quantitative comparisons on the samples.

In the case of the untreated samples (Fig. IV-7 (a) and Fig. IV-8(a)), only the sample containing an UL features a significant sidewall emission. However, this signal is broad. Moreover, Fig. IV-8(a) shows that the emission is inhomogeneous in intensity and is concentrated on the top part of the nanowire sidewalls. Moreover, a close look on the CL mapping of the sample with UL (Fig. IV-9) shows quantum dot-like structures with some similarities with the ones reported by Puchtler *et al.*[6]. The absence of any sidewall emissions for both the SQW and MQW samples confirms yet again that growing shell structures directly on a fully doped core will have a negative impact on the optical properties, as only one of the untreated sample features sidewall emission, and it is inhomogeneous.

In the case of the SF_6 samples (Fig. IV-8(b)), an improvement of one order of magnitude of the intensity signal can be noted using the underlayer, compared to the SQW sample. The MQW sample signal features an additional threefold increase when compared to the SQW+UL sample. The CL mapping (Fig. IV-8(b)) confirms that this emission is related to the sidewall QWs.

Last in the case of the H_3PO_4 treated samples (Fig IV-7(c)), no significant change can be noted on the 400 nm sidewall quantum signal by the addition of the underlayer. However, the MQW sample shows a one order of magnitude increase compared to the other structures. Moreover, the signal coming from the H_3PO_4 treated SQW and MQW samples have a sidewall QW signal 4 times more intense that of the corresponding SF_6 samples. Last, the corresponding mapping (Fig. IV-8(c)) shows that all samples feature some sidewall emission.

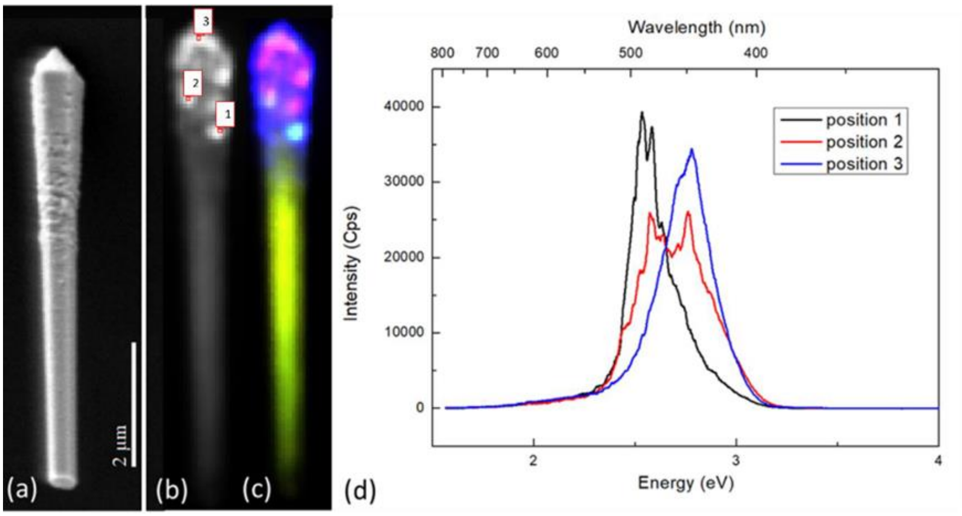

Figure IV-9: *(a) SEM image, (b) 300 K panchromatic CL map and (c) corresponding reconstituted color mapping of a reference SQW+UL nanowire. (d) spectra corresponding to the positions in (b)(from ref*[22]*).*

2.2.2.2 DISCUSSION

The proposed explanation to this different behavior of the UL is based on the impact of the treatment on the whole structure and is shown in Fig. IV-10.

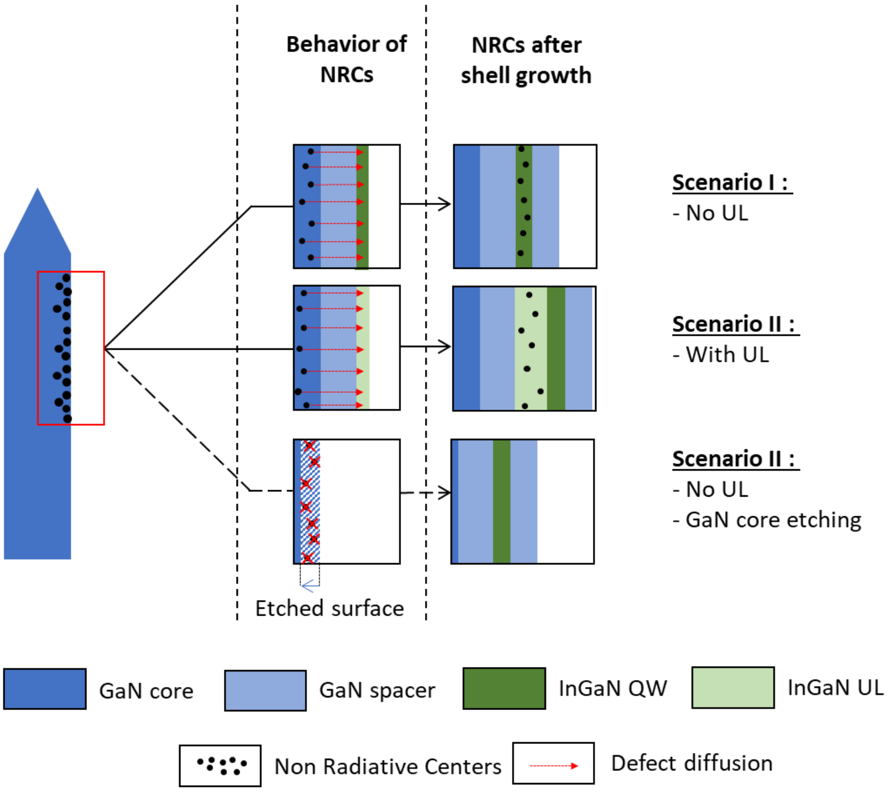

Figure IV-10: *Three possible scenarios when growing a shell on unpassivated core: (1) in the absence of any countermeasure, the defects diffuse toward the QWs, (2) In the presence of the UL, the defects are trapped before reaching the QWs, (3) the defects may however be kept from reaching the QW layer by being removed when etching the close surface of GaN.*

Indeed, in the SF_6 case, the SiGaN layer is expected to be removed, but there is no evidence of any effect of the treatment on the underlying GaN. Hence, as hypothesized, the non-radiative defects contained in the core are free to diffuse in the QWs, where they will degrade the intensity of the signal (scenario 1 of Fig. IV-10). SiGaN layer behaves thus as a barrier for the V_N diffusion. However, an underlayer on the sample allows a burial of the defects, which results in an increase of the intensity of the QW signal (scenario 2 of Fig. IV-10). Using several QWs will have the same effect, but the presence of additional QWs leads to a more intense output. However, in the case of the H_3PO_4 sample, an etching of the surface of the GaN has been observed in Fig. IV-4 (c), which is expected by the literature[18]. We also know that the V_N defects responsible for the UL effects are supposed to be located at the close surface of the sample. Hence, one possibility is that the chemical treatment led to their removal through the etching of the defective GaN (scenario 3 of Fig. IV-10). In this case, the presence of an underlayer would not lead to any significant change on the intensity of the 400 nm sidewall emission. The presence of additional QWs would then lead to a significant increase of the intensity of the signal, as all QWs would be mostly free of non-radiative defects. It should be noted that this mechanism has already been proposed by Han *et al.*[27], who observed an increase in IQE when etching the surface of a high temperature grown *c*-plane n-GaN, and subsequently growing a low temperature InGaN/GaN 5 period array and Mg-doped p-GaN.

2.2.3 EFFECT OF THE ETCHING ON THE INGAN SURFACE COVERAGE

The initial goal of this study was to investigate the effect of the etching of the SiGaN layer, and its possible use for the growth of fully luminescent nanowires by increasing the area of the shell coverage. However, up until this point, the methods used allowed to compare the relative emission from one sample to another, but not the variation of the signal on a single nanowire. Using CL hyperspectral mappings, it is possible to quantitatively track the signal at different heights of the nanowire. Hence, the SF_6 MQWs and H_3PO_4 MQWs have been studied alongside a vertical n-nid structure (as defined in 1.2.1) with 5 QWs. The reason why a n-nid structure was chosen instead of a fully doped structure is because mappings of the fully doped reference evidenced very little sidewall emission.. The different spectra at the top, middle and bottom of each sample are presented in Fig. IV-11. The CL parameters (such as acceleration voltage and beam current) used for the characterization of the n-nid structure differ from the ones used for the two other samples, as well as the number of QWs. Hence, while it allows to assess the gradual decrease of the quantum well signal, the relative intensities between samples are not comparable.

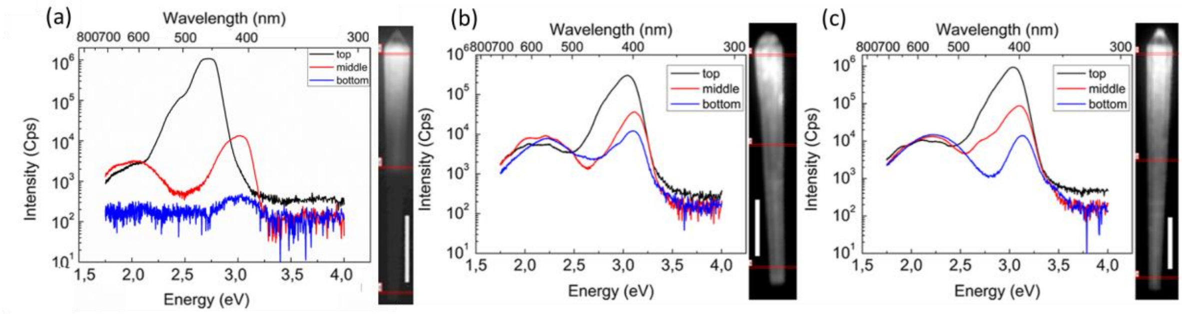

Figure IV-11: *Evolution of the spectrum between the top, middle and bottom of the nanowire for a n-nid structure with 5 QWs (a), SF_6 MQWs (b) and H_3PO_4 MQWs (c). The insets are panchromatic images for each nanowire.*

Fig. IV-11 (a) shows the typical behavior emission of a shell grown on a n-nid structure. At the top of the nanowire, the signal is intense, but starts decreasing and blue shifting when descending along the nanowire, until the middle of the nanowire is reached. It then sharply decreases and becomes almost undistinguishable from the noise. This sharp transition can be seen on the panchromatic image in the inset of Fig. IV-11 (a). It is often visible on SEM images (Fig. IV-12), as the thickness of the nanowire also decreases, corresponding to the interruption of the shell near the middle of the nanowire. However, in the case of both SF_6 MQW and H_3PO_4 MQW samples, this behavior is mostly absent. Indeed, the intensity of the signal of the nanowire decreases when going down along the nanowire in both samples but stays significant even at the foot of the nanowire, with an intensity comparable to the Yellow Band at this height, despite a drop of two orders of magnitude. Last, the yellow band stays at the same intensity on the whole nanowire. In Fig. IV-11 (a), the signal at the bottom of the nanowire does not show any significant luminescence, which suggests a high structural defect density of the material.

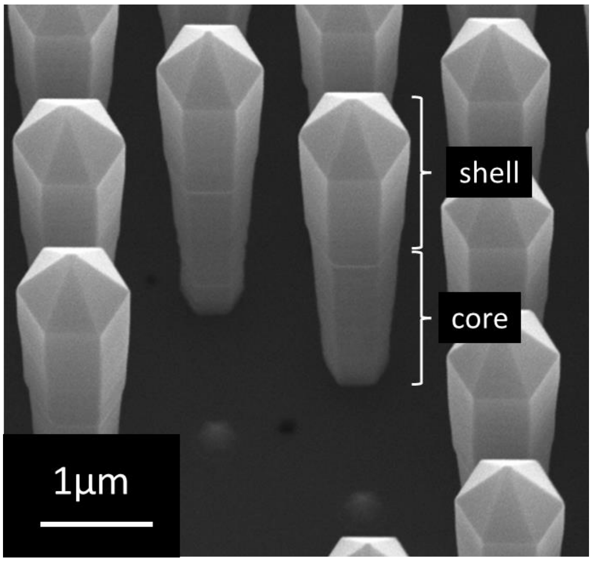

Figure IV-12: *SEM picture of a doped/undoped sample with a visible junction between core and shell*

In this paragraph we have demonstrated that it was possible to reach a full coverage of the nanowire by the shell using a treatment between core and shell growth. While both the SF_6 dry etching and H_3PO_4 etched samples have shown an improvement compared to the more commonly used n-nid method, the stronger intensity and potential removal of the defects provided by the H_3PO_4 made it the method of choice for this application. This method has hence been implemented on the growth in the rest of this study. However, no direct proof of the complete removal of the SiGaN layer has been provided. In order to do so, further work in transmission electron microscopy was required.

2.2.4 PROOF OF SIGAN REMOVAL BY TEM CHARACTERIZATION

In order to check the etching of the SiGaN, TEM lamellas of the untreated reference MQW and H_3PO_4-treated samples have been prepared. Fig. IV-13 presents an HAADF picture along the <0001> zone axis, at low and high magnification, at 2/3 of the height of the nanowires for the both samples.

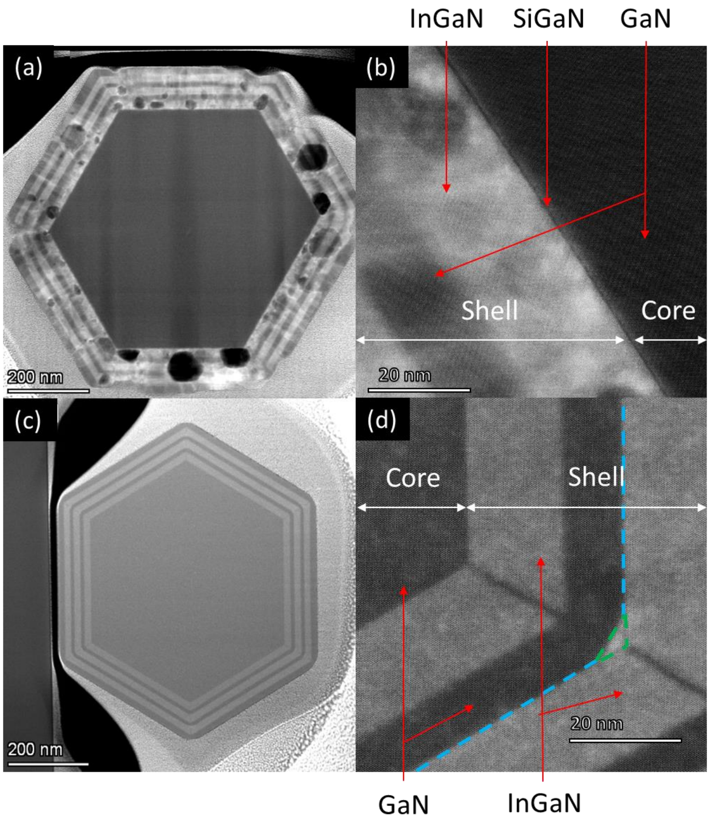

Figure IV-13: *HAADF-STEM images of the untreated (a)(b) and H_3PO_4 treated samples (c)(d) (low and high magnification respectively)*

We first look at the images taken on the untreated sample (Fig. IV-13 (a,b)). The InGaN QWs are clearly visible, which indicates that the absence of CL emission can be attributed to a high density of non-radiative extended defects, visible as white threading lines and attributed to prismatic stacking faults [7] as mentioned in 1.1.1. Voids are present too. It should be noted that while in the literature it was reported that the voids would originate at the junction between the core and the shell[3], some can clearly be seen in the middle of the shell structure, and one could argue that the roughness observed on the surface of the sample in Fig. IV-4 (g) is due to unclosed voids created in the shell. Last, the thin line which can be seen in Fig. IV-13 (b) between the core and the shell can be attributed to the presence of the SiGaN layer. On the other hand, the samples treated using H_3PO_4 do not exhibit any defect and show an excellent crystalline quality. Furthermore, Fig. IV-13 (d) lacks the dark line present on the reference samples, identified as the SiGaN layer but presents some "In rich" triangles (as can be seen by the chemical contrast on the HAADF image) on small *a*-planes at the junction between consecutive *m*-planes, which have already been reported in the literature[23,24]. Hence it can be concluded that there is a clear improvement of structural properties associated with the H_3PO_4 treatment of the core.

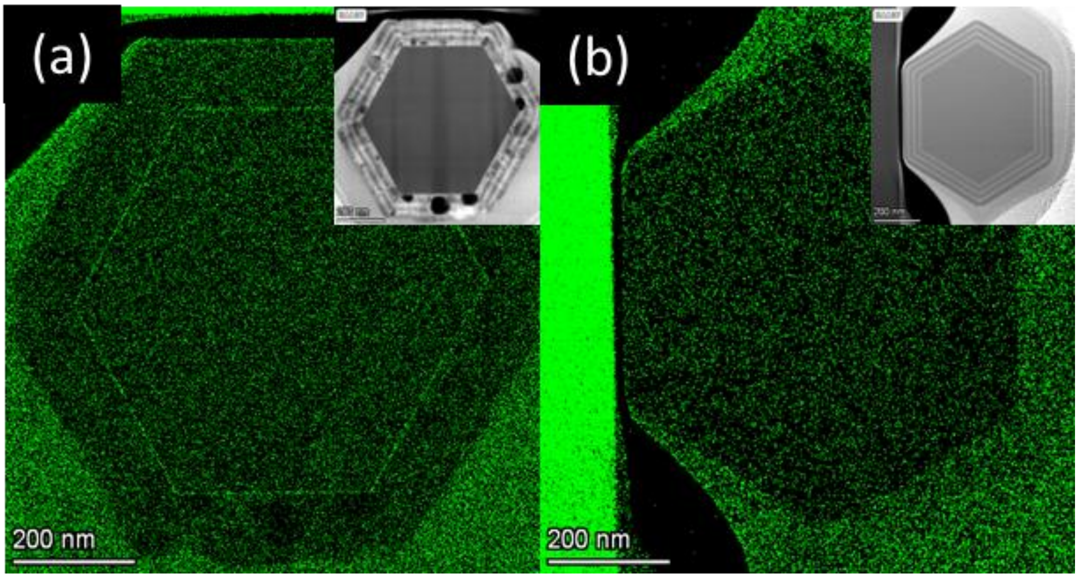

Figure III-14: *EDX mapping for the element Si for the untreated (a) and H_3PO_4 treated samples (inset: corresponding HAADF-STEM picture)*

Subsequently, EDX of Si was performed to assess the state of the SiGaN layer due to this treatment. In Fig. IV-14 (a), a signal indicating the presence of silicon is revealed at the junction between the core and the shell of the nanowire, indicating the presence of a continuous SiGaN 2ML-thick layer all around the nanowire core. However, this signal is absent from the mapping realized on the H_3PO_4 sample (Fig. IV-14(b)). This result clearly demonstrates that the SiGaN layer has been removed by the H_3PO_4 of the n-GaN core, proving that this process is the main cause of the improvement in shell coverage and defect removal in the shell.

3. CONCLUSION

In this chapter the detrimental impact of the SiGaN layer on the quality of the shell was evidenced. To optimize the quality of the shell the core was processed in order to remove the SiGaN, and hence to obtain a luminescent shell on the sidewalls of the nanowire, without any issue in coverage, structural defects, or injection. Several methods have been used to remove the SiGaN, categorized as wet, dry and thermal etching. Looking at the morphology of the sample as well as their optical properties with a SEM equipped with a CL setup, two processes (SF_6 plasma etching and H_3PO_4) were identified as effective solutions, as they dramatically increased the optically active coverage of the samples. On the other hand, further studies suggested that the SiGaN layer acted as a barrier for diffusing non-radiative centers, speculated as being V_N. In case of the SF_6 treated samples, a so-called underlayer needs to be grown before the QWs in order to order to trap the defects and prevent their diffusion in the active structure. However, in the case of the H_3PO_4, this was shown to be unnecessary, as it is suspected that the etching of the GaN core surface by the H_3PO_4 may lead to the entire removal of the non-radiative centers.

BIBLIOGRAPHY

1. Hartmann J, Wang X, Schuhmann H, et al. Growth mechanisms of GaN microrods for 3D core-shell LEDs: The influence of silane flow. *Physica Status Solidi (A) Applications and Materials Science*. 2015;212(12):2830-2836. doi:https://doi.org/10.1002/pssa.201532316

2. Markurt T, Lymperakis L, Neugebauer J, et al. Blocking growth by an electrically active subsurface layer: The effect of si as an antisurfactant in the growth of GaN. *Phys Rev Lett*. 2013;110(3):036103. doi:10.1103/PhysRevLett.110.036103

3. Kapoor A, Finot S, Grenier V, et al. Role of Underlayer for Efficient Core-Shell InGaN QWs Grown on m-plane GaN Wire Sidewalls. *ACS Appl Mater Interfaces*. 2020;12(16):19092-19101. doi:https://doi.org/10.1021/acsami.9b19314

4. Kapoor A, Guan N, Vallo M, et al. Green Electroluminescence from Radial m-Plane InGaN Quantum Wells Grown on GaN Wire Sidewalls by Metal-Organic Vapor Phase Epitaxy. *ACS Photonics*. 2018;5(11):4330-4337. doi:https://doi.org/10.1021/acsphotonics.8b00520

5. Tessarek C, Heilmann M, Butzen E, et al. The role of si during the growth of gan micro- and nanorods. *Cryst Growth Des*. 2014;14(3):1486-1492. doi:https://doi.org/10.1021/cg500054w

6. Puchtler TJ, Wang T, Ren CX, et al. Ultrafast, Polarized, Single-Photon Emission from m-Plane InGaN Quantum Dots on GaN Nanowires. *Nano Lett*. 2016;16(12):7779-7785. doi:https://doi.org/10.1021/acs.nanolett.6b03980

7. Koester R, Hwang JS, Salomon D, et al. M-plane core-shell InGaN/GaN multiple-quantum-wells on GaN wires for electroluminescent devices. *Nano Lett*. 2011;11(11):4839-4845. doi:https://doi.org/10.1021/nl202686n

8. Wu F, Lin Y Da, Chakraborty A, et al. Stacking fault formation in the long wavelength InGaN/GaN multiple quantum wells grown on m -plane GaN. *Appl Phys Lett*. 2010;96(23):231912. doi:https://doi.org/10.1063/1.3447940

9. Eymery J, Salomon D, Chen X, Durand C. Process for catalyst-free selective growth on a semiconductor structure. Published online April 3, 2012.

10. Schimpke T, Avramescu A, Koller A, et al. The influence of MOVPE growth conditions on the shell of core-shell GaN microrod structures. *J Cryst Growth*. 2017;465:34-42. doi:https://doi.org/10.1016/j.jcrysgro.2017.02.035

11. Schimpke T, Mandl M, Stoll I, et al. Phosphor-converted white light from blue-emitting InGaN microrod LEDs. *Physica Status Solidi (A) Applications and Materials Science*. 2016;213(6):1577-1584. doi:https://doi.org/10.1002/pssa.201532904

12. Banal RG, Funato M, Kawakami Y. Surface diffusion during metalorganic vapor phase epitaxy of AlN. *Physica Status Solidi (C) Current Topics in Solid State Physics*. 2009;6(2):599-602. doi:https://doi.org/10.1002/pssc.200880415

13. Grenier V, Finot S, Gayral B, et al. Toward Crack-Free Core–Shell GaN/AlGaN Quantum Wells. *Cryst Growth Des*. 2021;21(11):6504-6511. doi:https://doi.org/10.1021/acs.cgd.1c00943

14. Finot S, Grenier V, Zubialevich V, et al. Carrier dynamics near a crack in GaN microwires with AlGaN multiple quantum wells. *Appl Phys Lett*. 2020;117(22):221105. doi:https://doi.org/10.1063/5.0023545

15. Deeb MA, Wei J, Hartmann J, Wehmann HH, Waag A. Surface photovoltage behavior of GaN columns. *Physica Status Solidi (A) Applications and Materials Science*. 2015;212(4):732-735. doi:https://doi.org/10.1002/pssa.201400238

16. Van Gelder W, Hauser VE. The Etching of Silicon Nitride in Phosphoric Acid with Silicon Dioxide as a Mask. *Journal of The Electrochemical Society*. 1967;114(8):869-872. doi:10.1149/1.2426757

17. Wolf R, Wandel K, Gruska B. Low-temperature ICPECVD of silicon nitride in SiH4-NH3-Ar discharges analyzed by spectroscopic ellipsometry and etch behavior in KOH and BHF. *Surf Coat Technol*. 2001;142-144:786-791. doi:https://doi.org/10.1016/S0257-8972(01)01184-7

18. Shintani A, Minagawa S. Etching of GaN Using Phosphoric Acid. *J Electrochem Soc*. 1940;123(5):706. doi:10.1149/1.2132914

19. Li Q, Wright JB, Chow WW, et al. Single-mode GaN nanowire lasers. *Opt Express*. 2002;20(16):17873-17879. doi:https://doi.org/10.1364/OE.20.017873

20. Lai YY, Hsu SC, Chang HS, et al. The study of wet etching on GaN surface by potassium hydroxide solution. *Research on Chemical Intermediates*. 2017;43(6):3563-3572. doi:10.1007/s11164-016-2430-1

21. Toshihiko Tanaka, Mitsuaki Morigami, Nobufumi Atoda. Mechanism of Resist Pattern Collapse during Development Process. *Jpn J Appl Phys*. 1993;32(12S):6059. doi:10.1143/JJAP.32.6059

22. Bosch J, Coulon PM, Chenot S, et al. Etching of the SiGaxN yPassivation Layer for Full Emissive Lateral Facet Coverage in InGaN/GaN Core-Shell Nanowires by MOVPE. *Cryst Growth Des*. 2022;22(9):5206-5214. doi:https://doi.org/10.1021/acs.cgd.2c00286

23. Griffiths JT, Ren CX, Coulon PM, et al. Structural impact on the nanoscale optical properties of InGaN core-shell nanorods. *Appl Phys Lett*. 2017;110(17):172105. doi:https://doi.org/10.1063/1.4982594

24. Schmidt G, Müller M, Veit P, et al. Direct imaging of Indium-rich triangular nanoprisms self-organized formed at the edges of InGaN/GaN core-shell nanorods. *Sci Rep*. 2018;8. doi:10.1038/s41598-018-34382-y

25. Haller C, Carlin JF, Jacopin G, Martin D, Butté R, Grandjean N. Burying non-radiative defects in InGaN underlayer to increase InGaN/GaN quantum well efficiency. *Appl Phys Lett*. 2017;111(26):262101. doi:https://doi.org/10.1063/1.5007616

26. Armstrong A, Henry TA, Koleske DD, Crawford MH, Lee SR. Quantitative and depth-resolved deep level defect distributions in InGaN/GaN light emitting diodes. *Opt Express*. 2012;20(56):A812-A821. doi:https://doi.org/10.1364/OE.20.00A812

27. Han DP, Fujiki R, Takahashi R, et al. N-type GaN surface etched green light-emitting diode to reduce non-radiative recombination centers. *Appl Phys Lett*. 2021;118(2):021102. doi:https://doi.org/10.1063/5.0035343

Chapter 5:

From a core shell nanowire heterostructure to a flexible LED

CONTENTS

1. STATE OF THE ART

1.1 FLEXIBLE LIGHT EMITTING DEVICES IN THE LITTERATURE

1.1.1 INTEREST AND APPLICATIONS

The applications of flexible devices cover a wide range of domains, such as for example, flexible appliances (phones, computers …), on-skin medical sensing, or conformal photovoltaics. Hence, it is not surprising to see that the subject has seen a growing number of contributions since 2000. Indeed, as seen in Fig. V-1, the listed number of publications with the keywords "flexible electronics" started to increase in the late 2000s, and has, since then, been growing exponentially.

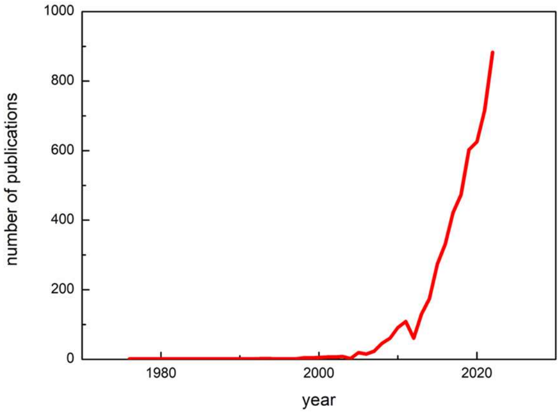

Figure V-1: *number of publications with the keywords "flexible electronics" listed by Scopus over the years.*

This rising interest can be explained by the promises of flexible devices. Indeed, their flexibility makes them able to fulfill applications that are not possible with rigid devices, such as their inclusion in textile or on skin medical sensors. In the case of flexible LEDs, the main applications are first conformal lighting, flexible screens and wearables. Currently these three applications are already fulfilled with millimeter scale rigid electronic devices that are embedded in flexible matrixes (Fig. V-2(a)). However, this technology implies to make a choice between light emission intensity and flexibility, as there is a trade-off between the density of LEDs and the flexibility of the strip. Another solution is to use Organic LEDs (OLEDs), as presented in a bendable phone as Fig. V-2(b). However, this technology does not yet yield commercially available fully flexible devices, and has its own set of issues, as further developed in 1.2.1.1. The current reported lowest radius of curvature (ROC) for the device presented in Fig. V-2(b) is 1.4 mm.

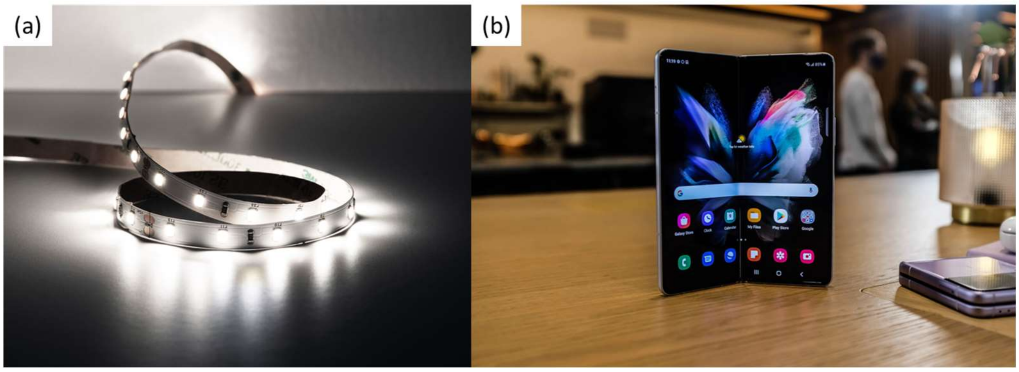

Figure V-2: *Rolls of LED (a) and bendable phones (b)*

Optogenetic is another promising application of flexible LEDs. This biological technic allows a genetic modification of targeted cells such as neurons, in order to make them sensitive to specific wavelengths. Thanks to the improvement of this method, it is now possible to stimulate or inhibit the cell activity with light. This opens the door to new brain/chip interface where a signal is transmitted by a chip to a neural system using an interface between a LED and a group of photosensitive neurons[1]. This method is of particular interest for the elaboration of a new generation of cochlear implants [2]. The advantages of using a light source as stimulation tools is a better temporal and spatial resolution, especially when compared to. However, such approach also requires a high-power light source for appropriate signal-to-noise ratio, small devices to fit inside the cochlea, as well as a low radius of curvature[3] because of the spiral shape of the targeted organ (Fig. V-3).

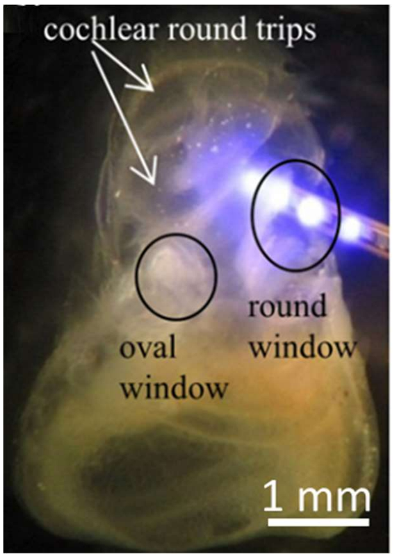

Figure V-3: *Flexible strip of LED inserted in a mice cochlea(from ref. [3])*

1.1.2 STRATEGIES

1.1.2.1 ORGANIC LEDS

There are different approaches that can be used for flexible LED fabrication. The first one is to use a flexible material, such as a polymer, as it is the case for organic LEDs (OLEDs). In this case, the light emission is carried out by single molecules, with weak Van Der Waals interactions as the main binding force. There are several advantages of using these compounds in the production of flexible LEDs. First the weak internal cohesion of the materials allows for more flexibility, so that the materials can be directly integrated in a flexible and planar layer[4]. Another advantage comes from the fact that the material is not monocrystalline but rather made of individual organic molecules, meaning that the properties of the device are not impacted by structural properties. The variety of compounds that can be used with associated wavelengths and properties is higher than with inorganic compounds[5–7], and they are mostly made of carbon and are generally described as being inexpensive and easy to manufacture[7].

The fact that the material is made of organic compounds comes however with some inherent disadvantages. First, the molecules might exhibit chemical stability issues, which means that additional layers are required to protect them from moisture and reactive O_2 in the air[8]. They also have a poor electrical conductivity and poor thermal resistance, and they are expected to have a smaller lifetime[9] than their inorganic counterparts. Because the lifetime varies from compound to compound, OLED screens may also suffer from differential aging, where the luminance decrease at different rates for each pixel[10]. This issue can however be mitigated by adjusting injection in the different pixels. Finally, OLEDs have generally a lower output power[11] and quantum efficiency[12] than nitride LEDs[13].

1.1.2.2 FROM PLANAR INORGANIC LEDS TOWARD NANOWIRE-BASED LEDS

The second option is to use inorganic LEDs. Some example of flexible devices with microLED array are shown on the Fig. V-4(a). However, there are several reasons that makes the flexible approach () more challenging on inorganic semiconductors. First, in the case of nitride visible LEDs, the process used to grow GaN is an epitaxial and high temperature process. It is thus not compatible with most flexible substrates that are organic in nature because they are neither crystalline nor thermally resistant. As GaN is mainly grown on crystalline substrates, the integration a GaN layer into a flexible device first requires to be detached from its substrate, which is difficult due of the covalent nature of the bond. Few methods can be used to this end such as Laser Lift Off (LLO)[3,14] set-up, a sacrificial easily etchable layer or an etching of the substrate[15]. Another method that has been used is to grow GaN on 2D materials[16,17], which allows to mechanically lift off the heterostructure (this latter approach has recently attracted a lot of attention and will be further discussed in chapter 6). The second issue is that GaN mechanical properties are not appropriate for its use in a flexible/bendable device. Indeed, the Young's modulus of GaN has a reported value of 295 GPa, and its yield strength is around 15 GPa[18]. It means that a deformation of 5% or more is expected to result in an irreversible plastic deformation, which fits with the results obtained by compression of GaN nanocrystals[19].

The mechanical property that describes the stress experienced by flexible devices is the bending stiffness[20], which, for a single-phase material, is described as[21]:

$$S = \frac{E \cdot t^3}{12} \quad \mathbf{(5.1)}$$

With S the bending stiffness of the material, E its Young's modulus and t its thickness. Hence, the two ways to avoid plastic deformation in the material during bending are to either make each individual LED smaller in size[22] to reduce the overall stress, or to reduce the overall thickness of the heterostructure[15]. The question of plastic deformation and dislocation generation remains and might cause a degradation of the device performances over time, even if inorganic nitride compounds are chemically resilient and expected to have long lifetimes. It should be noted that one contribution has addressed these issues by performing bending fatigue tests[22]. In this study, the LEDs had a size of 100 x 100 µm, and a fatigue test consisting of 2000 bending cycles (radius of curvature: 3.5 mm) resulted in a negligible modification of the properties, which is not surprising since the targeted radius of curvature is significantly bigger than the device.

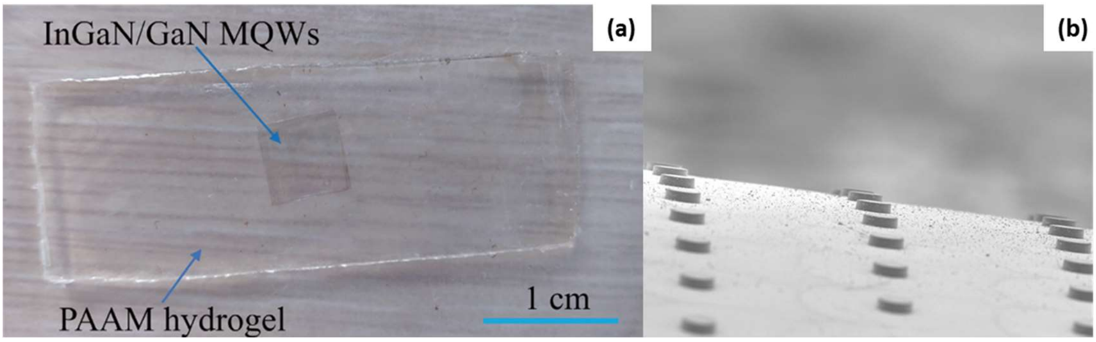

Figure V-4: *(a) Thin planar InGaN based flexible LED structure*[15] *and (b) µLED array on a polymer flexible membrane*[23].

Therefore, a good solution to improve the bending performance is then to make use of microLEDs[3,23–29] (Fig. V-4(b)). Indeed, because their foot-size (~µm) can be orders of magnitude smaller than the required radius of curvature (typically of the order of the cm to the mm), they do not suffer from plastic deformation due to the strain introduced by the bending. Their small footprint also makes them easier to remove from the substrate. One can also play with the aspect ratio of the device to facilitate the transfer. For example, in the case of nanowires, applying a shear stress on the top of the nanowire will create a torque on its base, making it easier to break. In this regard, the nanowire-based µLED structure appears well adapted for this application, not only because it allows us to move toward nano-LEDs with a wide range of possible sizes, but also because their high aspect ratio is suitable for lift-off and transfer. In the next paragraph, the methods to build nanowire-based flexible devices will be discussed, with an emphasis on work already existing in the literature.

1.2 NANOWIRE BASED FLEXIBLE LEDS

1.2.1 SELF-ORGANIZED NANOWIRE-BASED DEVICES

In the case of GaN growth, because of the high temperature growth processes and the general chemical incompatibility, nanorods cannot be grown on a flexible polymer film as it is the case for example with ZnO[30]. However, it can be noted that the direct growth of GaN nanowires on flexible metal foils by MBE has been achieved in 2016 and flexible LEDs were fabricated[31,32], however this approach was not pursued in the literature due to the poor control over the properties of NWs grown on metal.

Indeed, in most reports[33–39], the fabrication is a two-step process, in which the structures are first grown on a rigid substrate, encapsulated, and separated, with the last steps of the fabrication (typically including contact deposition) is carried on a flexible membrane. To our knowledge, one of the earliest reports of the elaboration of a flexible nanowire LED using encapsulation with a GaN/InGaN heterostructure was made in 2011 by Lee *et al.*[40] The method presented in this report has since then been reproduced by other teams with some slight changes : the encapsulation of the nanowires is usually performed in a polymer matrix (either in PDMS[34–36,39], in polyimide[37,38] or PET[33,40]. This matrix is separated from the substrate either by etching of the substrate[38,40], laser lift off[33], or mechanical peeling assisted by tape bonding[37] or not[34–36]. In addition to its flexibility, the polymer provides a physical separation between the p and n-contact, avoiding short circuits. [39]

In all the nanowire flexible LEDs presented above, the nanowires were grown following a self-organized process, that has already been described previously in this manuscript. This can be justified by an easier process since the growth can be carried out on an unprepared substrate. In MOCVD specifically, the characteristics of a self-organized sample are advantageous for their insertion in flexible devices as the samples usually consist in a low density array of long nanowires (>20µm). However, while their geometry makes them appropriate for flexible device fabrication, this comes at the cost of the control of optical properties, which will be explained in further details in the next paragraph.

1.2.2 LIMITATIONS DUE TO SELF ORGANIZED GROWTH

The drawbacks caused by the self-organized approach are due to the random position of the nanowires, as well as their variation in size and optical properties. Fig. V-5 (a-c) shows photographs of self-organized nanorod LEDs with and without current injection. What can be seen in Fig. V-5(c) combining picture with and without injection is that a part of the array produces limited amount of light, or no light at all. This can be caused by a difference in height in nanowires, as some of the structures are not high enough to go through the polyimide layer used as a matrix in this work. These structures are hence not contacted, and not injected during the operation.

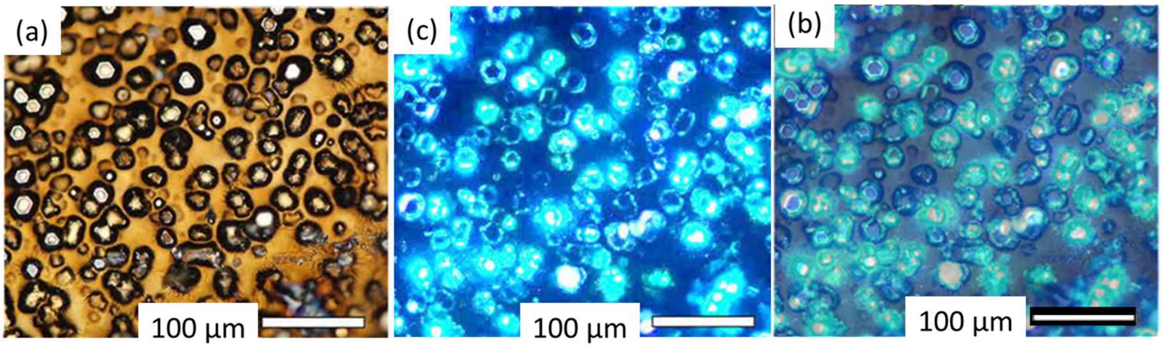

Figure V-5: Flexible NW-based LED device (a) under an optical microscope, (b) under a microscope under injection, (c) combined picture of (a) and (b) (from ref. [37]).

Another issue is the control of the emission properties of the active layers. Indeed, the aspect ratios and thus the relative area of each crystallographic planes vary from one nanowire to another. This leads first to a difference in relative intensities for each plane’s specific contribution , as the semipolar and polar planes have a redshifted emission due to QCSE as compared to c-plane. It can also lead to different quantum well thicknesses and In compositions due to diffusion of adatoms and preferential incorporation on different crystallographic planes[41]. Finally, the height difference also leads to inhomogeneity in the current injection. As a result, the samples may exhibit inhomogeneities in their emissive properties as observed in Fig. V-6 (a), which may be even more pronounced at the local level (Fig. V-6(b)).

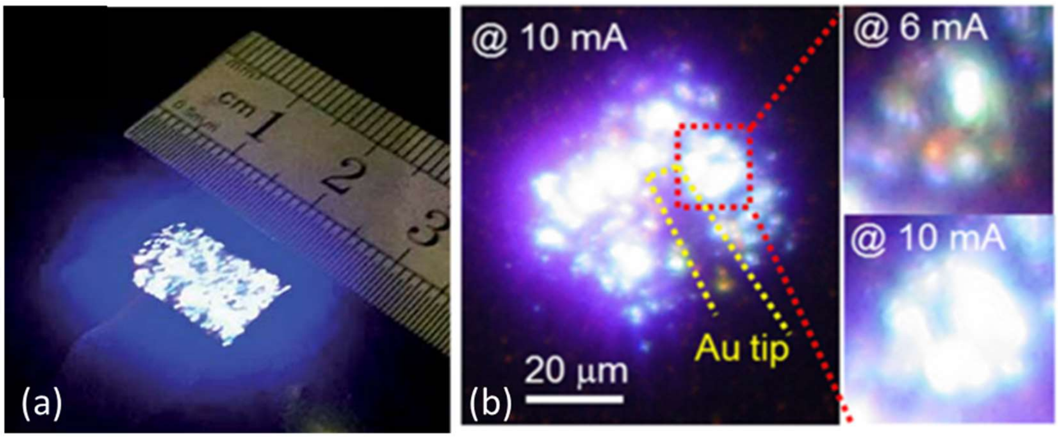

Figure V-6: *Photos of operating flexible LEDs using self-organized core-shell nanowires LEDs ((a,b) from refs.* [34] *and* [38]*, respectively).*

Last, because of the irregular nanowire locations, the density may also change from one region of the sample to another, which leads to inhomogeneous luminance from the samples. This is a clear obstacle for applications such as flexible screens requiring pixels or cochlear implants that require a high spatial resolution. In this context, selective area growth becomes an unavoidable method to achieve arrays of nanowires with homogeneous properties over large surfaces. This method has therefore been used with Silicon nanowires[42] for the fabrication of flexible electronics, but there are very few reports[43] about SAG-based flexible devices with GaN. Hence, one of the aims of this PhD was to use methods developed for self-organized systems and apply them to SAG samples in order to produce highly homogeneous flexible LEDs.

2. FLEXIBLE DEVICES BASED ON SAG NANOWIRES

2.1 FIRST SAMPLE

2.1.1 PREVIOUSLY ESTABLISHED PROCESS

In this paragraph, special attention will be given to one of the earliest reports using GaN nanowires by Dai *et al.*[34]. The team responsible for this report, led by M. Tchernycheva at the French Center for Nanoscience and Nanotechnology (C2N), has been collaborating with our group on the elaboration of SAG-based flexible nanowire devices in the scope of this PhD. For this reason, the process presented in ref [34], has been used as the basis for the elaboration of flexible devices in this PhD and is presented in Fig. V-7:

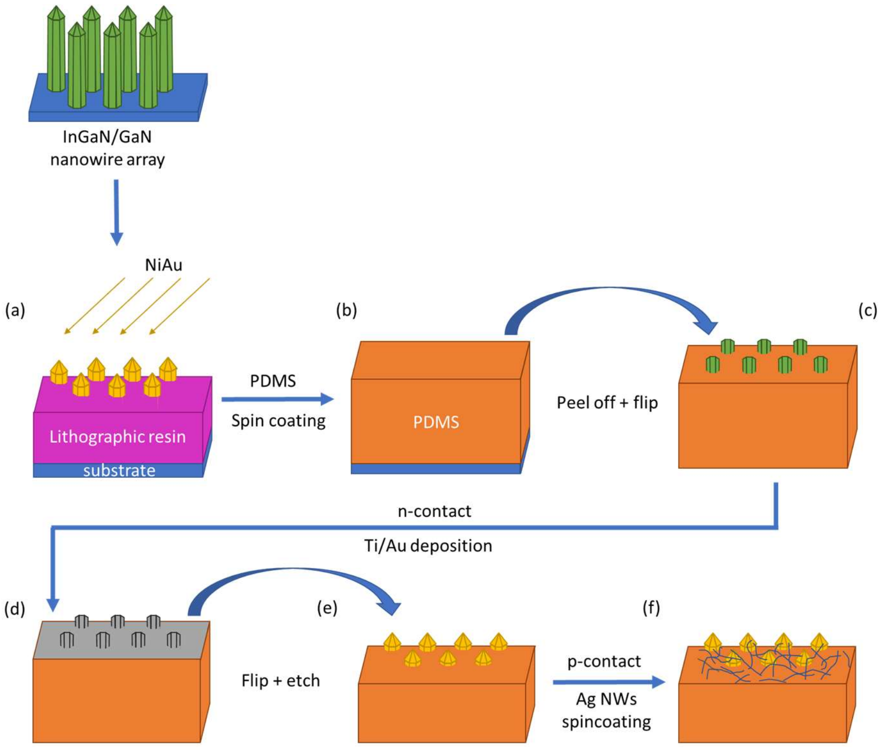

Figure V-7: *Step by step representation of the process detailed in ref.*[34] *using an InGaN/GaN core shell nanowire array.*

- The first step (Fig. V-7 (a)) is the growth of an array of nanowires with a full core shell LED structure, including an n-GaN core, an InGaN/GaN heterostructure array, and a p-GaN shell. This part of the process as already been described in previous chapters and will hence not be further detailed here.
- The nanowires are then covered with an ultrathin layer of Ni/Au (2-3 nm each). This layer helps forming an ohmic contact with the nanowires for the p-contact and needs to be deposited only where the p-GaN shell is present, and the foot of the nanowire needs to be protected with a photolithographic resist. The resist can then be lifted off, and the sample is then annealed at 400°C during 10 min in atmosphere containing oxygen, which oxidizes the Nickel to form NiO, which further helps to get an ohmic contact for the p-side.
- The nanowires are then encapsulated in polydimethylsiloxane named PDMS (Fig. V-7(b)), which is an elastomer of the formula $(SiCH_3)_2(C_2H_6SiO)_n$ and fits the requirements for the elaboration of a flexible membrane containing semiconducting nanowires. The PDMS can be bought in the form of an unreticulated viscous liquid of several grades, the one being used here is PDMS Sylgard® 184. Prior to use, it is mixed with a PDMS primer that will initiate the crosslinking between the chains. The PDMS can then be spin coated onto the desired sample. The crosslinking occurs at room temperature for several days, which can be reduced to several hours by baking at 80°C. It should be noted that the primer/PDMS mix can be kept at -40°C without solidification, or at refrigerator temperatures if dissolved in a solvent such as hexane or toluene.
- Once cured, the PDMS membrane can be peeled off the substrate (Fig. IV-7(c)). To do so, it is necessary to use microscalpels in order to scrape the thin membrane without breaking it. The ones that have been used in this work specifically were Graham-Field microfeather ophthalmic scalpel

with a blade angle of 15° for initiating the peel off, and 45° to scrape off the membrane once a tip has been separated. Once the membrane has been fully peeled off, it can be unfolded by wetting it with isopropanol, and be flipped to expose the n-GaN foot of the nanowires.

- Having been exposed, the n-side of the nanowires can be directly contacted (Fig. V-7(d)) by a Ti/Au layer deposited using an e-beam evaporator.
- The sample is flipped again, exposing once again the p-side of the nanowires (Fig. V-7 (e)). The PDMS is however expected to fully encapsulate the nanowires, and the surface consists in a flat polymer layer. To realize the p-contact, one needs to first etch the PDMS to expose the p-side of the nanowire. however, since PDMS backbone is formed from the monomer [$Si(CH_3)_2O$] units, it cannot be etched through classical methods used for organic materials, such as acetone, Remover PG or O_2 plasma. It requires the use of fluorinated compounds. The most reliable method is to perform a CF_4/O_2 plasma in an ICP-RIE apparatus, as the Fluor ions can break the Si-O bond. The samples were etched slowly to avoid burning the membrane and to obtain a homogeneous controlled etching.
- The last step consists in the spin-coating of Ag nanowires on the device, creating a transparent mesh that helps conducting the current to the whole area of the LED.

This process allows the fabrication of a semi-transparent flexible LED, with light being extracted from the top side of the device. An alternative process can yield fully transparent flexible LEDs by replacing the n-GaN metal deposited contact by an array of silver nanowires[34], as it is performed with the p-GaN contact. However, this variant of the process will not be discussed in many details here, as the n-contact has not been identified as a critical part of the process, and because a thick and reflective n-contact helps improving the light extraction from the device[44].

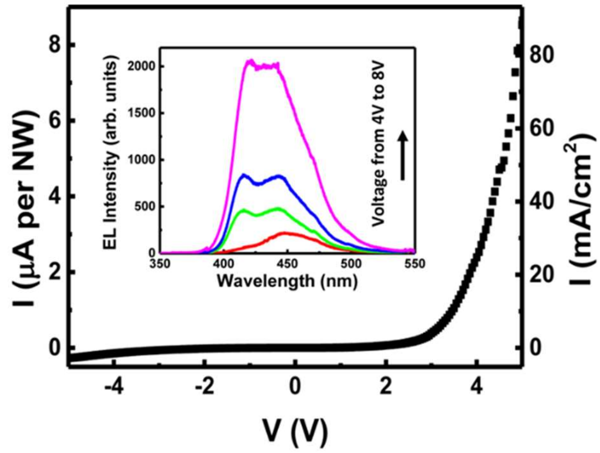

Figure V-8: *I-V curve and corresponding EL spectra at different biases of the LED presented in the ref.* [34]*.*

An electroluminescence spectrum of the device is provided in the reported study and is presented in Fig. V-8. It consists in applying a variable bias to the sample, and measuring the corresponding current flowing through the device, as well as its light emission. Fig. V-8 shows several features that are expected for InGaN/GaN based LEDs, and this figure will hence be used as a case example to quickly assess these features. First, the IV curve fits the behavior of a regular p-n junction, with a first regime featuring a negligible increase of the current with increasing voltage, until a turn-on voltage is reach. The current then increases with the voltage. This turn-up voltage, called the forward voltage, is expected to occur between 3 and 4 Volts[45,46], as verified here. In negative biases, the current stays at values close to 0, which indicates a high breakdown voltage and is a common characteristic for GaN-based LEDs[47,48]. One last characteristic feature of nanowire-based LEDs is the presence of 2 main emission peaks at different voltages. At low voltages, one can first see a 450 nm broad emission, followed by the rise of a second contribution at around 410 nm. This is because, as explained in Chapter 4, nanowires do not feature a single crystallographic plane of emission, and usually have either top semi-polar or polar QWs on Ga-polar[49] and N-polar[35] nanowires respectively[50], with higher wavelength emissions, which are preferentially activated at low currents. The report[34] also presented additional procedures that can be used with this process to produce white LEDs. The first one would be to stack several layers of the device using nanowires with different emissive properties, opening the way for RGB and white LED applications. This method takes advantage of the transparency of the device, which has a transmittance of about 60%[34], but it requires for the membrane with the lowest energy emission to be placed at the bottom of the stack to ensure that the high energy photons do not interact with lower energy junctions.

2.1.2 LIMITS OF SAG-NANOWIRES ENCAPSULATION

One of the first issues that arises with using our SAG nanowires stems from their size. Indeed, the height of the nanowires produced by SAG using our process is usually between 5 and 10 µm against more than 30 µm for the nanowires used by Dai *et al.*[34] However the PDMS membrane thickness is determined by the nanowire height. One could suggest first encapsulating the nanowires in a thick PDMS layer which would then be etched. But a long dry etching step is more challenging, because the longer the PDMS is etched, the more heterogeneous it becomes in thickness. The membrane may also heat up and start to burn in certain places. It is thus better to keep the PDMS thickness close to the height of the nanowires as shown on the Fig. V-9. The membrane is then expected to be limited to a thickness of 15 to 20 µm. This makes the manipulation of the membrane challenging, especially for the peel off, which is made mechanically, by hand, with scalpels and tweezers. Even in the case where one manages to obtain a full membrane after the peel off, there are usually some amounts of tears and holes in the PDMS, which are sources of leakage and short circuits.

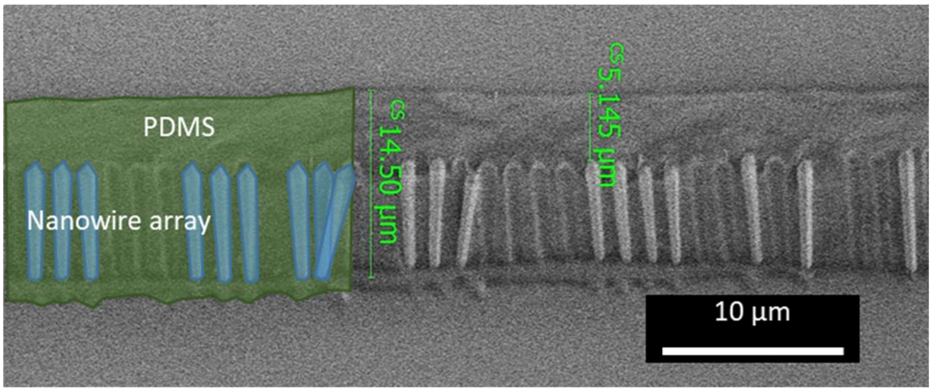

Figure V-9: *Array of nanowires in a PDMS membrane observed by SEM in cross section view.*

The second issue that was found with our SAG samples is the pitch between nanowires. Indeed, the nanowires are spaced by only 1.5 µm from center to center and considering that a nanowire diameter of roughly 1 µm, it leaves about 1 µm of spacing between each nanowire. This dimension constraint is imposed by the mask fabrication through Differential Talbot Lithography[51], which allows to produce a large and homogeneous array of holes on a full wafer. The pattern chosen for the SAG is a hexagonal, and the space enclosed by three neighboring nanowires forms a triangle that acts as a capillary for liquids. Indeed, this effect is usually visible on nanostructured sample when working with liquids such as water[52], and has been mentioned as a potential issue in Chapter 4 after wet etching. The PDMS covering is thus inhomogeneous (Fig. V-10(b)).

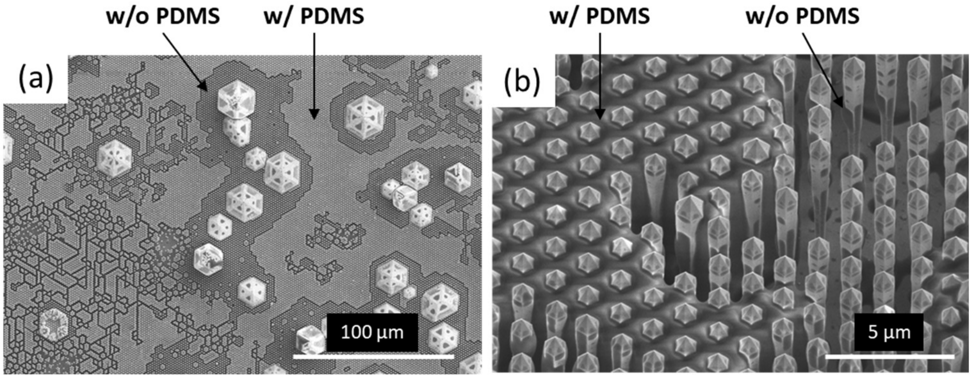

Figure V-10: *Low (a) and high (b) magnification SEM pictures of a SAG-nanowire sample encapsulated with PDMS*

Fig. V-10 shows this issue and its consequences with the formation of empty areas between the nanowires. As seen in Fig. V-10(a), the presence of large parasitic growth can also be responsible for empty areas. This issue is not only threatening for the sample properties but will also badly impact the fabrication of the sample itself and may lead to the failure of the sample during the peel-off stage. Therefore, finding a solution to drastically reduce the amount of empty areas in the sample has been the first step in fitting the process to SAG NW structures.

One easy solution is to use a solvent able to dilute PDMS such as hexane. We determined experimentally that a ratio of 3:1 by weight hexane:PDMS allowed to significantly reduce this effect. One explanation for this behavior comes from the Jurin's law, which describes the behavior of a liquid inside a capillary, and states that the strength of the force pushing a liquid up the capillary is directly proportional to the surface tension of the liquid, and inversely proportional to its density. Hence, a good solvent for this application should have either a low surface tension or a high density. Hexane has a low density but also has a very low surface tension in air (three times[53] less than as water[54]), which could explain the reduction of the capillary effect, despite its low density. One other advantage of this dilution is its volatility, meaning that it can be evaporated easily during the curing of the PDMS. **Hence, all following samples have been fabricated by diluting the PDMS precursor in hexane, with a 3:1 mix hexane/PDMS.**

2.1.3 FIRST DEVICE AND PROPERTIES

Considering the encountered problems, as described in the previous paragraph, we had to change slightly the process described by Dai *et al*[34]. The process was first modified by using a diluted form of

PDMS precursor to allow a better filling of the array and limit capillary effects, as explained previously. Second, [34] the metal semi-transparent p-GaN contact was realized after etching. Indeed, because of the aforementioned capillary effects, the deposition of a resist covering only the bottom of the nanowire is challenging and requires additional steps that need to be optimized. The contact was deposited after the PDMS etching and was not annealed in oxygen because of the presence of the polymer. Last, the n-GaN contact done here is a Ti/Al/Ti/Au stack with respective thicknesses of 10/20/10/100 nm. The core nanowires were grown in conditions similar to those described in the Chapter 3, and the nanowire were etched in a 115°C H_3PO_4 bath to remove the SiGaN layer. The growth was then done following the conditions presented in Table V-1. The obtained device is presented in Fig. IV-11, along with IV curves, EL and CL spectra.

	step	Pressure (mbar)	Temperature (°C)	Time (s)	NH3 (mmol.min^{-1})	TMGA (µmol.min^{-1})	TMAL (µmol.min^{-1})	TEGa (µmol.min^{-1})	TMIN (µmol.min^{-1})	Cp2Mg (sccm)	H2/N2
	annealing	150	1050	1800	135						H2/N2
	Spacer	10	1220	360	135	290					H2/N2
x5	QWs	100	840	750	600			7	2		Pure N2
	cap			300				7			Pure N2
	barrier	100	955	1800	600			21			Pure N2
	EBL:p	150	1220	72	365	85	8			300	H2/N2
	p-GaN	150	1220	335	365	72				380	H2/N2
	p+-GaN	150	1220	75		41				1800	H2/N2
	p-GaN annealing	300	935	1200							Pure N2

Table V-1: *growth parameters of the shell grown on core nanowire for the fabrication of flexible devices.*

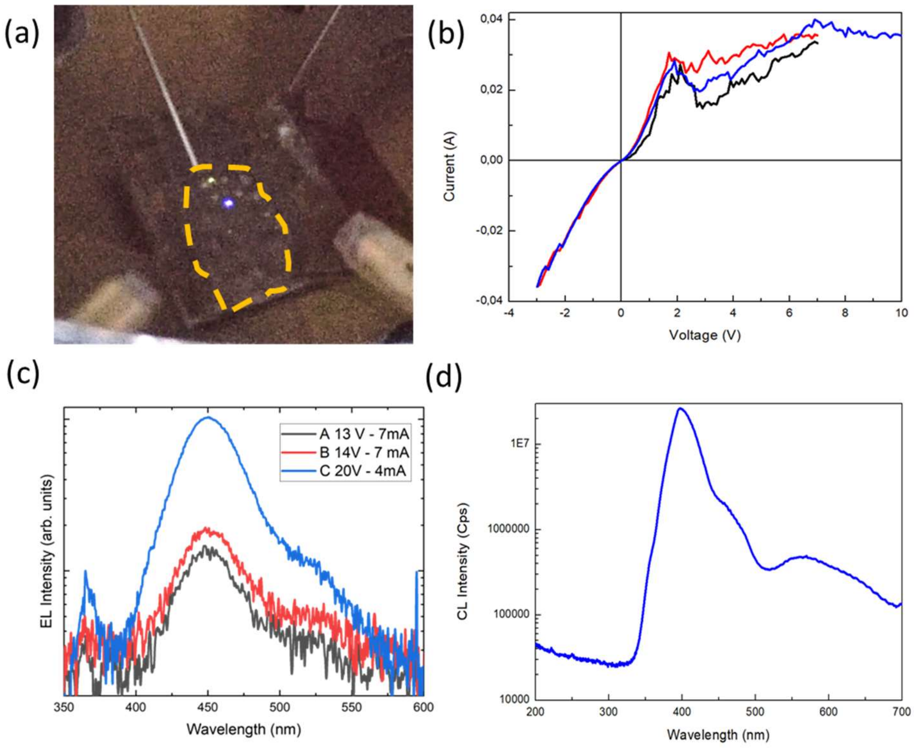

Figure V-11: *SAG flexible device (indicated by the orange outline) under injection (a), corresponding IV curve (b), measured EL emission (c) and corresponding CL spectrum (d).*

A clear difference can be noted between this sample and the one presented by Dai *et al.*[34].First, the area of emission is small, the sample emits light from a single localized spot, as observed in the Fig. V-11(a). The IV (see the Fig. V-11 (b)) is also far from the expected ideal curve, on several points. First, the “breakdown” voltage is very low, suggesting that the sample struggles blocking backward current. However, this is not caused by breakdown, but rather by leakage in parallel of the diode, as seen by the fact that the device continues to operate normally after several negative bias cycles. Hence, for the sake of accuracy, this “breakdown” voltage will be referred to as the leakage voltage in the following paragraphs. On the positive bias side, the current starts flowing at low voltages, which, along with the low breakdown voltage, is indicative of a leaky behavior. Overall, the curve seems linear which also suggests leakage, but other unexpected behavior can be observed: during operation, the current appears to saturate around 7V at a value close to 40mA. Also, the curve exhibits areas where the current drops, which is typically classified as a Negative Differential Resistance (NDR). This behavior is not typical of LED behaviors, and no explanation as been found for it. The comparison between EL and CL spectra shows additional issues: From the CL spectrum (Fig. V-11(d)), we expect a main contribution from the sidewalls around 400 nm. The 450 nm signal is coming from the semi-polar planes at the top of the nanowires. However, the EL spectra shows mainly a contribution at 450 nm (Fig. V-11(c)), even at voltages a lot above the threshold for visible emission. This suggests that the current injection reaches only the upper part of the nanostructure, and most electron do not recombine in the sidewall QWs. Additionally, the spectrum seems to feature a weak GaN band edge contribution, which is thought to be caused by electron overshoot into the p-GaN layer. An optimization work needs to be undertaken. In the next paragraphs, these issues will be presented, as well as the strategies that have been adopted to counteract them.

2.2 PROCESS OPTIMIZATION

2.2.1 STRUCTURAL OPTIMIZATION OF THE DEVICE

We performed SEM observation at different process steps to find some leverage of process improvement. The Fig. V-12(a) and (b) present SEM images of the membrane after the peel off. We can see that the metal contact layer on the n-GaN bottom part is conformal and continuous. We then concluded that the n-contact is probably not responsible for the current leakage. We then performed SEM characterizations at different steps of PDMS etching prior to p-contact deposition.

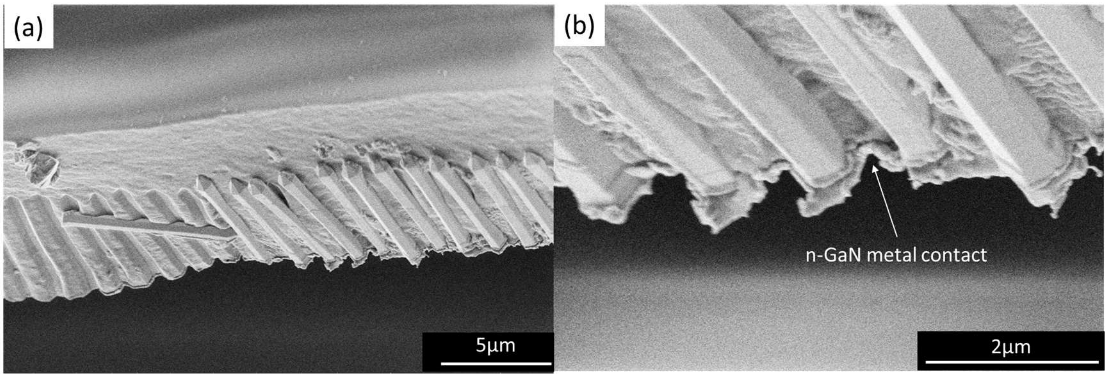

Figure IV-12: *Side view of the PDMS/nanowire membrane at a tear (a), and zoom showing the n-GaN contact (b).*

Fig. V-13 shows the different cases that can arise during the etching. In Fig. V-13(a), the tip of the nanowires can be seen on some areas, but others seem to be completely covered by PDMS. This is a common observation in early stages of the etching and shows the heterogeneity in PDMS thickness. In this case, the sample is extremely under-etched, as most of its surface can still not be contacted. In Fig. V-13(b), most of the structures have their tip and part of the top semi-polar planes out of the PDMS. In this situation, the sample is still under-etched, as this situation would only lead to the current injection in the top NW part giving semi-polar emission. The ideal situation to stop the etching is the one presented in Fig. V-13(c). Indeed, here, the top part of the sidewall can be contacted, which is expected to yield a m-plane sidewall emission. Going further in the etching would lead to the situation presented in Fig. V-13 (d). Here, the PDMS has been over-etched, and a significant part of the m-plane is out of the PDMS. Several issues appear in this case: first, the thickness of the PDMS is reduced, which increases the risk of tearing. Second, the p-GaN on the m-planes has been exposed to the dry etching environment, which could degrade its properties[55]. Last, the fact that nanowires are leaning could degrade the homogeneity of the p-GaN contact.

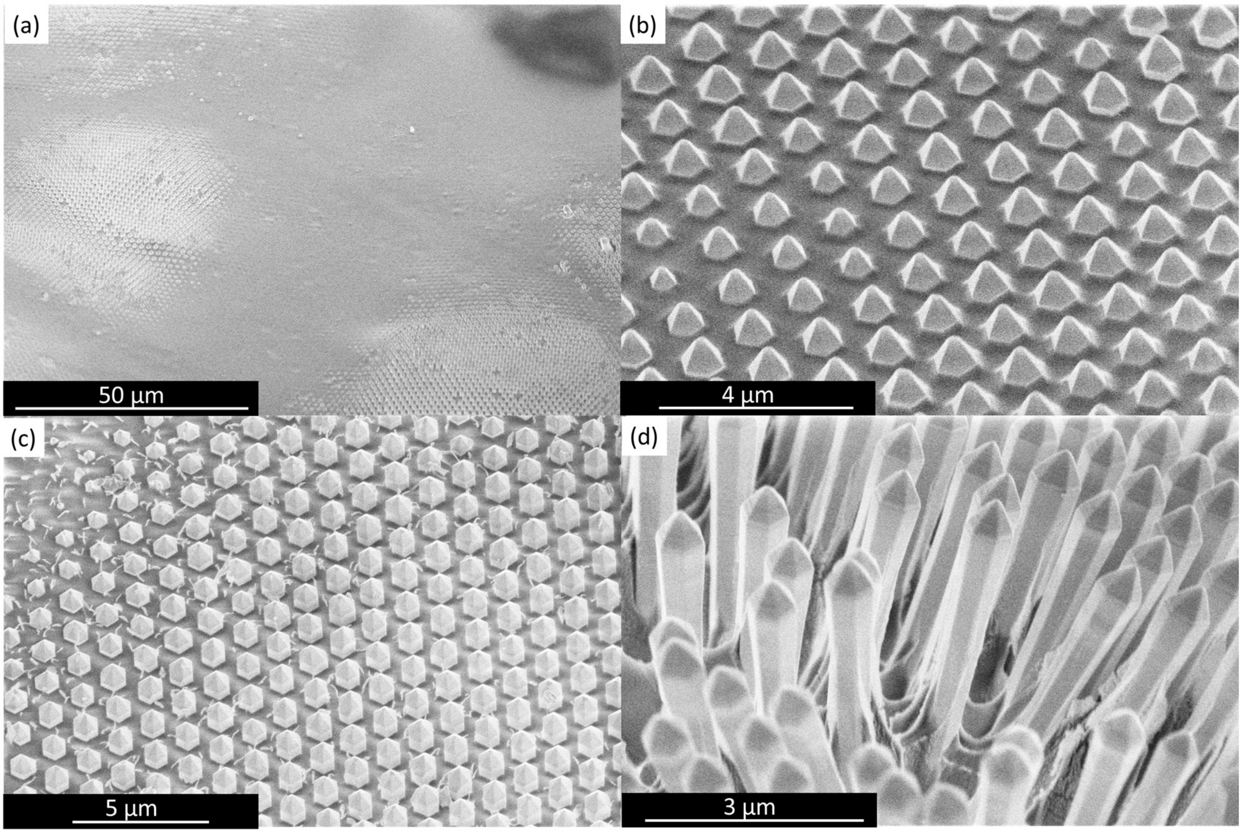

Figure V-13 *: SEM images of different stages of etching of the PDMS sample in order to make a p-GaN electrical contact : (a) very under-etched, (b) under-etched, (c) desired amount of etching, (d) overetched PDMS layer.*

Last, SEM observations have been used to control the density of the Ag-nanowire mesh, which are partly responsible for electrical contact in this case. A corresponding SEM picture is presented in Fig. V-14. The density of the silver nanowires is an important feature when it comes to the injection, as it will be directly proportional to the number of injected nanowires.

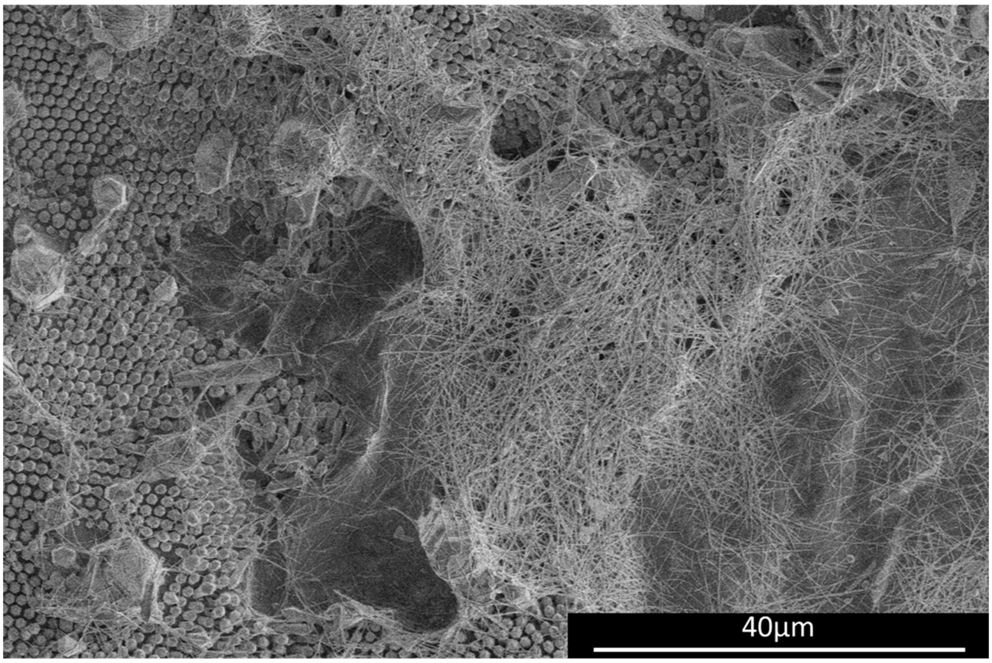

Figure V-14: *SEM picture of a sample after Ag-nanowire dispersion*

Thanks to these SEM measurements, several conclusions were drawn: First, the feet of the nanowire were indeed going through the PDMS layer and were contacted. It is assumed at this stage that the part that goes through the PDMS is the n-GaN core that grows inside the opening, which should limit the amount of current being injected directly into the conformal p-GaN shell. However, it allows to raise questions about two steps in the process, that require specific attention. The first one is the etching. Indeed, Fig. V-13 shows that the etching needs to be closely monitored in order to stop the process at the appropriate time. Indeed, an overetched sample might exhibit leaning nanowires, which is unfavorable as explained previously, for the thickness of the PDMS, the injection in the active structure, and the deposition of the p-GaN contact. **To counteract this issue, the etching was made by small increment of 30-60 seconds and observed between each increment** . Another issue, observed in Fig. V-13(a), is the inhomogeneity of the etching, but no solution was found to solve it so far. The second issue is that spin coating the Ag-nanowires leads to a low density of Ag nanowires on the top of the PDMS (Fig. V-14), which means that some GaN nanowires are not contacted and not injected. This difference with the ref.[34] can be explained by the difference in the dimensions and density of the array when compared to the self-organized structures, as the Ag-nanowires were observed to be held in place in the space between two nanowires in this study. **Hence, to limit the spreading of the Ag-nanowires, it was chosen to dropcast them instead of spin-coating** .

2.2.2 DEVICE PERFORMANCES

Electroluminescence has been performed to assess the process improvement. Indeed, the EL allows to measure both the optical and the electrical properties of the sample, and it brings a lot of information on the quality of elaboration, such as the injected planes, quality of electrical contacts, possible parasitic contributions, etc. Some information can already be directly obtained by looking at the emission also with the naked eye (Fig. V-15). For example, while the sample still exhibits issues in current spreading, some groups of nanowires were injected despite not being in close proximity with the fiber used for injection, as seen in Fig. V-15(b). In order to be able to have multiple point of emission, instead of a standard needle probe a coaxial cable was used for the injection separated into multiple wires that can be placed at different areas of the sample. This shows that there are some issues with the spreading and the injection of the carriers, which is suspected to be caused by the Ag nanowire mesh used as a contact to p-GaN shells. However, that the peak wavelength appears to be constant, and the injection occurs at several points on the sample, is already a clear improvement from the last sample.

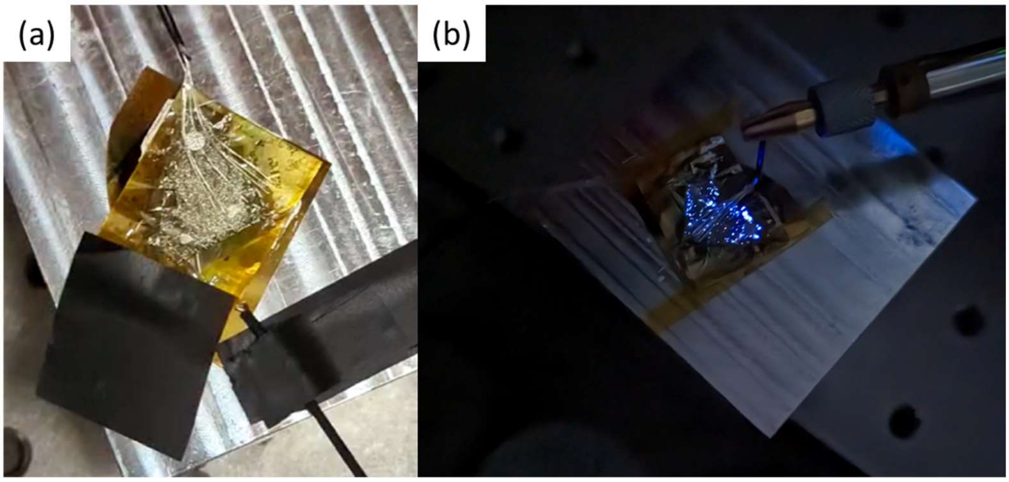

Figure V-15: *Picture of a SAG flexible LED without (a) and with (b) current injection*

In the present case, the EL spectra were taken under 15 V pulsed bias. This operation was repeated several times on the same area, to take into account the variations caused by sample instability. Spectra taken on three different areas of the sample presented in the Fig. V-15 are shown on the Fig. V-16. For each spectrum, the measurement was repeated under the same conditions several times as the intensity varied greatly from measurement to measurement, which is the reason why several spectra of varying intensities are shown on each graph. This shows that while injection was achieved, the light emission is unstable in intensity. However, the fact that the corresponding wavelength for each peak stays the same in all measurements rules out a degradation of the MQWs array, and points toward an issue with injection.

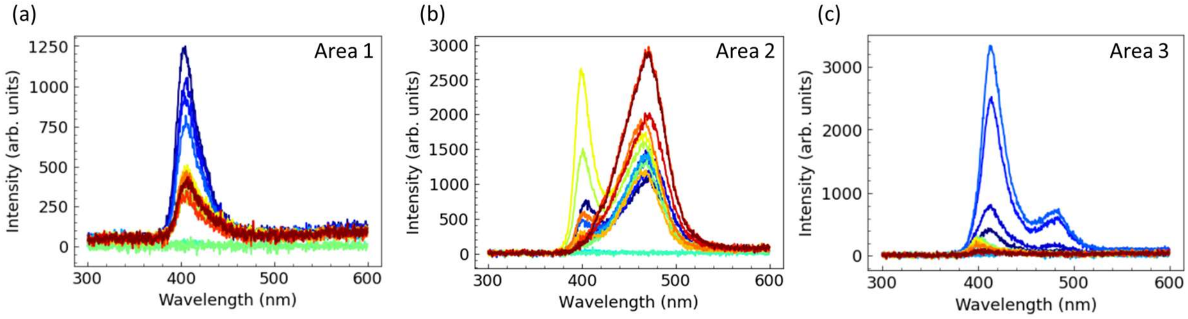

Figure V-16: *Electroluminescence spectra measured by pulsed EL at 15V for three different areas of the sample (a), (b) and (c).*

What can be seen from Fig. V-16 is that there are two main contributions, one between 400/450 nm, and the second one between 450/500nm. To confirm the origin of these contributions, CL was carried on the samples before the process, and can be used to identify the spatial origin of the contributions. A mapping of the corresponding sample is provided in Fig. V-17.

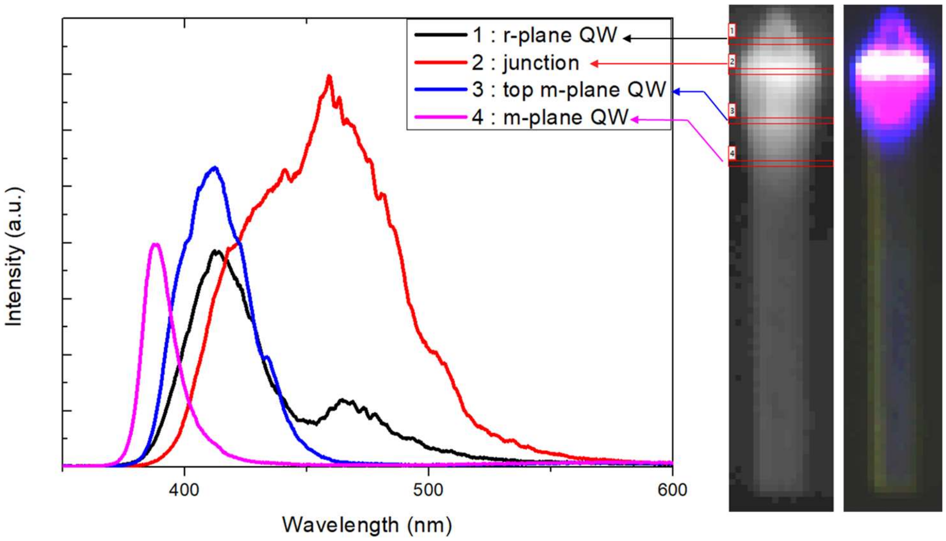

Figure V-17: *Intensity mapping and color reconstructed image of a single LED nanowire, and CL spectra corresponding to area 1, 2, 3 and 4.*

Figure V-17 shows the CL mapping and the corresponding spectra of a representative nanowire from the sample presented in Fig. V-16. While some of the results presented here were evoked in chapter IV, they need to be detailed further to better understand the different contributions in the structure. The spectra are taken on three nanowire regions, namely, the semi-polar planes, the non-polar planes, and their junction, which displays distinct emission wavelength:

The m-plane QW displays a signal centered at 405 nm at the top of the nanowire but decreases to 380 nm when going down the sidewalls of the nanowire, which is likely caused by a QW thickness decrease. As seen on another sample in Chapter 4, the intensity decreases when going down along the sidewalls of the nanowires.

The top of the non-polar plane and the semi-polar plane facets have a similar emission centered at 415 nm. This can be due to a compensation between low QW thickness on semi-polar planes and the QCSE. Indeed, the semi-polar QWs are thinner due to lower growth rates, which leads to a blue shift in emission, while the QCSE leads to a redshift as explained in Chapter I. The main result stemming from that is that, in the case of this sample, there is an ambiguity between the top of the sidewalls and the semi-polar facets. The semi-polar planes may also have either higher or lower In incorporation relative to non-polar planes depending on growth conditions, but the precise In compositions in both planes are unknown for this sample.

Third, the junction has a strong and broad emission centered around 470 nm. This can be due to the diffusion of the species from the semi-polar planes during growth, which locally increases the growth speeds, and artificially increases In incorporation by keeping it from desorbing. This creates a ring-shaped area around the nanowire with a two-dimensional localization, featuring a higher thickness of the QWs and results in a red shifting in this area.

In the EL graphs presented in Fig. IV-16, most of the contributions are present: Fig. V-16(a) features a single peak centered around 400 nm peak, which is consistent with top sidewall emission. This peak is also present in Fig. V-16(b), along with a strong signal around 475 nm, which is typical of the junction between non- and semi-polar QWs. Last, Fig. V-16(c) features the same 475 nm peak but is dominated by a peak around 415 nm, which can be either attributed to semi-polar QWs, or to the top part of the sidewalls. However, the absence of a contribution below 400 nm confirms that the injection is localized on the top of the nanowires.

In the previous paragraphs, we have presented the changes in EL from the first sample to the optimized one. We have shown (Fig. V-15(b)) that some amount of current spreading can be observed (independently from the use of multiple contact points), and that the emitted light does correspond to the targeted m-plane emission, which is a clear improvement as compared to the initial sample. However, this assessment would be incomplete without the electrical properties of the sample, and its IV characteristic presented in Fig. V-18.

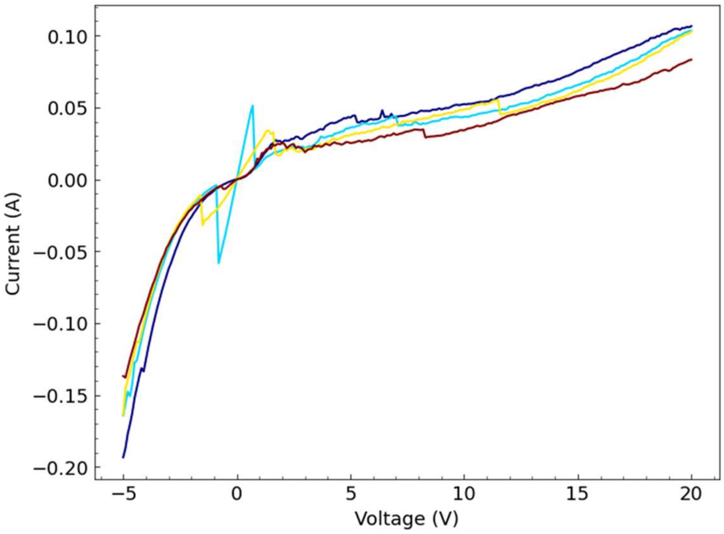

Figure V-18: *IVs taken by repeated measurements on the whole sample.*

Fig. V-18 shows the IV obtained on the sample used for the previously presented EL measurements. One of the visible improvements featured in this sample is that the IV curves are more reproducible than for the first device. Their behavior is also more stable and features a gradual nonlinear rise in positive biases that could be attributed to a LED behavior. However, the graph is still dominated by leakage currents, which are visible from the mostly linear shape of the curve for positive value, and a leakage voltage close to 0 V. The leakage current in reverse bias is higher than the operating current for a similar positive bias, at which the EL is observed. This suggests that the device provides a strong leakage path for the current to follow. While there is for the moment no clear origin of this issue, Ag-nanowires are suspected to be responsible for leakage paths by conduction toward the n-side in tears/holes in the membrane, but also because it is currently unclear if the contact between Ag-nanowires, the thin Ni/Au p-GaN contact and the p-GaN itself is ohmic.

2.2.3 MEASUREMENTS UNDER BENDING AND AN ALTERNATIVE TRANPARENT CONTACT USING SINGLE-WALLED CARBON NANOTUBES

One of the main objectives of the present work is to develop devices having a strong flexibility. This can be easily evaluated by bending the sample during current injection. The LED can be bent by hand, as it is shown in Fig. V-19(a), but this method does not allow to quantitatively assess the property variation with bending. In the framework of the PhD thesis of Jules Duraz at C2N, a specific apparatus has been built in order to measure the luminescence of the sample while applying a controlled bending to it, as presented in the Fig. V-19(b,c). In this apparatus, the bending radius of the membrane is controlled by applying the sample onto a cylinder of a desired curvature. The sample is maintained on its sides with two metal cylinders, while the central part is kept free to provide access to the optical fiber and can be used for EL measurements. This setup is however designed for samples of a size below 1 cm^2 so that we had to cut a region of our LED devices with scissors.

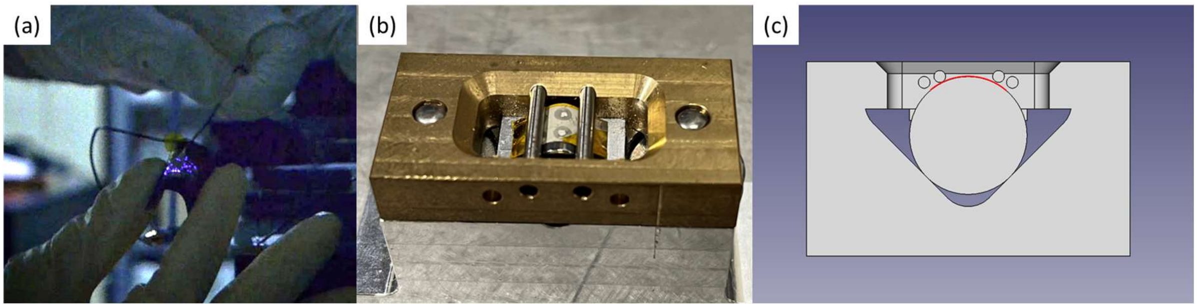

Figure V-19: *(a) Flexibleflexible device being bent by hand during operation, (b) image of the apparatus for measurements under controlled bending, and (c) scheme of the apparatus presented in (b) with the membrane in red.*

It was chosen here to cut a small region of the previously presented LED (approx. 5 mm x 1 cm). However, the small size of the device implies that the spin coating of silver nanowires might be detrimental to the sample. Indeed, the spreading of a high quantity of Ag-nanowires toward the sides of the device induces a non-negligible risk of short circuits, and it was chosen to drop-cast a small quantity of Ag-nanowires on this sample. This electrical contact was complemented by the addition of Single Wall Carbon NanoTubes (SWCNT), that were dried transferred and densified using isopropyl alcohol[39]. This addition was justified both by the poor electrical and optical properties and the small amount of Ag-nanowires. The optoelectronic properties of the samples were measured at different points, as presented in Fig. V-20

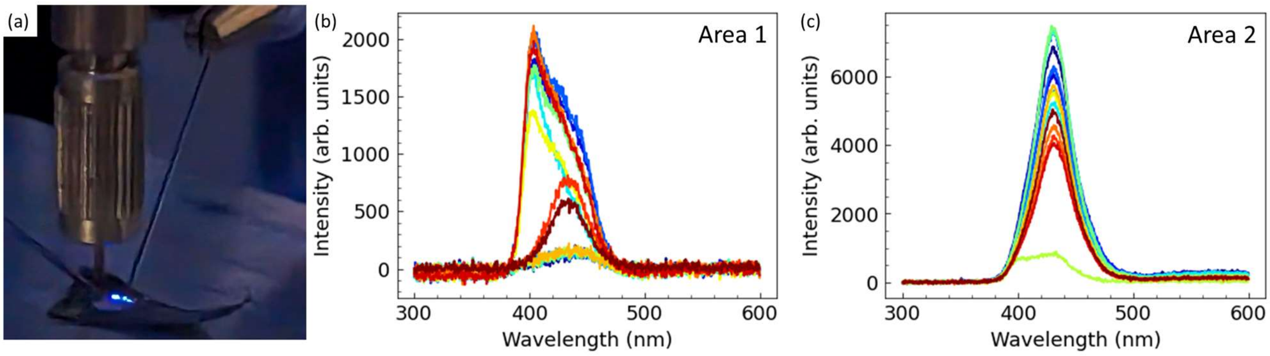

Figure V-20: *(a) Pictures of an LED with Ag-nanowire +SWCNT under electrical injection, and EL spectra taken by repeated measurements under a 15V pulsed bias at two different locations (b) and (c) in flat conditions.*

Fig. V-20(b) shows that this sample features 400 nm sidewall emission in some areas. However, most of the emission is dominated by the signal coming from the junction between semi-polar and non-polar QWs around 450 nm, as seen in Fig. V-20(c). This could be caused by the use of dry transfer of SWCNTs, that could contact preferentially the top of the structures and not conform to the GaN nanowires' shape.

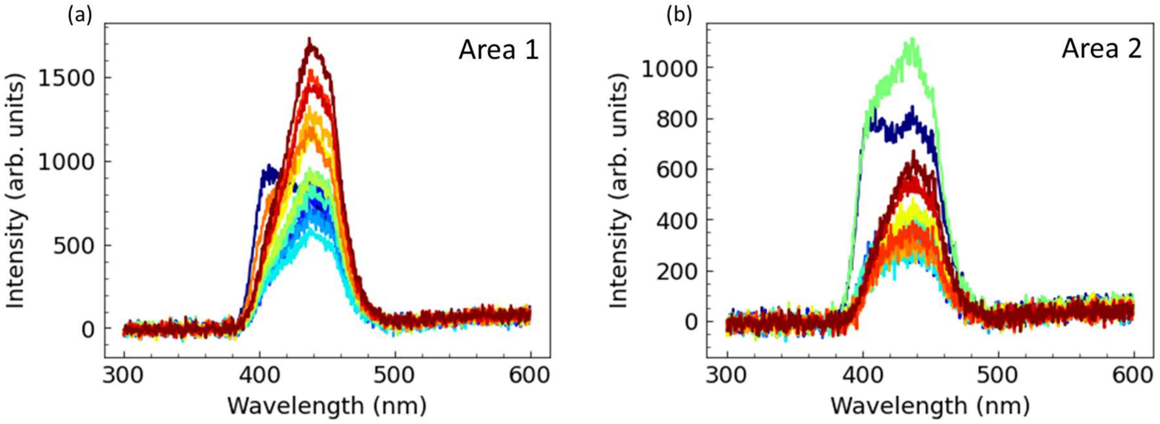

Figure IV-21: *Electroluminescence spectra, corresponding to repeated measurements taken under bending with a 3 mm radius of curvature under a 15V pulsed bias at two different locations (a) and (b).*

The EL spectra taken under bending are presented in Fig. V-21, and the sample exhibited a decrease in intensity as observed by a naked eye. We suggest that this issue is caused by the nature of the p-contact. Indeed, because the silver nanowires and SWCNTs are not bonded together and to the LED structures, the bending might disturb the mesh continuity In this case, a smaller proportion of the GaN nanowires could be contacted, which would result in a net decrease of the intensity. Another observation that supports this hypothesis is that most spectra under bending are dominated by the contribution from the top junction non/semi polar QWs of the nanowire, and the sidewall contribution is much less present in the data. This suggests that the p-contact are now mainly injecting the top of the nanowires, which also suggests that the contact array was modified by the bending.

In the last paragraphs, some clear issues have been noted with the electrical injection of the samples, and the p-GaN contact is the main suspect for this phenomenon. The silver nanowires particularly have been suspected of being responsible of some of the issues seen in the device. For example, a high resistivity due to a sheer number of contacts between silver nanowires could be responsible for spreading issues. They could also be responsible for the instabilities of the device, as an inhomogeneous repartition of the Ag-nanowires would lead to large biases across some of the wires, would lead to their oxidation or even melting through resistive heating. Inhomogeneities in their density could be responsible for the inhomogeneous behavior observed in the big samples (Fig. V-15). Last, because they are deposited through spin coating or drop casting, controlling their positioning is challenging, and they may be responsible for short-circuits extending in the holes of the PDMS membrane. The use of a complemented SWCNT contact on the currently presented sample offers an occasion to assess the effect of the Ag-nanowires on the injection. Indeed, dry-transferred SWCNT is expected to hold the same role as Ag-nanowires, namely spreading the electrical contact between nanowire through an electrical contact with the Ni/Au. An IV curve was taken at several locations on the sample and is presented in Fig. V-22.

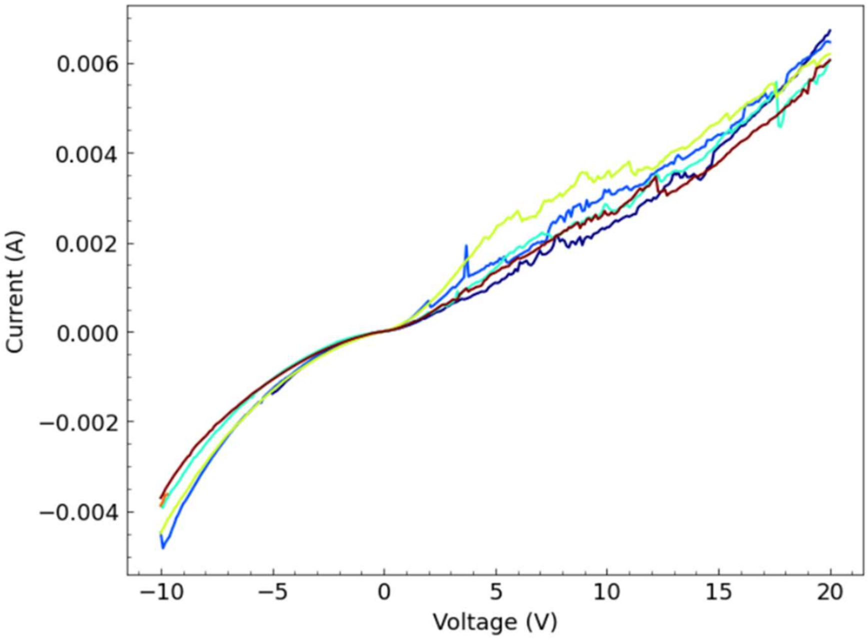

Figure V-22: *IV characteristic taken by repeated measurements on a sample featuring a hybrid p-GaN contact with a thin Ni/Au layer, Ag-nanowires and SWCNTs*

Fig. V-22 shows the IV curve of the sample presented in the last paragraph, which features an improvement of the characteristic in comparison with Fig. V-18, especially when it comes to the reverse branch. Indeed, the leakage current under negative bias remains quite low up to around -5V, a behavior that was not observed in previous samples which started leaking from very low biases. The positive bias side of the curve also features some amount of non-linearity, which also indicates that the sample exhibits a diode like behavior, even if clear signs of leakage currents are still present. While not groundbreaking, this result confirms that the use of other solutions for the p-contact might solve some of the issues observed and entirely replacing the Ag-nanowires by SWCNTs or another material for current spreading could be a way to limit the amount of leakage in the sample, if it does not come at the cost of the sidewall injection. This change was planned as part of this PhD but has not been realized because of time constraints. However, the improvements showed in Fig. V-22 are limited and suggest that other issues are at play. For example, it is possible that the contact between Ni/Au and p-GaN is non Ohmic due to a barrier created by etching damages. Steps have been taken toward elucidating this potential issue, and will be presented in the next paragraph

2.3 FURTHER OPTIMIZATION: TILTED P-GAN CONTACT

As explained in previous paragraphs, the p-GaN contact is suspected of being responsible for most of the issues observed on the device. In the original process reported by Dai *et al.*[34], the deposition of a thin semi-transparent Ni/Au layer on top of the nanowires was performed prior to the PDMS encapsulation. This allowed to anneal the Ni/Au in oxygen, which improves the electrical properties of the contact[56]. Additionally, inductively coupled plasmas have been shown to be detrimental for the p-GaN[57], and it is suspected that the Ni/Au protects the sample during the PDMS etching step. However, depositing the Ni/Au before PDMS encapsulation requires to cover the feet of the nanowires with resist for two reasons. The first reason is to isolate the feet (n-GaN) from the p-GaN contact. The second reason is that the electrical contact adheres to the PDMS a lot more than the SiN_x of the mask which makes the peel off impossible without destroying the membrane.

However, for similar reasons than the one presented for the PDMS in the previous paragraph, using SAG nanowires introduces new challenge to address, and makes this part of the process more complex. Indeed, the thickness of the layer cannot be directly controlled by spin-coating parameters as in the case of self-organized nanowires. Indeed, due to capillary effect, the lithographic resist covers the full nanowire length, so the process must include a step to remove the excess resist from the top. And as stated in 2.2.1, the smaller size of the nanowires means that the desired thickness of the resist layer is much smaller, typically of the order of 1µm, which is more difficult to control.

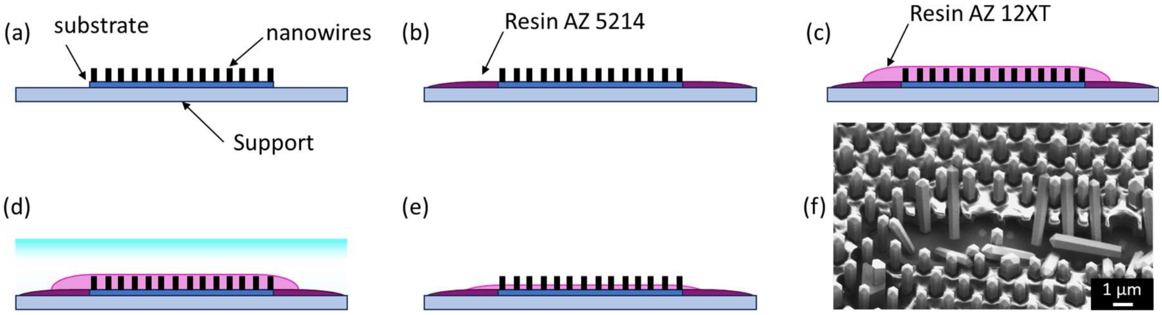

Figure V-23: *Process of resist deposition on the feet of the nanowires. The substrate is first bounded to a support with a few droplets of AZ 5214 (a). The support of the nanowire is then covered with AZ 5214 (b), and the AZ 12XT resist is spin coated. The sample is then exposed to UV light (d), and the resist is developed by 20 seconds increments. (f) SEM picture of a sample at the end of the process*

The process goes as follow. First, the sample is bonded to a support that can be used on a spin coater (Fig. V-23 (a)), in our case a dummy Sapphire wafer. To do so, a few droplets of AZ 5214 are deposited on the backside of the sample, which is deposited on the support and subsequently annealed. When the resist sticks the sample and the support together, additional resist is applied to the side of the sample (Fig. V-23 (b)). This prevents the arising of inhomogeneities on the side of the sample during spin coating. The samples are then annealed following the instructions of the provider. When the resist is fully cured, an AZ 12XT photolithographic resist is spin coated on the sample (Fig. V-23(c)), fully covering the nanowires, and subsequently annealed following the instructions of the provider. The sample is then exposed to a UV source. It should be noted that the irradiation dose of the resist is going to directly impact the depth at which the resist is going to be developed, and in the case of this work, a dose of 185 mJ.cm^{-2}. The sample is then developed in an AZ 726 MIF bath by increments of 20 seconds, checking systematically with an optical microscope when the nanowires are exposed.

While Fig. V-23(f) demonstrates the feasibility of such process, numerous issues need to be addressed. First, the process is not very reproducible, as the thickness of deposited resist and the speed at which it is etched by the developer will vary from sample to sample. Hence, the final thickness of resist is not going to be the same on all samples, which will impact the amount of injected area per NW in the final device. Another issue is that the resist is prone to compression during curing. This will manifest itself by the appearance of ridges in the resist layer once cured, that follow directions set by the nanowire array (Fig. V-24(a)). In some extreme cases, that might have been influenced by the variation of atmospheric parameters in the cleanroom, the compression of the resist was strong enough to rip the nanowires apart from the substrate, which ended up destroying the samples (Fig. V-24(b)). This shows that significant efforts are required for optimization of this process, both in the choice of the resist and in the parameters used. This has unfortunately not been performed during this PhD due to time constraints.

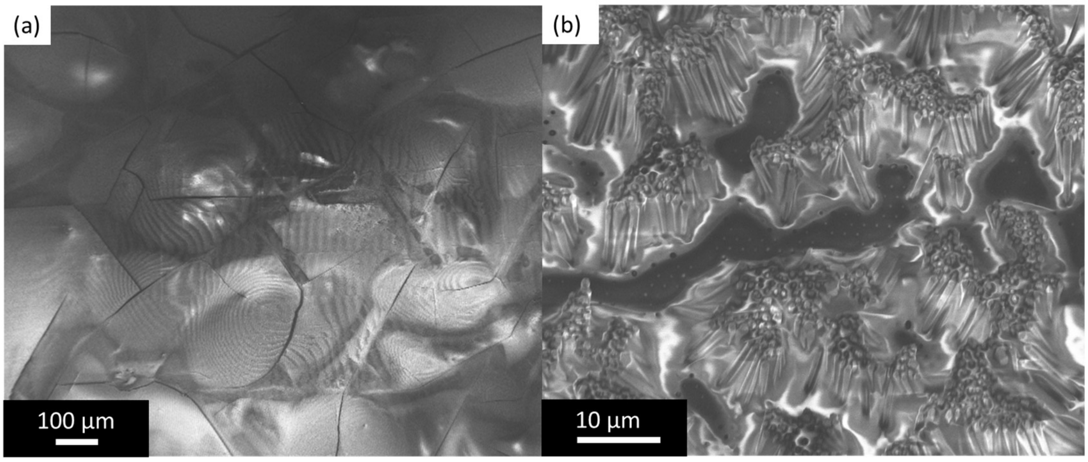

Figure V-24: *Issues caused by the use and development of a lithographic resist on a nanowire array. (a) Presence of cracks in the resist layer due to resist contraction. (b) Ripping of the nanowires form the substrate due to contraction. The presence of numerous cracks is also evidenced by the anisotropic development. Both samples were observed after resist deposition, annealing, exposition and development.*

Once the step presented in Fig. V-23(f) is reached, the sample is ready for metal deposition. Because the metal contact is realized on the sidewalls of the nanowires, the sample needs to be tilted to a sufficient angle to allow the deposition of a conformal and continuous metal layer. However, the tilt angle is also limited by the density of the array, as shadowing effects may arise when the angle gets too high, depending on the pitch of the structures and their height. In this case, part of the sidewalls would not be covered by the p-contact. Working with samples without a resist protection, it was found that a tilt angle of 25° was appropriate for the sample used in this PhD, as demonstrated in the Fig. V-25. Despite these first round of results being unsuccessful, Figure V-23(f) clearly demonstrates the feasibility of this process, and additional steps need to be undertaken to identify the critical parameters for making this method reliable and repeatable.

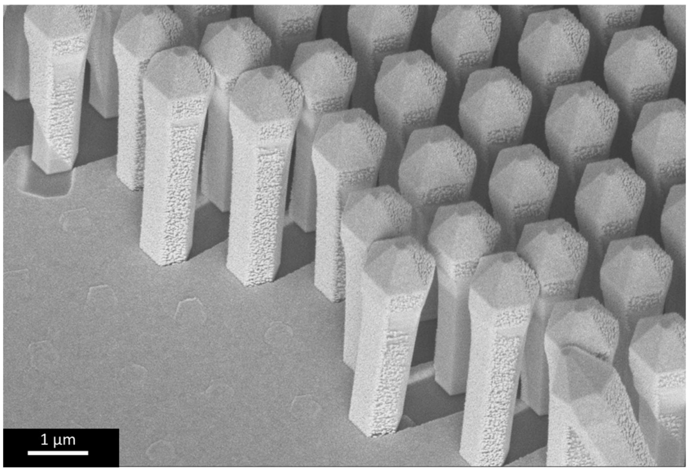

Figure V-25: *Tilted Ni/Au deposition on the sidewall of a nanowire array at a tilt angle of 25°, and without mask protection from the resist. The metal contact forms a smooth layer on the sides of the nanowire, while the shadowing effect is visible on the mask.*

3. CONCLUSION

In this work, we demonstrated the elaboration of a flexible device with embedded SAG InGaN/GaN nanowire core shell LED structure, adapting a process presented in a previous report[35] from self-organized nanowires to SAG nanowires. The electroluminescence of the device was measured and allowed to evidence the sidewall emission of the sample. However, some clear issues were demonstrated by the obtention of a leaky IV characteristic as well as a discontinuous and unstable light emission. Some clues were given toward optimizing the device and reaching a strong and homogeneous emission from the device. However other approaches described in the literature need to be considered: Among these approaches, one in particular is of significant interest, and consists in using 2D materials as a way to limit the adhesion of the grown structures to their host substrate. In the next chapter, we will provide some information on the attempts made during this PhD of using this property by growing light emitting structures on a well-known 2D material, graphene.

BIBLIOGRAPHY

1. Lee SH, Kim J, Shin JH, et al. Optogenetic control of body movements via flexible vertical light-emitting diodes on brain surface. *Nano Energy*. 2018;44:447-455. doi:https://doi.org/10.1016/j.nanoen.2017.12.011

2. Zeng FG, Rebscher S, Harrison W, Sun X, Feng H. Cochlear Implants: System Design, Integration, and Evaluation. *IEEE Rev Biomed Eng*. 2008;1:115-142. doi:10.1109/RBME.2008.2008250

3. Goßler C, Bierbrauer C, Moser R, et al. GaN-based micro-LED arrays on flexible substrates for optical cochlear implants. *J Phys D Appl Phys*. 2014;47(20):205401. doi:10.1088/0022-3727/47/20/205401

4. Sun N, Jiang C, Li Q, Tan D, Bi S, Song J. Performance of OLED under mechanical strain: a review. *Journal of Materials Science: Materials in Electronics*. 2020;31(23):20688-20729. doi:https://doi.org/10.1007/s10854-020-04652-5

5. Hong G, Gan X, Leonhardt C, et al. A Brief History of OLEDs—Emitter Development and Industry Milestones. *Advanced Materials*. 2021;33(9):2005630. doi:https://doi.org/10.1002/adma.202005630

6. Sasabe H, Kido J. Development of high performance OLEDs for general lighting. *J Mater Chem C Mater*. 2013;1(9):1699-1707. doi:https://doi.org/10.1039/C2TC00584K

7. Thejo Kalyani N, Dhoble SJ. Novel materials for fabrication and encapsulation of OLEDs. *Renewable and Sustainable Energy Reviews*. 2015;44:319-347. doi:https://doi.org/10.1016/j.rser.2014.11.070

8. Sugimoto A, Ochi H, Fujimura S, Yoshida A, Miyadera T, Tsuchida M. Flexible OLED displays using plastic substrates. *IEEE Journal on Selected Topics in Quantum Electronics*. 2004;10(1):107-114. doi:10.1109/JSTQE.2004.824112

9. Sudheendran Swayamprabha S, Dubey DK, Shahnawaz, et al. Approaches for Long Lifetime Organic Light Emitting Diodes. *Advanced Science*. 2021;8(1):2002254. doi:https://doi.org/10.1002/advs.202002254

10. Fish DA, Childs MJ, Deane SC, et al. Improved optical feedback for OLED differential ageing correction. *J Soc Inf Disp*. 2005;13(2):131-138. doi:https://doi.org/10.1889/1.2012595

11. Olivier F. *Etude Des Caractéristiques Électro-Optiques de Micro-LED GaN Pour Application Aux Micro-Écrans Haute-Luminance*. Université Grenoble Alpes; 2018. https://theses.hal.science/tel-01868252

12. Vasilopoulou M, Mohd Yusoff AR bin, Daboczi M, et al. High efficiency blue organic light-emitting diodes with below-bandgap electroluminescence. *Nat Commun*. 2021;12:4868. doi:https://doi.org/10.1038/s41467-021-25135-z

13. Fu J, Zhao L, Zhang N, Wang J, Li J. Influence of electron distribution on efficiency droop for GaN-based light emitting diodes. *Journal of Solid State Lighting*. 2015;2:5. doi:https://doi.org/10.1186/s40539-015-0024-y

14. Lee SH, Park SY, Lee KJ. Laser lift-off of GaN thin film and its application to the flexible light emitting diodes. In: *Biosensing and Nanomedicine V*. Vol 8460. SPIE; 2012:846011. doi:https://doi.org/10.1117/12.964095

15. Chen J, Wang J, Ji K, et al. Flexible, stretchable, and transparent InGaN/GaN multiple quantum wells/polyacrylamide hydrogel-based light emitting diodes. *Nano Res*. 2022;15:5492-5499. doi:https://doi.org/10.1007/s12274-022-4170-4

16. Chung K, Lee CH, Yi GC. Transferable GaN Layers Grown on ZnO-Coated Graphene Layers for Optoelectronic Devices. *Science (1979)*. 2010;330(6004):655-657. doi:https://doi.org/10.1126/science.1195403

17. Kobayashi Y, Kumakura K, Akasaka T, Makimoto T. Layered boron nitride as a release layer for mechanical transfer of GaN-based devices. *Nature*. 2012;484:223-227. doi:https://doi.org/10.1038/nature10970

18. Nowak R, Pessa M, Suganuma M, et al. Elastic and plastic properties of GaN determined by nano-indentation of bulk crystal. *Appl Phys Lett*. 1999;75(14):2070-2072. doi:https://doi.org/10.1063/1.124919

19. Fujikane M, Nagao S, Chrobak D, Yokogawa T, Nowak R. Room-Temperature Plasticity of a Nanosized GaN Crystal. *Nano Lett*. 2021;21(15):6425-6431. doi:https://doi.org/10.1021/acs.nanolett.1c00773

20. Javad Mirshojaeian Hosseini M, Nawrocki RA. A review of the progress of thin-film transistors and their technologies for flexible electronics. *Micromachines (Basel)*. 2021;12(6):655. doi:https://doi.org/10.3390/mi12060655

21. Wyser Y, Pelletier C, Lange J. Predicting and determining the bending stiffness of thin films and laminates. *Packaging Technology and Science*. 2001;14(3):97-108. doi:https://doi.org/10.1002/pts.540

22. Yoo HG, Park KI, Koo M, et al. Flexible GaN LED on a polyimide substrate for display applications. In: *Quantum Sensing and Nanophotonic Devices IX*. Vol 8268. SPIE; 2012:82681Y. doi:https://doi.org/10.1117/12.904772

23. Asad M, Li Q, Sachdev M, Wong WS. Thermal and optical properties of high-density GaN micro-LED arrays on flexible substrates. *Nano Energy*. 2020;73:104724. doi:https://doi.org/10.1016/j.nanoen.2020.104724

24. Kim T Il, McCall JG, Jung YH, et al. Injectable, cellular-scale optoelectronics with applications for wireless optogenetics. *Science (1979)*. 2013;340(6129):211-216. doi:https://doi.org/10.1126/science.1232437

25. Choi JH, Cho EH, Lee YS, et al. Fully flexible gan light-emitting diodes through nanovoid-mediated transfer. *Adv Opt Mater*. 2014;2(3):267-274. doi:https://doi.org/10.1002/adom.201300435

26. Chun J, Hwang Y, Choi YS, et al. Transfer of GaN LEDs from sapphire to flexible substrates by laser lift-off and contact printing. *IEEE Photonics Technology Letters*. 2012;24(23):2115-2118. doi:10.1109/LPT.2012.2221694

27. Wang L, Ma J, Liu Z, Yi X, Zhu H, Wang G. In Situ Fabrication of Bendable Microscale Hexagonal Pyramids Array Vertical Light Emitting Diodes with Graphene as Stretchable Electrical Interconnects. *ACS Photonics*. 2014;1(5):421-429. doi:https://doi.org/10.1021/ph500133w

28. Tian P, McKendry JJD, Gu E, et al. Fabrication, characterization and applications of flexible vertical InGaN micro-light emitting diode arrays. *Opt Express*. 2016;24(1):699-707. doi:https://doi.org/10.1364/OE.24.000699

29. Seo JH, Li J, Lee J, et al. A Simplified Method of Making Flexible Blue LEDs on a Plastic Substrate. *IEEE Photonics J*. 2015;7(2). doi:10.1109/JPHOT.2015.2412459

30. Reddy NK, Devika M, Tu CW. High-quality ZnO nanorod based flexible devices for electronic and biological applications. *RSC Adv*. 2014;4(71):37563-37568. doi:https://doi.org/10.1039/C4RA05712K

31. Calabrese G, Corfdir P, Gao G, et al. Molecular beam epitaxy of single crystalline GaN nanowires on a flexible Ti foil. *Appl Phys Lett*. 2016;108(20):202101. doi:https://doi.org/10.1063/1.4950707

32. May BJ, Sarwar ATMG, Myers RC. Nanowire LEDs grown directly on flexible metal foil. *Appl Phys Lett*. 2016;108(14):141103. doi:https://doi.org/10.1063/1.4945419

33. Asad M, Wang R, Ra YH, Gavirneni P, Mi Z, Wong WS. Optically invariant InGaN nanowire light-emitting diodes on flexible substrates under mechanical manipulation. *npj Flexible Electronics*. 2019;3(1):16. doi:https://doi.org/10.1038/s41528-019-0059-z

34. Dai X, Messanvi A, Zhang H, et al. Flexible Light-Emitting Diodes Based on Vertical Nitride Nanowires. *Nano Lett*. 2015;15(10):6958-6964. doi:https://doi.org/10.1021/acs.nanolett.5b02900

35. Guan N, Dai X, Babichev A V., Julien FH, Tchernycheva M. Flexible inorganic light emitting diodes based on semiconductor nanowires. *Chem Sci*. 2017;8(12):7904-7911. doi:https://doi.org/10.1039/C7SC02573D

36. Guan N, Dai X, Messanvi A, et al. Flexible White Light Emitting Diodes Based on Nitride Nanowires and Nanophosphors. *ACS Photonics*. 2016;3(4):597-603. doi:https://doi.org/10.1021/acsphotonics.5b00696

37. Jeong J, Wang Q, Cha J, et al. Remote heteroepitaxy of GaN microrod heterostructures for deformable light-emitting diodes and wafer recycle. *Sci Adv*. 2020;6(23). doi:https://doi.org/10.1126/sciadv.aaz5180

38. Chung K, Beak H, Tchoe Y, et al. Growth and characterizations of GaN micro-rods on graphene films for flexible light emitting diodes. *APL Mater*. 2014;2(9):092512. doi:https://doi.org/10.1063/1.4894780

39. Kochetkov FM, Neplokh V, Mastalieva VA, et al. Stretchable transparent light-emitting diodes based on ingan/gan quantum well microwires and carbon nanotube films. *Nanomaterials*. 2021;11(6):1503. doi:https://doi.org/10.3390/nano11061503

40. Lee CH, Kim YJ, Hong YJ, et al. Flexible inorganic nanostructure light-emitting diodes fabricated on graphene films. *Advanced Materials*. 2011;23(40):4614-4619. doi:10.1002/adma.201102407

41. Lu W, Goto N, Murakami H, et al. Controlled synthesis of nonpolar GaInN/GaN multiple-quantum-shells on GaN nanowires by metal-organic chemical vapour deposition. *Appl Surf Sci*. 2020;509:145271. doi:https://doi.org/10.1016/j.apsusc.2020.145271

42. Spurgeon JM, Boettcher SW, Kelzenberg MD, Brunschwig BS, Atwater HA, Lewis NS. Flexible, polymer-supported, si wire array photoelectrodes. *Advanced Materials*. 2010;22(30):3277-3281. doi:https://doi.org/10.1002/adma.201000602

43. Chung K, Yoo H, Hyun JK, et al. Flexible GaN Light-Emitting Diodes Using GaN Microdisks Epitaxial Laterally Overgrown on Graphene Dots. *Advanced Materials*. 2016;28(35):7688-7694. doi:https://doi.org/10.1002/adma.201601894

44. Lobo N, Rodriguez H, Knauer A, et al. Enhancement of light extraction in ultraviolet light-emitting diodes using nanopixel contact design with Al reflector. *Appl Phys Lett*. 2010;96(8):081109. doi:https://doi.org/10.1063/1.3334721

45. Liu YJ, Huang CC, Chen TY, et al. Improved performance of GaN-based light-emitting diodes by using short-period superlattice structures. *Progress in Natural Science: Materials International*. 2010;20:70-75. doi:https://doi.org/10.1016/S1002-0071(12)60009-4

46. Wuu DS, Huang SH, Horng RH, Hsieh CY, Yen KW. Highly efficient InGaN/GaN LEDs with double-sided textured surfaces and omni-directional mirror structure. In: *Gallium Nitride Materials and Devices III*. Vol 6894. SPIE; 2008:68941E. doi:https://doi.org/10.1117/12.763248

47. Han SH, Baek SH, Lee HJ, Kim H, Lee SN. Breakdown-induced conductive channel for III-nitride light-emitting devices. *Sci Rep*. 2018;8:16547. doi:https://doi.org/10.1038/s41598-018-34869-8

48. Ho WC, Liu YH, Wu WH, et al. The study of high breakdown voltage vertical gan-on-gan p-i-n diode with modified mesa structure. *Crystals (Basel)*. 2020;10(8):712. doi:https://doi.org/10.3390/cryst10080712

49. Bosch J, Coulon PM, Chenot S, et al. Etching of the SiGaxN yPassivation Layer for Full Emissive Lateral Facet Coverage in InGaN/GaN Core-Shell Nanowires by MOVPE. *Cryst Growth Des*. 2022;22(9):5206-5214. doi:https://doi.org/10.1021/acs.cgd.2c00286

50. Jung BO, Bae SY, Lee S, et al. Emission Characteristics of InGaN/GaN Core-Shell Nanorods Embedded in a 3D Light-Emitting Diode. *Nanoscale Res Lett*. 2016;11:215. doi:https://doi.org/10.1186/s11671-016-1441-6

51. Coulon PM, Damilano B, Alloing B, et al. Displacement Talbot lithography for nano-engineering of III-nitride materials. *Microsyst Nanoeng*. 2019;5:52. doi:https://doi.org/10.1038/s41378-019-0101-2

52. Toshihiko Tanaka, Mitsuaki Morigami, Nobufumi Atoda. Mechanism of Resist Pattern Collapse during Development Process. *Jpn J Appl Phys*. 1993;32(12S):6059. doi:10.1143/JJAP.32.6059

53. Klein T, Yan S, Cui J, et al. Liquid Viscosity and Surface Tension of n-Hexane, n-Octane, n-Decane, and n-Hexadecane up to 573 K by Surface Light Scattering. *J Chem Eng Data*. 2019;64(9):4116-4131. doi:https://doi.org/10.1021/acs.jced.9b00525

54. Thakur DK, Hickman K. Surface tension of water at 100°C. *J Colloid Interface Sci*. 1975;50(3):525-531. doi:https://doi.org/10.1016/0021-9797(75)90175-7

55. Lee JM, Lee KS, Park SJ. Removal of dry etch damage in p-type GaN by wet etching of sacrificial oxide layer. *Journal of Vacuum Science & Technology B*. 2004;22(2):479-482. doi:https://doi.org/10.1116/1.1645880

56. Koide Y, Maeda T, Kawakami T, et al. Effects of annealing in an oxygen ambient on electrical properties of ohmic contacts to p-type GaN. *J Electron Mater*. 1999;28:341-346. doi:https://doi.org/10.1007/s11664-999-0037-7

57. Cao XA, Pearton SJ, Zhang AP, et al. Electrical effects of plasma damage in p-GaN. *Appl Phys Lett*. 1999;75(17):2569-2571. doi:https://doi.org/10.1063/1.125080

Chapter 6 :

GaN nanostructures on graphene

TABLE DES MATIERES

In the previous chapter, a method for the elaboration of flexible Light emitting devices has been presented. However, this method is not the only strategy that has been used for the fabrication of such devices. Among the method used, one consists in using 2D materials for the growth of the heterostructures. Indeed, as explained in Chapter 1, growth on such materials results in a low cohesion between the grown material and its substrate, which is particularly interesting when it comes to peeling-off the structure off their substrate. In this PhD, some attention has been given to the growth on 2D materials, specifically on graphene. This work will be reported in this chapter. The methods used will be presented, along with a state of the art about MOCVD growth of GaN nanostructures on graphene. The structural properties of the samples have been studied, and a growth mechanism has been proposed. Last, the obtained nanostructures will be used for the growth of an InGaN/GaN heterostructure for their potential use in optically active components.

1. MOCVD GROWTH ON GRAPHENE: A CHALLENGING PROCESS

1.1 GROWTH AND PROPERTIES OF GRAPHENE USED

The first graphene elaboration is usually attributed to Novoselov *et al.*[1] by exfoliation, but its properties were predicted decades ago[2], and that some earlier reports observed a material with similarities with graphene[3,4]. There are today a variety of processing resulting in the formation of graphene, such as mechanical exfoliation[5], electrochemical exfoliation[6], CVD growth on various metals[7], and Si sublimation of SiC[8]. Graphene properties such as the number of layers, coverage of the substrate, domain size and defect density vary from one method to another, due to different involved growth mechanisms. This PhD work is only focused on graphene from CVD growth on SiC, which allows to achieve key-advantages as the complete coverage of the substrate by the graphene, the ability to work with monolayer graphene, and the low defect density.

When talking about CVD of graphene, it is important to mention one of the most popular methods in use: the graphene growth on metallic foil (usually copper) using methane/hydrogen CVD[9]. Indeed, this CVD method allows to get high coverages of graphene on commercial copper foil that drastically reduces the price of the process compared to process using crystalline wafer substrates. The growth on this substrate allows also to easily transfer the graphene on various substrates. However, the graphene itself is defective as can been seen on the SEM image of the Fig. V-1. Moreover, the direct use of graphene on copper is proscribed in a MOCVD setup, because the presence of copper in the chamber would lead to the uncontrolled growth of GaN parasitic structures on both the substrate and the parts of the reactor that could be contaminated with metal particulates.

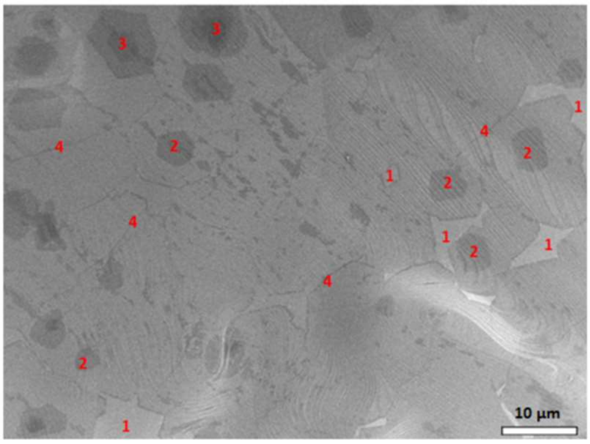

Figure VI-1: *SEM picture of graphene grown on copper foil with various common features (1: uncovered copper; 2: bilayer graphene; 3: trilayer island; 4: grain boundaries) from ref.* [10]

Hence, the option chosen in this PhD work is the use of graphene directly grown on SiC substrate by CVD. This process has several advantages. First, it does not require any transfers, as SiC has been commonly used as a substrate in MOCVD growths. Second, more interestingly, the properties of the graphene can be directly controlled, such as the number of layers, its poly or monocrystallinity nature, or its rotational order relative to the SiC[11]. In the next paragraphs, we will talk in more details about the properties of SiC and graphene, and the process used to produce monolayer graphene on SiC.

1.1.1 SiC, CRYSTALLOGRAPHIC STRUCTURE AND POLYTYPES

SiC is a semiconductor of the IV/IV family. The bandgap varies with the crystalline structure of the material but is usually indirect and between 2.2 and 3.3 eV[12].

When it comes to its crystalline structure, SiC has three main reported phases: a cubic Zinc Blende, a hexagonal Wurtzite structure and a rhombohedral structure[13]. However, this material is known to have a large variety of possible crystal[13] structures due to polytypism. This property consists in the existence of several crystalline structure sharing the same structure in the basal plane, but with different stacking. The notation for SiC polytypes consists in a letter indicating the base crystal structure (H, C and R for Hexagonal, Cubic and Rhombohedral respectively), as well as a number corresponding to the bilayer periodicity of the stack. For example, the basic wurtzite structure polytype corresponds to an AB stacking of two bilayers and is hence noted 2H-SiC, while the Zinc Blende structure consisting of an ABC stacking of 3 bilayers is noted 3C-SiC.

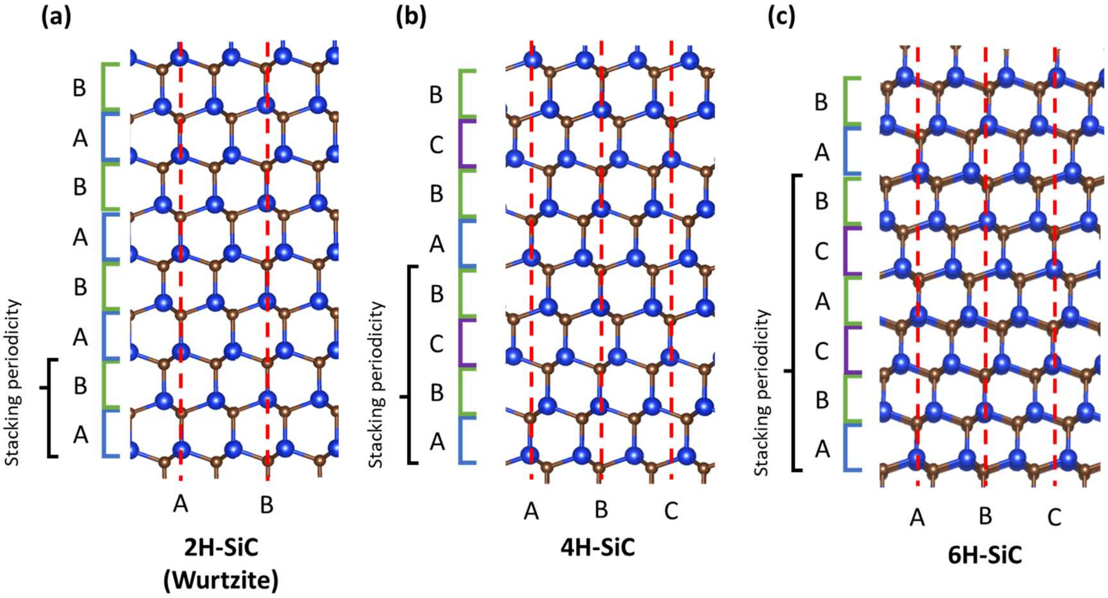

Figure VI-2: *Stacking order in different hexagonal polytypes of SiC: (a) Wurtzite, (b) 4H-SiC, (c) 6H-SiC*

In the scope of this work, the goal was to grow graphene and III-nitrides on top of the SiC. Both materials are expected to have a hexagonal basal structure, and hence, two hexagonal polytypes of SiC, 4H-SiC and 6H-SiC have been used to achieve remote epitaxy of GaN on SiC through the graphene layer. Both structures, presented in Fig. VI-2, are commercially available and have been already successfully used to grow graphene[11,14] by the group of A. Michon from CRHEA (CNRS).

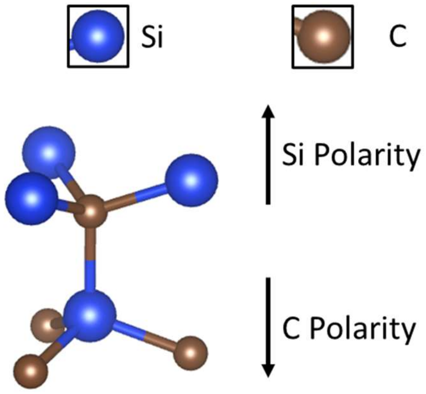

Figure VI-3: *Polarities of SiC around the (0001) vertical bound*

Due to the wurtzite arrangement, the H-polytypes of SiC exhibit polarity, much like III-nitride compounds. Here again, an electronegativity difference existing between Si and C involves spontaneous polarization. In 4H and 6H-SiC, the value of this polarization is significantly lower than in nitride materials, except for the 2H-SiC polytype that is comparable to that of GaN[15]. In the case of 4H and 6H-SiC that have been used in the PhD, the estimated values of polarization given in ref [15] are of the order of $1 \cdot 10^{-2} C.m^{-2}$, which is about three times lower than reported values for GaN[16]. Si-polar and C-polar surfaces (Fig. VI-3) have different thermochemical properties for similar reason to the ones explained in Chapter 1 for nitrides. Hence, it is important to take this parameter into account for the growth on SiC, as it will influence the properties of the grown structures, particularly graphene, as will be specified in next paragraph.

1.1.2 BUFFER ASSISTED GRAPHENE SYNTHESIS ON SiC

Before explaining how SiC can be used for graphene growth, the structural characteristics of graphene will be presented. Graphene is a 2D material consisting of a single layer of sp^2 hybridized carbon atoms, which means that each atom is bounded to three other neighboring atoms and shares a short-range delocalized π electron[17]. With such configuration, this material does not have any dangling bond. The atoms are organized in a characteristic honeycomb structure[18,19] (Fig. VI-4 (a)). The band structure of graphene is unusual, as it is neither a true semiconductor nor a metal, but strictly speaking a null bandgap semiconductor[18,19] (Fig. VI-4 (b)). The band structure corresponds to the energy levels of the bonding and anti-bonding orbitals of the π electrons, and the point where they meet is called the Dirac point. Graphene can be considered as a single graphite monolayer and stacking several graphene monolayers on top of each other will result in coupling between the layers, leading to a gradual collapse of the graphene properties towards graphite properties.

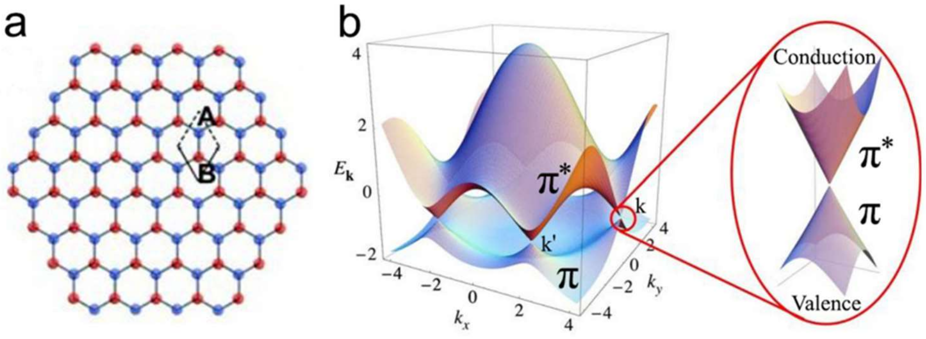

Figure VI-4: *Crystal structure of a single graphene sheet (a) and corresponding band structure (b)(taken from ref.* [20] *)*

The fabrication of graphene on SiC was first reported by preferentially sublimating the Si, leaving an excess of C atoms that can reconstruct into graphene layers[21,22]. While sublimation is not the method used in this PhD, propane-CVD, both processes share some mechanisms[23], such as the formation of a buffer layer. Indeed, in the case of Si-polar SiC, the graphene formation starts with the formation of a buffer carbon layer, which is referred to as the $6\sqrt{3} \times 6\sqrt{3} - R°30$, which will be simplified to $6\sqrt{3}$ or buffer here[24]. This layer shares similarities with the graphene, as its crystalline structure and lattice parameters[25], but this layer is partially covalently bonded to the SiC itself, and hence contains a significant amount of sp^3 carbon atoms[26]. The $6\sqrt{3}$ layer is also rotated with respect to the SiC, which allows to create a super lattice with it. This layer has no dangling bonds and can therefore be used as a buffer for the subsequent VdW of graphene, which follows the crystallographic direction of the $6\sqrt{3}$ layer. This make possible to grow large domains of monolayer graphene (1LG), since the graphene growth is driven by surface reconstruction on a partially sp^2 buffer, and can be controlled with greater precision, especially when the process is carried out under argon rather than vacuum[27]. The presence of this buffer is thought to be a necessary condition for the growth of 1LG[11], as its absence on C-polar graphene is thought to be responsible for the growth of multiLayer graphene (MLG) with rotational disorder[24]. However, while this process produces high-quality graphene, it necessarily means that there is always another $6\sqrt{3}$ layer underneath, as shown in the Fig. VI-5(a).

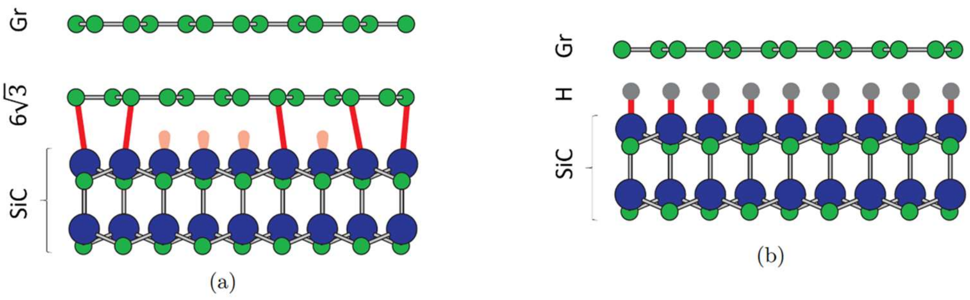

(a)

(b)

Figure VI-5: *Graphene grown on a* $6\sqrt{3}$ *buffer layer on SiC (a) and quasi-free-standing graphene on hydrogenated SiC (b) (taken from ref.* [28] *)*

However, there is another way to realize this fabrication, which is to provide an additional source of carbon (in the present case propane) for graphene growth, making this process a CVD process[11,29,30]. It should be noted that despite propane being a carbon contributor for the graphene formation, the sublimation of Si and surface reconstruction of SiC carbon atoms is still occurring[23]. In propane-CVD, it is also possible to grow graphene on Si-polar SiC without having to rely on the formation of a buffer layer. Indeed, several reports showed the possibility to decouple entirely the buffer layer from the SiC by annealing it under H_2 atmosphere[28,31] by hydrogenation the SiC-$6\sqrt{3}$ bonds, as shown in the Fig. VI-5(b). Michon *et al.*[11] from CRHEA reported that the H_2 addition during growth leads to the hydrogenation of the SiC prior to the growth of the buffer layer, which allow a direct growth of a single layer of graphene. However, because the $6\sqrt{3}$ buffer layer is expected to have an impact on the quality of the graphene, growing graphene on hydrogenated SiC leads to a multidomain graphene with different co-existing rotations, as is the case on C-polar graphene[11].

In the scope of this work, the method used to fabricate graphene on SiC was propane CVD. The precise conditions used to grow the graphene are specified in 2.3.1. It has been chosen to work with 1LG graphene, and MLG graphene grown with H_2 introduction on the Si-polar SiC. There are two reasons for this choice. The first one is that the apparatus on which the growth was performed is not optimized to work with C-polar SiC, and the growth would have yielded a lower quality graphene. The second is that the polarization of the underlying substrate can influence the subsequent growth on graphene in the case of remote epitaxy, as will be discusses in 2.3.1, and using this method allows to work with the same polarity of SiC.

2. GROWTH OF TETRAHEDRAL STRUCTURES ON GRAPHENE/SiC

Having presented the materials used as substrates in this study, the growth of GaN on such substrates can be presented. In the next paragraph, we will discuss about the issues of growing GaN on graphene, as well as the method used in this work to successfully grow GaN nanostructures on graphene/SiC.

2.1 ISSUES WITH MOCVD GROWTH ON A 2D MATERIAL

The presence of dangling bonds is partly responsible for surface energy and adatom adhesion during epitaxial growth. The complete absence of these dangling bonds in graphene involves a very low surface energy, which limits the ability of the adatoms to nucleate, and extends their diffusion length. This is responsible for several phenomena reported in the literature:

- **Nucleation at defects sites** : defects in graphene lead to the presence of sp^3 hybridized carbon atoms, which have an electronic cloud in a volume, unlike the planar sp^2 hybridized carbon atoms that form graphene. This sp^2 hybridization requires the presence of 3 surrounding carbon atoms. Therefore, carbon atoms located around vacancies, extrinsic defects, or domain boundaries exhibit a sp^3 hybridization, providing dangling bonds that act as preferred nucleation points.
- **Nucleation promoted by extended holes in the graphene** : the presence of holes in the graphene provides both carbon atoms in sp^3 configuration and openings to the underlying substrate. If the substrate under the graphene is crystalline, such as Si, SiC or Sapphire, the difference in surface energy leads to an adatom accumulation and subsequent nucleation at this point. This was pointed out by Tessarek *et al.*[32], who reported the growth of GaN nanowires on sapphire through holes in the graphene (see the Fig. VI-6(a)). This issue is problematic, as the growth of the GaN through nano-scale openings in the graphene cannot

always be noticed, even by means of TEM microscopy, since it would require the sample thinning by FIB to be realized exactly at the location of the opening. Defective graphene grown through copper-CVD and reported on sapphire have been successfully used to grow nanowires in this work, however these results were quickly discarded. To confirm this idea, growth performed under the same conditions on epitaxial graphene on SiC did not allow to grow any nanowire. Indeed, Fig. VI-6(b) shows a SEM picture of a graphene/SiC substrate used in a nanowire growth, which resulted in the growth of pyramidal crystallites. This result suggests that nanowires grown on transferred graphene on sapphire, as shows in Fig. VI-6(a), occur through holes in the graphene. It should be noted that some impactful studies failed to mention this issue, such in the case in ref [33]. Indeed, the authors reported the growth of GaN nanowires on transferred graphene but the remote epitaxy of GaN on graphene with 3 layers or more could not be performed. However, remote epitaxy on multilayer graphene with more than three layers has since then been performed, and this effect can probably be explained through a very low density of defects extending through all 3 layers of graphene, providing a window to the sapphire.

In addition to the nucleation promoted by defects and holes, there are other issues arising from the low surface energy of graphene. First, assuming that defect nucleation is not dominant, the nucleation density is expected to be low, because the adatom diffusion length is expected to be longer on a 2D material, and hence the distance between two nucleates may be longer. Second, due to the low nucleate density, there is also an accumulation of adatoms on the graphene surface, which leads to the formation of Ga metallic droplets on the surface. While they do not pose any issue during the growth, since their presence is related to the lack of reaction between gallium and nitrogen, they could be potentially problematic for subsequent steps in the process.

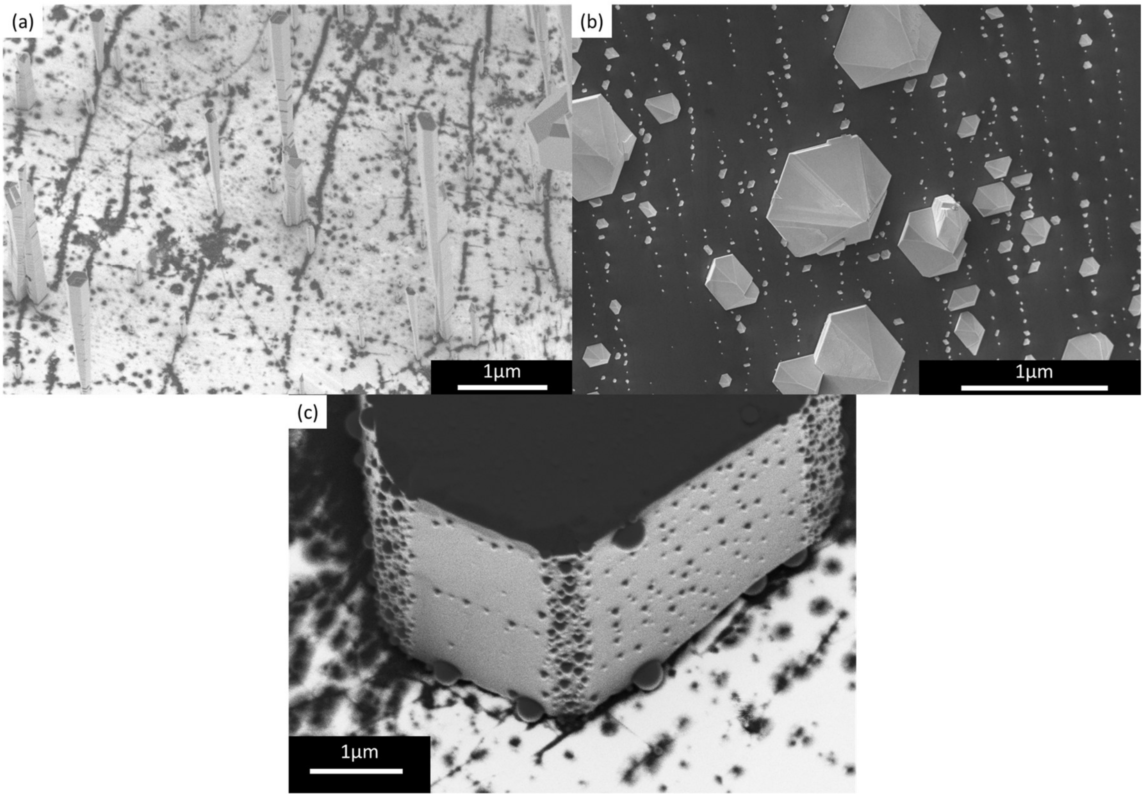

Figure VI-6: SEM images of *GaN growth under nanowire conditions on graphene grown on copper foil and transferred to sapphire (a) and on epitaxial graphene over 6H-SiC (b). Droplets on a sidewall of a platelet structure grown on transferred graphene, hypothesized as being Gallium droplets (c). (all growths were performed in the scope of this PhD)*

An example of these issues is presented in Fig. VI-6, which refers to experiments carried out for this thesis at PHELIQS (CEA-Grenoble). In this figure, both samples (Fig.VI-6 (a,b)) have been submitted to the same GaN growth under nanowire conditions, including a nucleation step followed by silane-assisted growth. The samples differ in the substrate used: one is sapphire covered with transferred graphene grown by CVD on Cu, and the other corresponds to an epitaxial graphene monolayer on 6H-SiC. In both cases, droplets have been observed on some of the structures, such as exhibited on Fig.VI-6 (c). Similar features have been observed in comparable systems and have been identified has being Ga metal droplets which show the difficulty to nucleate crystalline material on graphene. The striking difference observed when comparing the two samples is the achievement of nanowire growth only for the sample with transferred graphene. This observation is consistent with the growth driven by hole nucleation, following a similar mechanism as seen in SAG, where the holes act as a sink for incoming adatoms. This assumption is reasonable with respect to the defect density in the graphene layer. Note, however, that the wire density on graphene is still lower than the direct growth on sapphire. On the contrary, the growth on epitaxial graphene on SiC with very low defect density leads to the formation of pyramids usually related to the WdV epitaxy of GaN[34–36]. We assume that this modification of growth mode is responsible for the absence of nanowires, which could be caused by a preferential passivation of the semi-polar planes by SiN_x instead of non-polar, that stops the vertical growth of the nanowires.

2.2 TETRAHEDRAL GaN STUCTURES IN THE LITTERATURE

In the context of this work, the main object of study has been GaN nuclei in the shape of tetrahedra especially for growths on SiC, that we may refer to as nano-tetrahedron (Fig. VI-7). These 3-fold symmetry structures are unusual in the case of GaN nanostructures based on semipolar planes, which usually have a 6-fold symmetry. In this paragraph, we will provide a short review on this shape of nuclei and attempt to explain the formation of such structures.

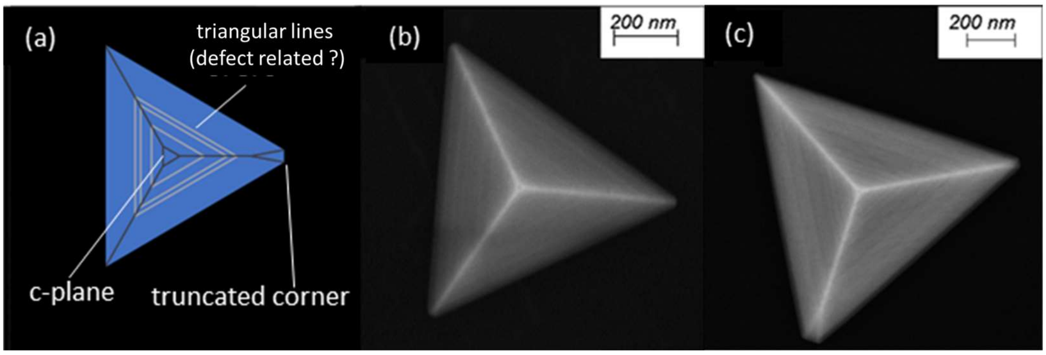

Figure VI-7: *(a) schematic representation of a typical GaN nano-tetrahedron, and SEM images of these structures grown on 1LG/6H-SiC (b) and on MLG/4H-SiC (ref*[14]*)*

The presence of tetrahedral GaN structures has already been reported in the literature, usually observed when the growth is performed on graphene. The study by Journot *et al.*[35,36], pointed out the basic properties of such structures grown on graphene over SiC, concluding a remote epitaxy of the WZ-GaN on SiC through the graphene. The study[35] pointed out the presence of tetrahedra for VdW epitaxy on graphene with, whereas hexagonal pyramids were obtained in the case of direct growth on SiC substrate through holes or defects in the graphene. C. Barbier[34] also mentioned the presence of such tetrahedral structures on graphene transferred to amorphous SiO_2/Si substrates, which suggests that this 3-fold structure results from Van Der Waals epitaxy on graphene, regardless of the nature of the underlying substrate. This latter study evidenced the presence of stacking faults in the structures, but more importantly that the structures themselves followed a mainly Zinc Blende crystal structure with WZ-GaN inclusions, unlike the previously mentioned structures obtained on graphene/SiC[35,36] It should be noted that such structures were also featured in other reports of growth on graphene in which they were not the object of interest and have hence not been characterized[37–39]. Last, it is interesting to note that this tetrahedral geometry has also been described in GaN grown on substrate without graphene such as SiN_x/sapphire[40,41] and in III-arsenide compounds[42].

2.3 IMPACT OF THE NUMBER OF GRAPHENE LAYERS

2.3.1 NUCLEATION

Assuming a pure Van Der Waals epitaxy[34], we expect no impact from the number of graphene layers on top of the substrate because the top graphene layer drives the growth. In remote epitaxy[35,36], the growth is explained by the electrostatic coupling[39,43–45] between the GaN and the potential field[46] of the underlying crystalline substrate because of field penetration through the graphene[47,48]. Therefore, growing on multilayer graphene will induce a larger distance and the underlying substrate. This could hence modify the mechanisms of growth if this distance gets high enough, as the grown GaN would not be electrostatically influenced by the substrate[45].

As part of this work, we have hence tried to grow GaN nano-tetrahedron on both a mono and multilayer GaN on SiC, has it could give key information on the growth mechanism of these structures. The growth conditions of graphene on 4H-SiC are reported in Ref. [14]. For the 1LG sample, the growth was performed at 1550°C and 800mbars for 15 minutes, and the gas fluxes were maintained at 10slm, 1slm and 10sccm for Ar, H_2 and C_3H_8 respectively. For the MLG sample, the growth was performed at 1450°C for 5 minutes, under a H_2 flux of 12slm, all other parameters being kept similar. This difference in H_2 flux is one of the key parameters for the obtention of MLG instead of 1LG, as it allows to decouple the $6\sqrt{3}$ buffer from the SiC into a standalone graphene layer by saturating SiC with hydrogen. Hence, the 1LG graphene is expected to feature a $6\sqrt{3}$ buffer, while the MLG features a SiC with dangling bonds fully passivated by hydrogen, as explained in 1.1.2. The MLG is expected to have between 3 and 5 graphene layers. The GaN growth step was carried under the same conditions for both samples, as they were processed in the same run of an MOCVD process. The samples are first annealed under NH_3 as described by Journot *et al.* [35,36] in order to prepare the surface for growth. The GaN growth was then performed at 950 °C and 150 mbar for 150 s. The gas fluxes were maintained at 67 $mmol.min^{-1}$ and 135 $\mu mol.min^{-1}$ for NH_3 and TMGa respectively.

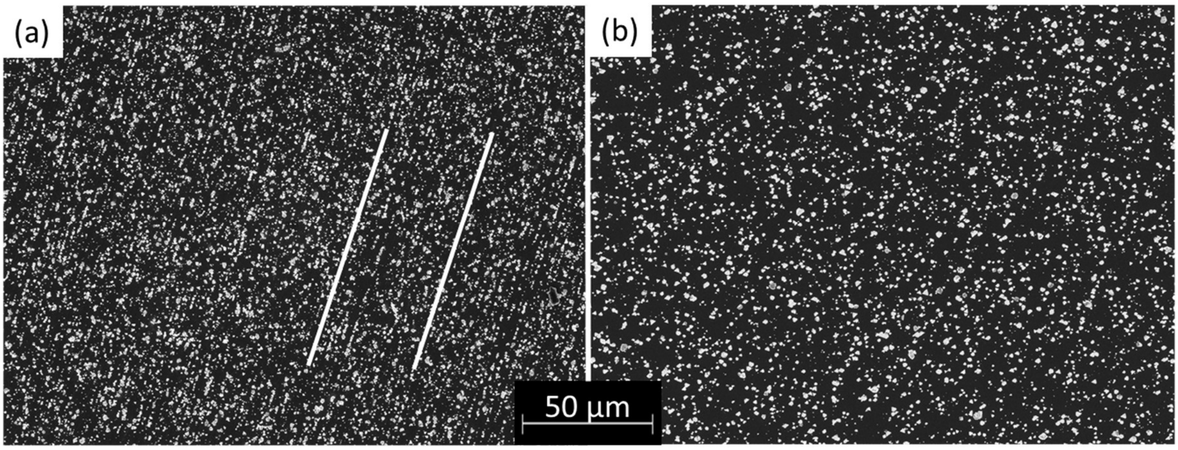

Figure VI-8: *Low magnification SEM images of tetrahedral GaN structures grown on 4H-SiC covered with a single graphene layer (a), and with multilayer graphene (b). (ref [14])*

Low magnification SEM images of the 1LG and MLG samples after GaN growth are presented in Fig. VI-8 and show several differences, such as a higher density and an isotropic distribution of the nuclei on the 1LG sample. Assuming remote epitaxy, the higher density could be a consequence of the distance from the SiC, that could help promoting nucleation on the 1LG sample because of its proximity. However, it is difficult to conclude since different samples have yielded a variety of nucleation densities, which also tend to modify the size of the structure. However, what can be observed is that the crystallites tend to nucleate following lines on the 1LG sample (Fig. VI-8 (a)), while the crystallites on the MLG sample seem to be randomly distributed (Fig. VI-8 (b)).

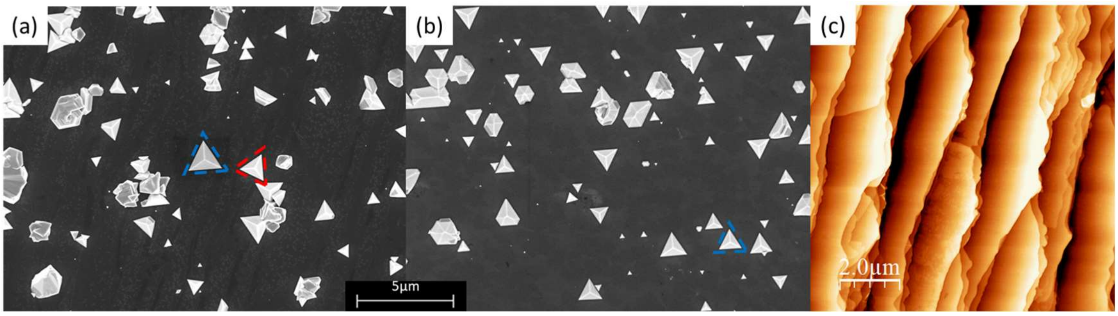

Figure VI-9: *High magnification SEM images of tetrahedral GaN structures on 4H-SiC covered with a single graphene layer (a) and with multilayer graphene (b). (c) AFM scan showing the surface step of a 1LG/4H-SiC stack before GaN growth.*

Fig. VI-9 gives an explanation to this behavior. Indeed, it is possible to see the presence of lines on the 1LG sample, corresponding to the atomic steps of the underlying SiC. This presence of steps is especially amplified on this sample because, as was seen in Fig. VI-9(c), AFM measurements revealed the presence of step bunching. The edge of the steps are areas propitious for nucleation, as they feature a higher density of dangling bonds in the SiC. Hence, it has been observed that on samples covered with 1LG, the nucleation tended to occur near atomic step edges, and formed recognizable line patterns of nucleation. On the other hand, the MLG sample does not share this behavior because of the presence of additional graphene layers. The presence of additional graphene layers indeed helps smoothing the surface, which can be directly seen from the SEM, as the features associated with the presence of steps are absent, and we instead see on the images contrasts that could be caused by a local variation of the number of graphene layers.[45] It also creates a larger distance between the growth surface and the underlying SiC, which limits the influence of higher densities of dangling bonds near the step edges.

Additionally, another difference between growths on 1LG and MLG is the orientation of the tetrahedra. Indeed, on the MLG surface, we notice that all the tetrahedra follow a single common orientation, which is expected in the case of remote epitaxy, as it is the case when growing GaN on graphene over SiC. However, the 1LG features two populations of tetrahedra with different orientation, that have a relative angle of 30°, as shown by the triangles of different color in Fig. VI-9 (a). The explanation can be directly found in the process used to grow the graphene. Indeed, the rotation of 30° is characteristic of the $6\sqrt{3}$ buffer, and one can then assume that part of the tetrahedra were oriented following the buffer instead of the SiC. Indeed, while the graphene is also rotated at an angle of 30° relative to the SiC, it is not polarized, and the presence of a polarization field due to the ionicity of the Si-C bound is the main influence driving the organization of adatoms into nuclei[45]. Hence, the presence of the buffer introduces new electrostatic field that might also influence the nucleation of GaN. The presence of both orientations on the substrate shows that the influence of both the $6\sqrt{3}$ buffer and the SiC are of comparable strength. This is why on the multi-layer sample in which the buffer is absent, only one common orientation is found (Fig. VI-9(b)).

2.3.2 X-RAY DIFFRACTION AND ELECTROSTATIC INFLUENCE

In the previous paragraph, it was assumed that the growth occurred following remote epitaxy on the SiC through the graphene, as previous work[35,36] observed on similar system. However, it was shown that the crystallinity of the nano-tetrahedra could vary from ZB to WZ, and could occur through either Van der Waals or remote epitaxy[34–36]. Hence, when working on this system, it is necessary to carry adequate characterization to check both the crystallinity and the growth mode. One of the best tools to do so is to use X-ray diffraction, as it allows to measure the crystallinity of both SiC and GaN, as well as the strain state of the GaN nuclei, which is critical because both VdW and remote epitaxy are expected to yield fully relaxed GaN. The methods used here were introduced in Chapter 2.

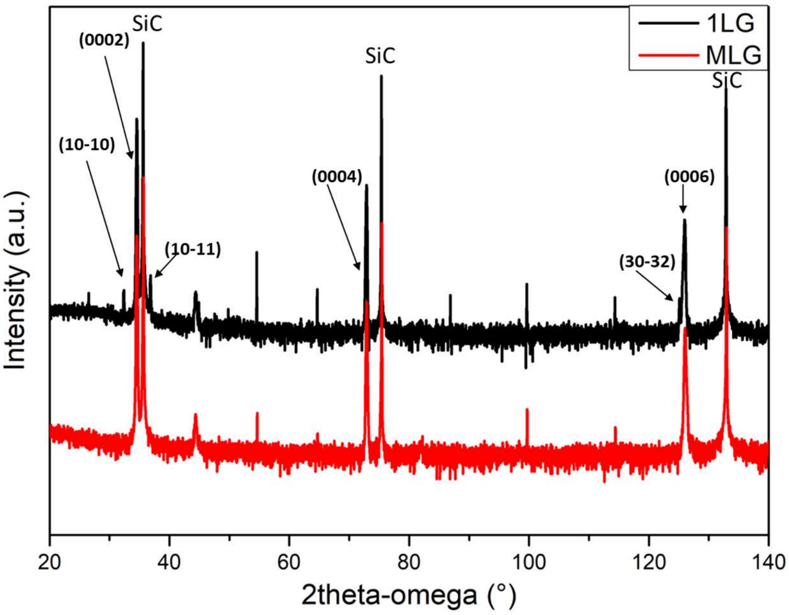

Figure VI-10: *2-Theta-omega scan on 1LG and MLG samples.*

The first measurement was to do a full range 2theta-omega scan, presented in Fig. VI-10. This allows to check the crystallinity of the samples and the substrate, if the GaN nuclei were ZB or WZ structures in the present case. Similar to previous reports of tetrahedral growth on graphene SiC, the only observed peaks corresponding to GaN were WZ-GaN families of planes. The peak observed for both samples corresponded to either the (0001) family or the $(10\bar{1}1)$ family of planes suspected to correspond to the pyramidal facets of the tetrahedra.

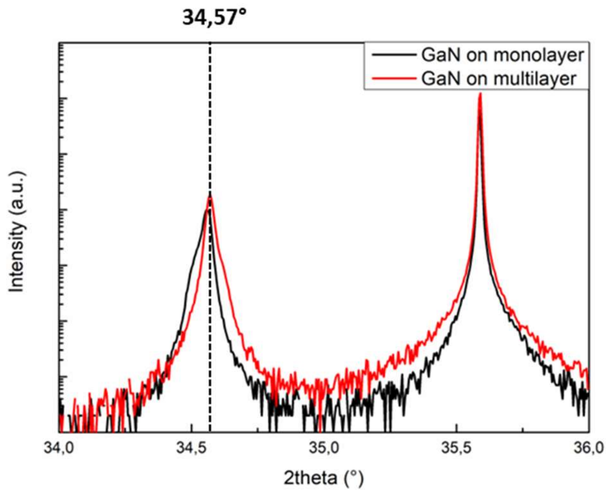

Figure VI-11: *2theta-omega X-ray diffraction diagram of the GaN structures around the (0002) peak for both 1LG and MLG*

Fig. VI-11 shows the 2theta-omega X-ray diffraction diagram, which is used to measure the strain state of the GaN. In both the monolayer and multilayer case, the peak (0002) is centered around 34.57°, which is expected for relaxed GaN[35,36]. Hence, it can be concluded that the growth does not occur through covalent epitaxy, as direct epitaxy on SiC leads to significant strain in the GaN material. The growth is driven through either VdW or remote epitaxy, and not through openings in the graphene. In both cases, the peak features some amount of asymmetry suggesting the presence of residual strain. It could be caused by the presence of a small number of nuclei growing through openings in the graphene, or because of WZ to ZB transition in the crystal during growth, which will be discussed further in 3.2.

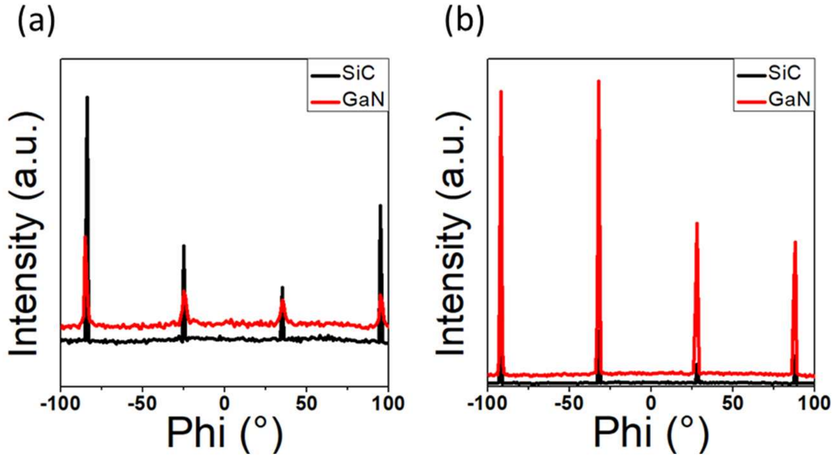

Figure V-12: *Phi-scan around the (0001) axis for GaN grown on 1LG (a) and MLG (b) grown on SiC.*

A subsequent Phi-scan was performed around the (0001) axis for both samples, showing the $(1\bar{1}01)$ reflections for both the GaN and the SiC to check the relative crystallographic orientation in the basal plane of GaN relative to the SiC substrate (Fig. VI-12). In both cases, the presence of a peak with a 60° repetition for both the GaN and SiC is observed. More importantly, the fact that the peak associated with GaN and SiC concur proves that the growth was done by remote epitaxy.

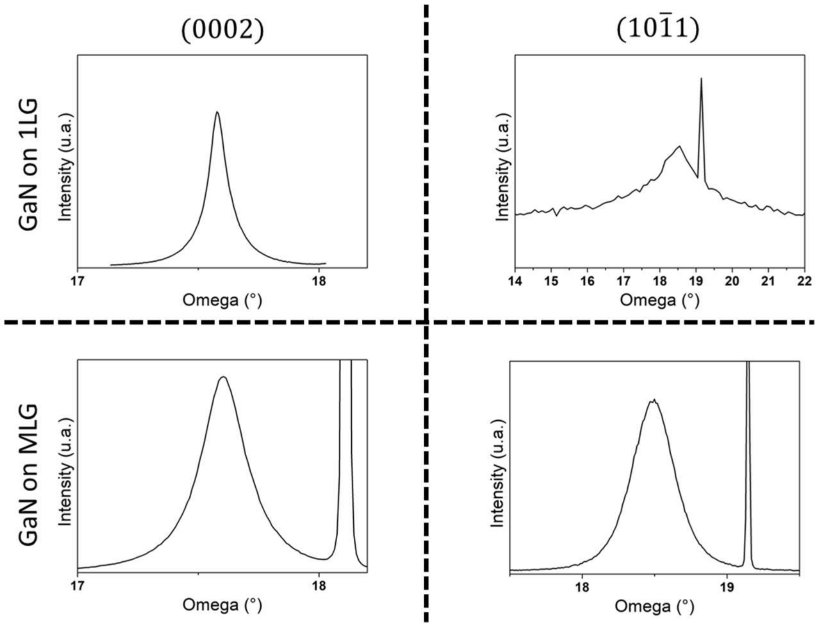

Figure VI-13: *Omega-scan centered around the* (0002) *and the* $(10\bar{1}1)$ *peak for GaN on both 1LG and MLG samples. (ref*[14]*)*

The last characterization that was made using XRD was Omega scans around the (0002) and $(10\bar{1}1)$ peaks of GaN, as they allow to quantify the tilt and twist respectively of GaN nuclei[49] (Fig. VI-13). Comparing the (0002) peak on both samples, the FWHM of the MLG sample (~0.23°) is more than twice as high as than the one on the 1LG (~0.1°), meaning that the nuclei have a higher tilt on this sample. It could be due to a stronger coupling with the [0001] direction of the SiC in the 1LG sample due to a shorter distance between SiC and the GaN, or it could be caused by a nucleation at the boundary of an additional graphene layer on the MLG sample. However, the critical difference between the two samples occurs on the $(10\bar{1}1)$ peak. Here, the FWHM is roughly four times higher on the 1LG sample (~1.2°) than on the MLG sample (~0.35°), revealing a lower twist of GaN grown on the MLG sample. This is surprising as one would expect a higher coupling of the GaN to the SiC with a single layer, but, as stated previously, the presence of the buffer could create disturbances in this coupling. Hence, the competition between the SiC and the buffer electrostatic influences leads to a poor coupling between the deposited GaN and SiC, and therefore a poor orientation homogeneity on such 1LG substrates. This is constituent with the observation made on Fig. VI-9(a), that show that some of the nuclei grown on the 1LG sample have a 30° rotation relative to the other nuclei, which corresponds to the relative rotation of the buffer with the SiC.

In conclusion, we have checked with this characterization method that the growth of GaN on graphene on SiC occurred through remote epitaxy and yielded WZ-GaN tetrahedral nuclei. This process has been done using 1LG and MLG samples and revealed that the presence of the buffer layer in 1LG samples had detrimental effects on the homogeneity of the nuclei, as it disturbed the electrostatic coupling between the adatoms and the SiC substrate. The use of several layers of graphene would reduce the probability of having holes extending to the substrate, making it also a good way to avoid the presence of covalently bonded structures. In the other hand, using too many layers of graphene will end up weakening the coupling of the GaN to the underlying substrate, meaning that there is a maximum of a graphene layer that can be used for remote epitaxy. This study proves that such remote epitaxy growth can occur with 3 to 5 layers of graphene. One solution that has not been tried in this work, and that could be an appropriate compromise would be to use a 1LG and decouple the buffer layer before growth by annealing under H_2 atmosphere. This would lead to a graphene bilayer, leading to a strong coupling to the SiC with no disturbance of a buffer layer, with limited effect from atomic steps and limited covalent growth.

2.4 TETRAHEDRA AND GROWTH MECHANISM

Despite having elucidated some of the parameters responsible for the growth, no explanation has been given for the unusual tetrahedral shape of the nuclei. However, the question of a 3-fold symmetry in GaN nuclei has already been addressed. Indeed, as pointed out in several reports[40,50,51], the m-planes in GaN are not equivalent, but can instead be distinguished into two different categories, as seen in Fig. VI-14 (a), with a 3-fold rotational symmetry. The so-called type A m-plane exhibits two dangling bonds, while the type B m-plane exhibits only one. Therefore, under conditions not limited by diffusion lengths, the growth of type A m-planes is expected to have a faster growth rate than type B. In the specific case of both graphene and dielectric masks such as SiN_x, the lack of dangling bonds and/or crystalline structures leads to extended diffusion lengths, which could explain why such geometries are promoted on such substrates. This mechanism is supported by several reports[40,50,51] suggesting that the triangular structure growth is caused by the distinction between type A and type B m-planes, if the reactive species have great diffusion lengths. Interestingly enough, because of the similarities between the WZ (0001) and the ZB (111) plane of GaN evoked in chapter I, a very similar behavior can be seen on (111) ZB GaN with the $(\bar{2}11)$ plane family (Fig. VI-14(a)). There is however a key difference between ZB and WZ GaN in this configuration, which is the alternation of the stacks. Indeed, as can be seen on Fig. VI-14(b), if a step is type-A oriented on a specific bilayer, the subsequently grown bilayer will be type-B oriented, and growth proceeds through an alternation of type-A and type-B steps. In planar structures, this phenomenon is responsible for step bunching, as the type-A steps will grow until it catches up with the type-B step it is grown on, creating a two-bilayer step[50,51]. In this case, the type-A face bilayer will grow until it reaches the edge of the type-B face, which explains why the WZ-tetrahedra keep a triangular basal shape despite the type of the facet alternating for each bilayer (Fig. VI-14(b)). On the other hand, the ZB structure keeps the type of the surface during stacking, meaning that there is no step bunching, and that the sidewalls of entire facets can be type-B, explaining the tetrahedral shape.

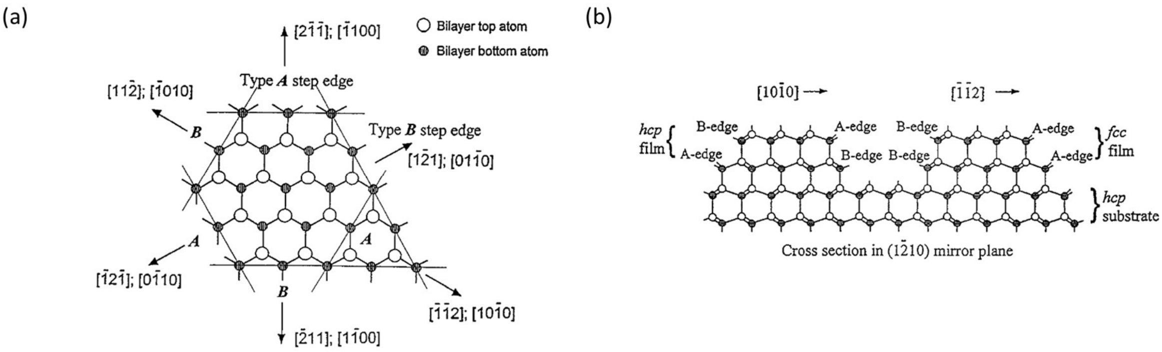

Figure VI-14: *(a) View of the GaN structure showing the difference between Type A and Type B of m-plane surfaces in a single bilayer, and (b) evolution of the type of edge in both ZB and WZ GaN stackings (from ref*[51]*).*

The study of the nucleation of triangular structures in MBE has been the object of several studies by Xie et al.[50,51] In these studies, the authors first prove the co-existence of ZB and WZ nuclei on a N-polar GaN buffer grown on 6H-SiC. The crystal structure was reportedly influenced by two parameters, mainly the temperature and the ratio of Ga to N introduction. Additionally, to growth conditions, one possibility to explain the ZB-GaN structure reported by C. Barbier[34] is the presence of excess GaN on the structure caused by an accumulation on graphene, as previously stated. On the other hand, Journot *et al.*[35,36] reported hexagonal WZ structures, which could have been influenced by the remote epitaxy on hexagonal 6H-SiC, which was absent in the graphene/amorphic SiO_2 substrate used by C. Barbier[34].

Proposed growth mechanism of tetrahedral pyramids:

In our case, we propose the following growth mechanism for tetrahedral nuclei:

- upon introducing the precursors in the growth chamber, a first bilayer of GaN is deposited (Fig. VI-15 (a)). Because of their higher density of dangling bonds, type-A crystallographic faces outgrow type-B faces, leading to a triangular nucleus.
- The growth of a second bilayer determines if the nuclei is going to organize following a ZB or WZ structure. In the case of WZ GaN (Fig. VI-15 (b)), despite an inversion of the types of the facets for each bilayer, the growth proceeds until it allows the formation of stable semipolar **$(1\bar{1}01)$** faces. In ZB GaN (Fig. VI-15 (c)), the subsequent layer will have a similar shape and orientation, as the stack conserves the type of surfaces, and the growth will yield (100) type-B faces with low density of dangling bonds. The structure (WZ or ZB) is expected to be determined by the temperature and Ga to N ratios but could also be affected by the nature of the growth, either Van Der Waals on the graphene, or remote through the graphene with the subsequent crystalline substrate.
- Finally, the tetrahedron reaches a size that does not allow the diffusion of the species to the Type-A surfaces preferentially. In many papers mentioned here, the growth is stopped before this stage is reached, but Zhilai *et al.*[40] report for WZ GaN that at this stage, type-A facets start to reappear (Fig. VI-15 (e)), as they can no longer outgrow the type-B facets due to the limited diffusion length. Continuing the growth has hence been shown to result in a gradual shift from triangular to hexagonal shape (Fig. VI-15 (f)).

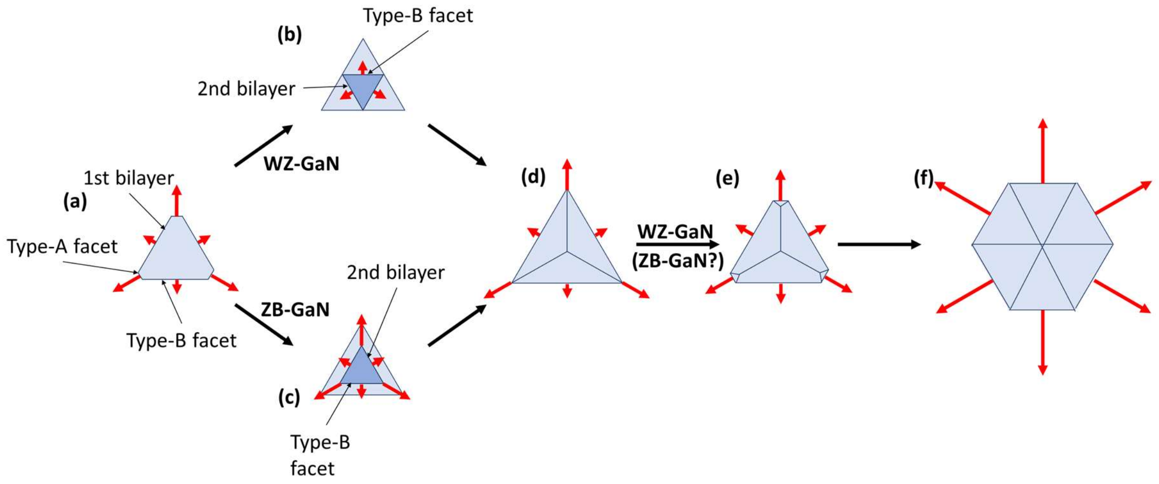

Figure V-15: *Proposed mechanism for the growth of GaN nano-tetrahedral structures: first nucleation of the first bilayer, with a faster growth of type-A facets, leading to a triangular shape (a). The second bilayer determines if the crystal is WZ or ZB. In the WZ case, the orientation of A and B facets is inversed in the second bilayer (b), while it is conserved in ZB-GaN. The growth proceeds to yield a tetrahedral GaN structure of either crystallographic configuration (d). Reportedly in the case, the growth speed of type-A facets slows down relative to type B facets (e), transitioning toward a regular hexagon shape (f)*

3. InGaN/GaN ACTIVE REGIONS ON GaN TETRAHEDRAL NANOSTRUCTURES

Having studied the structure of the GaN tetrahedral growths, the growth of active regions on such nanostructure has been tried. The next paragraph will focus on the growth of InGaN quantum wells on these structures, and their optical characterization by both PL and CL. Last, we will discuss how these results can be linked to the structural study presented previously.

3.1 TUNABLE LUMINESCENCE OF THE ACTIVE REGION ON GaN TETRAHEDRAL STRUCTURES

The use of quantum wells on semipolar structure has been reported in the literature as a strategy for active devices with longer wavelength and improved efficiency[52]. This, and the fact that the GaN tetrahedra are not covalently bounded to the substrate make them good candidates for the elaboration of flexible devices[53], as it allows to avoid a technically difficult process, while allowing wafer recycling[54].

The growth of the active layer is performed directly after GaN tetrahedral growth on 1LG/6H-SiC and consisted in the deposition of three period of InGaN quantum well separated by GaN barrier in order to target blue emission. The conditions of growth were as described in Ref [14]. The QWs were grown at 750°C at 400 mbar for 80 seconds each, with gas fluxes of 22mmol.min^{-1}, 8µmol.min^{-1} and 56µmol.min^{-1} for NH_3, TMIn and TMGa respectively. Subsequently to the growth the structures were characterized in a CL setup. The results are presented in Fig. VI-16.

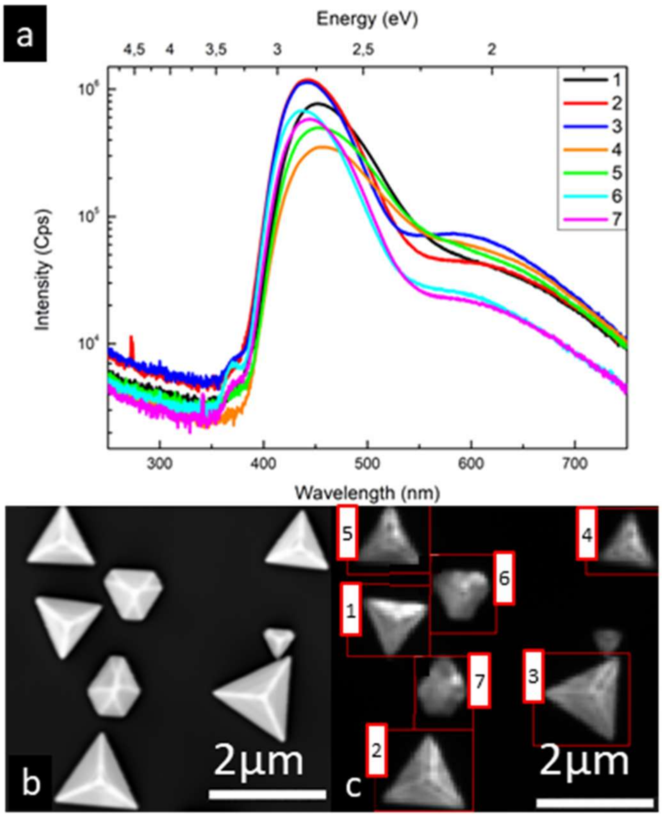

Figure VI-16: *Cathodoluminescence spectrum of different structures (a) with corresponding SEM (b) and panchromatic images (c). The labeling on the spectra in (a) corresponds to the measured structure seen in (c). (ref*[14]*)*

In the Fig. VI-16, four regions can be distinguished. The first one, between 350 and 400 nm is expected to be associated with the band edge. However, a further study of this contribution reveals some additional information on the crystalline quality of the structures and will hence be discussed in the next paragraph. The main contribution seen here is the quantum well peak, visible between 425 and 475 nm, which is within the usual emitted range of InGaN/GaN QWs. This contribution is followed by a tail up to 500 nm, which indicates variations in either the composition or thickness of the quantum wells. The last broad contribution can be witnessed around 600 nm. To identify the origin of these contribution, a CL mapping of the samples were performed as it would help determining the areas of emissions for each contribution. The results are presented in Fig. VI-17.

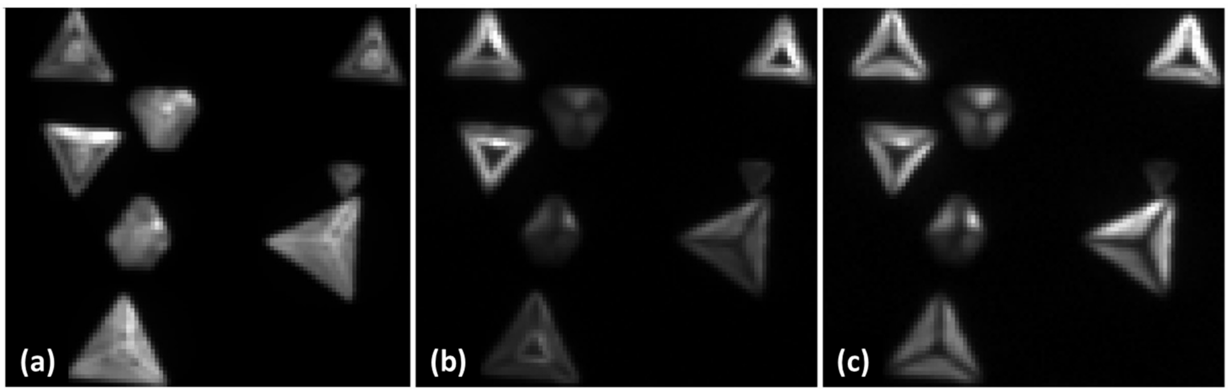

Figure VI-17: *CL mapping of the SEM picture of Fig. VI-16 at 450 (±20) nm (a), 550 (±20) nm (b) and 600 (±20) nm (c). (ref[14])*

From Fig. VI-17 (a), it can be concluded that the structures exhibit emission from InGaN quantum wells covering the entirety of most of the tetrahedra. However, three tetrahedra also exhibit a ring of lower intensity at a given height. Interestingly, for these given structures, a complementary signal emission is found at 550 nm (Fig. VI-17 (b)), featuring a bright ring, with the rest of the structures being less luminescent. This indicates that the QW energy shift occurs in a specific part of the nanostructure and are certainly not caused by random alloy fluctuation or by over-diffusion through neighboring crystallographic planes. The signal around 600 nm occurs in the whole facet, but not at edges. This behavior[55], combined with the fact that this contribution is broad and not dominant suggests that it is defect related. Finally, a low temperature and room temperature PL characterization were performed to get an approximate value of IQE, that can be roughly estimated through the ratio of intensities at 4K and room temperature: $IQE \approx \frac{I_{300K}}{I_{4K}}$. The spectrum at low temperature was measured at 8K due to experimental limitations. Both spectra are presented in Fig. VI-18 and allow us to estimate the IQE to be around 25%.

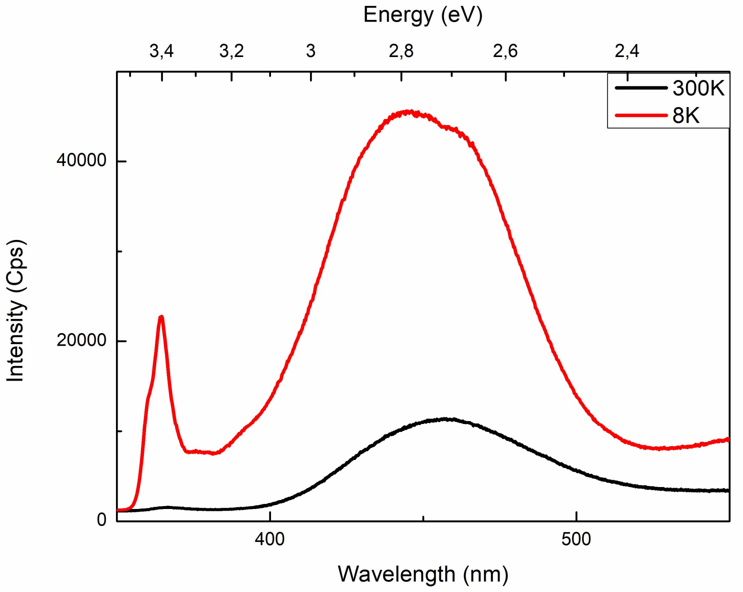

Figure VI-18: *Low and high temperature PL spectra of a sample with GaN nano-tetrahedra covered with a InGaN/GaN QWs.*

One detail that is especially striking at 8K is the double-peak nature of the GaN band edge emission near 350 nm, as shown in Fig. VI-18 for the low temperature PL measurement. This observation is unexpected in the case of pure WZ-GaN, suggesting the presence of a significant quantity of structural defects, that were investigated as part of this work. The corresponding results will be presented in the next paragraph.

3.2 IMPACT OF STACKING FAULTS ON THE LUMINESCENCE

The presence of structural defects in structures grown through remote epitaxy is unexpected due to the absence of covalent bonds limiting the strain and dislocation formation. However, there are several clues to the type of defect observed here. Indeed, by looking at Fig. VI-14 of part 2.4, we notice the presence of triangular ring-like shaped lines at different height on the tetrahedron, which do share similarities with the emission of the contribution at 550 nm in Fig.VI-17 in part 3.1. The fact that these features are seen at a constant height on the whole periphery of the structure suggest that it is a planar defect extending to a whole slice of the structure. The planar nature of this defect strongly suggests that it is some kind of stacking fault, which is confirmed by the fact that it occurs following the basal plane (according to the orientation of the defective area in both the SEM pictures and the CL mappings), and that it was also observed in a previous work[34].

The best way to characterize a defect such as a stacking fault is to do TEM microscopy, as it allows to get a direct observation of the stacking fault, and of its properties. However, TEM microscopy requires a FIB preparation, and hence to make a statistic over several nuclei, especially on self-organized samples that are expected to have some amount of irregularity from one individual nuclei to another. Here, it was chosen to use the data obtained by luminescence characterization to find the signature of stacking faults in the nuclei. Indeed, there are two ways that stacking faults are expected to influence the PL/CL response of an InGaN/GaN sample:

- First, ZB-GaN has a lower potential than that of WZ-GaN. Hence, the presence of a basal stacking fault in a WZ material can be seen as a quantum well, expected to have an associated signal that can be measured in PL/CL[56].
- Second, ZB-GaN has a higher In incorporation, and the presence of a stacking fault could hence be linked to a local redshift of the QW signal[57].

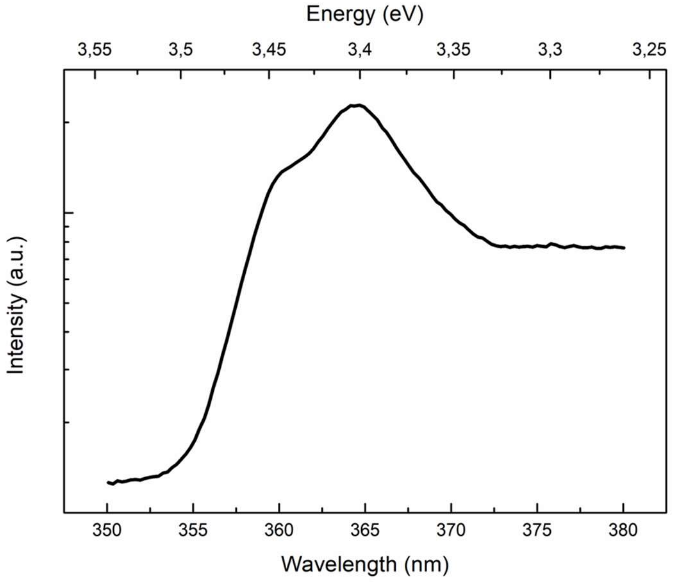

Figure VI-19: *PL spectra of a nano tetrahedron measured at 8K*

Fig. VI-19 shows the PL spectrum at low temperature. This spectrum exhibits a first 3.45 eV contribution, which can be linked to the band edge of the material. However, a second and stronger contribution at 3.4 eV can be seen, which, at low temperature, has been identified to be the signature of a I1 type BSF in GaN[58]. However, Fig. VI-16 shows a second type of contribution visible at room temperature. Because of the quenching of the photoluminescence signal of intrinsic stacking faults in GaN, it is likely that this signal is instead related to the presence of E type stacking faults, that act as thin ZB/WZ Gan QWs at room temperature[58]. Both these results would be consistent with the presence of ZB stacking inclusions in the material with thicknesses ranging from only one monolayer to thicker extrinsic stacks. This conclusion is further supported by the presence of a redshifted QW signal at 550 nm coming from localize areas in the tetrahedron, which is consistent with the presence of white lines seen in SEM pictures. As stated previously, stacking faults are expected to incorporate more In[57], therefore the presence of redshifted areas could be caused by high densities of stacking faults.

The formation of SF is also supported by a previous PhD study from C. Barbier[34]. Indeed, in this work, the nucleation was performed on transferred graphene over amorphous SiO_2 and yielded cubic GaN using the same growth conditions in the same MOCVD reactor. One prominent defect observed in Ref. [34] is the stacking fault, which, in the case of cubic GaN, exhibits the inclusion of WZ-stacking sequences inside the ZB crystal. While the crystalline structure is different in our case, it suggests that the stacking is susceptible to switch between the two crystalline structures during the growth. A similar conclusion has been made on crystallites grown in conditions allowing the formation of tetrahedral nuclei, as the authors have observed both ZB and WZ-GaN triangular layers grown on WZ GaN[50,51]. In this study, the authors suggest that changing parameters such as the temperature would allow to switch between both structures, with ranges allowing for both structures. Therefore, while Journot *et al.*[35,36] did not observe any stacking faults in their WZ-GaN tetrahedra, it could be due to parameters that strongly favored the WZ configuration. On the other hand, the conditions used by C. Barbier[34] did not favor either ZB and WZ, and the growth was driven by factors such as the graphene used or the presence or no of a crystalline template for remote epitaxy. As a result, the conditions allowed the occasional growth of a WZ stack in the ZB crystal, responsible for a stacking fault. Because the conditions used in this work are similar, we can then suppose that external factors to the growth (such as the substrate used) lead to the formation of a WZ stack, but the condition then allowed for the inclusions of ZB-GaN layers in the middle of the WZ crystallites. Because these stacking faults seem to be located in the upper part of the nano-tetrahedra, we can suppose that the presence of the ZB inclusions needed a precise window of conditions to occur. Previous studies have linked the switch from WZ to ZB to either temperature or diffusion. Therefore, the growth could momentarily oscillate irregularly between WZ and ZB stacking when specific growth conditions are met. For example, the diffusion length could change during growth because of the gradual covering of the low surface energy graphene by GaN. Hence, stacking fault generation could occur mid-growth, in a specific time when diffusion length is lower than early stages (with a graphene covered surface), but higher than late stage (with a surface covered by a high density of nuclei).

4. CONCLUSION

Our main goal in this work was to pave the way for the demonstration of light emitting flexible devices using GaN/InGaN structures grown by VdW or remote epitaxy on graphene. By choosing an already explored subject, namely the one of tetrahedral structures, we have been able to revisit it and bring new conclusions, particularly on the growth mechanism. The comparison between samples with one or several graphene layers allowed to understand the role of the $6\sqrt{3}$ buffer layer specific to the graphene grown on SiC. The growth of quantum wells on those structures showed that these structures might have uses as an optically active component, as previously shown by Journot *et al.*[35], but a more thorough investigation of the optoelectronic properties suggested the presence of stacking faults, as seen by C. Barbier[34]. The collected data allows to conclude that the growth of tetrahedral structure on graphene is probably a diffusion limited process, that occurs at the border between ZB-GaN and WZ-GaN conditions. In the case of epitaxial graphene on SiC, this process occurs through remote epitaxy, but is also able to occur through VdW epitaxy in the absence of an underlying crystal[34]. The main challenge regarding the use of such structure in a device will then be the integration of metallic contacts, as well as solving the issue of the stacking faults, which could be done by modifying the conditions to reach true WZ-GaN growth.

While this work leads to the growth and subsequent study of optically active structures on the GaN nanotetrahedra, the difficulty of the process should be considered. This is explained by the unusual properties of graphene, that are not suited for heteroepitaxial growth by MOCVD. One example of this statement is that it has not been possible to directly grow GaN nanowire by using VdW or remote epitaxy, as is the case in molecular beam epitaxy. Hence, hybrid growth methods might here represent a better strategy to tackle this issue, for instance, by using MBE grown GaN nanowires as a backbone for subsequent MOCVD growth of a InGaN/GaN shell.

BIBLIOGRAPHY

1. Novoselov KS, Geim AK, Morozov S V., et al. Electric field in atomically thin carbon films. *Science (1979)*. 2004;306(5696):666-669. doi:10.1126/science.1102896

2. Wallace PR. The Band Theory of Graphite. *Physical Review*. 1947;71(9):622-634. doi:10.1103/PhysRev.71.622

3. Engle GB. Low-temperature graphitization of cokes and binder-filler artifacts. *Carbon N Y*. 1972;10(4):409-415. doi:https://doi.org/10.1016/0008-6223(72)90057-7

4. Van Bommel AJ, Crombeen JE, Van Tooren A. LEED and Auger electron observations of the SiC(0001) surface. *Surf Sci*. 1975;48(2):463-472. doi:https://doi.org/10.1016/0039-6028(75)90419-7

5. Yi M, Shen Z. A review on mechanical exfoliation for the scalable production of graphene. *J Mater Chem A Mater*. 2015;3(22):11700-11715. doi:https://doi.org/10.1039/C5TA00252D

6. Parvez K, Wu ZS, Li R, et al. Exfoliation of graphite into graphene in aqueous solutions of inorganic salts. *J Am Chem Soc*. 2014;136(16):6083-6091. doi:https://doi.org/10.1021/ja5017156

7. Cabrero-Vilatela A, Weatherup RS, Braeuninger-Weimer P, Caneva S, Hofmann S. Towards a general growth model for graphene CVD on transition metal catalysts. *Nanoscale*. 2016;8(4):2149-2158. doi:https://doi.org/10.1039/C5NR06873H

8. Yazdi GR, Vasiliauskas R, Iakimov T, Zakharov A, Syväjärvi M, Yakimova R. Growth of large area monolayer graphene on 3C-SiC and a comparison with other SiC polytypes. *Carbon N Y*. 2013;57:477-484. doi:https://doi.org/10.1016/j.carbon.2013.02.022

9. Han Z, Kimouche A, Kalita D, et al. Homogeneous optical and electronic properties of graphene due to the suppression of multilayer patches during CVD on copper foils. *Adv Funct Mater*. 2014;24(7):964-970. doi:https://doi.org/10.1002/adfm.201301732

10. Lobet M, Reckinger N, Henrard L, Lambin P. Robust electromagnetic absorption by graphene/polymer heterostructures. *Nanotechnology*. 2015;26(28):285702. doi:10.1088/0957-4484/26/28/285702

11. Michon A, Vézian S, Roudon E, et al. Effects of pressure, temperature, and hydrogen during graphene growth on SiC(0001) using propane-hydrogen chemical vapor deposition. *J Appl Phys*. 2013;113(20):203501. doi:https://doi.org/10.1063/1.4806998

12. Lü J, Eisebitt S, Rubensson JE, Ellmers C, Eberhardt W. Electronic structure of silicon carbide polytypes studied by soft x-ray spectroscopy. *Phys Rev B*. 1999;59(16):10573-10582. doi:10.1103/PhysRevB.59.10573

13. Shaffer PTB. A review of the structure of silicon carbide. *Acta Crystallographica Section B*. 1969;25(3):477-488. doi:https://doi.org/10.1107/S0567740869002457

14. Bosch J, Valera L, Mastropasqua C, et al. InGaN/GaN QWs on tetrahedral structures grown on graphene/SiC. *Microelectron Eng*. 2023;275:111995. doi:https://doi.org/10.1016/j.mee.2023.111995

15. Davydov SY, Troshin A V. Estimates of the spontaneous polarization in silicon carbide. *Physics of the Solid State*. 2007;49(4):759-761. doi:https://doi.org/10.1134/S1063783407040270

16. Bernardini F, Fiorentini V, Vanderbilt D. Spontaneous polarization and piezoelectric constants of III-V nitrides. *Phys Rev B*. 1997;56(16):R10024-R10027. doi:https://doi.org/10.1103/PhysRevB.56.R10024

17. Popov IA, Bozhenko K V., Boldyrev AI. Is graphene aromatic? *Nano Res*. 2012;5(2):117-123. doi:https://doi.org/10.1007/s12274-011-0192-z

18. Yang G, Li L, Lee WB, Ng MC. Structure of graphene and its disorders: a review. *Sci Technol Adv Mater*. 2018;19(1):613-648. doi:https://doi.org/10.1080/14686996.2018.1494493

19. Castro Neto AH, Guinea F, Peres NMR, Novoselov KS, Geim AK. The electronic properties of graphene. *Rev Mod Phys*. 2009;81(1):109-162. doi:10.1103/RevModPhys.81.109

20. Shi Z, Khaledialidusti R, Malaki M, Zhang H. MXene-based materials for solar cell applications. *Nanomaterials*. 2021;11(12):3170. doi:https://doi.org/10.3390/nano11123170

21. Strupinski W, Grodecki K, Caban P, Ciepielewski P, Jozwik-Biala I, Baranowski JM. Formation mechanism of graphene buffer layer on SiC(0001). *Carbon N Y*. 2015;81:63-72. doi:https://doi.org/10.1016/j.carbon.2014.08.099

22. Ohta T, Bartelt NC, Nie S, Thürmer K, Kellogg GL. Role of carbon surface diffusion on the growth of epitaxial graphene on SiC. *Physical Review B* . 2010;81(12):121411. doi:10.1103/PhysRevB.81.121411

23. Dagher R, Blanquet E, Chatillon C, et al. A comparative study of graphene growth on SiC by hydrogen-CVD or Si sublimation through thermodynamic simulations. *CrystEngComm*. 2018;20(26):3702-3710. doi:https://doi.org/10.1039/C8CE00383A

24. Srivastava N, He G, Luxmi, Mende PC, Feenstra RM, Sun Y. Graphene formed on SiC under various environments: Comparison of Si-face and C-face. *J Phys D Appl Phys*. 2012;45(15):145001. doi:10.1088/0022-3727/45/15/154001

25. Goler S, Coletti C, Piazza V, et al. Revealing the atomic structure of the buffer layer between SiC(0 0 0 1) and epitaxial graphene. *Carbon N Y*. 2013;51:249-254. doi:https://doi.org/10.1016/j.carbon.2012.08.050

26. Emtsev K V., Speck F, Seyller T, Ley L, Riley JD. Interaction, growth, and ordering of epitaxial graphene on SiC{0001} surfaces: A comparative photoelectron spectroscopy study. *Phys Rev B Condens Matter Mater Phys*. 2008;77(15). doi:10.1103/PhysRevB.77.155303

27. Momeni Pakdehi D, Pierz K, Wundrack S, et al. Homogeneous Large-Area Quasi-Free-Standing Monolayer and Bilayer Graphene on SiC. *ACS Appl Nano Mater*. 2019;2(2):844-852. doi:https://doi.org/10.1021/acsanm.8b02093

28. Riedl C, Coletti C, Iwasaki T, Zakharov AA, Starke U. Quasi-free-standing epitaxial graphene on SiC obtained by hydrogen intercalation. *Phys Rev Lett*. 2009;103(24):246804. doi:10.1103/PhysRevLett.103.246804

29. Jabakhanji B, Michon A, Consejo C, et al. Tuning the transport properties of graphene films grown by CVD on SiC(0001): Effect of in situ hydrogenation and annealing. *Phys Rev B*. 2014;89(8):085422. doi:10.1103/PhysRevB.89.085422

30. Michon A, V́ezian S, Ouerghi A, Zielinski M, Chassagne T, Portail M. Direct growth of few-layer graphene on 6H-SiC and 3C-SiC/Si via propane chemical vapor deposition. *Appl Phys Lett*. 2010;97(17):171909. doi:https://doi.org/10.1063/1.3503972

31. Speck F, Jobst J, Fromm F, et al. The quasi-free-standing nature of graphene on H-saturated SiC(0001). *Appl Phys Lett*. 2011;99(12):122106. doi:https://doi.org/10.1063/1.3643034

32. Heilmann M, Sarau G, Göbelt M, et al. Growth of GaN micro- and nanorods on graphene-covered sapphire: Enabling conductivity to semiconductor nanostructures on insulating substrates. *Cryst Growth Des*. 2015;15(5):2079-2086. doi:https://doi.org/10.1021/cg5015219

33. Jeong J, Wang Q, Cha J, et al. Remote heteroepitaxy of GaN microrod heterostructures for deformable light-emitting diodes and wafer recycle. *Sci Adv*. 2020;6(23). doi:https://doi.org/10.1126/sciadv.aaz5180

34. Barbier C. *Epitaxie de GaN Sur Substrat de Graphène*. Sorbonne Université; 2021. https://theses.hal.science/tel-03469445

35. Timotée Journot. *Epitaxie van Der Waals de GaN Sur Graphène Pour Des Applications En Photonique.* Université Grenoble Alpes; 2018. https://theses.hal.science/tel-01990542

36. Journot T, Okuno H, Mollard N, et al. Remote epitaxy using graphene enables growth of stress-free GaN. *Nanotechnology*. 2019;30(50):505603. doi:10.1088/1361-6528/ab4501

37. Badokas K, Kadys A, Augulis D, et al. MOVPE Growth of GaN via Graphene Layers on GaN/Sapphire Templates. *Nanomaterials*. 2022;12(5):785. doi:https://doi.org/10.3390/nano12050785

38. Sarau G, Heilmann M, Latzel M, Tessarek C, Christiansen S. GaN-Based Nanorods/Graphene Heterostructures for Optoelectronic Applications. *Physica Status Solidi B*. 2019;256(4):1800454. doi:https://doi.org/10.1002/pssb.201800454

39. Qu Y, Xu Y, Cao B, et al. Long-Range Orbital Hybridization in Remote Epitaxy: The Nucleation Mechanism of GaN on Different Substrates via Single-Layer Graphene. *ACS Appl Mater Interfaces*. 2022;14(1):2263-2274. doi:https://doi.org/10.1021/acsami.1c18926

40. Zhilai F, Junyong K. Self-organization of 3D triangular GaN nanoislands and the shape variation to hexagonal. *Journal of Physical Chemistry C*. 2007;111(22):7889-7892. doi:https://doi.org/10.1021/jp071803c

41. Adhikari S, Lysevych M, Jagadish C, Tan HH. Selective Area Growth of GaN Nanowire: Partial Pressures and Temperature as the Key Growth Parameters. *Cryst Growth Des*. 2022;22(9):5345-5353. doi:https://doi.org/10.1021/acs.cgd.2c00453

42. Surrente A, Carron R, Gallo P, Rudra A, Dwir B, Kapon E. Self-formation of hexagonal nanotemplates for growth of pyramidal quantum dots by metalorganic vapor phase epitaxy on patterned substrates. *Nano Res*. 2016;9:3279-3290. doi:https://doi.org/10.1007/s12274-016-1206-7

43. Kim H, Kim JC, Jeong Y, et al. Role of transferred graphene on atomic interaction of GaAs for remote epitaxy. *J Appl Phys*. 2021;130(17):174901. doi:https://doi.org/10.1063/5.0064232

44. Lu Z, Sun X, Xie W, et al. Remote epitaxy of copper on sapphire through monolayer graphene buffer. *Nanotechnology*. 2018;29(44):445702. doi:10.1088/1361-6528/aadb78

45. Kong W, Li H, Qiao K, et al. Polarity governs atomic interaction through two-dimensional materials. *Nat Mater*. 2018;17(11):999-1004. doi:https://doi.org/10.1038/s41563-018-0176-4

46. Kim Y, Cruz SS, Lee K, et al. Remote epitaxy through graphene enables two-dimensional material-based layer transfer. *Nature*. 2017;544:340-343. doi:https://doi.org/10.1038/nature22053

47. Shih CJ, Pfattner R, Chiu YC, et al. Partially-Screened Field Effect and Selective Carrier Injection at Organic Semiconductor/Graphene Heterointerface. *Nano Lett*. 2015;15(11):7587-7595. doi:https://doi.org/10.1021/acs.nanolett.5b03378

48. Tian T, Rice P, Santos EJG, Shih CJ. Multiscale Analysis for Field-Effect Penetration through Two-Dimensional Materials. *Nano Lett*. 2016;16(8):5044-5052. doi:https://doi.org/10.1021/acs.nanolett.6b01876

49. Kobayashi K, Yamaguchi AA, Kimura S, Sunakawa H, Kimura A, Usui A. X-Ray Rocking Curve Determination of Twist and Tilt Angles in GaN Films Grown by an Epitaxial-Lateral-Overgrowth Technique. *Jpn J Appl Phys*. 1999;38(6A):L611. doi:10.1143/JJAP.38.L611

50. Shi BM, Xie MH, Wu HS, Wang N, Tong SY. Transition between wurtzite and zinc-blende GaN: An effect of deposition condition of molecular-beam epitaxy. *Appl Phys Lett*. 2006;89(15):151921. doi:https://doi.org/10.1063/1.2360916

51. Xie MH, Seutter SM, Zhu WK, Zheng LX, Wu H, Tong SY. Anisotropic Step-Flow Growth and Island Growth of GaN(0001) by Molecular Beam Epitaxy. *Phys Rev Lett*. 1999;82(13):2749-2752. doi:10.1103/PhysRevLett.82.2749

52. Ko YH, Kim JH, Gong SH, Kim J, Kim T, Cho YH. Red emission of InGaN/GaN double heterostructures on GaN nanopyramid structures. *ACS Photonics*. 2015;2(4):515-520. doi:https://doi.org/10.1021/ph500415c

53. Chung K, Beak H, Tchoe Y, et al. Growth and characterizations of GaN micro-rods on graphene films for flexible light emitting diodes. *APL Mater*. 2014;2(9):092512. doi:https://doi.org/10.1063/1.4894780

54. Roh I, Goh SH, Meng Y, et al. Applications of remote epitaxy and van der Waals epitaxy. *Nano Converg*. 2023;10(1):20. doi:https://doi.org/10.1186/s40580-023-00369-3

55. Griffiths JT, Ren CX, Coulon PM, et al. Structural impact on the nanoscale optical properties of InGaN core-shell nanorods. *Appl Phys Lett*. 2017;110(17):172105. doi:https://doi.org/10.1063/1.4982594

56. Stampfl C, Van De Walle CG. Energetics and electronic structure of stacking faults in AlN, GaN, and InN. *Phys Rev B*. 1998;57(24):R15052-R15055. doi:10.1103/PhysRevB.57.R15052

57. Ding B, Frentrup M, Fairclough SM, et al. Alloy segregation at stacking faults in zincblende GaN heterostructures. *J Appl Phys*. 2020;128(14):145703. doi:https://doi.org/10.1063/5.0015157

58. Lähnemann J, Jahn U, Brandt O, Flissikowski T, Dogan P, Grahn HT. Luminescence associated with stacking faults in GaN. *J Phys D Appl Phys*. 2014;47(42):423001. doi:10.1088/0022-3727/47/42/423001

Conclusion:

In this PhD the issue of flexible LEDs fabrication has been addressed, mainly through the scope of organized nanowires by SAG and, to some extent, through the scope of growth on 2D materials. In this conclusion part we provide the reader with a summary of the major results of this work and give some perspectives to the next actions that can be taken to push further the domain.

- The growth of the GaN nanowires core through a Si-assisted process has been investigated in detail, confirming the formation of the Si-rich layer described in the literature. This layer has been identified for the first time as a continuous 2ML thick crystalline SiGaN layer with a WZ structure, with an estimated stoichiometry of $SiGa_2N_3$, and a large density of vacancies. Similar compounds have been observed on *c*-plane[1,2] nitrides, and their antisurfactant/mask behavior was attributed to a modification of chemical potentials by charge transfers through the vacancies.

- The presence of this SiGaN compound is critical for the growth of long nanowire (>10µm) with high aspect ratios. The presence of time-periodic markers within the GaN nanowires reveals that before the crystallization of SiGaN, the growth partly proceeds on the sidewall. After SiGaN is deposited, the growth proceeds fully upwards, and a gradual widening of the nanowire occurs through the formation of atomic steps on the sidewalls. This deposition follows a segregation driven process, in which Si accumulates on free *m*-plane surfaces until a critical concentration is reached, at which point SiGaN is formed. Last, the study of the markers revealed kinetic mechanisms similar to the one presented by Hartman *et al.*[3,4] confirming that the process is mass transport limited (i.e. limited by adatom diffusion on the different surfaces).

- Having observed the SiGaN layer, its properties, and its specific role in the core growth, one can easily conclude that the SiGaN hinders the growth of the subsequent shell on the core. This can also be observed on the structural quality and coverage of the shell. Because of that, the removal of the SiGaN layer prior to the shell growth was studied as a way to greatly improve the coverage and crystalline quality of the core-shell heterostructures[5]. Several methods have been investigated, but the most effective appears to be a treatment in hot H_3PO_4. EDX measurement confirmed that this treatment did remove the SiGaN layer. Samples undergoing this treatment feature a much larger shell coverage, as attested by CL, and better crystalline quality, as observed in STEM. They are moreover unaffected by the growth of an UL, contrarily to other effective treatment, such as SF_6 dry etching. Because ULs improve the emitted light intensity by trapping point defects that diffuse toward the surface during growth, it was concluded that the H_3PO_4 treatment solves this issue by slowly etching the GaN surface.

- The integration of the GaN nanowires in a flexible matrix has been demonstrated. The fabricated device has shown successful electrical injection, its light emission has been measured, and it has been operated under bending, which demonstrates its flexibility. However, the sample was not homogeneous and suffered from current spreading issues. We observed an unstable behavior, and inhomogeneous emission due to the injection of different crystallographic planes at different locations. Furthermore, the emission typically changed during bending, with a visible drop in intensity. We suspect the p contact to be responsible for this behavior as it consists in a hybrid structure with an ultrathin NiAu layer and an Ag-NWs mesh. This mesh is discontinuous and its homogeneity is questionable, and the Ag-NWs mesh is suspected to be responsible for poor device performances. This suspicion was further strengthened when the addition of SWCNTs to the p-contact improved the properties.

- The growth on graphene has also been explored and revealed a different growth mode[6]. First, the growth of nanowires on graphene has not been achieved in this work, given that pyramids tend to form. It is suspected that this behavior is caused by the small surface energy of the material, which originates from its lack of dangling bonds. Because of that, graphene behaves more as a mask than as a substrate and promotes thereby diffusion of the species. This resulted, in the case of this study, in tetrahedral nuclei, which is caused by the extended diffusion of the adatoms. Such structures had already been observed in the literature, which allowed to propose general conclusions to their properties. While these structures have been shown to grow following both a WZ and a ZB structure, in this PhD the tetrahedral nanostructures were in majority WZ. In our case, the growth occurs by remote epitaxy with SiC through the graphene; however, these structures have also been grown on graphene over amorphous materials, suggesting that such tetrahedral nanostructures can also grow through Van der Waals epitaxy.

- The growth of InGaN/GaN heterostructures on these structures resulted in a broad signal centered around 450 nm, measured both by CL and PL. Comparison between intensities at room and low temperatures gives an IQE around 25%. The presence of luminescence contributions consistent with basal stacking faults has been observed, further suggesting the interrelation between these structures and the ZB Vs WZ growth, given that a stacking fault in GaN can be understood as a cubic inclusion in a hexagonal lattice.

From these results we conclude that the SAG growth of core-shell InGaN/GaN is a robust process, that can be reliably studied and used. Most of the result obtained on the SiGaN or the kinetics of growth are consistent with the literature, which proves that the process used is highly repeatable. The nature of the passivation layer enabling the growth of long GaN nanowires was finally unraveled. This fundamental understanding will enable not only to tame this layer and use it to form new nanostructures[7]. One example of this is the removal of the SiGaN prior to shell growth, which has been linked to the optimization of the homogeneity and structural properties of the shell, as well as an improved light emission.

The integration of nanowire structures into flexible devices was shown to be technologically complex, requiring several critical steps, as metal contact deposition, encapsulation and separation from the original substrate. In later stage of this PhD, one solution, consisting in depositing the p-contact prior to encapsulation has been investigated, and is described in the last paragraph of the Chapter V. Due to time constraints, this process could not be fully optimized, and no luminescing sample has been produced through this method. Another solution could be to develop a growth process on a metal foil. Indeed, some studies mention the successful self-assembled growth of GaN nanowire on Ti and Ni by MBE, which could be adapted to selective area growth by MOCVD. Doing so would allow to get rid of the need for peel off and n-GaN contact, which may facilitate the process, yield a membrane with less tears and holes, and could facilitate/improve the quality of the p-contact.

When it comes to the growth on 2D materials, the present study reports the growth of tetrahedral structures, but was originally meant to achieve nanowire growth. This deviation from the original goal can be explained by the fundamental differences in behavior of the species on graphene when compared to classical substrate. While this work demonstrated the feasibility of the deposition of optically active InGaN/GaN heterostructures on graphene, it also showed that the growth on 2D materials requires disruptive approaches, as adopting approaches established on other substrates will not yield comparable results. In the future, other 2D materials can be explored for the growth of GaN nanostructures, such as the h-BN that can be used to easily detach GaN growth from substrates[8]. Also, the fabrication of organized domains of graphene can be imagined to favor growth through dangling bonds on the domain edges in order to perform in selective growth mode on 2D materials.

In conclusion, the results obtained in this PhD have allowed to get a more complete understanding of nanowire growth mechanisms, opened the way to integrate SAG structures in flexible LEDs, and provided additional result toward the comprehension on growth on 2D material, which could emerge as an alternative route for flexible device fabrication. Furthermore, graphene has already been used as a p-contact for GaN, and the growth on 2D such as graphene could be optimized to not only ease the encapsulation/peel-off step, but also to provide the structures with a p-GaN contact[9] early in the process.

BIBLIOGRAPHY

1. Dagher R, Lymperakis L, Delaye V, et al. Al5+αSi5+δN12, a new Nitride compound. *Sci Rep*. 2019;9:15907. doi:https://doi.org/10.1038/s41598-019-52363-7

2. Markurt T, Lymperakis L, Neugebauer J, et al. Blocking growth by an electrically active subsurface layer: The effect of si as an antisurfactant in the growth of GaN. *Phys Rev Lett*. 2013;110(3):036103. doi:10.1103/PhysRevLett.110.036103

3. Hartmann J, Wang X, Schuhmann H, et al. Growth mechanisms of GaN microrods for 3D core-shell LEDs: The influence of silane flow. *Physica Status Solidi (A) Applications and Materials Science*. 2015;212(12):2830-2836. doi:10.1002/pssa.201532316

4. Wang X, Hartmann J, Mandl M, et al. Growth kinetics and mass transport mechanisms of GaN columns by selective area metal organic vapor phase epitaxy. *J Appl Phys*. 2014;115(16):163104. doi:https://doi.org/10.1063/1.4871782

5. Bosch J, Coulon PM, Chenot S, et al. Etching of the SiGaxN yPassivation Layer for Full Emissive Lateral Facet Coverage in InGaN/GaN Core-Shell Nanowires by MOVPE. *Cryst Growth Des*. 2022;22(9):5206-5214. doi:https://doi.org/10.1021/acs.cgd.2c00286

6. Bosch J, Valera L, Mastropasqua C, et al. InGaN/GaN QWs on tetrahedral structures grown on graphene/SiC. *Microelectron Eng*. 2023;275:111995. doi:https://doi.org/10.1016/j.mee.2023.111995

7. Puchtler TJ, Wang T, Ren CX, et al. Ultrafast, Polarized, Single-Photon Emission from m-Plane InGaN Quantum Dots on GaN Nanowires. *Nano Lett*. 2016;16(12):7779-7785. doi:https://doi.org/10.1021/acs.nanolett.6b03980

8. Shin J, Kim H, Sundaram S, et al. Vertical full-colour micro-LEDs via 2D materials-based layer transfer. *Nature*. 2023;614:81-87. doi:https://doi.org/10.1038/s41586-022-05612-1

9. Tchernycheva M, Lavenus P, Zhang H, et al. InGaN/GaN core-shell single nanowire light emitting diodes with graphene-based P-contact. *Nano Lett*. 2014;14(5):2456-2465. doi:https://doi.org/10.1021/nl5001295

Annexes:

ANNEX A: FIB PREPARATION DIRECTLY ON SAMPLE

To explain the issues linked to FIB preparation directly on the sample, Fig. A-1 shows an example of preparation and subsequent observation of a full core-shell sample.

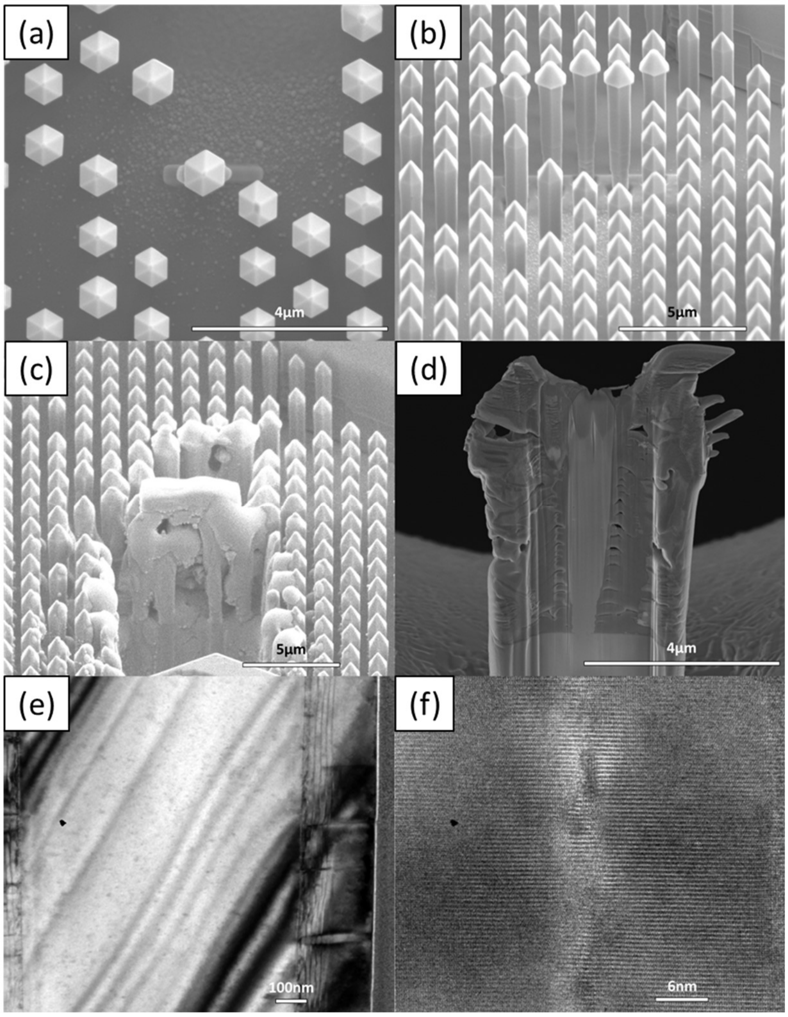

Figure A-1 : *sample at the start of the preparation seen from above (a) and the side (b). after full Pt encapsulation (c), the sample is transferred to a holder and thinned (d). The sample was then imaged using a TEM at low (e) and high (f) magnification.*

The main issues with using the sample as grown are seen all throughout preparation and observation. While no issue is noted at the initial stage (Fig. A-1(a)), one can quickly see that the Pt beam use for the encapsulation deposits on more than one nanowire because of the density of nanowires and angle used (Fig. A-1(b)). The Pt-encapsulation results in an unstructured accumulation of material (Fig. A-1(c)) making it difficult for the user to precisely pick one nanowire. As the lamella is thinned, it reveals some amount of porosity in the Pt (Fig. A-1(c)), which might be of concern for the overall mechanical stability of the sample. The thinning itself is difficult, as it is difficult to recognize the crystallographic directions, since the shape of the nanowires are hidden in the Pt. This leads to off-axis thinning, which may result in a thickness variation. This can be seen during observation in a transmission electron microscope setup as an interference pattern, as seen in Fig. A-1(d), and it may also lead to poor imaging quality, such as seen in Fig. A-1(e). While preparing on the sample allows to see both the sample and the substrate, it also means a difficult preparation and a poor quality of imaging. Therefore, unless stated otherwise, the nanowires presented in this manuscript have been separated from the substrate with a razor blade and laid on a SiO/Si wafer.

ANNEX B: CONCENTRATION ESTIMATION BY EDX IN STEM

Quantitative EDX is a challenging process, as various processes may influence the X-ray intensity response and detection, leading to a limited precision in the measurement process. One exemple of this issue can be seen clearly when looking at the measurements presented in Chapter 3. Figure B-1 shows an HAADF measurement around the SiGaN junction (Fig. B-1(a)) and corresponding EDX measurement (Fig. B-1(b)). As observed several times in Chapter 3, the HAADF measured thickness is 2ML. Because HAADF is sensitive to the chemical nature of the sample, this measurement is reliable. However, in Fig. B-1(b), the Si signal corresponding to the SiGaN is measured over 2nm, which is significantly thicker.

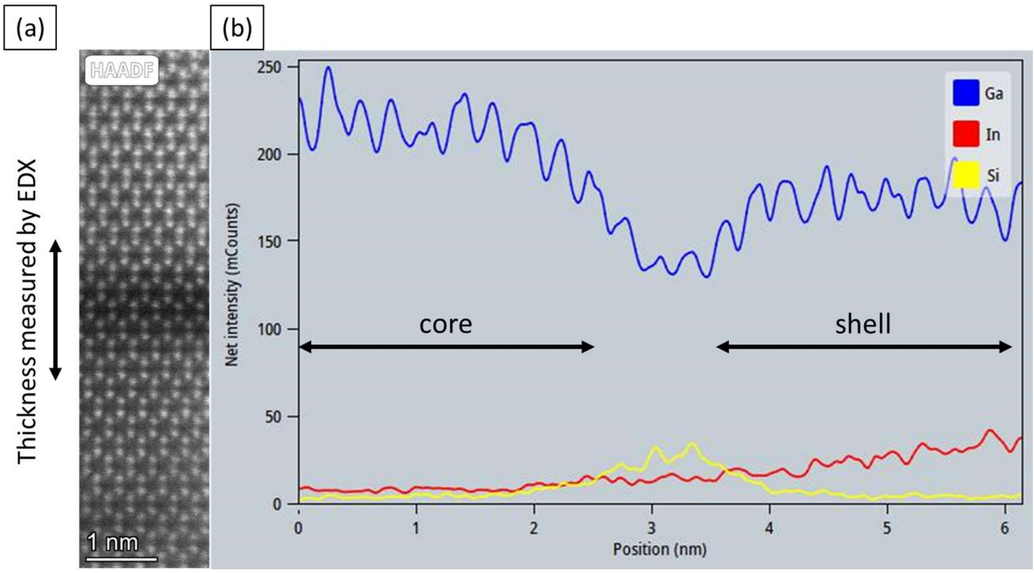

Figure B-1: *HAADF measurement around the GaN/SiGaN/InGaN junction (a), and corresponding EDX intensity profile (transversal lamella, sample A)*

This origin of this discrepancy is known and is caused by the convergence of the beam used for high resolution measurements. While high convergence is required to characterize layers with a thickness of the order of the ML, it also implies that the EDX cross section is higher than the intended beam size, as schematized in Fig. B-1.

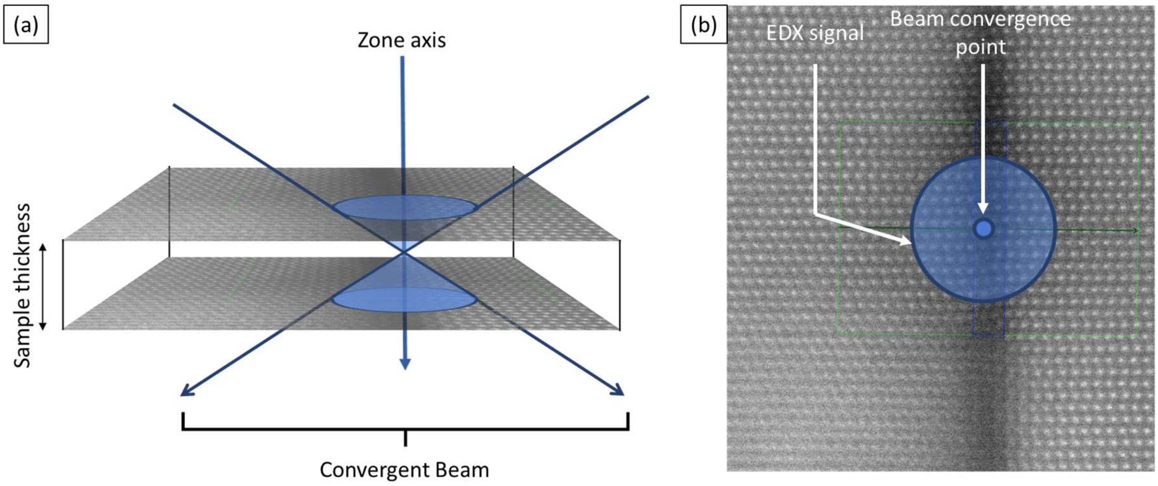

Figure B-2: *convergent beam and EDX measurement seen from the side (a) and from above (b).*

Therefore, to get a truthful estimation of the Si-content in the layer, the data first needs to be processed to correspond to HAADF observation. It can be noted the In profile follows a linear increase from the GaN to the InGaN layer, as seen in Fig. B-1(b). Therefore, the In concentration given without any data treatment is going to be less affected by the beam convergence than a local spike in concentration, as is the case with Si. This In concentration is below 5% in the SiGaN, and the presence of In in SiGaN can hence be negliged, which simplifies the calculation.

First, the signal I corresponding to each element in the SiGaN layer is integrated on the thickness of the layer, l. The thickness of the layer is determined by the presence of a significant Si-content. I is measured relative to the intensity in the GaN core, I_0. It is assumed that for Si that $I_0 = 0$, while it can be directly measured on the EDX profile for Ga. The calculation assumes that for each element, I is constant in SiGaN. The integrated intensity, A, is calculated such as:

For Si:

$$A = \frac{\sum_i I_i}{n_{total}} \cdot l \quad \mathbf{(B.1)}$$

For Ga:

$$A = \left(I_0 - \frac{\sum_i I_i}{n_{total}}\right) \cdot l \quad \mathbf{(B.2)}$$

From the integrated intensity, it is possible to obtain the equivalent intensity in SiGaN for each element:

For Si:

$$I_{Si} = \frac{A}{l_{SiGaN}} \quad \mathbf{(B.3)}$$

For Ga:

$$I_{Ga} = I_0 - \frac{A}{l_{SiGaN}} \quad \mathbf{(B.4)}$$

The intensities can then be used to estimate the relative concentrations. To do so, we used the so-called method of the k-factors, which is an empirical method that estimate relative concentration by a factor k established in a material with known concentrations, and defined as:

$$\frac{C_{Ga}}{C_{Si}} = k_{GaSi}\frac{I_{Ga}}{I_{Si}} \quad \mathbf{(B.5)}$$

The software allows to get the value of $k_{GaSi} = 2.04$, I_{Si} and I_{Ga} are given in $\mathbf{(B.3)}$ and $\mathbf{(B.4)}$. Assuming $C_{Ga} + C_{Si} = 1$, we can write:

$$C_{Ga} + C_{Si} = 1 \overset{\mathbf{(B.5)}}{\Longrightarrow} C_{Si} \cdot \left(1 + k_{GaSi}\frac{I_{Ga}}{I_{Si}}\right) = 1 \Rightarrow C_{Si} = \frac{1}{1 + k_{GaSi}\frac{I_{Ga}}{I_{Si}}} \quad \mathbf{(B.6)}$$

$$C_{Ga} = 1 - C_{Si} \quad \mathbf{(B.7)}$$

From $\mathbf{(B.6)}$ and $\mathbf{(B.7)}$, we obtain the concentrations of Si and Ga, as presented in Chapter 3, Table III-1.

ANNEX C: SiGaN DENSITY AND VACANCIES

To explain the results presented in Fig. III-8, the data will be interpreted following the ζ-factor model. This method considers the EDX intensity as following the equation $\mathbf{(C.1)}$:

$$I_A = {}^{C_A \cdot D \cdot \rho t}\!/_{\zeta_A} \quad \mathbf{(C.1)}$$

With $I_A$and C_A the EDX intensity and concentration of element A, D the electronic dose, ρ the density of the material, and t t the thickness of the lamella. ζ_A is the ζ-factor of element A, and is defined as:

$$\zeta_A = {}^{M_A}\!\Big/_{N_V \cdot Q_A \cdot w_A \cdot \varepsilon_A \cdot \frac{\Omega}{4\pi}} \quad \mathbf{(C.2)}$$

With N_V Avogadro's number, $\frac{\Omega}{4\pi}$ the solid angle of detection, M_A, Q_A, w_A and ε_A respectively the atomic mass, ionization cross section, fluorescence efficiency, and detector's sensitivity for element A. Note that these parameters are element specific but stay constant during the measurement.

In the next calculations, t and D are assumed to be constant. Owing to low In concentration in both the InGaN and the SiGaN, we assume that $\rho_{InGaN} \approx \rho_{GaN} = \rho$

<u>In GaN :</u>

In GaN, both the In and Si concentration are assumed to be negligible. Hence:

$$C_{Ga} = 1 \Rightarrow I_{Ga} = {}^{D \cdot \rho \cdot t}\!/_{\zeta_A} \quad \mathbf{(C.3)}$$

<u>In InGaN :</u>

In InGaN, the Si concentration is assumed to be negligible. Hence:

$$I_{InGaN} = D \cdot \rho \cdot t \cdot \left(\frac{C_{Ga}}{\zeta_{Ga}} + \frac{C_{In}}{\zeta_{In}}\right)$$

The difference in EDX intensity in GaN and InGaN is assumed to be negligible, and the In concentration in InGaN is measured to be below 5%. We can conclude that:

$$I_{InGaN} \approx I_{GaN} \Rightarrow \frac{C_{Ga}}{\zeta_{Ga}} + \frac{C_{In}}{\zeta_{In}} \approx \frac{C_{Ga}}{\xi_{Ga}} \quad \mathbf{(C.4)}$$

<u>In SiGaN :</u>

$$I_{SiGaN} = D \cdot \rho_{SiGaN} \cdot t \cdot \left(\frac{C_{Ga}}{\zeta_{Ga}} + \frac{C_{In}}{\zeta_{In}} + \frac{C_{Si}}{\zeta_{Si}}\right) \xRightarrow{\mathbf{(C.4)}} I_{SiGaN} = D \cdot \rho_{SiGa} \cdot t \cdot \left(\frac{C_{Ga}}{\zeta_{Ga}} + \frac{C_{Si}}{\zeta_{Si}}\right) \quad \mathbf{(C.5)}$$

By dividing $\mathbf{(C.3)}$ and $\mathbf{(C.5)}$, we obtain:

$$\frac{I_{SiGaN}}{I_{GaN}} = \frac{\rho_{SiGaN}}{\rho} \cdot \frac{\left(\frac{C_{Ga}^{SiGaN}}{\zeta_{Ga}} + \frac{C_{Si}^{SiGaN}}{\zeta_{Si}}\right)}{\frac{C_{Ga}^{GaN}}{\zeta_{Ga}}}$$

With C_{Ga}^{SiGaN} and C_{Si}^{SiGaN} respectively the cationic concentration of Ga and Si in SiGaN, and C_{Ga}^{GaN} the cationic concentration of Ga in GaN.

From Table. III-1 (Chapter 3): $C_{Ga}^{SiGaN} \approx \frac{2}{3}; C_{Si}^{SiGaN} \approx \frac{1}{3}$

From $\mathbf{(C.3)}$: C_{Ga}^{GaN}=1

Therefore:

$$\frac{I_{SiGaN}}{I_{GaN}} = \frac{1}{3} \cdot \frac{\rho_{SiGaN}}{\rho} \cdot \frac{\left(\frac{2}{\zeta_{Ga}} + \frac{1}{\zeta_{Si}}\right)}{\frac{1}{\zeta_{Ga}}} \quad \mathbf{(C.5)}$$

By definition of the k-factor given in Annex B $\mathbf{(B.5)}$, in any given material:

$$k_{GaSi} = \frac{I_{Ga} \cdot c_{Si}}{I_{Si} \cdot c_{Ga}} = \frac{c_{Si} \cdot c_{Ga} \cdot D \cdot \rho \cdot t}{c_{Si} \cdot c_{Ga} \cdot D \cdot \rho \cdot t} \cdot \frac{\zeta_{Ga}}{\zeta_{Si}} = \frac{\zeta_{Ga}}{\zeta_{Si}} \Rightarrow \zeta_{Si} = \frac{\zeta_{Ga}}{k_{GaSi}} \quad \mathbf{(C.6)}$$

Combining $\mathbf{(C.5)}$ and $\mathbf{(C.6)}$:

$$\frac{I_{SiGaN}}{I_{GaN}} = \frac{1}{3} \cdot \frac{\rho_{SiGaN}}{\rho} \cdot \frac{\left(\frac{2}{\zeta_{Ga}} + \frac{k_{GaSi}}{\zeta_{Ga}}\right)}{\frac{1}{\xi_{Ga}}} = \frac{1}{3} \cdot \frac{\rho_{SiGaN}}{\rho} \cdot (2 + k_{GaSi})$$

We can hence estimate the variation of density, ρ, between the GaN and the SiGaN:

$$\frac{\rho_{SiGaN}}{\rho} = \frac{I_{SiGaN}}{I_{GaN}} \cdot \frac{1}{\frac{1}{3} \cdot (2 + k_{GaSi})} = 0.77 \cdot \frac{1}{\frac{1}{3} \cdot (2 + 2{,}04)} = 0.57 \quad \mathbf{(C.7)}$$

This calculation yields a 43% reduction in cationic density in SiGaN compared to GaN. This difference can be partly attributed to the lower atomic weight of Si compared to Ga. However, replacing half of the cationic sites by a Si atom should only result in a 30% decrease in cationic density. Because no other cationic specie lighter than GaN has been identified in significant amounts in SiGaN, a drop of in intensity can be attributed to the presence of significant amounts of vacancies. When accounting for a similar concentration for Ga, Si and v_{Ga} on the cationic sites in SiGaN, a 53% drop of cationic density compared to GaN is expected. While this value is close to the value obtained in $(\mathbf{C.7})$, two assumptions make this value unprecise. First, the impact of the In was neglected, despite a difference in EDX intensity between GaN and InGaN. Second, this calculation does not consider the effect of the beam convergence, as is the case in annex B. Therefore, despite strongly hinting at a significant concentration of vacancies, no quantitative conclusions can be drawn from this calculation.

ANNEX D: VOLUMIC RATE CALCULATION

In this annex, the methods used to obtain the volume variation as function of marker's width and spacing will be provided. The structure is represented in Annex D-1, showing the projection of the structure in the c-direction (Annex D-1(a)) and a-direction (Annex D-1(b)). In annex D-1(b), two markers are also represented to show the spacing between two markers dx. The geometrical parameters used in this annex are marked in red on the figure.

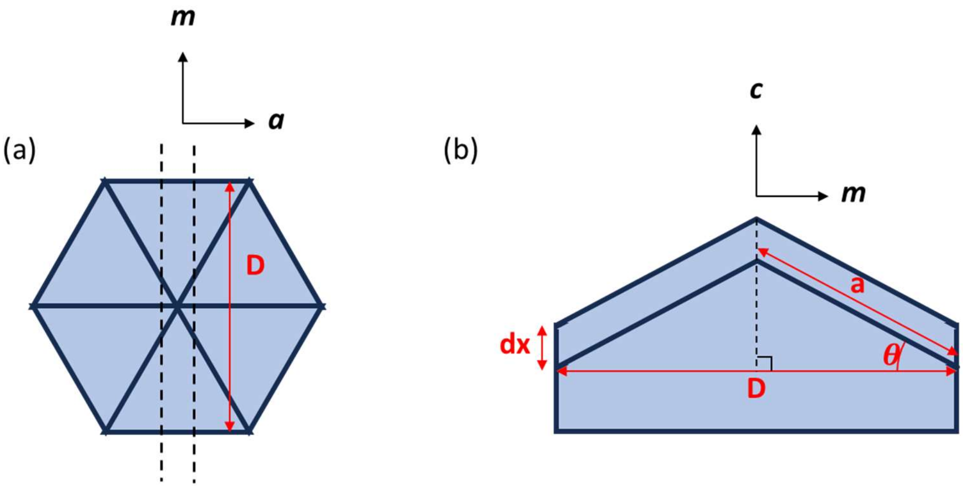

Figure D-1: *Geometrical parameters of the Si-rich markers in transveral (a) and longitudinal (b) view*

For the sake of the calculation, the hexagonal shape of the nanowire will be assumed to correspond to a perfect regular hexagon. The combined areas of the lateral faces of a hexagonal pyramid can be calculated as:

$$A = \frac{P \cdot a}{2} \quad (\mathbf{D.1})$$

With P the perimeter of the base and a the apothem of the pyramid.

In the case of an hexagon, it can be shown that the perimeter is equal to:

$$P = 12 \cdot \frac{\frac{D}{2}}{\sqrt{3}} = 2\sqrt{3} \cdot D \quad \mathbf{(D.2)}$$

a could be realistically measured for each measurement. However, looking at Annex D-1(b), we can also express it as :

$$\frac{a}{D/2} = \cos(\theta) \Longrightarrow a = \frac{\cos(\theta)}{2} \cdot D \quad \mathbf{(D.3)}$$

θ is the angle between the c-plane and the semipolar planes of the markers and can be assumed to be constant, which has also be verified on the pictures. This simplification avoid to measure a for each marker. Hence, combining $\mathbf{(D.1)}$, $\mathbf{(D.2)}$ and $\mathbf{(D.3)}$, we obtain:

$$A = \cos(\theta) \cdot \frac{\sqrt{3}}{8} \cdot D^2 \quad \mathbf{(D.4)}$$

In order to calculate the volume deposited between each marker, A just needs to be multiplied by dx. This directly stems from the assumption that $\theta = Cste$, as it means that dx is constant throughout the surface of the hexagonal pyramid.

Hence :

$$dV = A \cdot dx \quad \mathbf{(D.5)}$$